ABSTRACT

Title of dissertation: ORIENTATION-DEPENDENT SURFACE ENERGY CHARACTERIZATION OF MAGNETOSTRICTIVE ALLOYS FOR ABNORMAL GRAIN GROWTH MODELING

Michael Van Order, Doctor of Philosophy, 2018

Dissertation directed by: Professor Alison B. Flatau
Materials Science and Engineering

High sensitivity semiconductor, optical, and sensing devices require single crystal metals for their isotropy which allows for unique material properties. However they are expensive and difficult to produce. By using abnormal grain growth (AGG) techniques, our group can produce single-crystal-like materials that achieve 90% performance of true single-crystals at 5% of the cost. Fully understanding AGG mechanisms is crucial to the growth of high quality, cost effective alloy fabrication. Many advances have been made to understand key parameters of AGG, and we postulate that the final piece lies in understanding the surface energy of our alloys. While several surface energy measurement techniques have been developed for low-energy plastic surfaces, high-energy metal surfaces have largely been ignored due to the complexity of sample preparation and experimentation. This dissertation investigates three measurement techniques targeted for high-surface-energy iron-alloy crystal facets.

The first of these techniques, the gallium drop contact angle method, examined a droplet of liquid metal gallium resting on our metal sample. By recording the shape

of this droplet, a value for surface energy of targeted crystal orientations is acquired using our derived thermodynamically-based mathematical model. This study experimentally confirmed trends that are predicted in theoretical models, but identified that oxide formation on the sample surface interferes with acquisition of accurate quantitative results. This revelation led to a more robust study that expands on classic drop shape analysis techniques and eliminates complications associated with oxide layer formation. For this, multiple oxide removal procedures were performed and analyzed using X-ray photoelectron spectroscopy. The most promising procedures are polishing in an inert atmosphere and ion bombardment cleaning. Immersing the sample in an oil environment isolates this unstable iron-alloy surface from air and prevents oxidation. While in this environment, samples are probed with a deionized water droplet and a shape analysis is performed to calculate surface energy values using the Schultz method. This dissertation describes modifications to this method that utilize a technique previously only used on plastics to prevent water from spreading. I hypothesize that patterning sample surfaces with an ion mill will stabilize droplets during shape measurements, thus generating reliable surface energy calculations. Success of each technique could allow metallurgists to finally experimentally measure surface energy for any metal surface, thus providing confirmations of theory and sparking new ideas of how grain growth in metals can be controlled and even manipulated.

ORIENTATION-DEPENDENT SURFACE ENERGY CHARACTERIZATION OF MAGNETOSTRICTIVE ALLOYS FOR ABNORMAL GRAIN GROWTH MODELING

by

Michael Norman Van Order

Dissertation submitted to the Faculty of the Graduate School of the
University of Maryland, College Park in partial fulfillment
of the requirements for the degree of
Doctor of Philosophy
2018

Advisory Committee:
Professor Alison B. Flatau: *Advisor, Chair*
Professor Norman M. Wereley: *Dean's Representative*
Professor Raymond J. Phaneuf
Professor Ichiro Takeuchi
Professor Robert M. Briber

Acknowledgments

There are many who have helped me along this journey. Listed below are a few who stand out, but at this moment I would like to thank everyone I have met and talked with over the course of my graduate career. I have grown significantly over the past five years and it is largely due to the lessons I have learned from people. Thank you all.

I must first thank Dr. Suok-Min Na without whom I would not have this project. He produced the highly-textured polycrystalline Galfenol I measured, taught me the rolling and annealing process, and first had the idea for measuring surface energy on Galfenol. The Ames Laboratory was also instrumental in producing single crystal Galfenol samples that were integral to my surface energy measurements.

The Magnetic Materials group at the Naval Surface Warfare Center: Carderock Division allowed me access to the automatic polishing system and vibratory polisher. My samples would not have been flat enough for contact angle measurements were it not for the vibratory polisher. I thank Nick Jones, Paul Lambert, Jin-Hyeong Yoo, and Marilyn Wun-Fogle for their advice and support.

The UMD Nanocenter had a wide breadth of equipment and knowledge of material processing and measurement that I gladly took advantage of during this project. Tom Loughran was essential to my photolithography techniques, ion milling, and plasma-processing experiments. I would also like to thank the rest of the Nanocenter staff, Jonathan Hummel, Mark Lecates, and John Abrahams, for their support and guidance.

The Department of Civil and Environmental Engineering provided the contact angle goniometer. I would not have known about it or had access to it without the help of Marya Anderson. Her wonderful personality and amazing perspective is something I will always appreciated everytime I passed by her office. I thank her for always trying to answer my chemistry questions and letting me back into the lab when I locked myself out.

The Department of Aerospace Engineering at UMD is a world-class department that I was lucky to be affiliated with during this project. I have learned so much about the aerospace field from talking with colleagues and friends. So much so that I now consider the aerospace industry as a viable career. I thank Jonathan Lefebvre, Hülya Biler, and Girguis Sedky for their constant support while I wrote this dissertation.

TU Dresden was my lab from abroad where I learned the power of working with a team in research. From this team, I learned how to code in Python, develop devices, and communicate with international audience. I would like to thank Phillip Frank, Sebastian Haefner, and Andreas Richter for accepting me into their group for the summer and providing all the instruction and guidance I needed to succeed.

My labmates over the years for stimulating conversation and support. I enjoyed learning from all of you. I thank Steve Day for welcoming me to the Aerosmart group with his positivity. I thank Ganesh Raghunath for always inspiring me to do my best in lab and never settle. I thank Chris Damion for his grounding personality and high quality work. I thank my collaborator and writing partner Shayandev Sinha for his unending positivity and encouragment that helped me publish my first paper. I thank Liz Barranco for her commitment and ability to focus despite my constant

interruptions. It has been refreshing to see her accomplish so much in such a short amount of time. I thank Julia Downing for giving me a reason to be a better mentor and a better all around person. Her hard work and intelligence has flourished since she first joined our group and I am extremely proud of her. I thank Brooks Muller for his friendship and constant encouragement. There were many days when I felt very down and he went out of his way to help me feel better. I thank JJ Park for his support and encouragement to figure out problems that seem insurmountable. He was the first person to sit down and show me how to use an instrument with extreme patience. I have taken this lesson with me to students that I instruct, and hopefully they can learn as well as I did from JJ. Finally, I thank Dr. Alison Flatau without whom none of these group members, projects, and inspirations would have thrived to their highest potential. I have yet to meet a better communicator of science to any audience she comes across. She spends long hours giving everyone she meets the time they need and more to understand a concept, edit a communication, or flesh out some new data. I will always be in her debt for her patience, attention, and encouragement that allowed me to grow and produce work that I am proud of. I thank her for all that she does.

I must thank my friends who are always around for me to vent my frustrations and celebrate my accomplishments. My family has supported me my entire life. I thank my mother for her strong will and desire to always ask questions. I thank my father for inspring me to pursue a doctorate at a young age and guiding me through all my significant life events. I thank my sister whose ambition inspires me to step outside my comfort zones.

More than anyone, I thank my best friend and partner, Alyson Becker. She is my everything in this world. She has helped me grow to be the best version of myself in multiple ways. I am more confident and competent person because of her undying support. I owe her more than I could ever repay.

Contents

List of Figures

List of Tables

Chapter 1

Introduction

1.1 Magnetostriction Physics

Unpaired electrons in the valence shell, or unbalanced spins, can produce significant magnetism in an atom. Their contribution to magnetism is negligible since these electrons are used in bonding when forming a solid.[15] The preserved magnetic moments in solids are more characteristic of an element's ionic electron configuration (Fe^{3+} rather than Fe) or with sufficient bonding electrons added to complete the shell. The only groups of elements in the periodic table which exhibit magnetic moments in the solid phase are those in which the unbalanced electron populations occur in an inner shell, namely the transition metals ($3d$, $4d$, and $5d$), rare earths ($4f$), and actinides ($5f$). It is clear that the more tightly bound an unfilled orbital shell is the less the unpaired electrons will have to do with bonding and the more they will contribute to magnetism. This is why we see very strong magnetic responses in rare earth materials which use $6s$ and $5d$ shells for bonding before using the very tightly bound $4f$ shell

electrons. The $3d$ electrons in transition metals are less tightly bound to the nucleus, and sometimes $3d$ electrons are used for bonding.

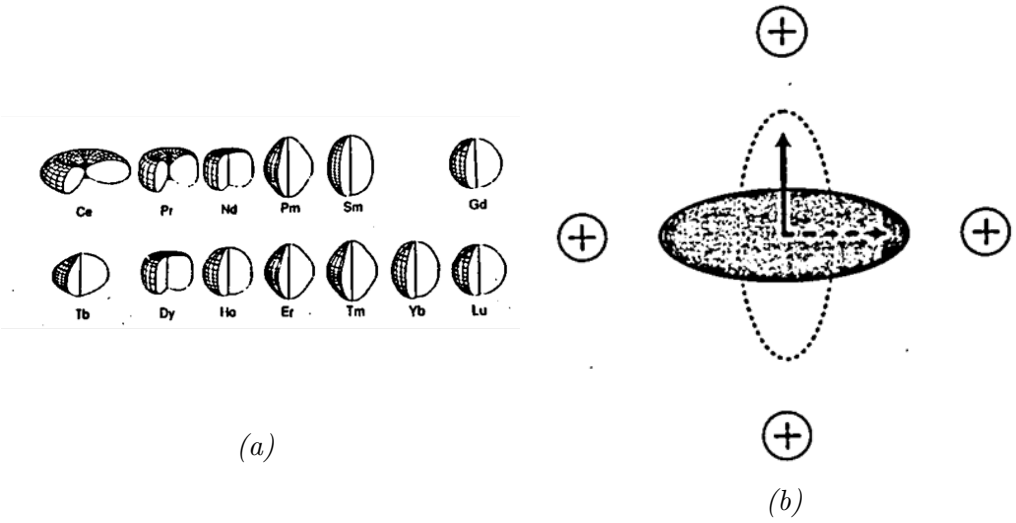

Figure 1.1: (a) 4f electron charge cloud densities for a number of rare earth elements. (b) Schematic of oblate 4f charge density of a rare earth element with + nearest neighbors, such as Tb, rotating in a magnetic field. Extracted from Engdahl et al.[1]

Magneto-elasticity is the coupling between the classical properties of elasticity and strain in a material and the quantum mechanical and relativistic phenomena of magnetism. When a spin imbalance occurs, electrons can order in such a way that the net magnetic moment points in a particular direction which lowers the crystal symmetry and produces new properties, like magnetostriction.[15] This coupling between magnetism and elasticity derives from the large contribution of the spin moment to the magnetic moment. Hence, coupling occurs if there is a strong coupling between the *direction* of the atom's spin moment and the *orientation* of its anisotropically shaped electron charge cloud, as seen in Figure 1.1. This coupling that exists at the individual electron level is called spin-orbit coupling. It is one of the smallest energies

used to describe the state of an atom because it derives from relativistic aspects of the electron motion. It is easiest to see this coupling in rare earth elements where the spin directions of rapidly moving $4f$ electrons are strongly coupled to the orientation of their orbits. This individual electron spin-orbit coupling leads to strong coupling between the total spin moment and the total electron density. Thus, in rare earth elements the spin moment can be envisioned as rigidly attached to the anisotropically shaped electron charge cloud. We can now define magnetic anisotropy as the tendency of a magnetic moment to point in a specific crystalline direction, the easy magnetization direction, because of the electrical attraction/repulsion between the rotating electronic charge cloud and neighboring charged ions, as seen in Figure 1.1b. It is important to note that $3d$ electrons obey the same magnetoelastic trends, but with a factor of ten less for spin-orbit coupling.[1]

This interaction causes ion movement which results in a macroscopic strain that can be measured at the parts per million (ppm) scale. When an applied magnetic field causes a change in the material's magnetic moment direction, a strain arises from positive ion movement, as shown in Figure 1.2. This is called Joule magnetostriction named after James Prescott Joule who discovered the effect in 1842 when observing a sample of iron. The increase in length (longitudinal strain) or the contraction of diameter (lateral strain) is roughly proportional to the applied magnetic field and this can be used for various purposes in an actuator mechanism.[2]

Another widely utilized effect related to magnetostriction is the Villari Effect. When a mechanical stress is imposed on a sample, there is a change in the magnetic flux density which flows through the sample as a result of the generated magnetic field.

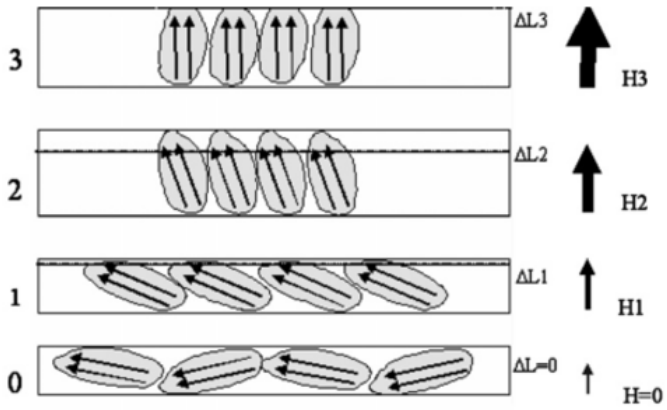

Figure 1.2: An illustration of joule magnetostriction. The magnetic moments align themselves with the applied field and cause the positive ions around them to shift and cause a strain. Extracted from Olabi et al.[2]

The change in flux density is proportional to the level of the applied stress. This flux density change can be detected by a pickup coil to use the magnetostrictive material for sensing applications. To quantitatively understand the contributing factors of magnetostriction, consider a basic example of a two dimensional planar magnet. The magnet is elastically isotropic in the x-y plane, with uniaxial magnetic anisotropy such that the magnetization with magnitude M_s prefers to lie along the x-axis,[1] as seen in Figure 1.3.

The total energy consists of energies from the Zeeman or magnetic field, uniaxial magnetic anisotropy, magnetoelastic coupling, intrinsic elastic stiffness, and coupling energy between strain and stress:

$$\begin{aligned} E_{total} &= E_H + E_{anis} + E_{me} + E_{elas} + E_{stress} \\ &= -HM_s\alpha_y - K\alpha_x^2 - b(\epsilon_{xx}\alpha_x^2 + \epsilon_{yy}\alpha_y^2 + \epsilon_{xy}\alpha_x\alpha_y) \\ &+ \left[\frac{1}{2}C_{11}\epsilon_{xx}^2 + \frac{1}{2}C_{11}\epsilon_{yy}^2 + C_{12}\epsilon_{xx}\epsilon_{yy} + \frac{1}{2}(\frac{C_{11}-C_{12}}{2})\epsilon_{xy}^2\right] - \sigma\epsilon_{yy} \end{aligned} \tag{1.1}$$

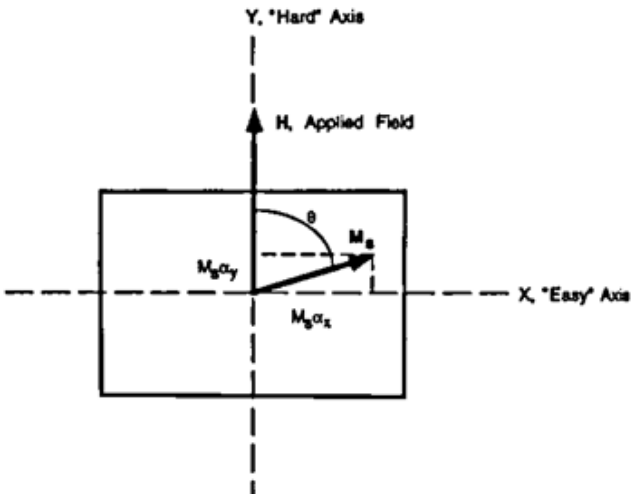

Figure 1.3: Schematic for planar magnet showing the magnetization, M_s, rotating in the x-y plane away from the easy x-axis toward the field, H, applied along the y-axis. Extracted from Engdahl et al.[1]

where H is the applied auxiliary field, α_y is the normalized component of magnetization in the y-direction M_y/M_s, K is the energy difference between M_x and M_y, b is the magnitude of coupling, ϵ_{xx} is the strain in the x-direction, C_{11} and C_{12} are independent elastic constants, and σ is the applied stress. If there is no magnetoelastic coupling, $b = 0$, the planar magnet would respond independently to field and stress. Magnetostriction is determined by measuring the change in length along some direction as the magnetization rotates. To determine the coupled response, we minimize the total energy with respect to strain and magnetization direction. Solving for the difference in ϵ_{yy} for M along the y-direction and M along the x-direction:

$$\frac{\Delta l}{l} = \Delta\epsilon_{yy} = \frac{b}{C_{11} - C_{12}} \equiv \lambda \tag{1.2}$$

where λ is the magnetostriction constant, an effective figure of merit for magnetostrictive materials. This definition shows us the observed change in length along

the magnetization direction if the sample was initially magnetized perpendicular to the applied field. If a magnetic field is applied to the material at an angle to an easy axis of magnetization the material will tend to rearrange its structure. This rearrangement will align the easy axis with the field to minimize the free energy of the system, as depicted in Figure 1.3.

Since different crystal directions are associated with different lengths this effect induces a strain in the material. In a three dimensional isotropic material where $K = 0$, the total energy must sum all terms in the elastic strain tensor ϵ_{ii} as well as the normalized magnetization direction vectors α_i. Similar to the planar case, energy minimization gives us the magnetostrictive strain in 3D:

$$\frac{\Delta l}{l} = \frac{b}{C_{11} - C_{12}} \left(\alpha^2 - \frac{1}{3} \right) \equiv \frac{3}{2} \lambda_s \left(\alpha^2 - \frac{1}{3} \right) \tag{1.3}$$

where α is the cosine of the angle between magnetization and measured directions, and λ_s is the saturation magnetostriction constant. Equations 1.2 and 1.3 make it clear that increasing the magnetoelastic coupling and decreasing the elastic constants will increase the magnetostrictive constant. However, when considering the force of a magnetostrictive material ($\sim \lambda C$), a reasonably high elastic constant becomes more desirable. From this observation, a rare-earth metal with its very high spin-orbit coupling would seem to be a perfect candidate for magnetostrictive applications.

1.2 Magnetostrictive Materials

As we have seen, the magnetic moments in magnetostrictive materials are already aligned in a particular direction because they are intrinsically ferromagnetic. Materials like Tb and Fe have Curie temperatures of 220 K and 1044 K, respectively. These temperatures tend to change when alloyed with other metals: Terfenol-D ($Tb_xDy_{1-x}Fe_2$) has $T_C = 653$ K and Galfenol ($Fe_{100-x}Ga_x$) has $T_C = 978$ K.[16] Most magnetostrictive materials are soft magnets, so they have a low coercivity. Hard magnet magnetostriction has only been seen in thin films at very low temperatures.[17,18] This property enables easy switching of the magnetization direction for potential applications in energy harvesting.[19]

Terfenol-D (Ter for terbium, Fe for iron, NOL for Naval Ordnance Laboratory, and D for dysprosium) is a rare-earth alloy developed by Ames Laboratory in the 1980s that exhibits about 2000 ppm magnetostriction in a field of 2 kOe (160 kA/m) at room temperature. Many magnetostrictive alloy materials have been fabricated to increase saturation magnetostriction to a level of 5000 ppm.[2] However, Table 1.1 shows us that Curie temperatures of materials with the highest λ_s, like $Tb_{0.5}Dy_xZn_{1-x}$, are not high enough for commercial application. Terfenol-D operates at the highest saturation strain and Curie temperature than any other magnetostrictive materials to date.

Terfenol-D attains optimum magnetostrictive properties in the form of single crystals. Since the easy axis of magnetization for Terfenol-D is <111>, it is desirable to produce single-crystal rod having such an axial orientation.[20] It is also advantageous

Table 1.1: This table compares the magnetostrictive strain capabilities of pure materials and alloys. Extracted from Olabi et al..[2]

Material	Saturation strain (ppm)	Curie temperature (K)
Ni	-50	630
Fe	-14	1040
Fe_3O_4	60	860
Terfenol-D	2000	650
$Tb_{0.5}Dy_xZn_{1-x}$	5000	200

to achieve a minimum defect concentration so that domain wall motion is not hindered by pinning mechanisms between defects and domain walls.[21] Researchers and manufacturers tend to use the float-zone solidification method, FZSM, and the Bridgman method to produce these high quality single crystals.

The FSZM method is limited to rods of 8 mm diameter maximum because the process is containerless and surface tension limits the size of the molten zone that can be generated during the process. The modified Bridgman is limited to a minimum rod size of 10 mm because of side nucleation from the mold walls overwhelming the primary, axial dendritic crystal growth.[22] In both cases, secondary machining is required to generate complex geometries beyond right-angle cylinders, which can be very costly and only add to the long processing time. If these methods are sped up to meet commercial demands, resulting materials can develop many defects in the crystal structure leading to mechanical failure. Terfenol-D is already very brittle in tension, so the possibility of more brittle failure does not bode well for some applications involving bending and tesnsile stress.[2]

Applications for the magnetostrictive properties of Terfenol-D revolve around actuators and sensors. An actuator is a type of motor that is responsible for moving

or controlling a mechanism or system. It is operated by a source of energy, typically electric current, hydraulic pressure, or pneumatic pressure, and converts that energy into motion. In the case of magnetostrictive actuators, movement is controlled by varying the current through a driving coil wrapped around the magnetostrictive material. Varying the current through the wire coil produces a time-varying magnetic field in the magnetostrictive core of the drive coil. The change in magnetic field causes a change in the lengths and diameter of the magnetostrictive core and drives a vibration. Etrema designed, built, and validated a Terfenol-D actuator device capable of generating seismic waves, although it can operate over a wide bandwidth of frequencies. It can generate a force of 4000 N or an acceleration of 30 g at the device's resonant frequency of 635 Hz.[2]

The challenges for processing Terfenol-D stems from its high material cost. Terbium of 99% purity currently costs $724.50 per kg which does not count shipping rates from China.[23] China makes up about 97% of the rare mineral trade worldwide, and it is not predicted to change in the near future.[24] High temperature and high controllability of production methods contribute to the slow production and high cost of Terfenol-D and further leads to the financial cost of its devices. We have discussed the brittleness of Terfenol-D, which limits its ability to withstand shock loads or operate in tension.[25] Large anisotropies exhibited by rare earth metals, like terbium, usually require very large fields to change the direction of the magnetization.[1]

Galfenol, an iron-gallium alloy, has recently gained attention as an alternative to Terfenol-D because of its large magneto-mechanical coupling, low hysteresis loss, and high saturation magnetization.[26] It was developed as an alternative to rare-earth

magnetostrictive materials. The magnetostriction in Galfenol arises from its $3d$-shell spin-orbit coupling. While this is weaker than $4f$ spin-orbit coupling, Galfenol has seen saturation strains up to ∼400 ppm under very low magnetic fields ∼100 Oe (8000 A/m).[27] It has demonstrated high tensile strength (∼500 MPa) with limited variation in magnetomechanical properties for temperatures between −20 and 80°C.[25] Iron is a very cheap and commonly used material, and gallium is priced at $280.44 per kg, less than half of the price of bulk terbium.[23] Like Terfenol-D, Galfenol was first produced by directional solidification methods. It was met with the same problems of brittleness under commercially demanding production speeds. However, due to the mechanical robustness of Galfenol, more conventional metal working techniques can be utilized such as ingot casting followed by forging, extrusion, or texture rolling.

Due to the anisotropic nature of the magnetostrictive property, the texture of the rolled Galfenol sheet should align with the magnetic easy axes, <100> directions. Therefore the development of strong <100> ||RD (RD=rolling direction, ND=normal direction to the sheet surface, and TD=transverse direction) texture in the rolled sheets is critical in order to achieve maximum performance.[28] Of these textures, the {001} <100> orientation, or cube texture, is particularly desirable because it provides two <100> easy axes of magnetization in the plane of the sheet.[29] An added benefit of developing cubic texture is that it will make it feasible to use magnetic field annealing to maximize performance.[30,31] This will eliminate the need for stress annealing or use of pre-stress components in the design of devices that use these materials.[32,33] Goss textures have only one easy magnetization axis, but it much easier to grow in the rolling and annealing method than the cube texture. Both Goss and Cube textures

are illustrated in Figure 1.4, and both are quite effective for use in design of actuators, sensors, and energy harvesters.

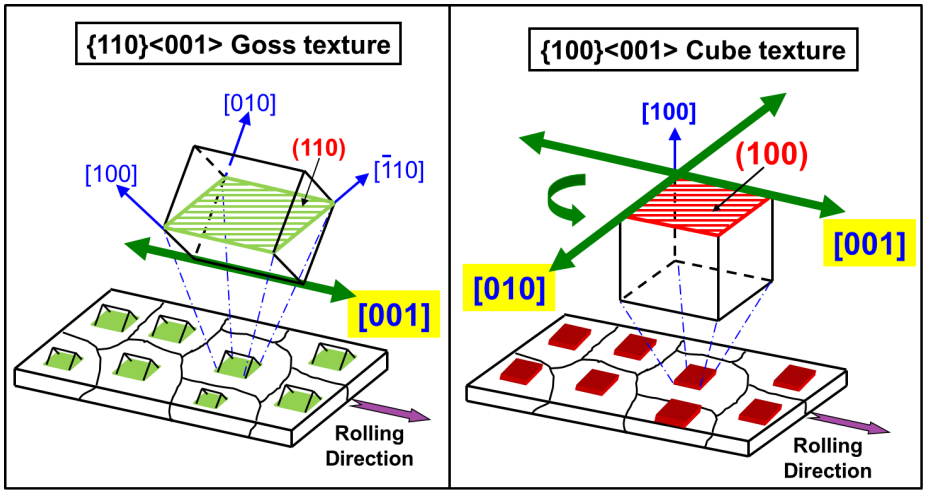

Figure 1.4: This is an illustration of Goss and Cube textures shown with their respective axes of easy magnetization. Goss has one easy axis, and Cube has two easy axes.

After rolling, annealing technique are used to preferentially grow abnormally large cube or Goss grain textures that maximize magnetostriction. This introduces the need to suppress normal grain growth (NGG) in which grains of all oriejntations grow at similar rates to silmilar sizes. To control abnormal grain growth (AGG), Na *et al.* dopes samples with sulfur or anneals in a sulfur environment to control the sulfur concentration on the surface of samples during annealing. By doing this, he has shown that sulfur segregation, which is known to control surface energy,[34] can be correlated to the selective growth of {100} grains.[35] He has also used NbC pinning particles in a mixed H_2S and Ar environment to halt grain growth of undesirable grains, thus abnormally growing {1 0 0} grains on 88.3% of the sample area.

Abnormal grain growth is not very well understood and even harder to control. There have been many models, like the coincident site lattice (CSL) boundary method

and high energy grain boundary (HEGB), that have tried to characterize the underlying mechanisms of AGG, but none have produced a correct formula of growth parameters for cube texture AGG. Na *et al.* suggests that these parameters are hidden in the surface energy of the $\{1\,0\,0\}$, $\{1\,1\,0\}$, and $\{1\,1\,1\}$ grains of Galfenol. The following section will discuss theory behind AGG mechanics.

The ratio of the magnetoelastic coupling b to the shear modulus ($\lambda = b/C'$) is defined as the magnetostrictive coefficient λ. This serves as a figure of merit for magnetostrictive performance. Magnetostriction in Terfenol-D can be traced back to the strong spin-orbit (magnetoelastic) coupling of the lattice to the anisotropic electron cloud surrounding the Tb ion. Although some extrinsic origins have been proposed, it is believed that the enhanced magnetostrictive response of Galfenol results from intrinsic factors, namely, changes in the electronic structure due to Ga ordering. DFT calculations reproduce experimentally observed ordered structures of FeGa as a function of Ga concentration. From these structures, simulations are done to predict λ_{100} in FeGa as a function of Ga concentrations. Figure 1.5 shows an excellent agreement between DFT calculations and experimental measurements of λ_{100} as a function of Ga concentration.

When dealing with real alloys with varying degrees of chemical order, Wu *et al.* used ab-initio AIMD for the determination of structures in a reasonably large supercell, and the trend of magnetostriction around $x = 19\%$ can also be captured.[27] Similar to the auxetic properties of Galfenol, growth of the magnetostriction can be explained by growing elastic anisotropy and the softening of the shear modulus, C'. However, the evolution of magnetoelastic coupling with composition is equally

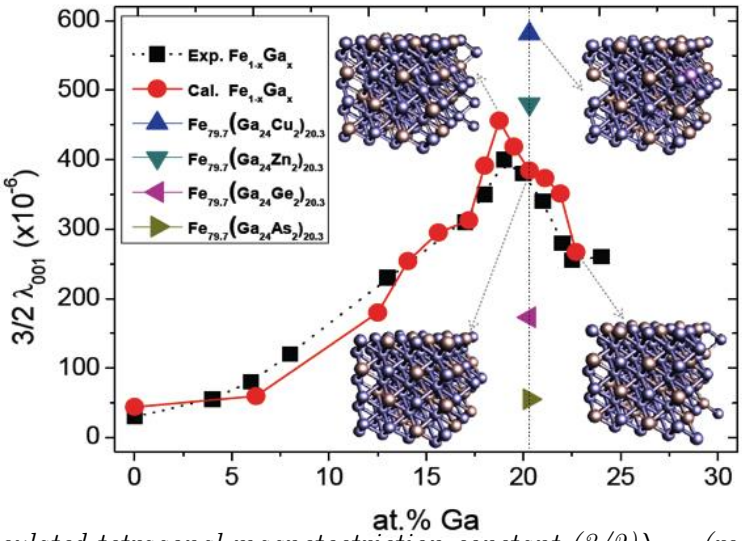

Figure 1.5: Calculated tetragonal magnetostriction constant (3/2)λ_{001} (red circles) and experimental data taken at room temperature (black squares at different Ga concentrations). Triangles show results of four ternary alloys with addition of Cu, Zn, Ge and As. Insets give the crystal structures with purple and red balls for Fe and Ga atoms, respectively.

important. With the complete quantum mechanical information, the origin of largely enhanced magnetostriction is traced to individual atoms and pairs of electronic states. In particular, the local short range ordering such as the formation of B2 and $D0_3$ coordinates becomes an extremely important factor in the magnetostriction at high Ga concentrations. We expect that the composition ratios and atomic arrangements in the surface and interface regions differ from that in the bulk and can be modified with the exposure to different gases during high temperature anneal.

1.2.1 Energy Harvester

One exciting application of Galfenol is its use in energy harvesting devices. Energy harvesting from ambient vibrations has the potential to bring battery-free wireless electronics to fruition in the commercial sector. In vehicles, a tire pressure monitoring system equipped with the harvester can be operated without a button cell by using

vibrations from the engine as power source. Self-powered autonomous wireless sensor systems can notify factories of structure or machine abnormalities without the need of external power or the hassle of battery replacement. The technology will also be applicable for battery-free remotes used in home automation by pushing a button to send on-off infrared signals, or powering hallway lights from floor vibrations as someone walks. Vibrational energy harvesters can work in conjunction with high capacitance devices, supercapacitors, for energy storage undergoing frequent charge and discharge cycles at high current and short duration, like a portable, self-charging cell phone charger. Technologies that convert vibrational energy into electrical power include piezoelectric materials,[36] electromagnetic induction,[37] and magnetostriction.[19]

There are few commercial energy harvesters being used effectively as barriers to widespread implementation exist. Specifically, piezoelectrics are brittle with poor robustness to bending and tension. They also suffer from high output impedance in the MΩ range, which is a result of their capacitive properties, that transfer only small amounts of electrical energy to external loads. In moving-magnet type harvesters, poor coupling and low resonant frequency up to several Hz results in low output voltage. Galfenol is of interest for actuation, sensing and energy harvesting applications because in addition to its magnetostrictive properties, it is ductile and it has robust mechanical properties,[38] relatively high permeability and good saturation magnetization (∼1.7 T).[16] These properties allow our collaborator at Kanazawa University, Toshiyuki Ueno, to prototype highly-scalable Galfenol energy harvester devices with high efficiency, high power output, and low impedance,[39] as seen in Figure 1.6. FeAl (Alfenol, $Fe_{100-x}Al_x$) has been overlooked as an actuactor because it

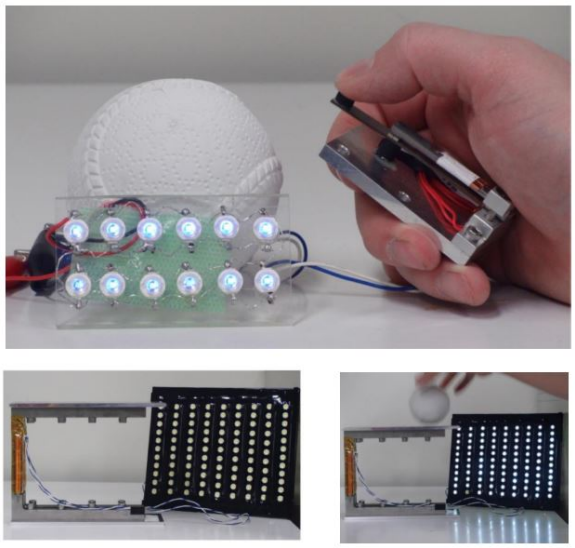

Figure 1.6: Galfenol resonant beam energy harvester. Photo courtesy of Dr. Toshiyuki Ueno, Kanazawa University, Japan. Galfenol beams are in the same region as the coils and have dimensions of 3 mm thick x 15 mm width x 80 mm length.[3]

has about half the magnetostriction of FeGa alloys. However, FeAl has similar saturation magnetization (∼1.5 T) and similar mechanical properties to FeGa, making it an attractive energy harvester with the added benefit of being more earth abundant and less expensive than FeGa.[40,41]

FeAl is sufficiently magneto-elastic that coupling between bending stress and magnetic moment rotation yields readily observable time-varying magnetization changes in the alloy. In harvesters, power is generated in a copper coil that surrounds a magnetostrictive material when a time varying stress, e.g. vibration of the magnetostrictive material, produces a voltage in the coil (per Faraday's law).[42] FeAl is a body-centered cubic alloy textured to develop a preferred orientation along the length of the strips by abnormal grain growth (AGG).[43–45] The $\langle 1\,0\,0 \rangle$ directions are the magnetic easy axes. Subsequently, the stress annealing protocol was performed to introduce built-in uniaxial anisotropy perpendicular to the length of the strips.[31]

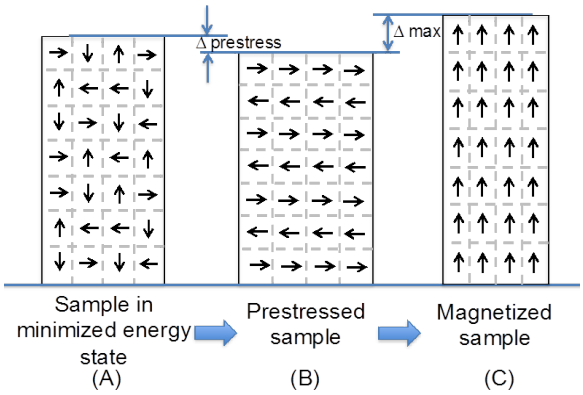

Figure 1.7: Cartoons depicting a perfectly aligned cubic alloy with $\langle 1\,0\,0 \rangle$ *magnetic easy axes as indicated. Arrows depict idealized orientation of magnetic domains.(A) Energy minimized state with closure domains randomly distributed throughout sample. (B) Prestressed sample with aligned antiparallel magnetization vectors and sample length minimized due to stress-induced moment rotation. (C) Sample magnetized along length with* Δmax *as the maximum achievable magnetostriction due to 90* $^\circ$ *magnetic moment rotation.*

This was done to maximize 90° rotation of magnetic moments when the strip bends. Successful stress-anneal-induced magnetic anisotropy was achieved, but this stress annealing process could not provide uniform compressive stress on each tested sample leading to non-uniform magnetic flux change along the strip length. As a viable alternative for a uniform magnetic flux change, Brooks *et al.* have used magnetic field annealing to achieve nearly identical saturation magnetostriction under compressive and no preload values.[46]

1.3 Abnormal grain growth

AGG is characterized by fast growth of a few large grains in a matrix of fine grains. The size change of the fine grains with annealing time is almost zero or at least negligible compared to that of the abnormal grains. AGG is often detrimental in piezoelectric ceramics because it lowers the hardness and the larger developed grain

sizes lead to degradation of the piezoelectric effect.[47] In magnetostrictive materials, AGG promotes growth of textures with easy magnetization axes. If a large grain grows to the full area of the sample surface, the magnetostrictive performance can reach over 95% of a single crystal at 5% of the cost.

1.3.1 Observation in magnetic materials

AGG has been observed in Fe-Al, Fe-V, Fe-Cr, Fe-W, and Fe-Mo binary systems,[48] as well as thin sheets of Ta, Pt, and Si.[5] The most seminal work on AGG comes from Dale Kohler in 1960 in his study of Fe-Si under a high temperature anneal in a hydrogen sulfide atmosphere. He first observed AGG of (1 1 0) grains in Fe-Si after an anneal in an inert argon environment. After adding hydrogen sulfide to the atmospheric mixture, he observed AGG of (1 0 0) grains. Adding an even higher concentration of hydrogen sulfide gas, no significant AGG occured. Kohler hypothesized that sulfur particles from the hydrogen sulfide gas adsorbed onto the Fe-Si surface, thus lowering the surface energy of each plane. The high polarizability of hydrogen sulfide allows for better adsorption to a surface. Higher concentrations of hydrogen sulfide would adjust the plane-dependent surface energy further, but the energy differences would decrease as depicted in Figure 1.8.

Based on Kohler's work, Dr. Suok-Min Na of the Aerosmart group has performed extensive research on the experimental fabrication of highly-textured FeGa and FeAl by AGG. Studies around AGG include hydrogen sulfide concentration, magnetic field annealling, tension and strain annealing, temperature dependence, particle pinning,

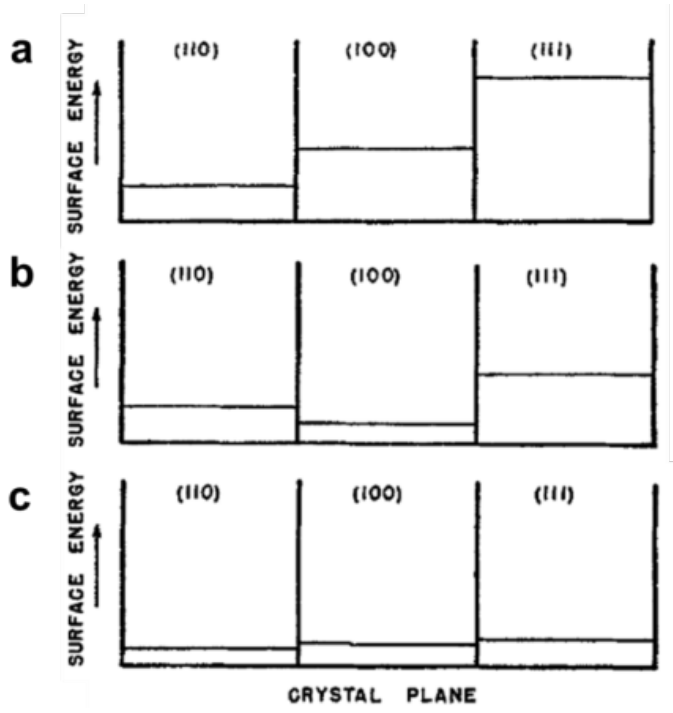

Figure 1.8: Diagrams of surface energies of low index crystal planes for metal surfaces: (a) "clean" surface, (b) "slightly contaminated" surface, (c) "severely contaminated" surface. Extracted from Kohler et al.[4]

ternary substitutions, thickness dependence, and misorientation/coincident site lattice boundaries.[11,29,35,40,43–45,49–55]

1.3.2 Theory

Walter *et al.* explains that surface energy differences between crystal orientations are a driving force for grain growth. This derives from differences in the gas-metal interfacial energies of different crystallographic surfaces.[56] The thermodynamic origins of surface energy will be discussed in the following section. For this section, the impact of surface energy on abnormal grain growth is described.

Surface atoms will have half the number of nearest neighbors compared to bulk atoms. According to Kohler, surface atoms will have twice the number of bonds and

a higher strength per bond than the lattice. This assumes that an electron-shared bond distributes itself among all available positions. Higher bond strength means that the atomic radius of the will be less than the average for the lattice, as shown in Figure 1.9. Values of surface energy will change with different crystal orientations

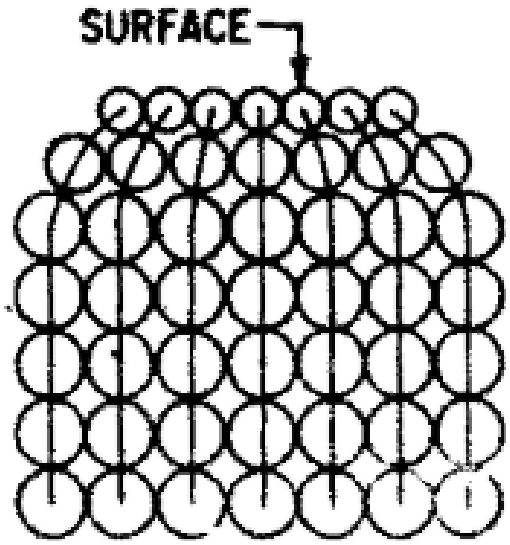

Figure 1.9: Surface atoms have lower atomic radius than atoms in the lattice. This causes tension at the surface which represents excess energy at the surface per unit area, or surface energy. Extracted from Kohler et al.[4]

since each will have different interatomic spacing.

As with any grain growth mechanism in metals, AGG is most active at high temperatures. Kramer considers the conditions for AGG laid out by W.W. Mullins in 1957.[5,57,58] The abnormally grown grain extends through a thin sheet in a catenoid shape, as depicted in Figure 1.10. The catenoid shape forms an angle Θ with the normal direction of the surface.

The movement of a grain boundary in the absence of driving forces from strain or phase transformations. At high annealing temperatures, two grains will form a

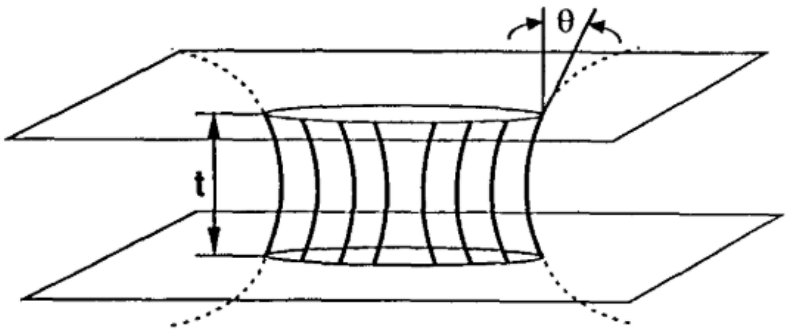

Figure 1.10: Catenoid shape for single isolated grain in a sheet of thickness t. Grain boundary is pinned at the surface. Extracted from Kramer et al.[5]

thermal groove at the surface of the boundary. Figure 1.11 considers two grains in a metal that meet at a grain boundary: grain 1 and grain 2. Two grains meet at a

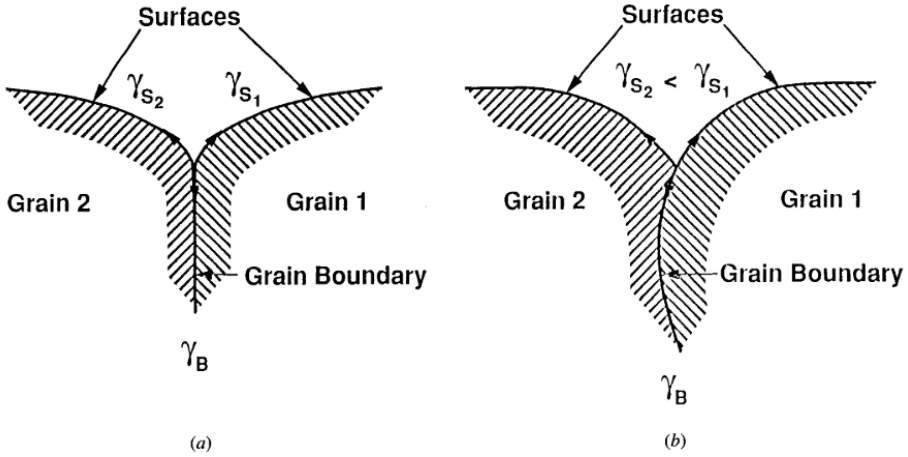

Figure 1.11: Thermal groove at the intersection of the grain boundary with the surface: (a) surface energies equivalent; (b) surface energy of grain 1 greater than that of grain 2. Extracted from Kramer et al.[5]

grain boundary and form a thermal groove in a high temperature anneal. If there is a surface energy difference between the two catenoid shaped grains, grains with low surface energy have catenoid angles of $\Theta > \Theta_C$ and can escape the groove. The abnormally growing grain consumes the surrounding grains of higher surface energy. This critical angle is dependent on grain size, sheet thickness, and thermal grooving. Through bicrystal studies on the $\{1\,0\,0\}/\{1\,1\,0\}$ surface of Fe-Si annealed under H_2S

at 1300℃, {1 0 0} grains showed vivid thermal-etched structures in the cross-section. This corresponds to a heavy $\Theta > \Theta_C$ condition. This was only present when sulfur was incorporated. It is consistent with equilibrium theories of low index planes where cusps sharpen on the {1 0 0} surface when sulfur adsorption occurs.[59]

AGG is also desribed by Walter *et al.* in his studies of thermal grooving.[34] If the temperature of a metal is sufficiently high, then transfer of atoms may occur across a grain boundary by volume and surface diffusion. This transfer is always in a direction that decreases the over-all free energy of the system. Thus, it would be expected that the surface of grain 1, having the lower energy, would tend to expand at the expense of grain 2. This could only occur if the boundary between the two grains 1 and 2 were able to migrate under the small force on it at the point where it intersects the surface. As grain 1 enlarges, it moves the point of intersection of the boundary towards the center of grain 2 which imparts a curvature, and hence a driving force, to the boundary in the cross section such that the whole of the boundary will migrate toward its net center of curvature. At the same time, however, it is seen that the boundary on the top surface would bulge outward from the center of grain A while moving into grain B. This movement of the boundary away from its center of curvature (on the surface) is the only positive identification of a surface energy driving force.

It must be noted that while 90% of the driving force for AGG comes from grain boundary interactions, the initial stage of AGG is more significantly driven by surface energy. This is referred to as the nucleation event in AGG.[5] AGG does not initiate immediately. A period of time is needed to create the right surface conditions for

grains to grow abnormally. Preliminary events include the removal of surface oxides, establishing a sulfur layer on the surface, and the development of a thermally etched surface structure on the AGG grain.

1.3.3 Galfenol

For the Aerosmart group's application goals, AGG is advantageous for targeting Goss {1 1 0} and Cube {1 0 0} textures to obtain one and two directions, respectively, of easy magnetic axes and high magnetostriction in the plane of rolled sheets. This process avoids lengthy and expensive single-crystal growth methods while still producing Galfenol with sufficient magnetostrictive properties for device application. Aerosmart has studied the development of Goss- and Cube-textured Galfenol rolled sheet as a low-cost alternative to magnetostrictive single-crystal Galfenol for several years. Na *et al.* has incorporated pinning particles during the rolling process, experimented with different annealing temperatures and times, and modified the annealing environment to optimize grain growth of these textures.[29,35,50,51]

A limiting factor of AGG is the thickness of the sample before annealing.[11] Final area coverage of an abnormally grown (1 1 0) grain on $Fe_{81}Ga_{19}$ is maximized at $\sim$0.45mm thickness.[11] This is most likely because grains must go through the entire thickness of a thin sheet in order to experience AGG. If the sample is too thick, through-thickness grains will be less frequently occurring.

Electron backscatter diffraction (EBSD) scanned images spatially map crystal orientations on well-polished specimen by using backscattered electron patterns from

the electron beam in a scanning electron microscope (SEM). From these patterns, we can use statistical tools to measure average misorientation, grain size, and crystallographic texture on the surface of our samples. Figure 1.12 depicts EBSD scanned images of successful annealing conditions we have tested. As-rolled polycrystalline Galfenol (left image) exhibits a strong γ-fiber $\langle 1\,1\,1\rangle \| \mathrm{ND}$ (normal direction to the sheet surface) and weak rotated cube textures, and starts with an α-iron (B2) structure. A partly grown Goss texture developed over $\sim$39% of the sample surface area during a 3h argon-anneal (upper right image) due to grain boundary energy alone. This is because inert argon particles do not react with the Galfenol surface, and do not modify the surface energy.[5] We have demonstrated that small variations in surface energy have a significant impact of the development of texture.[53,60] The two lower right images show AGG with fully developed (1 0 0) and (1 1 0) grains over 90-95% of the sample surface. This occurs because 0.5%H_2S is added to the Ar atmosphere under the 3 hr 1200°C anneal. Abnormal growth of (1 1 0) grains are very reproducible and insensitive to small variations in anneal conditions, while the development of (1 0 0) grains are challenging to produce or reproduce due to highly sensitive to anneal conditions. Saturation magnetostriction values equal to 90% and 84% of single-crystal (1 0 0) values for alloy of the same composition were measured in sulfur-annealed samples with (1 0 0) Cube and (1 1 0) Goss grain growth, respectively.

Developing protocols for making thin sheet Galfenol with Goss or Cube textures has been challenging because the mechanisms that regulate grain boundary mobility and texture development in these alloys are not well understood. The Aerosmart group has produced a Cube textured sample only twice, while Goss textured samples

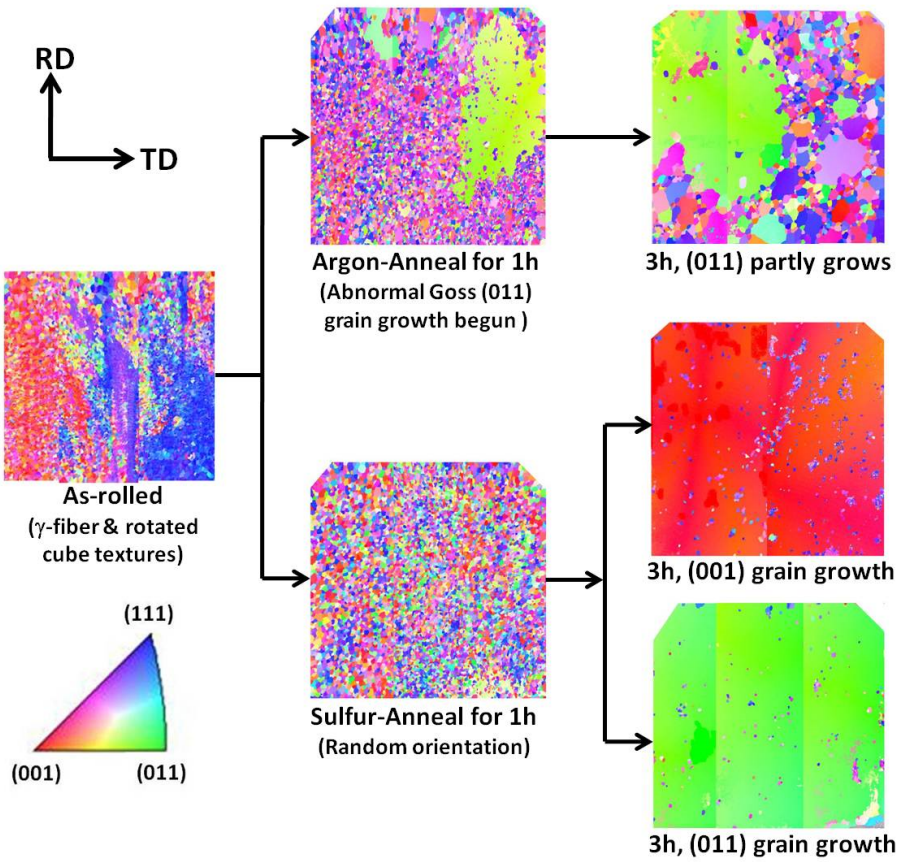

Figure 1.12: Diagram of AGG from as-rolled sample of (Fe-19%Ga)+1.0%NbC alloy (left) to argon- (upper) and sulfur-annealed (lower) samples for annealing times of 1h (middle) and 3h (right). EBSD images scanned along the normal direction of 12x12x0.45 mm^3 sheet. Red, green and blue indicate (1 0 0), (1 1 0) *and* (1 1 1) *grains, respectively.*

are readily reproducible. Modeling techniques that examine grain boundary interactions, coincident site lattice (CSL) and high energy grain boundary (HEGB), have been investigated to understand AGG mechanisms. These techniques sufficiently describe abnormally grown Goss grains in $Fe_{100-x}Ga_x$ (x=19)+1.0 mol% NbC rolled sheets, but mechanisms for abnormally grown Cube-grains are still not understood.[60] We postulate that these models are insufficient because driving forces caused by the control of surface energy from atmospheric annealing conditions, as described by Kramer *et al.*, are not properly incorporated. By characterizing the surface energy of

specific Galfenol grains, we can develop a more accurate thermodynamic-based framework for modeling AGG and texture development. This will be used to understand why a high temperature atmospheric anneal transforms myriad crystallite grains into the highly textured, single-crystal-like polycrystalline material. In this way, surface energy differences between grains could potentially be controlled through non-inert gas contamination. This allows for selective grain growth of either Goss or Cube textures at any time.

1.4 Surface Energy

Gibbs formulates the thermodynamics of a surface through the excess free energy per unit area, γ, simply by the existence of a surface. This surface energy, γ, is also defined as the reversible work per unit area needed to create a new surface.

The excess Gibbs free energy can be written as Equation 1.4,

$$G_{xs} = U_{xs} + (PV)_{xs} - (TS)_{xs} = \sum_i \gamma_i A_i \tag{1.4}$$

where xs denotes excess for the internal energy U, pressure/volume of surface atoms PV, and temperature/entropy TS. The summation of the surface energies of all crystal facets γ_i of area A_i at the surface can be written as the excess free energy. There are clearly other terms present in the excess Gibbs free energy like the $(PV)_{xs}$ term. This term can denote the relaxation of atoms at the surface of a metal, as depicted in Figure 1.9. The relaxation volume and pressure of the surface atoms

will change with different crystallographic facets, thus contributing to the surface energy. There is also a temperature dependence where an increase in temperature will decrease the surface energy. This is a consistently confirmed experimental observation for surface energy.[8,61]

Another way to differentiate between surface energy of different crystal faces is by considering the density of broken bonds at the surface. Porter and Easterling describes this as follows. At the macroscopic surface plane, a surface will appear as a stepped structure where each layer is a close-packed plane. A crystal plane at angle θ to the close-packed plane will contain bonds in the excess of the close-packed plane due to the atoms at the steps, shown in Figure 1.13. A higher density of broken bonds at the surface will mean a higher surface energy. Each value of θ can be assigned to

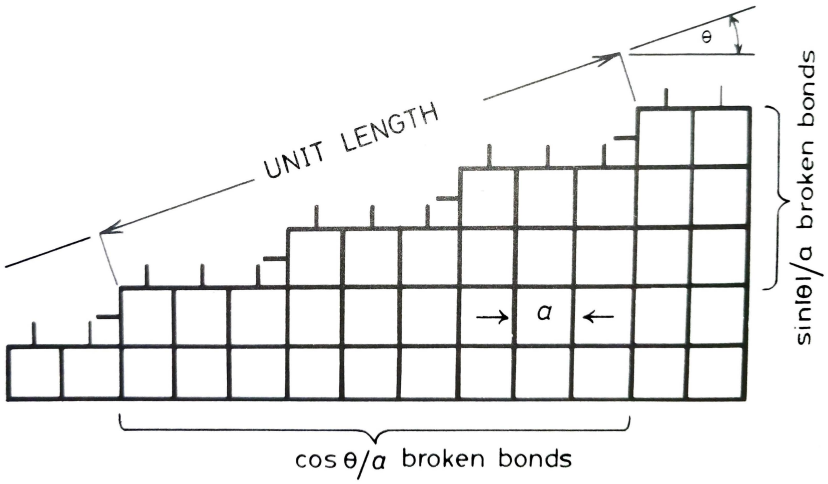

Figure 1.13: An illustration of the broken-bond model for surface energy. Extracted from Porter and Easterling.[6]

a different crystal face $\{h\,k\,l\}$. Since we know crystal facets have different values of surface energy, we can express the surface energy as a function of θ, as seen in

Equation 1.5.

$$\gamma_{SV} = (\cos\theta + \sin|\theta|)\varepsilon/2a^2 \tag{1.5}$$

The energy of a broken bond is expressed as $\varepsilon/2$.

When plotted in polar coordinates, where the surface energy γ is the magnitude of the coordinate, all the lowest surface energy facets will manifest in a shape called a Wulff construction.[62–65] Cusps in this plot indicate low surface energy planes, as shown in Figure 1.14. Inscribing a Wulff construction will reveal the equilibrium crystal shape of the material. The faces of the equilibrium crystal shape correspond to the lowest energy faces. Growth of these shapes are purely dictated by the surface energy differences between crystal faces. Equilibrium crystal shapes have been observed experimentally using ultra-high vaccuum (UHV) techniques combined with scanning tunneling microscopy and scanning electron microscopy, as shown in Figure 1.15.[7,62,64,66] Observation of these shapes show the true lowest surface energy faces and give an absolute measurement of surface energy for a specific crystal. They are very difficult to obtain even with a UHV system.

At pressures near atmosphere, growth shapes of crystals are still influenced by surface energy anisotropy of low index planes. Additionally, growth shapes must consider factors like growth velocity on the Wulff construction. Constructions will be similar as they are generated by expanding the polar surface free energy plot uniformly.[62] Eventually, rounding of edges on the equilibrium crystal shape will arise, and mass acretion will not allow for relaxations necessary to maintain the shape. Most grain growth procedures, including AGG, are included in this growth shape regime

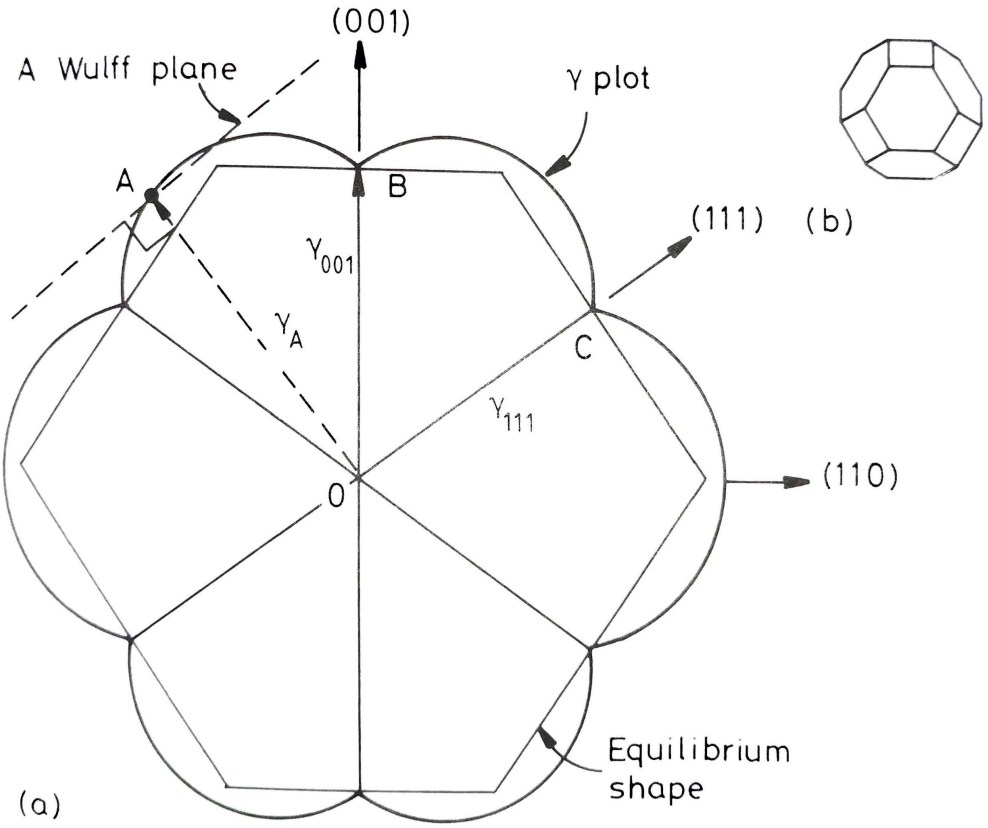

Figure 1.14: (a) The Wulff construction of a possible $(1\bar{1}0)$ *section of an fcc crystal. Cusps indicate low energy crystal planes. (b) A 3D Wulff construction of a fcc crystal, which is also called an equilibrium crystal shape. Extracted from Porter and Easterling.*[6]

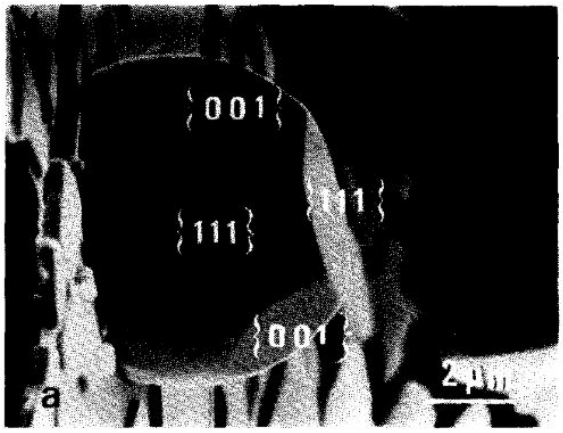

Figure 1.15: Equilbrium crystal shapes of lead crystals. Extracted from Heyraud et al.[7]

rather than equilbrium crystal shapes.

Grain growth in polycrystalline materials is determined by conditions at grain

boundaries. Boundaries are metastable equilibriums as they increase the free energy of a polycrystal relative to a single crystal. If a boundary is mobile, forces in the x- and y-direction must act at the surface to maintain equilibrium, as shown in Figure 1.16. The force in the x-direction is equal to the surface energy γ. The force in the y-direction is equal to the instantaneous slope of the γ vs. θ plot at a given value θ, or a specific crystal direction. This term is known as the torque term. A force of $d\gamma/d\theta$ must be applied to the ends of the boundary to prevent it from rotating into a lower energy orientation.

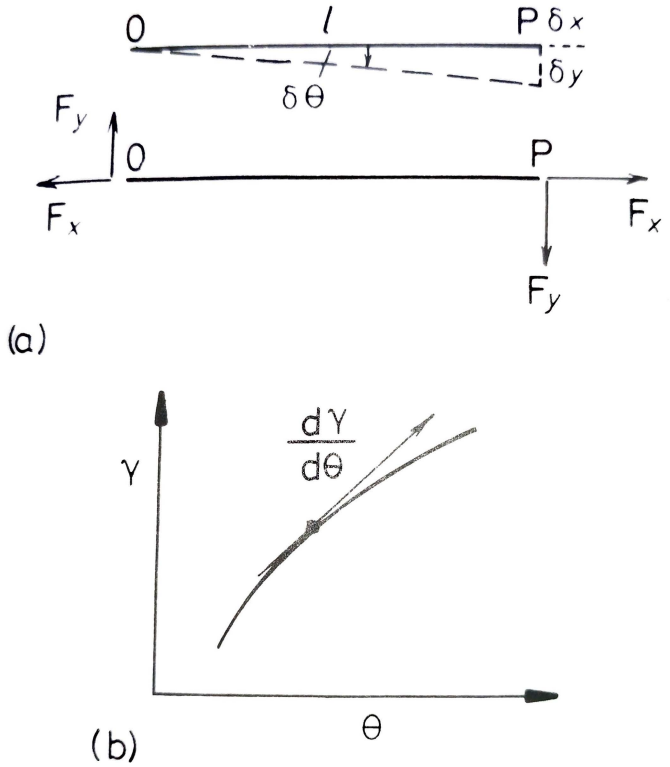

Figure 1.16: The . Extracted from Porter and Easterling.[6]

A simple way to create a new area on a solid is by cleavage. If we consider the amount of reversible work, dW, required to create a new area, dA, of a surface, we

have the relation in Equation 1.6.

$$dW = \gamma dA \tag{1.6}$$

The total work required to create a planar surface of area A, or the excess free energy of the surface, is equal to γA. The work required to elastically stretch a a pre-existing surface per unit area is the surface stress, g. A surface deformation can be expressed by an infinitesmal change dA of the elastic strain tensor ϵ_{ij}

$$dA = Ad\epsilon_{ij}\delta_{ij} \tag{1.7}$$

where δ_{ij} is the Kronecker delta function. A repeated index indicates a summation over this index. The relationship between the surface energy and surface stress starts with the variation in the excess surface energy in Equation 1.8,

$$\begin{aligned} d(\gamma A) &= \gamma dA + Ad\gamma \\ &= \gamma dA\delta_{ij} + A\frac{\partial \gamma}{\partial \epsilon_{ij}} \end{aligned} \tag{1.8}$$

The work needed to enlarge the surface area is expressed as the work against the surface stress,

$$dL = Ag_{ij}d\epsilon_{ij} \tag{1.9}$$

where g_{ij} is the surface stress tensor, and $d\epsilon_{ij}$ is the variation in the surface elastic

strain tensor. Equations 1.8 and 1.9 are equated to relate the surface stress and surface energy in Equation

$$\begin{aligned} g_{ij} &= \frac{1}{A}\frac{\partial(\gamma A)}{\partial \epsilon_{ij}} \\ &= \gamma\delta_{ij} + A\frac{\partial(\gamma)}{\partial \epsilon_{ij}} \end{aligned} \tag{1.10}$$

In the case of an isotropic surface where the off-diagonals of the strain tensor are zero, the surface stress is simply

$$g = \gamma + A\frac{d\gamma}{d\epsilon} \tag{1.11}$$

When a liquid is stretched isothermally, atoms from the bulk will move to surface positions and the surface stress will stay constant, therefore $g = \gamma$. For a solid, $d\gamma/d\epsilon \neq 0$, and usually of the same magnitude as γ. This means that the surface stress is generally of the same order of magnitude as the surface energy.

The simplest way to determine to determine whether g or γ is the relevant parameter is described by Cammarata *et al.*:[67] "if a small variation in area does not change the surface atomic density, then the specific surface work is equal to γ; if the variation is due to an elastic strain that changes the surface density of atoms, then the specific surface work is g." It is very possible that in Kohler and Walter's definition of surface energy driving the initial stages of AGG surface stress was neglected. Walter justifies this by stating if the temperature of the metal is sufficiently high, then transfer of atoms may occur across the boundary by volume and surface diffusion.[56] Porter and Easterling also suggest that at high enough temperatures close to the melting point of a metal, the surface stress term can approach zero.[6] Galfenol has a melting temper-

ature of $T_m = 1443$℃ and the Aerosmart group anneals its polycrystalline FeGa for AGG at $T_A = 1200$℃.[49] This high temperature argument is disputed by Cammarata *et al.* for the case of a creep test where plastic strain is much greater than elastic strain, making surface energy the driving force.

Mullins, in his derivation for thermal grooving and the effect it has on grain boundary motion in AGG, considers the movement of grain boundaries in the absence of a driving force from elastic strain or a phase transformation. This eliminates consideration of a surface stress term and focuses on surface energy as a driving force in AGG for high temperature anneals. With these ideas of surface energy in mind, this thesis will focus on the experimental measurement of surface energy on metals.

1.4.1 Experimental measurements of surface energy

As discussed previously, the physical origin of the surface free energy is the excess Gibbs free energy of matter at the interface. There is a negative free energy change when two flat surfaces, A and B, are brought into adhesive contact in a medium. Israelachvili describes this as twice the interfacial energy γ_{AB} of the A-B interface, which is positive by convention,[68] as seen in Equation 1.12.

$$\Delta W = -2\gamma_{AB} \tag{1.12}$$

In principle, Equation 1.12 can be used to calculate the surface tension of a condensed phase held together by the long-range forces. However, measurement of these forces require perfectly flat surfaces and no external forces. This is experimentally infeasible,

and would likely be far too expensive.

The change in free energy is positive when a material is split to create two new surfaces, as shown in Equation 1.13. This is a more feasible experimental measurement where a single material dipped in liquid nitrogen is cleaved by a wedge that is forced through a crack.[69] The force and crack geometry are measured, and the surface energy of the cleaved plane is directly calculated.

$$\Delta W = 2\gamma_{AB} \tag{1.13}$$

The problems with this method lie in the low predictability of the cleaving plane and the destruction of the samples. A cleaving experiment will need very specific requirements for different materials, thus making a single experimental apparatus for all samples impossible. In the case of ductile alloys like Fe-Si, the cleave loses energy to twinning and plastic deformation which skews results. Ultimately, this method destroys samples and this is not financially feasible.

Another method that has been used to characterize metal surface energies is by melting the metals. The shape that a metal droplet forms past the intrinsic melting point can be analyzed to measure the surface energy.[70] This is a very reliable method since it stems from classic pendant drop methods for organic liquids.[71] Unfortunately, all crystallographic information of the solid is lost since the metal is in a liquid state. The measured surface tension of the liquid metal is more representative of an average surface energy of all crystal facets.

Potential methods

Some measurement techniques were suggested by my committee members to non-destructively measure the surface energy of a targeted metal crystallographic facet. The most promising suggestion was a force curve measurement since it is a direct measurement of surface energy. Force curve measurements use the cantilever tip (preferably a sphere) of an atomic force microscope (AFM) to measure short-range surface adhesion forces to measure the interaction energy between the cantilever tip and the surface. If the cantilever tip and the surface are of the same composition, the surface energy of that composition can be measured. The physics of such a process are well described by Jacob Israelachlivi in his book, *Intermolecular and Surface Forces*.[68] It is not difficult to perform this experiment since force curve measurements are common procedures on modern AFMs and coating an AFM tip with another material is possible at the UMD Nanocenter. The problem comes with the intrinsic behavior of metals in air. Metals tend to form passivation layers of oxides when in the presence of air. This passivation layer must be removed and the bare metal must sustained afterwards. A vacuum line or inert atmosphere line between the oxide removal process and the AFM would have to be created, which is an extremely expensive venture. This would also require removal of oxides from both the cantilever tip and surface, as well as the attachment of the cantilever tip under inert conditions.

1.4.2 Contact angles

The least destructive method for measuring the surface energy of specific regions on a sample surface is the contact angle method. It is an indirect measurement of surface energy because it measures contact angles of one or more probe liquids to infer the solid surface energy. There is still an issue of oxide removal, but we are now only limited to one passivated surface rather than two. Oxide removal procedures are addressed in Chapter 3. The interaction of a liquid with a solid is characterized by the term "wetting," which is defined as the spreading of a liquid over a solid surface. The simplest way to quantify a liquid's surface wetting characteristics is to measure the contact angle of a drop of liquid placed on the surface of an object, as depicted in Figure 1.17. A droplet in this form is called a sessile drop. The contact angle is formed at the triple-phase boundary, a point where the solid-liquid (SL), liquid-vapor (LV), and solid-vapor (SV) interface energies. The LV and SV interfacial energies are the surface tension of the sessile drop and the surface energy of the solid, respectively, in a given vapor environment. The SL interfacial energy is a measure of the energy required to form a new unit area of the SL interface.

As mentioned previously, a solid surface always has a surface free energy. A state of surface stress, g, will usually also exist where, in Equation 1.11, we see elastic energy stored in a strain field in the surface region. For a probe liquid, the state of surface stress is zero. Hence, there is no connection between the surface tension for a liquid and the state of surface stress. For a solid, the surface stress state does contribute one component to the total surface energy through the stored elastic energy. The main

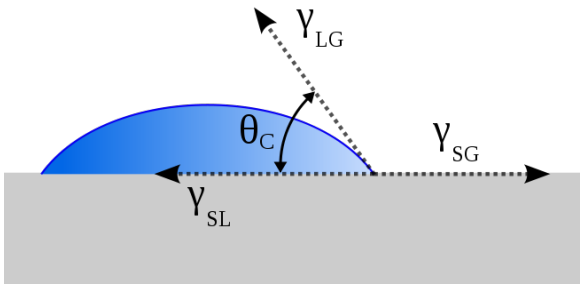

Figure 1.17: This illustration shows a vector representation of the interfacial tensions involved in a solid-liquid-gas contact angle experiment. [Image available in public domain: wikimedia.org]

component of surface free energy of a solid is due to the force field of the atoms or molecules or the unbalanced force directed normal to the surface. In addition, there is a density gradient across the phase boundary, and there are orientation (excess entropy) effects. Only the component of surface free energy due to the normal force field (not the components due to surface stress, to density gradients, and to excess entropy) that is estimated by contact angles in equilibrium systems.[72] This suits the goals of this project for measuring the surface energy as defined in AGG mechanisms.

The adhesive forces between the liquid and the solid substance will compete against the cohesive forces of the liquid to characterize the wetting behavior. Liquids with strong cohesive bonds and weaker adhesive forces will tend to bead-up or form a droplet when in contact with another material.[73] Liquids with relatively weak cohesive bonds and a strong attraction to another material will tend to spread over that material. Here, the energetically favorable outcome is the formation of adhesive bonds. Such is the case with water droplets on high-surface energy metal substrates.

There are two types of contact angles can be defined: static and dynamic contact angles. A dynamic contact angle is measured if the contact angle is measured when either the liquid drop continues to spread by continued dispensing from a syringe or

when its thermodynamic state conditions continue to change. A static contact angle is measured if the contact angle is measured under conditions in which the liquid drop is stationary and the surrounding conditions are in the steady state.

The solid-liquid interface plays a fundamental role in a number of research areas. Fields of interest include catalysis, lubrication, electrochemistry, colloidal systems, biological reactions, and, most relevantly, crystal growth.

Described by Thomas Young in 1805, contact angle measurements remain the most accurate method for determining the interaction energy between a liquid and a solid. Young described the equilibrium contact angle at the three-phase boundary in terms of the vectorial sum, as shown in Figure 1.17, resulting in an equilibrium force balance. The famous Young's equation is derived in Appendix A from the Gibbs free energy at equilibrium.

$$\boxed{\gamma_{SV} = \gamma_{SL} + \gamma_{LV} \cos\theta} \tag{1.14}$$

There are three main factors that influence a contact angle in an experiment: roughness, environment, and surface composition. A high roughness surface will have a higher contact angle. This has been experimentally confirmed many times and is a widely accepted conclusion. The environment the solid and probe droplet are immersed in determines the spreading of the contact angle on the solid. An air environment will do little to impede the motion of a sessile drop initially spreading because air has a very low viscosity. A secondary liquid environment will slow the spreading and increase the contact angle of a sessile drop due to the increased viscosity.

The surface composition of the solid will change the surface energy of the solid. For example, iron oxide has a theoretical surface energy of $\sim$ 1300 mJ/m^2 whereas α-Fe is $\sim$ 2000 mJ/m^2. Simply adding oxygen to iron changes the material structure, composition, and the surface energy. For these reasons, iron oxide will have a higher contact angle than α-Fe. Each of these factors will be modified in each chapter of this dissertation to best utilize the contact angle method for measuring the surface energy of our Galfenol facets.

Dispersive and polar surface energy

Another consideration in the measurement of solid surface energy using contact angles is the manner in which the surface energy is broken up. One of the forerunners in contact angle measurements, Frederick Fowkes, split the surface energy of all materials in to forces based on polar interactions and dispersive interactions.[74] Polar interactions encompass all interactions between the solid and the liquid (dipole-dipole, dipole-induced dipole, hydrogen bonds, π bonds, etc.). Dispersive interactions are largely due to London dispersion interactions.

Polar interactions occur in molecules with a dipole moment. Such molecules have an inequality of the electron density due to different electronegativities of the bonding partners. Molecules with a dipole moment can form polar interactions with one another. Surfaces have this inquality of electron densities due to broken bonds, which is also a reason for the relaxation layer described in Figure 1.9. Since the entire surface has this electron density inequality, the whole surface should be covered with effective dipoles, according to Lang *et al.*[75] This means that there should be a significant

contribution to the surface energy from polar interactions depending on the density of effective dipoles at the surface.

Fowkes hypothesized that an atomically clean oxygen-free metal surface, without possibility of hydrogen bonding, would interact with water by dispersion forces only. He expected this to be adequate to yield a zero contact angle, which is the expected result on a clean metal surface because of the extremely high surface energy. This idea came from the observation of only dispersive interactions between mercury and water.[76] This idea was further confirmed through contact angle measurements on gold surface where almost zero oxygen adsorbs.[77]

Fowkes related the Hamaker coefficient to the dispersive component of solid surface energy by Equation 1.15.

$$A_{ii} = 6\pi r_{ii}^2 \gamma_i^2 \tag{1.15}$$

where r_{ii} is the distance between interacting atoms or molecules. He found the value of $6\pi r_{ii}^2$ to be 1.44 x 10^{-14} cm^2 for most materials.[78] The Hamaker coefficient gives a means to determine the interaction parameter C from the Van der Waals pair potential $w(r) = -C/r^6$. Another way to define the Hamaker coefficient is the proportionality constant for force exerted by a material based on the pairwise summation of the dispersion force of atomic size surface segments of another surface. The Hamaker coefficient, in the macroscopic case, can be related to the dielectric constant. Plasma cleaning has been known to effect the dielectric constant of materials.[79,80] This will be relevant in Chapter 3 during the sample preparation stage. We hypothesize that the surface energy of Galfenol will have a majority contribution from dispersive in-

teractions.

1.5 Preliminary investigations

For glass and polymeric solids with relatively low surface energies, the water-drop method has been shown to be effective for the determination of surface energy at room temperature.[81–83] A previous group member, Hyunsuk Chun, attempted to use the water drop method for contact angle measurements on (0 0 1), (0 1 1) and (1 1 1) facets of 17.9%Ga Galfenol single-crystal samples using facilities at NIST.[84] Averaging water contact angles in air on (0 0 1), (0 1 1) and (1 1 1) facets from 20-30 measurements resulted in 72.±5.3°, 87.01±5.4°, and 63.11°, respectively. These measurements were used to estimate surface energy using the Girifalco–Good–Fowkes–Young (GGFY) equation, $\gamma_{LV}(1 + \cos\theta) = 2\sqrt{\gamma_{LV}\gamma_{SV}}$. Determined values of γ_{SV} for each facet (γ_{001}= 0.0277 J/m^2, γ_{011} = 0.0199 J/m^2, γ_{111} = 0.0380 J/m^2) are too small to be correct. The values are about two orders of magnitude smaller than expected when compared to values of α-iron DFT calculations (γ_{100} = 2.6660 J/m^2, γ_{110} = 2.0535 J/m^2, γ_{111} = 2.5271 J/m^2).[85] A water contact angle in air works well for estimating surface energy of solids with magnitudes less than water surface tension ($\gamma_W \sim$ 72 mJ/m^2), and fails for metallic solids, where the drop surface tension is several orders of magnitude lower than that of metals. The sample preparation was not sufficient for these Galfenol samples. The sample roughnesses are likely high and the surface is likely passivated with an oxide layer since it is in air. Both assumptions would show an increase in the observed water contact angle in air, hence a low surface energy will

be calculated. Also, the GGFY equation has an upper limit of the possible surface energy equal to the surface tension of the probe droplet, $\gamma_W \sim 72$ mJ/m^2 in this case.

1.5.1 Thermal Grooving

The thermal grooving technique was considered as a possible approach to understanding the interactions between adjacent grains in Galfenol that we target for AGG. Annealed samples were polished and re-annealed to develop thermal grooves. EBSD identified where (1 0 0), (1 1 0), and (1 1 1) orientations met on each sample. By measuring the dihedral angle formed at these grain boundaries, the ratio of grain boundary energy and surface energy was calculated according to the following equation:

$$\frac{\gamma_{GB}}{\gamma_S} = 2\cos\left(\frac{\Psi_S}{2}\right) \tag{1.16}$$

where γ_{GB} is the grain boundary energy, γ_S is the surface energy, and Ψ_S is the dihedral angle, as described in Rohrer *et al.*.[86] The most symmetric thermal groove came from a (1 1 0)/(1 1 1) grain boundary on a rolled and annealed (Fe-19%Ga)+1.0%NbC sample, as seen in the Figure 1.18.

The grain boundary profiles were measured using atomic force microscopy (AFM), and the dihedral angles were extrapolated from the profiles using both AFM software by Bruker and a quadratic fit. The results are shown in Table 1.2. This groove in particular had a depth of ∼8 nm which is significantly smaller in depth compared to grooves of other metal alloys.[87] Relative energies between 1/4 and 1/2 are expected for metals, but this unusually small groove might explain why we see high variation

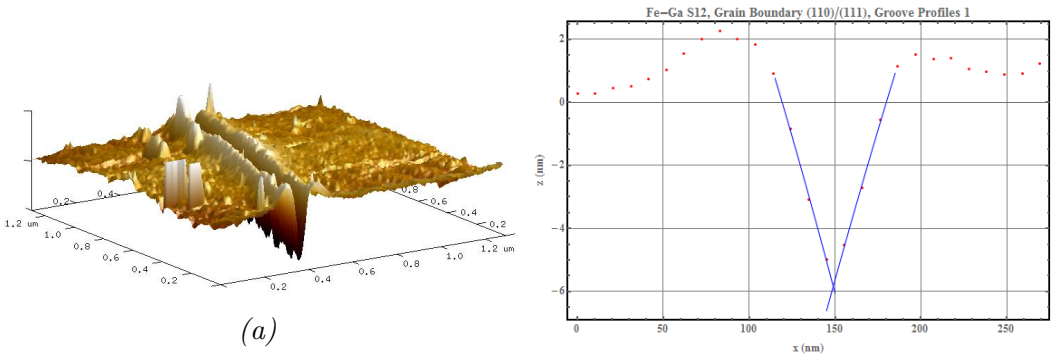

(a) (b)

Figure 1.18: (a) 3D rendering of (110)/(111) grain boundary on surface of for (Fe-19%Ga)+1.0%NbC sample where the depth of groove is 8 nm. (b) A quadratic fit of a (110)/(111) grain boundary profile for a (Fe-19%Ga)+1.0%NbC sample.

in dihedral angles. To properly analyze the thermal grooving technique, an extensive grain boundary study of the effect annealing temperatures and times have on Galfenol would need to be investigated. While this may be an interesting avenue of research in the future, the resultant calculations of relative grain energies do not contribute to the ultimate goal of achieving a comprehensive AGG model for Galfenol. Realization of this project's goal lies in the measurement of orientation-dependent surface energy using contact angle measurements.

Table 1.2: Calculated dihedral angles and relative energies from our most symmetric grain boundary groove.

fe-ga-s12-006 profile analysis - GB (110)/(111)				
	Bruker Software		Quadratic Fit	
Profile	Dihedral Angle (°)	Relative Energy	Dihedral Angle (°)	Relative Energy
1	156.9	0.3994	151.2	0.4964
2	156.2	0.4116	157.0	0.3971
3	154.4	0.4430	155.5	0.4234
4	157.2	0.3949	152.7	0.4705
5	154.7	0.4374	154.9	0.4334
6	158.3	0.3750	154.4	0.4417
Avg	156.3 ±1.5	0.4102 ±0.02611	154.3 ±2.069	0.4437 ±0.03519

1.6 Proposed research

The main focus of this project will be the development of an experimental procedure to characterize metals of high surface energy using contact angle methods. The interactions of a probe droplet (sessile drop) with a low-energy and high-energy solid surface differ significantly. Solids with weak molecular crystals (e.g., fluorocarbons, hydrocarbons, etc.) where the molecules are held together by weak physical forces (e.g., van der Waals and hydrogen bonds) are termed low-energy solids. A very low input of energy is required to break these solids, thus they typically have surface energy values <72 mJ/m^2. Metals, glasses, and ceramics are known as "hard solids" because the chemical bonds that hold them together (e.g., covalent, ionic, or metallic) are very strong. Thus, these surfaces are high-energy because of the high amount of energy needed to break these solids to make two new surfaces, (e.g. see Equation 1.12 in Section 1.4.1). High energy solids typically have surfaces energies >72 mJ/m^2. The threshold between these two types of surfaces lies in their surface energy values relative to the surface tension of water, ∼72 mJ/m^2. Water tends to partially wet a low energy surface and completely wet a high energy surface based on how much lesser or greater the surface energy of the solid is compared to water, respectively.

Two approaches are investigated to overcome the challenges involved in measuring the surface energy of metals using contact angle measurements in the next three chapters. The first will use gallium contact angles to observe surface energy changes with temperature. The high surface tension of gallium will allow the probe droplet

to form a contact angle on the high surface energy Galfenol, rather than completely wetting the surface like water on a high energy surface. The second will build on the two-liquid-phase technique to form a measurable water contact angle on the surface of Galfenol. The third chapter will supplement this measurement, Galfenol samples will be patterned with a planned surface geometry to increase the water contact angle and properly determine the Young's contact angle to be used in surface energy calculations. Both experiments will use highly Goss textured Galfenol as well as single-crystal Galfenol samples to assure isotropic crystal orientation for contact angle measurements.

Once experimental results are validated with published values, DFT predictions of the surface energy associated with different crystallographic orientations in FeGa will be tested and verified. This experimental investigation should have broad applicability beyond the needs of this dissertation for extension to polycrystalline textured metals and thin films. This method has the potential to become a valuable tool for obtaining empirical surface energy data associated with AGG of Galfenol grains as well as other metallurgical studies.

Chapter 2

Gallium Drop Contact Angle Experiment

This chapter will focus on the gallium drop contact angle experiment. Its development, results, and thoughts on improvement in future studies.

The gallium drop contact angle technique uses classic contact angle measurement techniques and drop size analysis on a liquid metal, gallium, resting on a metal surface as the metal is heated. This qualitative study serves to explore the trends of orientation dependent surface energy on Galfenol. Gallium was chosen as the probe liquid for our high surface energy metals, γ_{SV} ~2000 mJ/m^2, because it is a liquid above 29.8°C and it has an average surface tension of γ_{Ga} ~715.3 mJ/m^2.[8] This means that liquid Ga will not completely wet a bare metal surface as water does. Water has a relatively low surface tension, γ_{water} ~72.0 mJ/m^2, compared to a solid metal surface energy, hence when interacting with a bare metal surface the water contact angle will reduce to zero, and no solid surface energy can be calculated, which can be seen

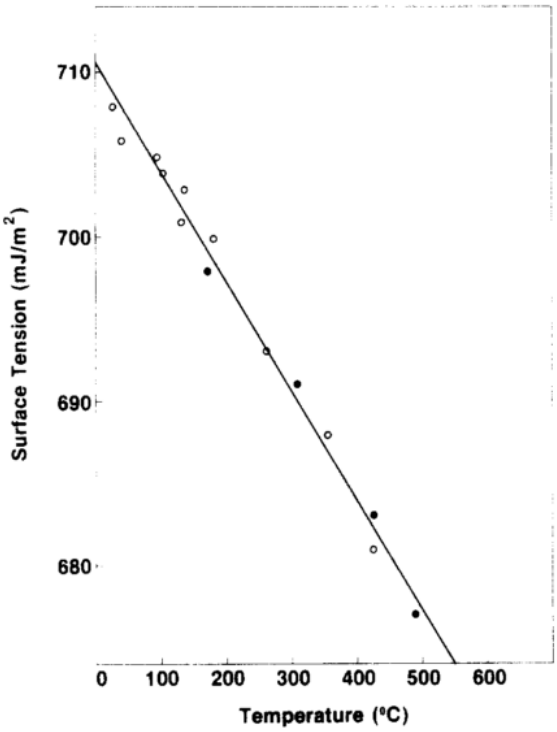

Figure 2.1: This figure plots the surface tension of pure Ga as temperature increases. Extracted from Hardy et al.[8]

in Equation 1.14. The surface tension of Ga varies by 5 mJ/m^2 in the temperature range that this experiment will be carried out, ∼30-100℃. Ga surface tension varies linearly with temperature as $\gamma_{Ga} = 709 - 0.066(T - 29.8)$, where T is the temperature and 29.8℃ is the melting point of Ga.[8] A plot of Ga surface tension vs. temperature from Hardy *et al.* is shown in Figure 2.1.

2.1 Preliminary experiments

2.1.1 Sample Preparation

In order to perform contact angle measurements on any material, the surface of that material must be pristine and well characterized. There can be no doubt that the

probed surface is free of debris, organics, or oxides, for the case of metals, lest the contact angle be influenced by something other than the probed material. Proper sample storage and chemical cleaning (acetone $\Rightarrow$ methanol $\Rightarrow$ DI rinse $\Rightarrow$ N_2 dry) is satisfactory for removing particulates and organic residue, but exposing a bare metal surface by removing the native oxide layer is challenging. This chapter provides basic oxide removal techniques, but there is a more detailed oxide removal study in Chapter 3. The surface must also be as close to atomically flat as possible. Most literature will approximate their surfaces as flat as long as the roughness is 10^2 lesser than the contact area radius. This research strives to obtain nanometer or sub-nanometer roughness on all samples through an extensive polishing protocol.

One of the challenges in developing this new surface energy measurement capability is the need to expose the surface of the metal substrate that is shielded by surface oxides. The following strategies for removing the oxide layer and preventing natural oxidation, thereby increasing the accuracy of measurement, will be employed independently and in combination:

- A flux used in high-temperature metal joining processes plays roles of dissolving of the oxides on the metal surface and preventing of re-oxidation as a chemical agent.

- Colloidal silica polishing with nano-sized particles, such as is used for precise surface observations, like EBSD scans, which require clean surfaces to accurately detect patterns.

- Electro-polishing is effective for passivation of clean surfaces after chemical and

mechanical polishing for removal of surface oxides.

It should be noted that all of these techniques will not prevent oxides from forming for an extended period of time. Therefore, the cleaning would have to be followed by isolation in high vacuum, an inert environment, or another liquid environment that prevents oxidation.

Single crystals and polyscrystalline preparation

Single crystal ingots were prepared by DOE Ames Laboratory, using the modified Bridgman method.[88] Polycrystalline samples are prepared in the Aerosmart lab by Dr. Suok-Min Na using a progressive hot, warm, then cold rolling technique from a polycrystalline Galfenol ingot.[51] The annealing process is described in Chapter 1. Single crystal samples are preferred for contact angle experiments because the prepared surface is isotropic, therefore multiple locations on a single sample surface can be probed and compared as equal surfaces.

Polishing

Samples were prepared by manual grinding with incrementally higher grit SiC paper up to 1200 fine grit and then fine polishing using silica gel with 60 nm sized particles to minimize the roughness as well as the stressed surface states created during grinding.[89] Roughness measurements were performed on ten different 1μm x 1μm areas with an atomic force microscope (Veeco Dimension 3100) after fine polishing. Surface roughness values of 1 nm were measured, thus there is minimal roughness influence on the contact angle measurements. Figure 2.3 shows AFM images of the difference

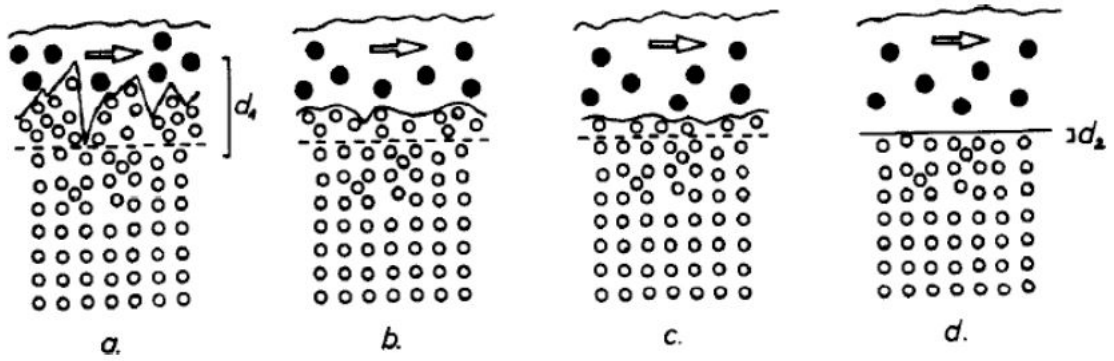

Figure 2.2: (a) Highly stressed surface layer with effective thickness d_1 after polishing with alumina powder. (b,c) Reduction of the stressed layer thickness with silica gel polishing. (d) Extremely smooth surface with stessed later thickness $d_2 \ll d_1$. Taken from Hoffman et al.[9]

between 1200 grit polishing and subsequent silica gel polishing. There is a clear change in surface topography from 1200 grit polish in Figure 2.3a to silica polish in Figure 2.3d where all surface striations from the SiC polishing paper are almost completely removed to produce a nanometer roughness surface. Over a twenty-five AFM scans, silica polished AFM height maps have an average roughness of 1.35±0.30 nm, whereas the 1200 grit average roughness was $R_a \sim 10.03 \pm 2.14$ nm.

Atomic Force Microscopy

AFM is one of the simplest ways to determine roughness at the sub-nanometer scale, as opposed to profilometry which tends to lack the <100 nm resolution. In Figures 2.4a and 2.4b, the same 1200 grit polished polycrystalline Galfenol sample was scanned using a profilometer and AFM, respectively. The profilometer stylus has too large of a tip diameter to resolve surface topographies that are easily visible using an AFM tip. Even the profilometer built-in software is incapable of calculating a roughness measurements in increments <5nm. Granted, the available profilometer

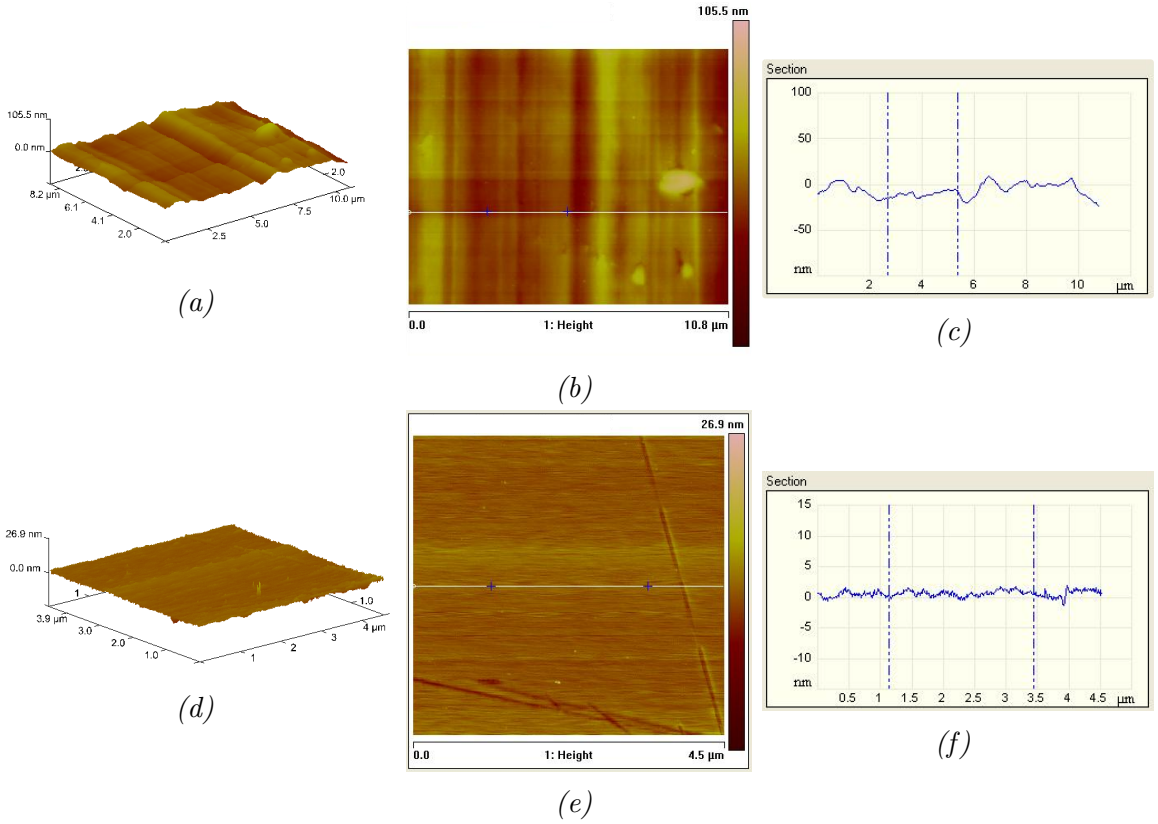

Figure 2.3: These are AFM scans of polycrystalline Galfenol used to measure roughness where (a), (b), and (c) are a 3D plot of surface topography, a height map with a sectioned line, a profile of sectioned line in (b) for a sample polished up to 1200 grit SiC paper. The next three figures, (d), (e), and (f) are the same types of plots for a sample polished up to 0.6µm colloidal silica. The 1200 grit polish had a roughness of R_a = 6.58 nm, and the colloidal silica polish had a roughness of R_a = 0.573 nm.

to this lab is a very old model, and many other profilometers on the market have much better resolution. Nevertheless, due to the constraints of this lab and time, it is clearly preferable to use the AFM for roughness measurements as long as a statistically significant number of measurements are carried out. While operating an AFM can be a long and tedious process, time is saved with precise and accurate roughness measurements based on thousands of section profiles per run, versus one profile at a time with the profilometer.

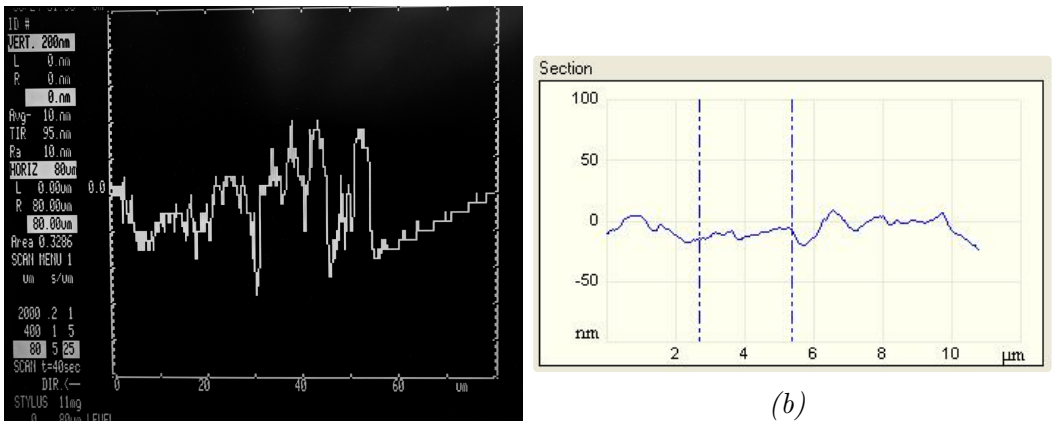

(a) (b)

Figure 2.4: (a) A profilometer section measured on a polycrystalline FeGa sample polished to 1200 grit SiC paper. (b) An AFM section of the same sample.

2.1.2 Thermal Chamber Design Progression

Contact Angle Goniometer (Verison 1)

Preliminary designs of my contact angle goniometer implement a radiative temperature control box which encloses an argon gas filled container where the sample resides, as seen in Figure 2.5a. The presence of argon is meant to prevent any further oxidation of the Galfenol sample as well as the gallium droplet. The container was initially made of a clear acrylic plastic, but prolonged exposure to temperatures above 80°C caused thermal deformation of the plastic making longer experiments impossible to perform without environment contamination. A clear pyrex container replaced the acrylic box to fix this issue. Application of the liquid gallium drop to our surfaces was done via a mounted plastic syringe with disposable stainless steel hypodermic needles that were available at the time. Liquid gallium tends to adhere strongly to the stainless steel needle tips which makes wetting to the sample very difficult. The stainless

steel tip tends to deform the highly viscous gallium drop resulting in non-uniform hemispheric drop shapes, as shown in Figure 2.5b.

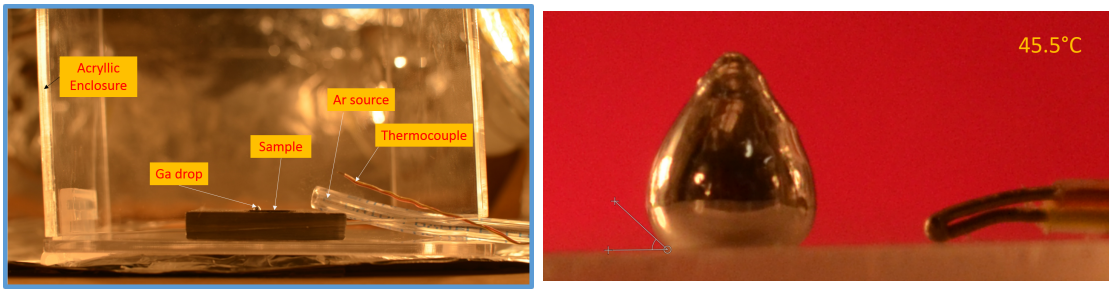

(a) *(b)*

Figure 2.5: (a) The first design of our contact angle goniometer. The acrylic container houses the argon environment and sample. This design was modified with a more stable glass enclosure. (b) A highly deformed gallium drop next to the thermocouple on a ceramic YAG test sample at 45.5°C. The angle measured on this droplet was subtracted from 180° since it was not measured through the liquid.

The radiative box that housed this experiment had a high variability in temperature according to thermocouple readings, so a smaller apparatus with a top-side syringe opening is made to properly perform gallium drop tests at specific temperatures and prevent interaction with the experiment environment. There must also be bright white backlighting to obtain a high contrast drop profile. In this radiative box configuration, the high-reflecting liquid metal surface prevents a high contrast drop profile image, as seen in Figure 2.5b. Proper contact angle measurements also require the gallium droplets to carefully wet the surface while forming an axisymmetric and spherical-like shape on the solid surface. A height adjustment system must be used to move the gallium pendant drop close enough to the sample surface for solid adhesive forces to overcome the adhesion to the needle. Lastly, the argon gas environment could be more well contained, instead of just filling up the glass sample enclosure from the bottom and spilling out the top due to higher density argon displacing the

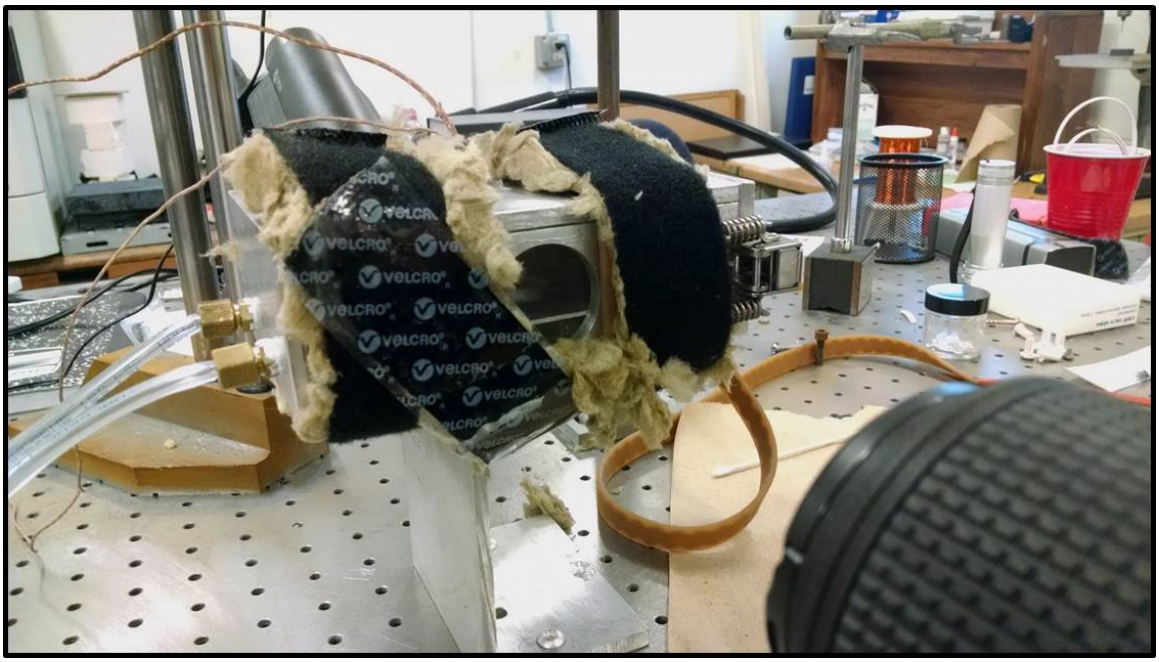

Figure 2.6: The second version of our gallium contact angle goniometer. The aluminum enclosure conductively transfers heat, the gas lines flow Ar gas into the chamber, top-mounted thermocouples monitor the gas and sample temperature, and the glass windows allow for backlighting of the drop profile along with high resolution image capture using a DSLR camera.

surrounding air environment.

Version 2

The new experimental apparatus can be seen in Figure 2.6. The main structure is made of aluminum with two round glass windows on the front and back. The aluminum is meant to conductively transfer heat to the substrate by means of a heating cable wrapped around the outside of the structure. The high thermal conductivity of aluminum allows for a quick transfer of heat, thus an increased control of sample temperature. The time percentage dial controller attached to the heating tape is calibrated with the sample temperature using a thermocouple placed on the sample surface. Sample temperature can be consistently controlled with ± 0.5°C accuracy. Backlighting greatly improved the drop profile contrast by having only one white

Figure 2.7: This is a photograph of a picture being taken of a gallium droplet on highly-textured polycrystalline at 94.4℃ (seen from thermocouple meter) using a Nikon DSLR camera with a long macro-lens.

light source coming from one side of the droplet, as seen in Figure 2.8. The Ar environment is also far more contained and controlled. The silicone sealant creates a nearly air-tight system where the Ar gas will displace all gas contaminants that could further oxidize the sample or gallium droplet. Once the sample is inserted and sealed in the environmental chamber, Ar gas prevents further oxidation throughout the experiment. A positive partial pressure is achieved in the chamber with an in- and out-valve to constant flow air out of the chamber. A high quality macro lens (Nikon AF Micro Nikkor 200-mm 1:4 D) is used to precisely quantify dimension changes in substrate and liquid metal drop during thermal expansion.

2.1.3 Gallium Oxide removal

While extensive steps have been taken to inhibit oxidation on the metal surfaces, preventing oxidation on the surface of liquid gallium was a greater challenge. Pure gallium and Gallium-based alloy surfaces very quickly oxidize in ambient air environments, and form turning a thin layer of gallium oxide (Ga_2O_3 and Ga_2O).[90–92] Like any other metal, Ga has a high potential for spontaneous oxidation, or passivation, with a reduction potential of -0.56 V for the chemical reaction shown below in Equation 2.1:[93]

$$Ga^{3+} + 3e^{-} \rightleftharpoons Ga \tag{2.1}$$

This oxide layer is solid and remains elastic until it experiences a yield stress. Therefore, that an oxidized gallium droplet does not behave as a simple liquid, but as a viscoelastic material. In addition, the oxide layer of gallium is known to adhere to almost any solid surface, causing a severe stiction problem that interferes with interfacial energy measurements.[92] This shows how dramatically the gallium surface tension decreases when the oxide forms. Khan *et al.* showed that gallium oxide forms hydroxyl groups on their exterior surface, making the drops lyophilic as opposed to the expected lyophobic behavior of pure gallium, a high surface tension liquid.[8,94]

Figure 2.8 shows our direct observation of this phenomenon with teardrop shaped droplets formed by adhering to the iron surface while simultaneously being pulled upwards by the deposition needle. The general shape of these drops were unchanged for many hours even at temperatures approaching ∼100℃, thus exhibiting the sta-

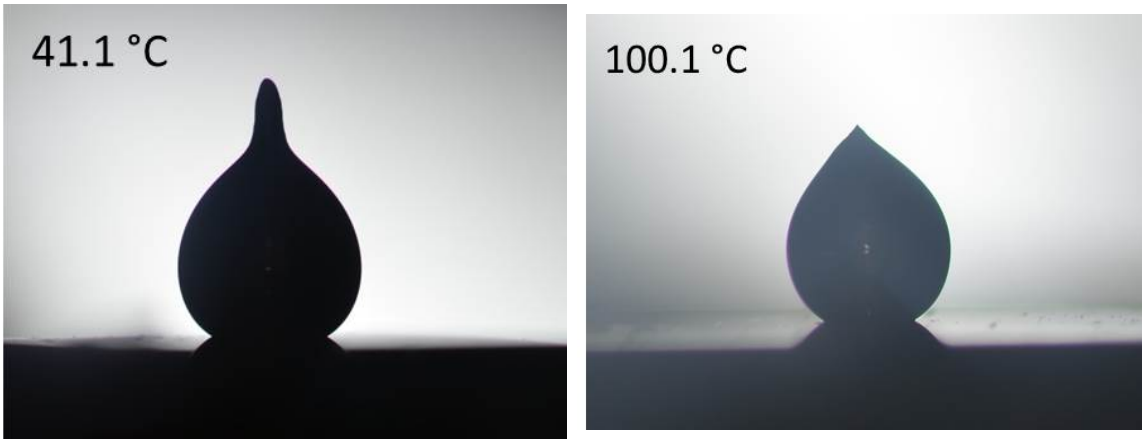

(a) *(b)*

Figure 2.8: Pure liquid gallium obtains viscoelastic properties when trace amounts of oxygen are present via formation of oxide shell. Non-axisymmetric Ga drops form on this iron substrate.

bility of viscoelastic properties caused by the solid oxide layer. Removing the oxide layer from liquid gallium will return normal liquid properties to gallium and allow the use of axisymmetric drop analysis calculations: Young-Laplace equation, tangent method, and circle approximation method.

Oxide removal permits liquid gallium to directly interact with metal surfaces instead of gallium oxide. A number of techniques have been developed to remove and recover gallium oxide on liquid gallium: ultra-high vacuum (UHV) techniques,[90,91] chemical vapor etching,[95,96] and electrohydrodynamic phenomena.[97] A chemical vapor etch is the best option for this experiment because it has a minimal effect on the surface of metals and the experimental apparatus does not need to be changed. To execute the vapor etch, a pendant drop of gallium was formed and a pipette of 37wt% HCl was brought in close proximity to etch away the oxide layer. The same procedure was performed on the sessile drop of gallium on the desired surface to etch away any oxide left on top of the droplet, as seen in Figure 2.9. The contact angles of

gallium on bare glass before and after HCl vapor treatment are similar to respective contact angle values in Kim *et al.*[95] From this, it can be assumed that the surface tension of the gallium sessile drop with a gallium chloride shell is similar to that of pure gallium, as determined by Kim *et al.*[95] This is verified using the pendant drop technique on HCl treated gallium. The HCl vapor etch may even have the benefit of removing any native iron oxides (Fe_2O_3) from the FeGa surface itself since HCl is a known etchant of Fe_2O_3.[98]

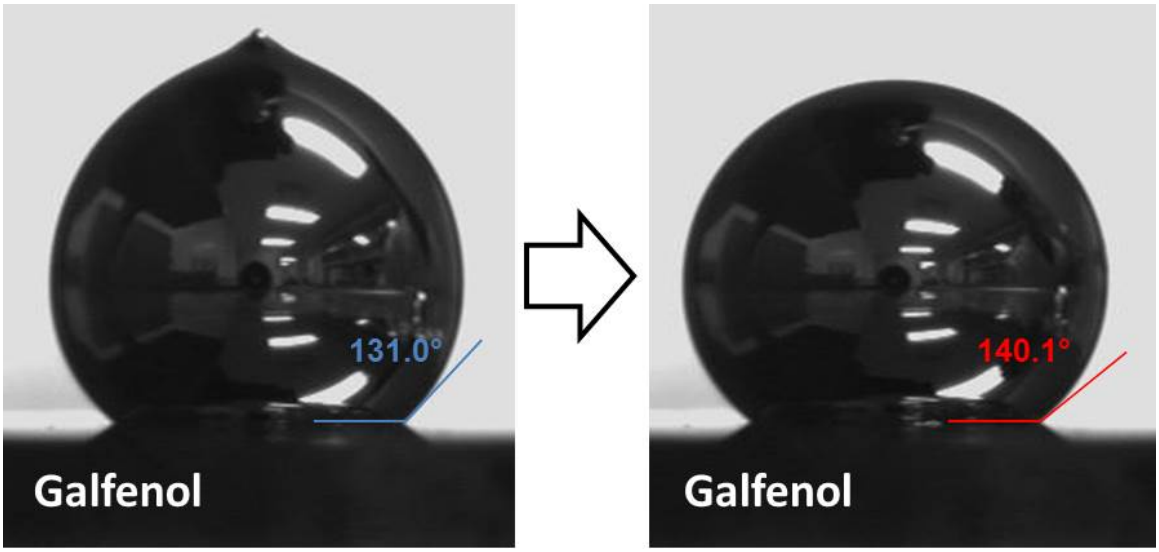

Figure 2.9: This image shows the contact angle of gallium on a Galfenol sample in an argon environment before and after HCl vapor treatment.

2.2 Final experimental design and results

Polycrystalline Metals

With the HCl vapor treatment added to the procedure, temperature-varying gallium contact angle measurements in an argon environment were executed in the aluminum chamber on multiple metal substrates. Polycrystalline samples of high purity

(>99.99%) tin, copper, and iron were polished and had liquid gallium deposited on their surfaces. The temperature in the chamber was slowly (<10℃/min) increased from 30℃ to just below 100℃. Beyond 100℃, the heating tape becomes inconsistent with the intervals of heat applied to the chamber. Photographs of gallium drop profiles are taken at 10℃ intervals to observe progression of the drop shape as temperature increases. The same procedure is done as the temperature is decreased to 30℃ to observe reversibility of this process.

A chemical vapor etch is used to replace the gallium oxide (GaO) layer with a gallium chloride layer, restoring the droplet surface tension to nearly that of pure Ga, as shown by Kim *et al.* To execute the vapor etch, a sessile drop of gallium was formed on the desired surface and a pipette of 37wt% HCl was brought within 2 cm to etch away the gallium oxide layer.

It is known that liquid gallium tends to corrode most metal surfaces.[99–101] Since experiments lasted for less than one hour, corrosion between the two metals should not be significant enough to effect the measurement. Later in this section, the surface stoichiometry effects of the liquid Ga droplet on Galfenol for varying temperatures is examined using X-ray photoelectron spectroscopy (XPS). For the polycrystalline tin and copper samples, gallium began to visibly corrode through the surface between 60℃ and 70℃, as evident by a rapid contact angle decrease on only one side of the drop profile, as seen in Figure 2.10. Polycrystalline iron samples did not experience corrosion problems throughout the experiments. It is expected that as the temperature increases, the gallium contact angle will increase. This is becuase the surface energy of a metal should decrease with an increase in temperature. Some gallium

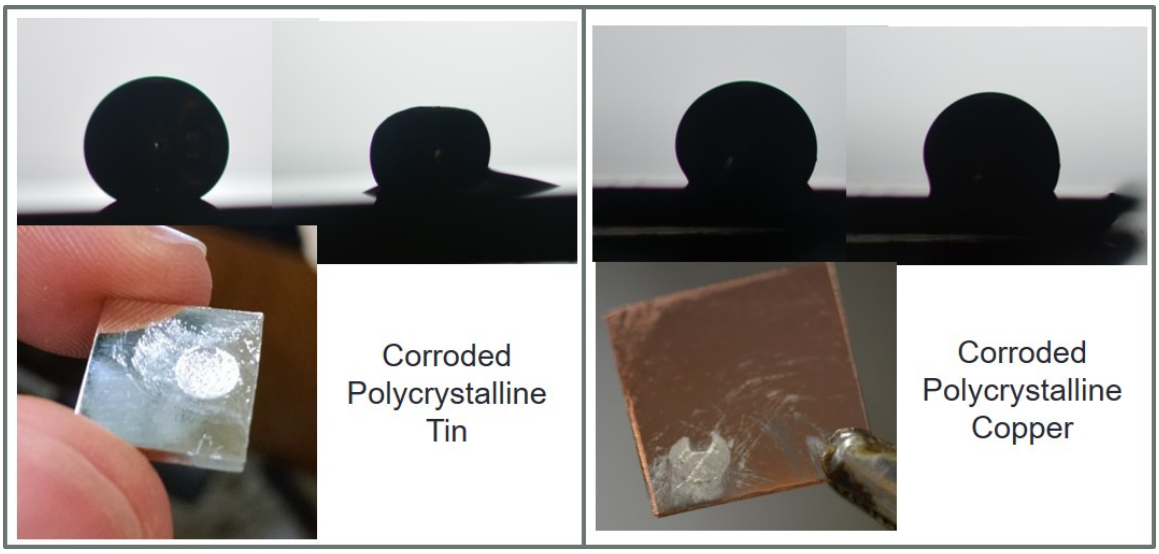

Figure 2.10: These photographs show a gallium drop contact angle on polycrystalline Sn (left) and polycrystalline Cu (right), and the corrosive effects of the gallium on the same substrates.

contact angles decrease on iron, but it is often that the decrease occurs on one side of the drop profile as the temperature increases. This is likely due to anisotropies on the surface in the form of kinks, steps, or grain boundaries. This suggests that a single-crystal grain or highly-textured surface grain is needed to properly observe an isotropic drop expansion.

Since the iron sample did not corrode in the presence of gallium, we proceeded to a Galfenol sample with an abnormally grown (1 1 0) grain. Figure 2.11 shows the location of a gallium droplet in contact with the highly Goss-textured surface. Using the same temperature intervals, the right and left contact angles were measured. The contact angle measurements are shown in Figure 2.12. The contact angle measurements show anisotropic spreading behavior since the left contact angle recedes as temperature increases while the right contact angle advances. At 60.7℃, the contact angles reached close to the same value which may indicate an equilibrium point of

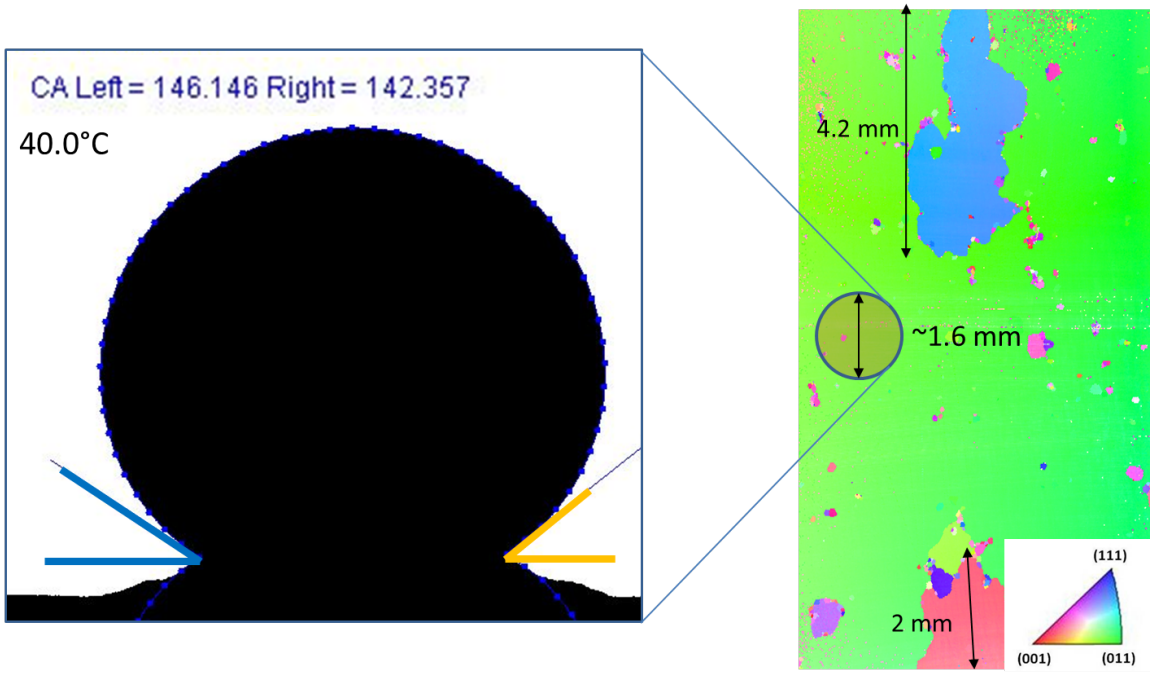

Figure 2.11: The location of a gallium drop on highly Goss-textured surface. The contact angle is measured using the ImageJ plugin, DropSnake.

combating thermal expansions caused by nearby island grains.

Both right and left contact angles were measured at each temperature. Plots of contact angle measurements in Figure 2.12. The contact angle measurements show anisotropic spreading behavior since the left contact angle recedes as temperature increases while the right contact angle advances. Asymmetries may be associated with nearby island grains that are evident in the electron backscatter diffraction (EBSD) scan of Figure 2.11. We had also expected a decrease in surface energy with increasing temperature. This is because surface energy depends on the net inward cohesive force between atoms, and the cohesive force binding atoms to one another will decrease as a temperature increase causes atoms to vibrate more rapidly.

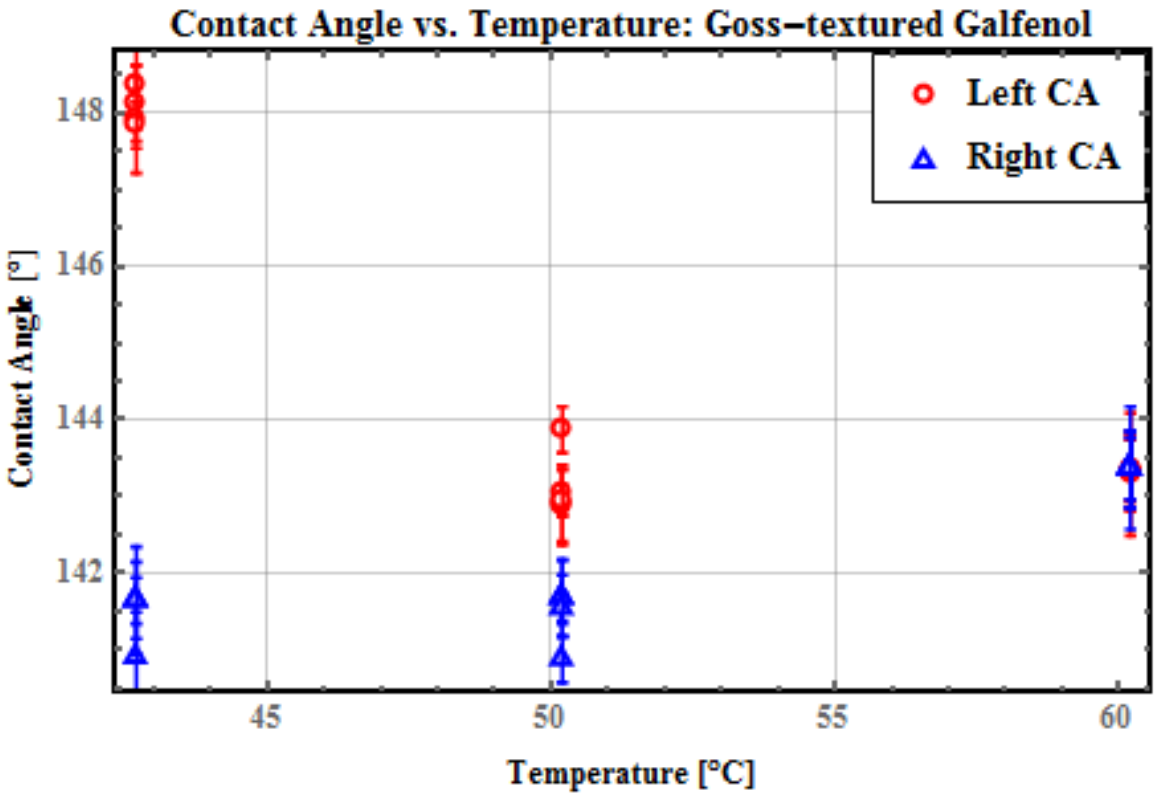

Figure 2.12: Blue and red dots show left and right contact angle, respectively, of liquid gallium on (1 1 0) *Fe-Ga.*

Single-crystal Galfenol

Using the same acid vapor etch, Ga droplets were placed on samples of single crystal Galfenol. Contact angle values decrease from the (110), (100), and (111) facets, in that order, although the angles for the (100) and (111) facets are not statistically different (within one standard deviation of one another). According to Young's equation, these contact angles should be inversely proportional to surface energy. The measurements indicate that the surface energy of a (110) surface has the lowest surface energy as expected based on DFT predictions.[86] The magnitudes of angles for (100) and (111) surfaces were statistically similar. Ga contact angles values on highly-textured Goss (110) grains and the (110) single crystal facet are within one standard

deviation of one another, and thus in excellent agreement.

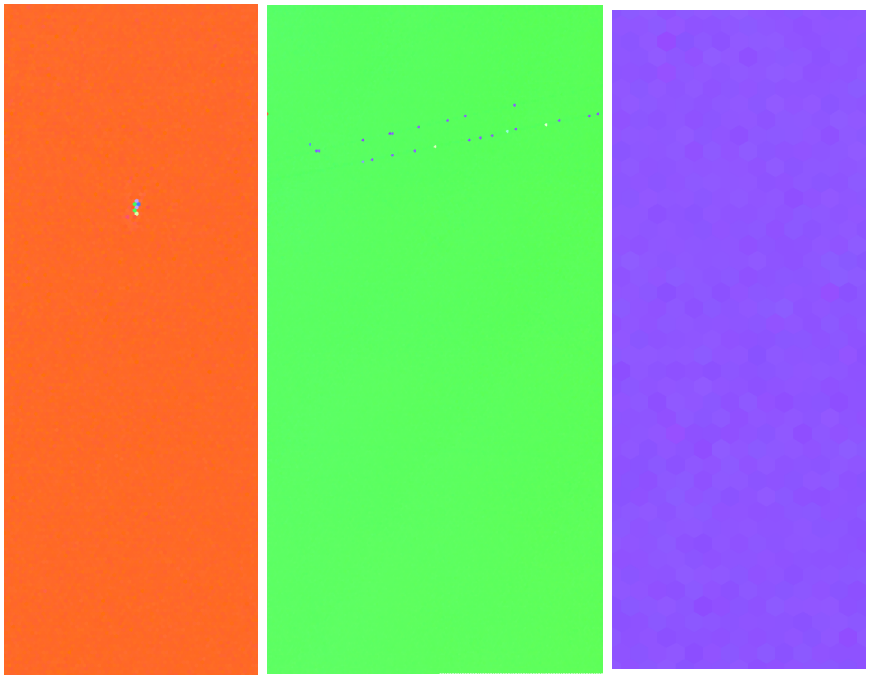

(a) *(b)* *(c)*

Figure 2.13: EBSD images of single crystal $Fe_{82}Ga_{18}$ *where (a) is* (1 0 0)*, (b)* (1 1 0)*, (c)* (1 1 1)*.*

X-ray photoelectron spectroscopy study on Ga corrosion

XPS measurements were performed after Ga drop experiments at the University of Maryland Surface Analysis Center using a high sensitivity Kratos AXIS 165 spectrometer to examine the effect of Ga droplets with a chloride shell affects the surface stoichiometry of Galfenol. Samples were prepared by placing a Ga drop on the Galfenol surface, heating the sample to a temperature of 30°C, 50°C, 70°C or 90°C, and holding that temperature for 15 minutes. The 70°C sample was damaged during XPS testing. XPS was also performed on a control sample that was not exposed to a Ga drop or elevated temperatures.

XPS measurements show an increasing intensity in the Ga_2O_3 (1116.7 eV) peak in samples at elevated temperatures. Figure 2.14 the Ga 2p peak increases as the temperature increases. This was expected as surface adhesion of Ga was likely greater in samples exposed to higher temperatures. Excess surface Ga would have oxidized in the time between the thermal tests and XPS due to exposure to ambient conditions. In the Fe region, a strong signal of Fe_2O_3 (710.8 eV) with a small peak of metallic Fe (706.7 eV) was present on the control sample. On the 30℃, 50℃ and 90℃ samples, the Fe_2O_3 peaks diminished and the metallic Fe peak became dominant. The increased presence of Ga at elevated temperatures suggests that the Ga may have etched away the Fe_2O_3 and exposed metallic Fe, as Ga is a corrosive element in the liquid state. The Ga signal is attributed solely to the Ga droplet as Fe has a higher potential for oxidation than Ga, shown by the heavy presence of Fe_2O_3 at the surface, and therefore Fe has a dominant concentration at the surface.

2.3 Conclusions and next steps

We have developed a new method for measuring the contact angle of gallium on metal surfaces with targeted crystal orientations. The model calculates surface energies on Goss-textured polycrystalline Galfenol and single crystal samples that are two orders of magnitude greater than theoretical predictions for α-Fe. We have observed a qualitative trend in single crystal samples of different crystallographic orientations that matches predictions made using DFT simulations, where γ_{100} and γ_{111} are similar in magnitude (<5% difference) and γ_{110} is 20% less than values of γ_{100} and γ_{111}.

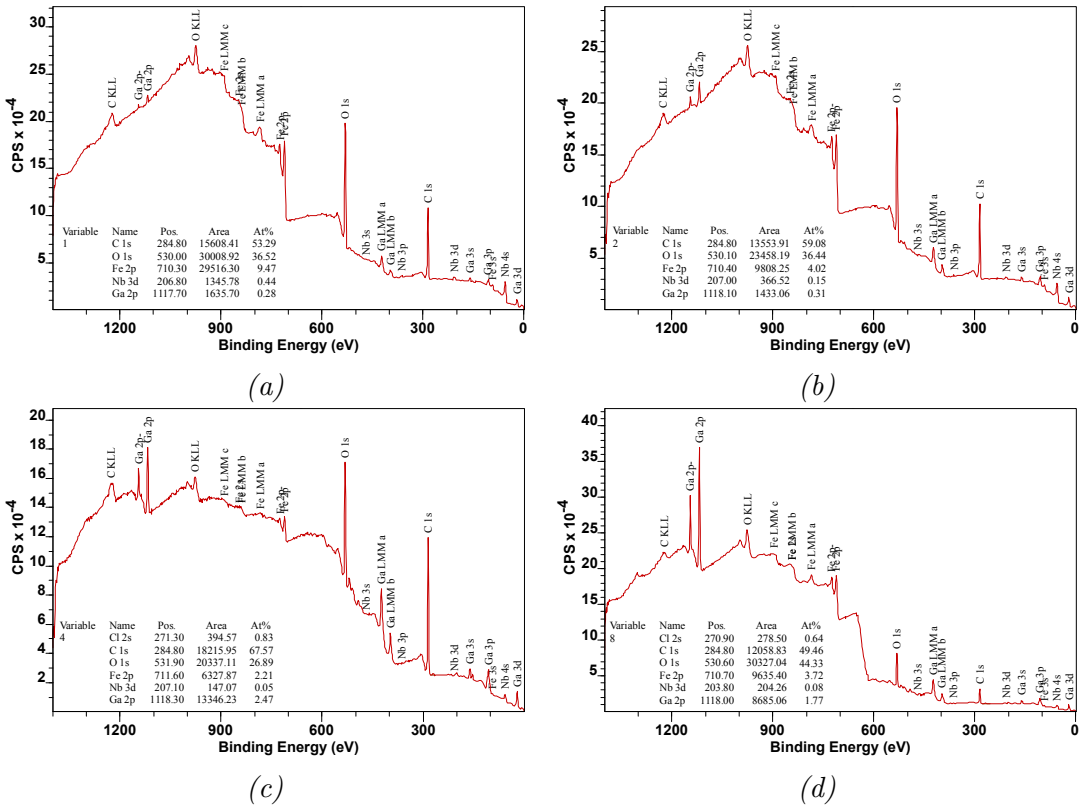

Figure 2.14: (a),(b),(c) These are plots of the full survey, Fe 2p, and O 1s binding energy regions, respectively, at the surface of polycrystalline $Fe_{81}Ga_{19}$ that was well-polished, acetone sonicated, and polished again with a dry silica pad in a nitrogen glovebox.

Future contact angle experiments will be performed strictly on single crystal samples due to greater uniformity of crystal orientations at the surface when compared to highly-textured rolled Galfenol sheets with multiple island grains at the surface, as seen Figure 2.11 on the right. Island grains can pin the triple-phase-boundary line, or contact line, and potentially skew results. Only the contact line matters in contact angle measurements. This uniformity will guarantee consistent interactions at the Ga-Galfenol-Ar triple line. The presence of a passivation layer of Fe_2O_3 on Galfenol hinders this surface energy measurement. More thorough cleaning and polishing techniques, including chemical and plasma etches, in inert environments will be employed to eliminate or mitigate this layer formation. The interaction between

the Ga and Galfenol interface is not well understood, and an in-situ measurement would need to be done to observe this reaction or lack thereof. Currently, this in-situ measurement is beyond current capabilities, so it is unknown how it would even affect the Ga contact angle measurement.

After presenting these preliminary findings at the XXIV International Materials Research Congress and 2015 MRS Fall Meeting,[102,103] I discussed possible avenues of improvement for the gallium contact angle experiment with colleagues and potential collaborators. A more concrete measurement of γ_{SL} between liquid gallium and solid would need to be examined, a very non-trivial task. Ultimately, we decided to suspend the gallium drop experiment and re-evaluate the measurement strategy.

Overall, this was an exploration of well-proposed and innovative research. Much was learned about the complexity of contact angle experimentation from both a theoretical and experimental perspective. This setback persuaded me to find a more robust and promising method for accomplishing project goals within the constraints of orientation-dependent surface energy characterization.

Chapter 3

Two-Liquid-Phase Method

The gallium drop technique study experimentally confirmed trends that are predicted in theoretical models, but identified that oxide formation on the sample surface interferes with acquisition of accurate quantitative results. This revelation led to a more robust study that expands on a classic drop shape analysis technique, the two-liquid-phase method, and eliminates complications associated with oxide layer formation. By immersing the sample in an oil environment, Galfenol surfaces are isolated from air, thus preventing oxidation. While in this environment, samples are probed with a deionized water droplet and a shape analysis is performed to calculate surface energy values using the Schultz method. Due to the added pressure from an immiscible liquid, the water droplet will not completely wet the Galfenol surface as it would in air due to the very high surface energy. I modified this method by utilizing a technique previous only used on plastics to prevent water from spreading. I hypothesize that patterning sample surfaces with an ion mill will stabilize droplets during shape measurements, thus generating reliable surface energy calculations. I performed and analyzed mul-

tiple oxide removal procedures using X-ray photoelectron spectroscopy. The most promising procedures, polishing in an inert atmosphere and ion bombardment cleaning, show much greater surface wetting of Galfenol by water while immersed in a hydrocarbon environment.

Success of this experiment could allow metallurgists to finally experimentally measure surface energy for any metal surface, thus providing confirmations of theory and sparking new ideas of how grain growth in metals can be controlled and even manipulated.

3.1 Two-liquid-phase contact angle method

3.1.1 Two-liquid-phase contact angle method

This method returns to the idea of water contact angles on metal surfaces. As described previously, water will spread completely on a nearly-flat metal surface surrounded by a gaseous environment. Instead of a gaseous environment, the water-metal system can be surrounded by another liquid. It has been observed that instead of wetting completely, a water droplet will only partially wet a metal when the surrounding environment is an immiscible liquid. This is called the two-liquid-phase contact angle method developed by Jacques Schultz.[104–106] Schultz divides the surface energy into dispersive and polar components, as proposed by Fowkes.[74] As discussed in Chapter 1, water is predicted to interact with a metal by dispersive interactions only.[72,74,77] For this reason, we expect to see a high contribution to the surface energy of Galfenol

from dispersive interactions.

A full derivation of this method can be found in Appendix B. In order to calculate the dispersive component of γ_{SV} for a solid surface, the water contact angle must be measured on a solid immersed in n-alkanes. By interpreting Equation B.5 as a classic linear function, $y = mx + b$:

$$\underbrace{\gamma_W - \gamma_H + \gamma_{WH}\cos\theta_W}_{y} = \underbrace{2(\gamma_S^D)^{1/2}}_{m}\underbrace{[(\gamma_W^D)^{1/2} - (\gamma_H^D)^{1/2}]}_{x} + \underbrace{I_{SW}^P}_{b}$$

γ_W, γ_H, and γ_{WH} are known from consistently confirmed literature values,[107–110] and are listed in Table 3.1. In the case of the equation above, the probe liquid L_1 is water denoted by W, the bulk liquid L_2 is a hydrocarbon denoted by H, and the solid being probed is denoted by S.

A data set of xy-coordinates will be made by dropping water in an n-alkane environment to determine γ_S^D and I_{SW}^P. The value of γ_S^D will be calculated from the slope of the measured dataset and I_{SW}^P is calculated through the y-intercept.

Table 3.1: Hydrocarbon surface tension and water-hydrocarbon interfacial energy

***n*-alkanes**	$\boldsymbol{\gamma_H}$ **(mJ/m²)**	$\boldsymbol{\gamma_{WH}}$ **(mJ/m²)**
hexane	18.4	50.1
octane	21.7	49.8
decane	23.8	51.0
hexadecane	27.5	51.3

The polar component of the solid surface energy is determined using the same method described above,[104] but the bulk liquids now have both dispersive and polar components. This is also derived in Appendix B. These bulk liquids of chloroalkanes, nitroalkanes, aromatics, or alcohols are expected to establish a linear relationship

between $I^P_{SL_2}$ and the square root of the polar component of surface tension from the bulk liquids. Schultz *et al.* suggests that this result allows all nondispersive interactions to be grouped together as a polar interaction, and they may be represented by the geometric mean of the polar component of the surface free energy of liquid and solid, as proposed by Owens and Wendt in Equation 3.1. This expression is verified experimentally, but there are no theoretical reasons why all nondispersive interactions should be represented by a geometric-mean expression.[78]

$$\begin{aligned} I^P_{SL_2} &= 2(\gamma^P_S \gamma^P_{L_2})^{1/2} \\ \rightarrow \ \gamma^P_S &= \frac{(I^P_{SL_2})^2}{4\gamma^P_{L_2}} \end{aligned} \tag{3.1}$$

The solid surface energy can then be determined from Equation 3.2:

$$\gamma_S = \gamma^D_S + \gamma^P_S \tag{3.2}$$

3.1.2 Preliminary investigation of Cleaved Mica

Preliminary two-liquid-phase method experiments on muscovite mica showed quick and complete wetting of water on pristine mica surfaces cleaved in decane and hexadecane, contradictory to published results.[106] Mica is regularly used as a substrate in fields such as scanning probe microscopy, biotechnology, and material science, because its perfect cleavage along its {1 0 0} face and sub-nanometer roughness makes it suitable for depositing thin films.[111] Clearly, more iterations of this experiment

must be done to recreate this seminal paper's data, but this made me consider how a water droplet on a mirror-finished material of even greater surface energy (e.g. Fe and Fe alloys) would spread even faster than it had on a pristine mica surface. A contact angle may not stabilize on a well-polished Galfenol sample even using this two-liquid-phase method, thus we must consider more options to create a measurable contact angle that can extract Young's contact angle.

When mica samples were removed from the decane environment, they were wiped clean with lint-free wipes and further cleaned with acetone. When the samples were returned to the decane environment, a droplet wet the surface with an observable contact angle. When this process was repeated in hexadecane, the observed contact angle increased to the contact angle measured in Schultz *et al.* This is a revealing result for two reasons: 1) Schultz *et al.* may have had mica samples that were roughened or air contaminated in his seminal paper, 2) rough surfaces will increase the contact angle from a flat surface contact angle in a two-liquid-phase experiment.

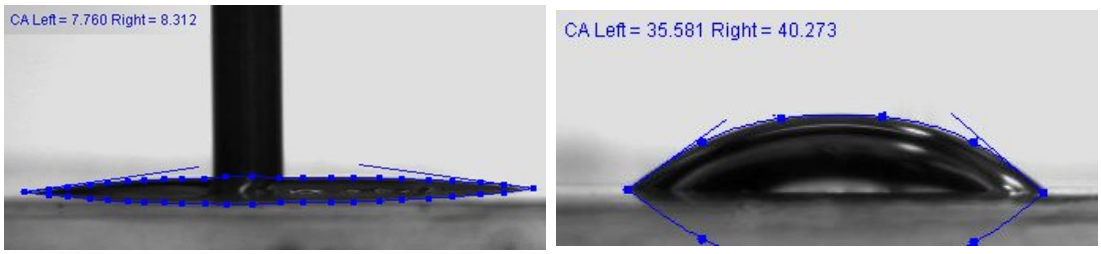

(a) *(b)*

Figure 3.1: (a) Contact angle measurement on mica freshly cleaved in decane. (b) Contact angle measurement on contaminated mica.

If this roughness is controlled by patterning the surface to a specific geometry, the same trend can be observed with the added benefit of a robust calculation of Young's contact angle by way of Equation 3.3 or 3.4, which are the Wenzel and Cassie-Baxter

equations, respectively.

$$\cos\theta_{Wen} = r\cos\theta_Y \tag{3.3}$$

$$\cos\theta_{CB} = f_1\cos\theta_Y - f_2 \tag{3.4}$$

where r is the ratio of the actual solid surface area to the apparent projection area of the rough surface (Wenzel roughness factor), f_1 is the *total* area of solid under the drop per unit projected area under the drop, f_2 is total area of the bulk medium (air or second liquid) under the probe drop per unit area, and $\theta_Y, 1$ is the contact angle on a smooth surface of material 1 (solid).

3.2 Development of experiment

There were a number of challenges faced in preparing both samples and apparatuses for this experiment. Some were obvious (equipment locations and availability), while others (oxide removal, patterning metal surfaces, and modeling a two-liquid contact angle system) were found along the way to the final experimental procedure.

3.2.1 Developing two-liquid-phase contact angle experiment

The experimental apparatus pictured below consisted of a Kruss DSA10 telescopic goniometer, inverted New Era Programmable Single Syringe Pump NE1000 attached to a height gauge, Hamilton Model 1001 Luer-tip gas-tight syringe, a quartz cube container, and a Thor-Labs GN2 dual-axis goniometer stage. The telescopic goniometer

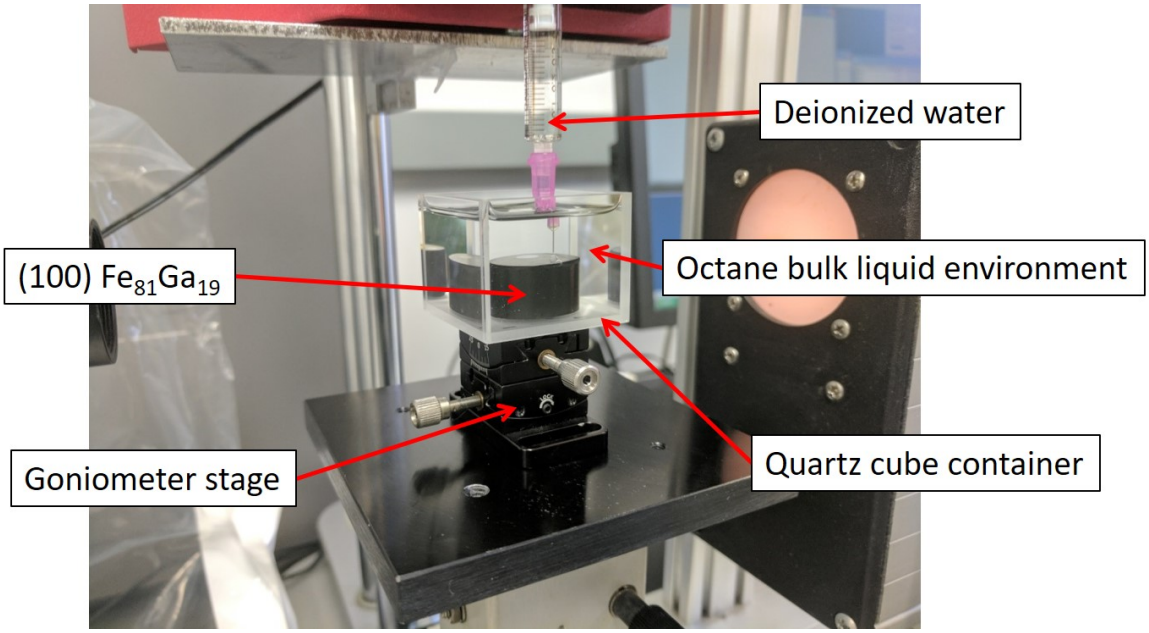

Figure 3.2: This photograph shows a two-liquid-phase contact angle experiment in progress on a (1 0 0) *single crystal FeGa sample.*

was provided through collaboration with the Department of Civil & Environmental Engineering at the University of Maryland. This instrument provides a high quality image of the sessile drop profile by zooming in close to the target and focusing to obtain a clear contact angle. The Kruss DSA10 has a 6.5x magnification. Figure 3.2 shows the backlighting arrangement in the form of a diffusely lit circle. This light can be dimmed manually which allows control of the image brightness. Too bright of an image will skew the ability of DSA10, a proprietary software of the Kruss goniometer, to extract a droplet profile, as seen in Figure 3.3. The stage can be smoothly translated manually in the x-, y-, and z-directions to properly place the sample in the center of the frame. Translation in the x-direction is particularly useful when placing multiple drops on one sample.

First attempts of fabricating a vessel for the two-liquid-phase experiment were

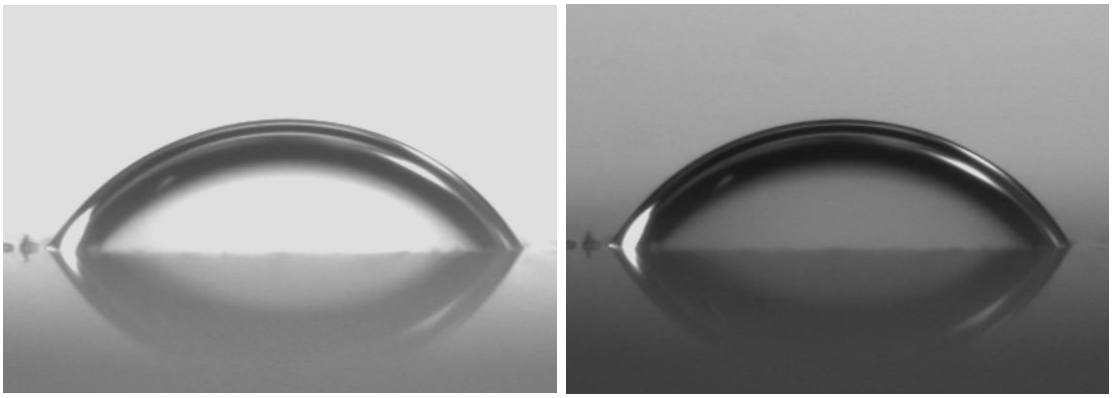

(a) *(b)*

Figure 3.3: These are photos of the same water sessile drop in an octane bulk liquid environment. (a) The backlight is too bright in this photo to properly resolve the sessile drop profile. The shine on the drop does not contrast enough with the background. (b) This is the proper amount of backlighting. The backgound is a light grey, and the drop profile edge has plenty of contrast to extract a clean profile.

done by cutting and cleaving clear acryllic sheets and bonding them together with a solvent welding agent to form a box with an open top. Sealing these boxes to be n-alkane-tight was a great challenge because surface tension of n-alkanes are less than water, hence they will more readily wet any surface and leak through cracks that water could not. Once sealed, acryllic boxes were used for exclusively one bulk liquid n-alkane due to cleaning solvents used to routinely clean chemistry equipment (acetone and methanol) react with acryllic to make it opaque instead of transparent. This avenue was too time-consuming and left many opportunities for contamination of the experiment. Fortunately, an extremely high quality glass cube container designed for liquid chromatography, hence sealed to any liquid penetration, was found unused in a collaborating laboratory, and I was permitted to use it for my experiments. Since it is made of quartz glass, it is able to be cleaned without any adverse effect to its transparency. The quartz cube container is prepared by washing with Alconox powder,

rinsed thrice with deionized water, isopropanol, acetone and then methanol, in that order. The methanol guarantees significant removal of any nonpolar solvents (e.g. n-alkanes). The container is then filled with $\sim$15 mL of the bulk liquid environment, and the polished sample is placed the container.

Polishing protocol is similar to the procedure described in Section 2.1.1 where an automatic polisher is now used for grinding, and a vibratory polisher finishes with colloidal silica. Use of the automatic polisher and vibratory polisher is generously provided by an ongoing collaboration with the Magnetic Materials Laboratory at the Naval Surface Warface Center (NSWC) in Carderock, MD. The polishing procedure is outlined in Table 3.2.

In the likely case that a sample is not flat with respect to the live image on the computer screen, stage tilt is adjusted using the goniometer stage and a horizontal line on the live image provided by the software. Both angles, θ and φ, can be adjusted using the telescopic lens image and the same macro-lens Nikon camera used in Chapter 2, shown in Figure 3.4a. The telescopic lens is positioned at 0° with respect to the stage, and the macro-lens is at 90°, as seen in Figure 3.4b.

Deionized water is drawn into the gas-tight syringe through a 30-gauge stainless steel HPLC (flat-tipped) needle. The drop volumes can start at 1μL and expand to 20μL during an advancing contact angle measurement. To purge air bubbles, the syringe is inverted (pointing upward) and the chamber is flicked allowing air bubbles to float toward the syringe entrance. This is a common practice among medical professionals when injecting any fluid into a patient's body. The syringe is mounted to the inverted syringe pump and lowered into the quartz cube container. Using

Table 3.2: Polishing procedure developed by NWSC Carderock Division for subnanometer roughness on Galfenol.

Paper	**Lubr./Susp.**	**Time**	**Force**	**Wheel/Head speed**
SiC 220	Water	1 min	200 N	150/150 rpm
SiC 320	Water	1 min	200 N	150/150 rpm
SiC 1200	Water	1 min	150 N	150/150 rpm
SiC 2400	Water	1 min	150 N	150/150 rpm
MD-Mol	DP-Suspension, A 9μm level 2/15 DP-Lubricant, Blue level 5/15	3 min	200 N	150/150 rpm
MD-Nap	DP-Suspension, A 1μm level 2/18 DP-Lubricant, Blue level 7/15	1 min 30s	160 N	150/150 rpm
Chem-MD	OP-U level 2/16, Colloidal Silica	3 min	150 N	150/150 rpm
MD-Nap	OP-U level 2/16, Colloidal Silica	3 min	60 N	150/150 rpm
MD-Nap	Colloidal Silica on vibratory polisher	3 hours	N/A	N/A

the programming settings on the NE-1000, the user enters the inner diameter of the syringe to allow the NE-1000 program to dispense correct liquid volumes.

The most stable contact angle will be calculated using advancing and receding contact angles measurements in Equation 3.5.

$$\cos\theta_{ms} = (\cos\theta_a + \cos\theta_r)/2 \tag{3.5}$$

The lowest minima in Figure 3.6 represents the most stable contact angle which can be called Young's angle for an atomically flat surface. An averaging of advancing and

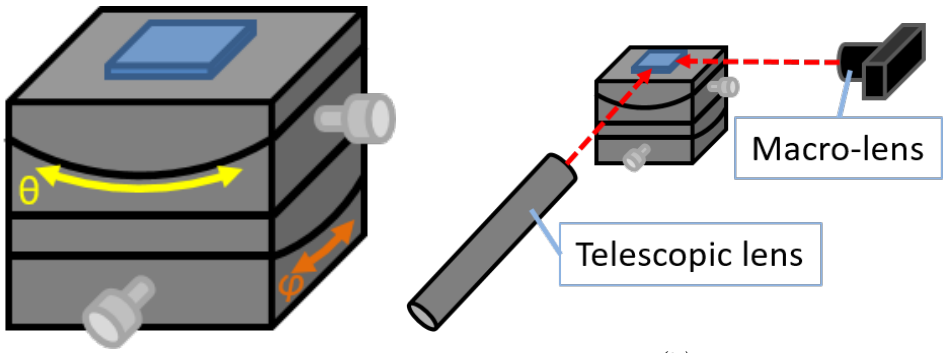

Figure 3.4: (a) This is an illustration of the dual-axis goniometer stage that can adjust both θ and φ parameters. (b) This illustration shows the two cameras used to completely level the sample stage by placing them at 0° and 90° with respect to the stage.

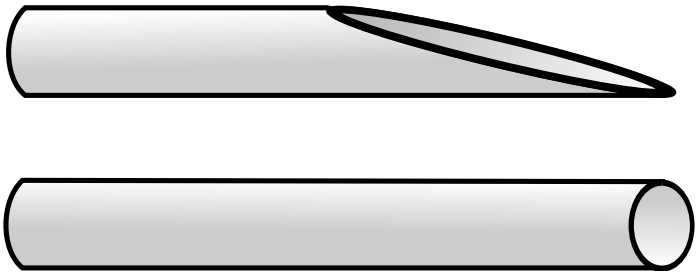

Figure 3.5: The top illustration is a hypodermic needle, the bottom is a flat needle. The flat needle is used to dispense droplets in pendant and sessile drop experiments.

receding contact angles is reasonable considering the practical advancing and receding contact angles are metastable states on opposite sides of the most stable state on a Gibbs energy vs. contact angle curve.

The drop volumes of advancing and receding contact angles will give us a range of volumes for static contact angle measurements on the same surfaces, which are also expected to totally wet our flat surfaces, but will be measured to validate that assumption.

Videos are an efficient way to record dynamic contact angles since many can be recorded in one file. This is because a dynamic contact angle remains the same regardless of drop size, as illustrated in Figure 3.7. Advancing and receding contact

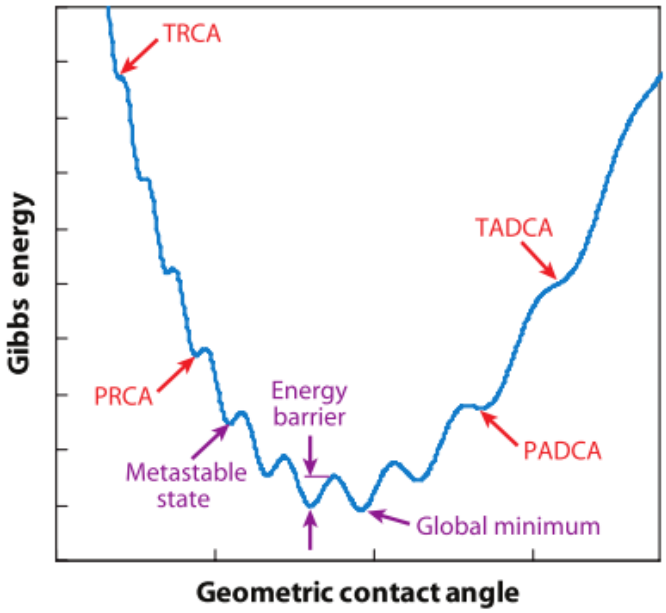

Figure 3.6: The curve of Gibbs energy versus geometric contact angle for a two-dimensional drop on a heterogeneous solid surface. Each minimum represents a metastable equilibrium state. The lowest of all minima indicates the most stable state. In between every pair of equilibrium states there exists an energy barrier. Abbreviations used: PADCA, practical advancing contact angle; PRCA, practical receding contact angle; TADCA, theoretical advancing contact angle; TRCA, theoretical receding contact angle.[10]

angles should not change with drop volume. This will remain true unless a surface contaminant is encountered or the drop volume becomes too small. As the drop volume decreases, the sessile drop diameter approaches the surface roughness. In this small volume case, the contact angle is not reliable.

For each case, advancing and receding contact angles, the pinning force at the triple line of the sessile drop reaches a maximum, and the pressure of the expanding or receding drop volume becomes too great to hold. Therefore, the contact line breaks under the volume pressure and relaxes at a new pinning point where the expansion or recession process begins again. Advancing and receding contact angles are recorded in succession for three runs each. If the size of the sample permits, at least three

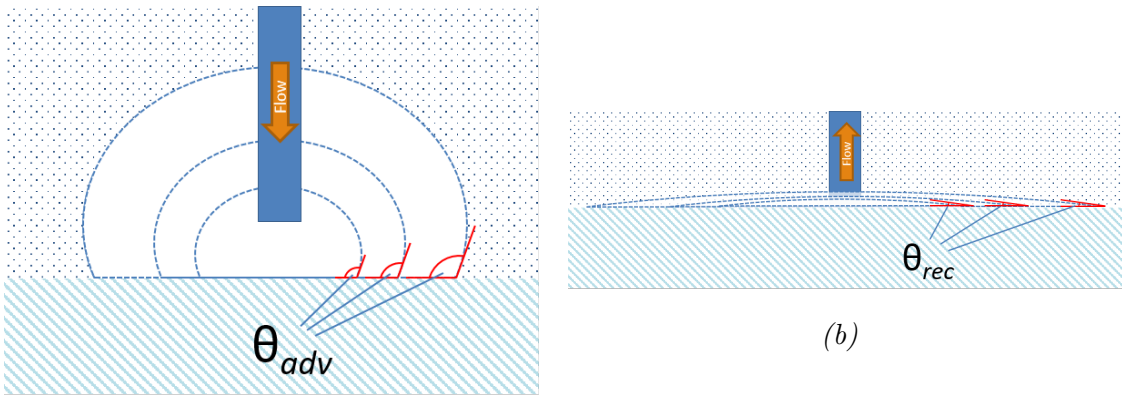

Figure 3.7: (a,b) These are illustrations of the two different dynamic contact angles. Just before the contact line breaks from the pressure of increasing or decreasing sessile drop volume, an advancing or receding contact angle is recorded, respectively.

spots on the surface are measured.

The dispensing rate is set to 5 μL/min, according to conventional dynamic contact angle techniques,[112] and the pumping is started/stopped manually. Pressing the start button on the syringe pump does not affect the contact angle because for a static contact angle the specific drop volume is dispensed before contact with the surface. In the case of dynamic contact angles, any perturbation caused by pressing the start button dissipates far before an advancing or receding contact angle is reached. Once the syringe needle is lowered into frame, the telescopic lens is used to zoom in and focus on the needle. This is a proper reference focus as it will ideally always be in the center of the dispensed drop, hence the contact lines seen in the sessile drop profile will be at the same focal length. It is also important for the syringe needle to be visible on the video feed. The outer diameter of the needles provides a reference dimension to the DSA10 software. This allows a measurement of the sessile drop dimensions: drop height, drop volume, and contact diameter.

In the event that an advancing contact angle is not identified by a noticeable jump in the three-phase contact line, a measured contact angle can be identified as the advancing contact angle when the angle does not increase significantly with an increase in drop volume. Similarly, the receding contact angle can be identified when the angle does not decrease considerably with a decrease in drop volume. Ten measurements are routinely made on samples for both static and dynamic contact angles to assure statistical significance.

First measurement on FeGa

The first experiment performed on FeGa using the two-liquid-phase method was on a vibratory polished sample of (1 0 0) single crystal $Fe_{81}Ga_{19}$. The main focus was to develop protocol for using advancing and receding contact angles to calculate a most-stable contact angle, seen in Equation 3.5.[113]

Figures 3.8a and 3.8b are snapshots of videos that record the expansion and reduction, respectively, of the sessile drop volume. Snapshots are taken at points just before the contact line moves, which are defined as the dynamic contact angles.

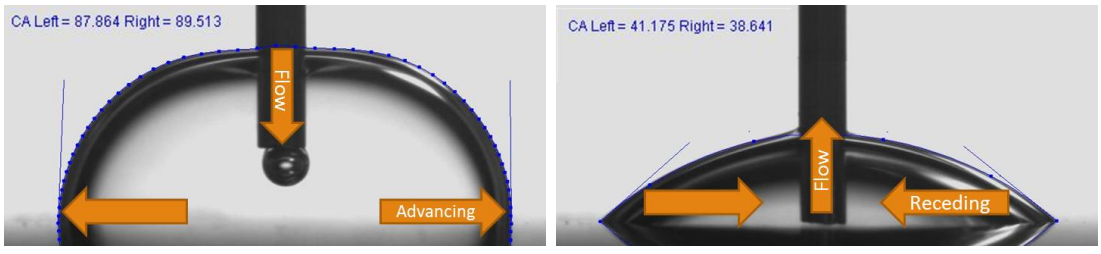

(a) *(b)*

Figure 3.8: (a,b) These are images of deionized water advancing and receding contact angle measurements,respectively, made on (1 0 0) *single crystal* $Fe_{81}Ga_{19}$ *immersed in an n-Octane environment.*

Table 3.3 show the results for measured advancing and receding contact angles as well as the calculated most stable contact angle for three n-alkane environments: n-octane, n-decane, and n-hexadecane. Error for the most stable contact angle is calculated through conventional error propagation methods. The contact angle error tends to stay below 1.5°, attributing to reasonably precise measurements.

Table 3.3: Advancing, receding, and most stable contact angles for (1 0 0) *single crystal* $Fe_{81}Ga_{19}$ *in bulk n-alkane environment. Sample prepared using conventional polishing and cleaning techniques described in Section 3.2.1.*

Bulk Liquids	θ_{adv} (°)	θ_{rec} (°)	θ_{ms} (°)
n-octane	87.72 ± 3.04	38.14 ± 1.32	65.60 ± 1.73
n-decane	92.40 ± 1.38	34.18 ± 0.24	66.88 ± 0.75
n-hexadecane	109.55 ± 3.02	30.88 ± 1.99	74.82 ± 1.56

Data is plotted in accordance with Equation B.5, where the most stable contact angle is the Young contact angle for each bulk liquid environment, and interfacial and surface tensions of water and n-alkanes are used from Table 3.1. In Figure 3.9, $[\gamma_W - \gamma_H + \gamma_{WH}\cos\theta_W]$ is plotted against $[(\gamma_W^D)^{1/2} - (\gamma_H^D)^{1/2}]$ to find the slope, $2(\gamma_S^D)^{1/2}$.

From this plot, the slope is used to calculate the dispersive component of the solid surface energy from Equation B.5, $\gamma^D_{(1\,0\,0)} = 126.8 \pm 14.6$ mJ/m^2. Values are one order of magnitude smaller than DFT predictions on α-iron (1 0 0), $\gamma_{Fe(1\,0\,0)} = 2660$ mJ/m^2.[85] We compare surface energy values of α-iron to any FeGa surface energy we measure because FeGa has an α-iron body centered cubic (bcc) structure.

The difference between these two values results from our sample not having pure FeGa at the surface. This is revealed in x-ray photoelectron spectroscopy (XPS) carried out on FeGa samples that were prepared with the same polishing and cleaning procedure above, seen in Figure 3.18e in future sections. XPS data was recorded on

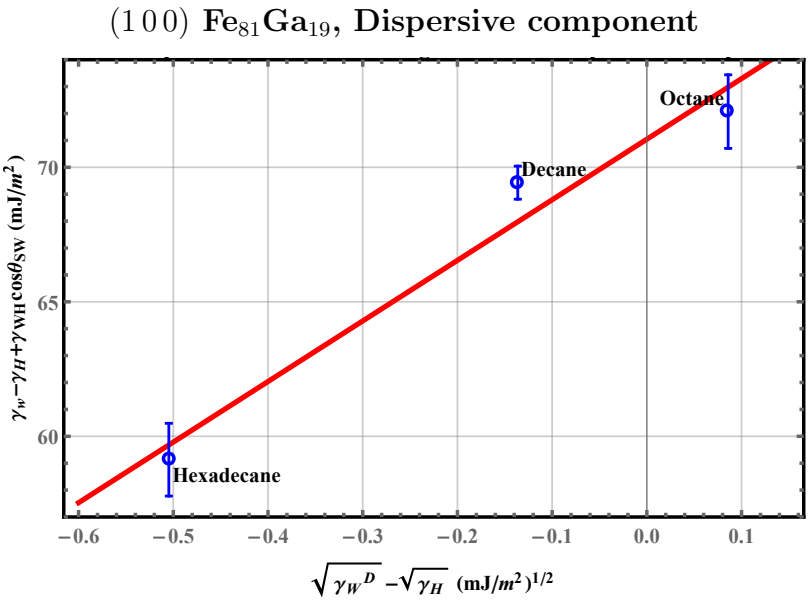

Figure 3.9: The plot shows data from the two-liquid-phase contact angle experiment. Data is presented as $[\gamma_W - \gamma_H + \gamma_{WH}\cos\theta_W]$ *vs.* $[(\gamma_W^D)^{1/2} - (\gamma_H^D)^{1/2}]$ *in order to obtain the dispersive component of the Galfenol surface energy from the slope,* $2(\gamma_S^D)^{1/2}$.

a Kratos Axis 165 X-ray photoelectron spectrometer operating in hybrid mode using monochromatic aluminum radiation (240 W). Survey spectra and high resolution spectra were collected with pass energies of 160 eV and 20 eV respectively. Argon ion sputtering (4 kV, 25 mA emission current) was done using a rastered beam resulting in a sputter crater of $\sim$ 7mm by 7mm. The reference sputtering rate of Ta_2O_5 was recorded as 1.3 nm/min. Data analysis was done using CASA XPS, peak fitting was done after application of a Shirley background using peaks with a 30 Lorentzian 70% Gaussian product function.

3.2.2 Removing Oxide layer of FeGa

There were five techniques attempted to remove this oxide layer of Fe_2O_3 or Ga_2O_3 of <10 nm. The first attempt centered around chemical etchants for removal. Hy-

drochloric acid in particular is a known etchant of iron oxides.[98] However, HCl will also etch Fe at the same time, thus corroding the surface. HCl would need an inhibitor to halt the Fe etching process when the Fe_2O_3 is removed. It is possible to use an HCl + hexamine (inhibitor) solution to inhibit Fe corrosion, but all this would accomplish is the creation of a protective organic film that will skew contact angle measurements of the bare FeGa surface. It is clear that most chemical etchants will need an inhibitor which will produce an unwanted film on the FeGa surface. For this reason, chemical etchants are not a viable solution for our needs.

25W plasma cleaning

The next attempt at oxide removal involved using a plasma cleaner in the University of Maryland Atomic Imaging & Microscopy Lab. An Ar source was exclusively used to bombard the surface, as Ar ions are inert and will not cause a chemical reaction at the surface. The maximum power output of this cleaner is approximately 25 W, but it is quite unstable at this power rating, shifting down by 5 W at random intervals. In addition to this problem, the chamber of this plasma cleaner must be purged with air after the cleaning procedure finishes. This exposure to air contaminates the bare and highly active FeGa surface that has been exposed through the plasma bombardment, thus forming the native oxide layer we are trying to remove. Regardless, after a 10 min exposure to 25 W Ar plasma in this chamber, the sample was quickly transferred to an inert *n*-octane vial, taken to a N_2 glovebox, and taken out of the vial to dry. XPS was used to examine the surface stoichiometry and evaluate the effectiveness of the low power plasma cleaner for oxide removal.

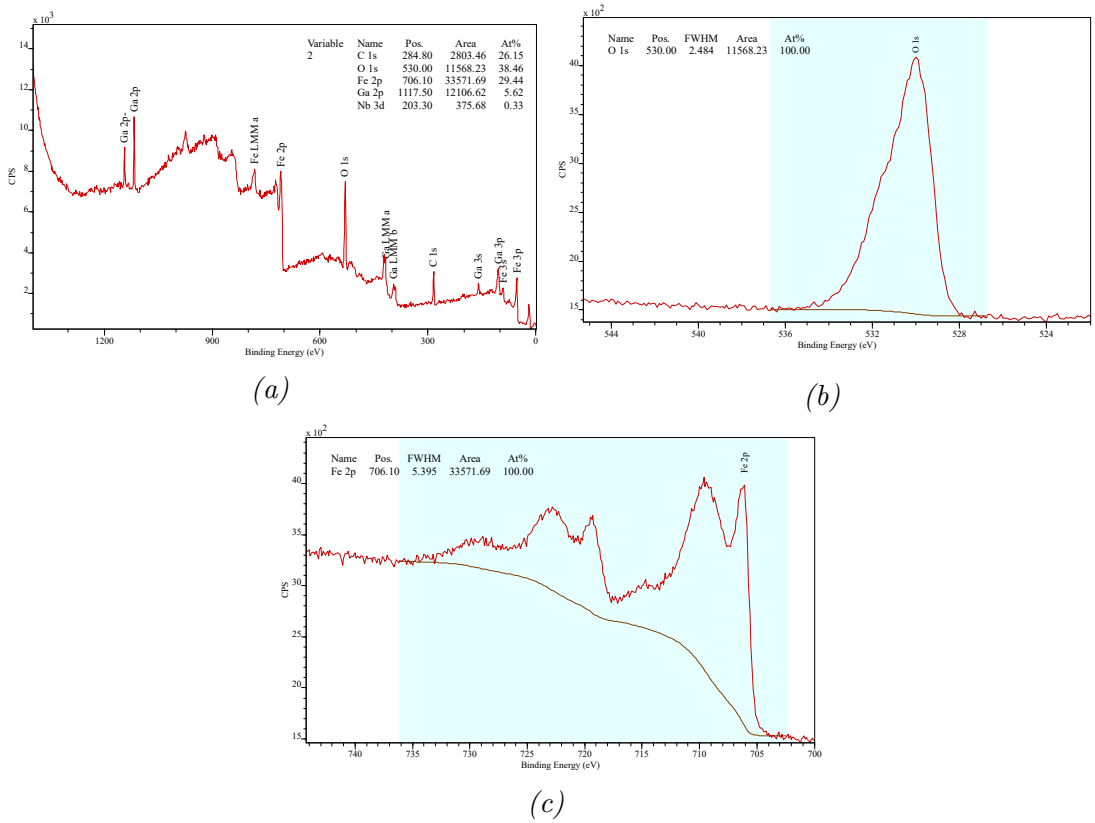

Figure 3.10: (a),(b),(c) These are plots of the full survey, Fe 2p, and O 1s binding energy regions, respectively, at the surface of polycrystalline $Fe_{81}Ga_{19}$ that was well-polished, acetone sonicated, and plasma cleaned with Ar ions at 25 W *for 3 mins.*

Dry silica polish in N_2 glovebox

The next cleaning procedure attempted utilized the inert atmosphere of the Braun nitrogen glovebox provided in collaboration with the Phaneuf Group. A felt pad that was used during the colloidal silica polishing step was soaked with the collodial silica solution while spinning on the polishing wheel and dried without being washed with water. This allowed the 0.6 micron silica particles to stay on the felt pad in air dried form. The pad is placed in the glovebox with another polycrystalline FeGa sample, as seen in Figure 3.11.

Hands were inserted into the glovebox where an extra layer of Nitrile gloves were

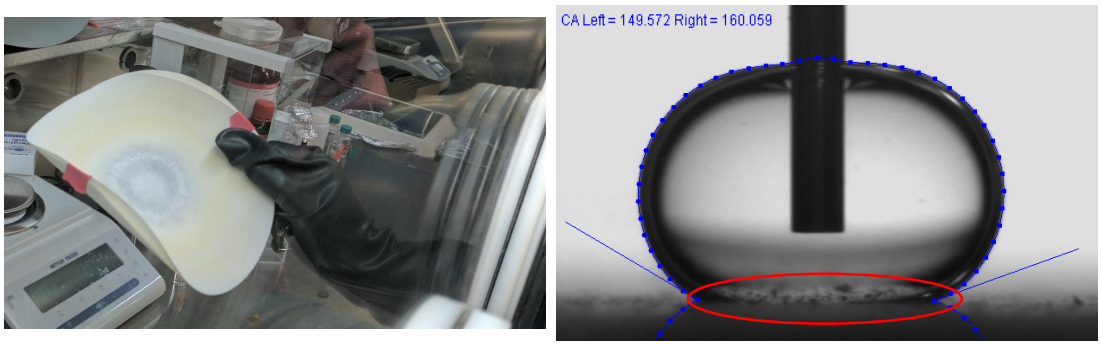

(a) (b)

Figure 3.11: (a) This is a photograph of the dry silica pad being held while in the nitrogen glovebox. (b) This advancing contact angle measurement is on a single crystal (1 0 0) Fe_84Ga_16 *after a dry silica glovebox polish. There is clear contamination of silica particles at the surface, seen here circled in red.*

put on. Pad was flattened with one hand and the sample was placed polished side down on the pad. Using one finger on the other hand, the sample is circularly rotated on the dry silica pad for 60s with moderate pressure, three times successively. XPS measurements reveal a significant decrease in the iron oxide peaks seen in the Fe 2p region, Figure 3.12c, and an increase in the elemental Fe peak at a binding energy of 706.7 eV. The gallium oxide peak in the O 1s region is still significantly present, and does not decrease from the base polishing procedure.

While this was a more successful oxide removal protocol, it suffers from leaving silica particle residue on the surface of Galfenol. These residual particles cause the contact angle to increase as it would on any nano-structured surface with similarly sized features of the silica particles. Dry polishing can also introduce large scratches on the surface relative to the nanometer level average roughness. Without the lubrication of water in a colloidal silica solution polish, silica particles can agglomerate on the pad and create films up to a thickness of 68μm.[114]

The impact of dry silica polishing on the surface of Galfenol is examined by mea-

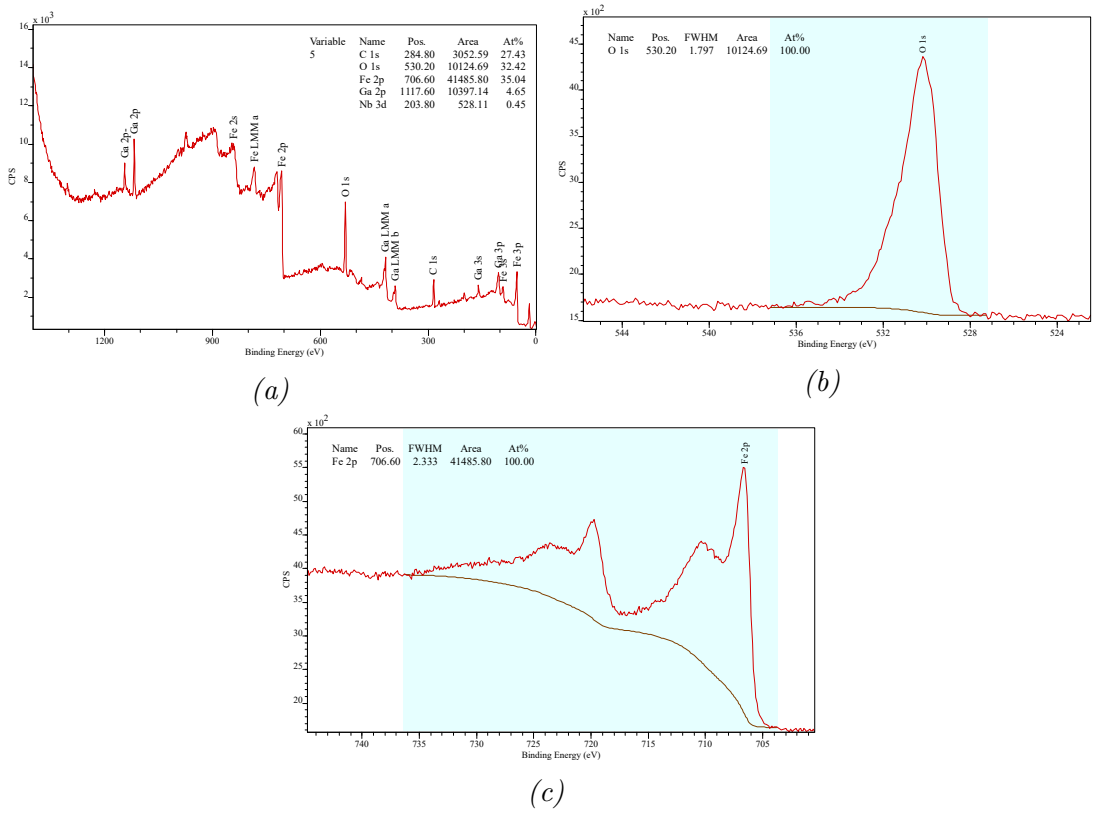

Figure 3.12: (a),(b),(c) These are plots of the full survey, Fe 2p, and O 1s binding energy regions, respectively, at the surface of polycrystalline $Fe_{81}Ga_{19}$ that was well-polished, acetone sonicated, and polished again with a dry silica pad in a nitrogen glovebox.

suring the roughness after this procedure is carried out. AFM images in Figure 3.13 show multiple large scratches in surface ranging from widths of 0.1-0.5μm. These widths are likely the size of silica particles that broke off from the silica film that formed after the pad dried. Scratches of this size are not sufficient for the approximation of a flat surface in the measurement of an approximate Young's angle. Silica particles could be removed using a methanol rinse, but there is no telling what this rinse could do to the surface of Galfenol. Methanol will likely adsorb onto the Galfenol surface by adding hydroxyl(OH) or methyl (CH_3) groups to the bond ends of any bare iron or gallium exposed after the oxide removal process. Hydroxyl groups have been

known to greatly effect polymer surfaces by decreasing or increasing wettability properties.[115,116] It is known that hydroxyl groups can adsorb to metal oxide surfaces or nanoparticles, so it is reasonable to assume that an even more active surface like bare iron could react with methanol to form new bond ends that would ultimately skew surface energy measurements of a bare Galfenol substrate.[117]

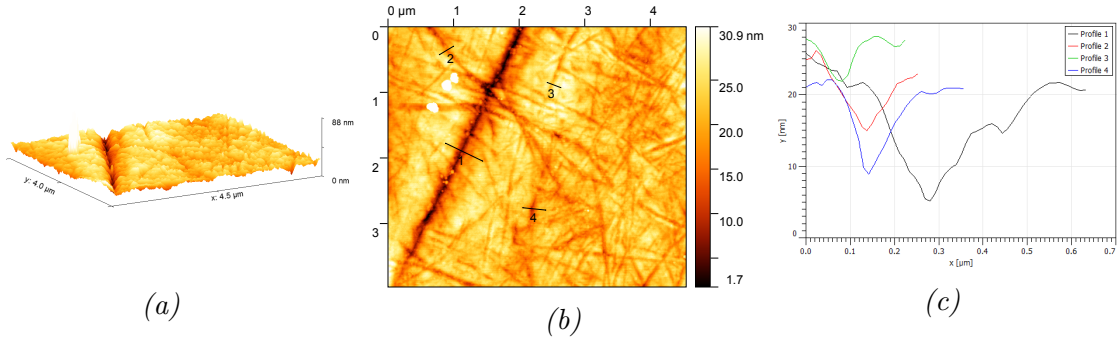

(a) *(b)* *(c)*

Figure 3.13: These are AFM scans of polycrystalline Galfenol after dry silica polishing inside a nitrogen glovebox. The scan area is 4.5 µm x 4.5 µm. (a) A 3D plot of surface topography. (b) Height map with sectioned lines. (c) Profile of sectioned line in (b). This particular scan had an average roughness of 3.156 nm.

100W plasma cleaning

The most successful cleaning method was found at the suggestion of the FabLab staff. The Branson Barrel Resist Stripper is a high powered plasma cleaner capable of cleaning surfaces with baked on photoresist or thick oxide films. Two ion sources, oxygen and argon, can be used on this particular machine up to beam powers of 200W, as indicated by the operations manual. For proof of concept, well-polished polycrystalline Galfenol substrates were only exposed to 100W beams for a limited amount of time. After exposing samples of polycrystalline $Fe_{81}Ga_{19}$ to 100W Ar plasma for 10 mins, the N_2 backfill was kept on as barrel stripper door was opened

to ensure an oxygen-free environment as the sample was placed into a vial of n-octane. The n-octane vial also isolates the sample from any oxygen exposure while being transported to the experiment site. Once in the proper lab, the plasma cleaned sample is left in the n-octane for 8 hours to guarantee n-octane infiltration into any gaps on the Galfenol surface. This is experimental detail is more important for well-patterned surfaces where a Cassie-Baxter state of wetting in the $S - L_1 - L_2$ system is attempted to be achieved.[14] This method will be discussed more in Section 4.3. The sample is transferred from the vial of n-octane to the glass cuvette cube also filled with 15μm of n-octane. While it was a very quick transfer from one container to the next where it was observed that n-octane remained fully wetted to the cleaned Galfenol surface, there is a chance that some of the substrate surface was exposed to air during the transfer. Nevertheless, the experiment proceeded with the following results.

The SyringePump was set to dispense 2μL of DI water while immersed in the n-octane medium above the cleaned surface, far enough away to allow the formation of a pendant drop. After beginning a video recording in the software, the drop is slowly lowered to the cleaned surface using the height gauge. As the pendant drop nears the surface, it vibrates up and down more and more rapidly with decreasing distance from the surface. The hypothesis for this interaction is the system's desire to form a solid-water interface due to the high relative surface energy of γ_S to γ_W. This may be explained by the spreading coefficient of this system, described below in Equation 3.6.

$$S_{SL} = \gamma_S - \gamma_{SW} - \gamma_W \tag{3.6}$$

The spreading parameter characterizes the extent of the wetting of a surface by a liquid, where $\gamma_S, \gamma_{SW}, and \gamma_W$ are the surface free energy of the solid, interfacial solid-water energy, and the surface tension of water, respectively.

The pendant drop is lowered in contact with the solid surface. Now in sessile drop form, the initial contact angle is $\theta_{SW}|_{t=0} = 98.35 \pm 0.10°$ at $t = 0$s. The sessile drop continued to spread very quickly on the surface, contact angle dramatically dropping over 23s. At $t = 23$s, the triple line halts from the force balance governed by Young's equation with a contact angle of $\theta_{SW}|_{t=23} = 24.13 \pm 0.20°$.

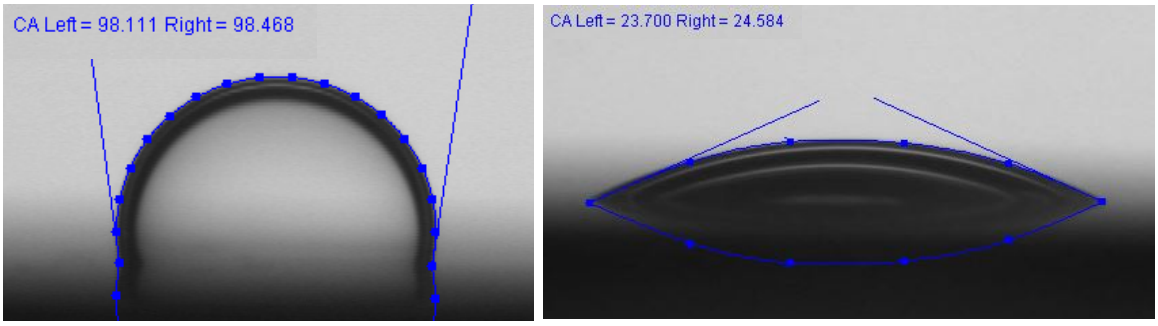

(a) *(b)*

Figure 3.14: These contact angle images show polished and plasma cleaned polycrystalline $Fe_{81}Ga_{19}$ surfaces probed by DI water sessile drop in an n-octane environment, where (a) occurs once the sessile drop has detached from the needle by attraction to the surface, t=0, and (b) is a snapshot at t=23s when the sessile drop stopped spreading. This can be considered a static contact angle.

This is a stark difference in static contact angle on an approximately-flat Galfenol surface when compared to the results in Table 3.3 for a Galfenol surface prepared without plasma treatment. The most-stable contact angle for non-plasma-treated substrates in *n*-octane is $65.60 \pm 1.73°$, and the contact angle drops by $\sim 41.47°$ after the 100W Ar plasma treatment. We cannot be fully certain that this means the Galfenol surface is completely void of oxides until we evaluate the surface stoichiom-

etry using XPS, but this is an extremely good indicator that most of the exposed surface is bare Galfenol because of this dramatic decrease in static contact angle. As discussed in Chapter 1, higher surface energy substrates will exhibit very low contact angles. The presence of the bulk immiscible liquid inhibits the probe water droplet from completely wetting the surface ($\theta_{SW} = 0°$) as it might in a solid-water-air system. This is a promising result for the next sections of this experiment because we can now fine tune the plasma treatment regimen by modifying the time of exposure, flow rate, and beam power.

3.3 Results for (100), (110) and (111) FeGa surface

3.3.1 (100) $Fe_{82}Ga_{18}$ surface

DFT determination of surface energy

Work from Hui Wang and Ruqian Wu from University of California, Irvine. Adapted from previously published work.

To understand the experimental observations, density functional simulations were performed with the Vienna Ab-initio Simulation Package (VASP).[118,119] The spin-polarized generalized gradient approximation (GGA) was used for the description of the exchange-correlation interaction among electrons.[120] Since Galfenol is metallic and the states near the Fermi level is delocalized, we did not consider the +U correc-

tion, which is typically needed for materials with band gaps or localized orbitals. We treated Fe-3d4s and Ga-4s4p as valence states and adopted the projector-augmented wave (PAW) pseudopotentials to represent the effect of their ionic cores.[121,122] We used $D0_3$-like bulk $Fe_{81.25}Ga_{18.75}$ to build the structural models as we did in previous work,[123,124] and FeGa (0 0 1) surface was mimicked by building a slab with 9 atomic layers and a vacuum space of 12 Å to avoid spurious interactions between them. The energy cutoff for the plane-wave expansion was 400 eV, sufficient for Fe-Ga systems according to our test calculations. Structures were optimized with a criterion that the atomic force on each atom becomes weaker than 0.01 eV/Å and the energy convergence is better than 10^{-5} eV. We sampled the Brillouin zone with a 7x7x1 Monkhorst-Pack k-mesh in all calculations.[125]

Since FeGa samples were treated at high temperature, it is possible that the chemical composition at the surface is different from that in bulk as Ga atoms may migrate to the topmost layer, depending on the growth and annealing condition.[84] To give a reasonable estimate of surface Ga components, we calculated their ensemble averages for different surface terminations according to Boltzmann statistics:

$$\langle Q \rangle = \frac{\sum_{n=1}^{N} Q_n \exp(E_n/k_B T)}{\sum_{n=1}^{N} \exp(E_n/k_B T)} \tag{3.7}$$

Here, N is the number of configurations in the ensemble for (0 0 1) surface (N = 5 termination in the present studies, corresponding to different surface Ga coverage as demonstrated in Figure 3.15(a)) and E_n and Q_n are the total energies and the physical quantities of different configurations respectively. Since contributions from

configurations that have energies more than 500 meV higher than that of the best configuration are negligible due to their Boltzmann factors, we didn't calculate their corresponding properties. Note that our models maximally avoided the formation of Ga-Ga first neighbors in the surface layer. They should have lower energy than other distributions such as random configurations. Furthermore, the surface Ga concentration with practical Ga reservoirs approaches 100%, so we believe the random configurations are not important for this case.

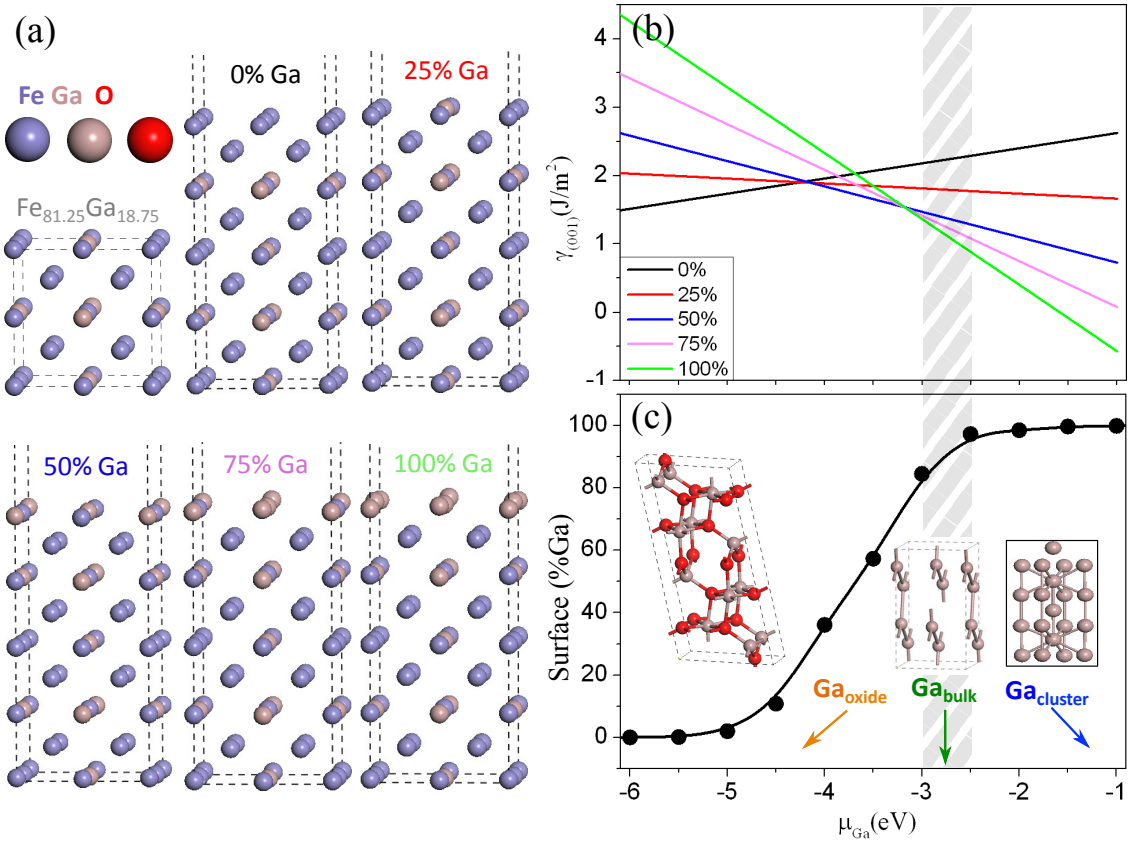

Figure 3.15: (a) Atomic structures for bulk $Fe_{81.25}Ga_{18.75}$ and its (0 0 1) surface with different terminations (corresponding to 0%, 25%, 50%, 75% and 100% Ga coverage). (b) The calculated $Fe_{81.25}Ga_{18.75}$ surface energies for (0 0 1) surfaces with different surface terminations at different Ga chemical potential. (c) The dependence of Ga chemical potential on surface Ga coverage according to Boltzmann energy distribution. Grey shaded area, $Ga_{cluster}$ and Ga_{oxide} corresponds to the chemical potential of Ga atoms in bulk, cluster and oxide, respectively.

As shown in Figure 3.15(b), in the Ga-rich region ($\mu_{Ga}\rightarrow$ -1 eV), the 100% Ga curve has the lowest surface energy, suggesting that the Ga atoms favor the topmost layers. Figure 3.15(b) shows negative surface energy values in this region for the 100% Ga surface, which correspond to a condensation of Ga atoms from the Ga atoms or small clusters on the surface. In contrast, the surface termination with 0% Ga coverage becomes more stable at the extreme of Ga poor condition ($\mu_{Ga}\rightarrow$ -5 eV corresponding to oxidized Ga condition). Boltzmann statistics of the surface Ga component at these two conditions gives almost 100% and 0%, respectively. In the typical Ga-poor condition with $\mu_{Ga}\sim$ -2.7 eV [shaded area in Figures 3.15(b-c)], the Ga component in the surface layer gradually decreases from that for the Ga-rich condition. Interestingly, after $\mu_{Ga} <$ -3.0 eV, one can see a sudden drop of surface Ga concentration from 80% ($\mu_{Ga} \sim$ -3.0 eV) to 20 % ($\mu_{Ga} \sim$ -4.0 eV) as depicted in Figure 3.15(c). The lower Ga chemical potential ($\mu_{Ga} <$ -3.0 eV) indicates that part of Ga atoms from the bulk start to oxidize once the sample is exposed to ambient conditions, leading to a surface where small Ga coverage becomes favorable.

Experimental results

Table 3.4 shows the results for measured advancing and receding contact angles as well as the calculated most stable contact angle for three n-alkane environments: n-octane, n-decane, and n-hexadecane. The contact angle error is defined as $\pm$1.0 deviation from the mean acquired from ten observations of the contact angle. Data is plotted in accordance with Equation B.5, where the most stable contact angle is the Young contact angle for each bulk liquid environment, and interfacial and

surface tensions of water and n-alkanes are used from Schultz *et al.*.[104] In Figure 3.16, $[\gamma_W - \gamma_H + \gamma_{WH}\cos\theta_W]$ is plotted against $[(\gamma_W^D)^{1/2} - (\gamma_H^D)^{1/2}]$ to find the slope, $2(\gamma_S^D)^{1/2}$.

Table 3.4: Most stable contact angles for (1 0 0) *single crystal* $Fe_{82}Ga_{18}$ *in bulk n-alkane environment for a passivated and plasma-cleaned case.*

	Passivated	**Plasma-cleaned**
Bulk Liquids	θ_{ms} (°)	θ_{ms} (°)
n-octane	65.6 ± 1.7	32.1 ± 0.2
n-decane	66.9 ± 0.8	54.5 ± 0.7
n-hexadecane	74.8 ± 1.6	76.6 ± 1.8

The decrease in contact angle from passivated to plasma-cleaned for n-octane is a good indication of a reduction or elimination of the passive oxide layer. Of the three n-alkanes used, n-octane has the lowest viscosity (0.51 mPa·s), therefore it has the closest viscosity to air (0.01 mPa·s). A bare FeGa surface in air should experience complete wetting ($\theta_c = 0°$) of a probe water droplet. Further confirmation of oxide removal comes from a dramatic increase in droplet spreading speed. In the Supplementary Section, videos of initial droplet contact on Galfenol show spreading on the passivated surface at 30s and spreading on the plasma-cleaned surface at <0.03s (between frames of video).

From Figure 3.16, the slope is used to calculate the dispersive component of the solid surface energy from Equation B.5. The red curve representing the passivated (1 0 0) $Fe_{82}Ga_{18}$ surface has a slope of 22.5. The blue curve representing the plasma-cleaned surface shows a significant increases in slope to 60.8. This provided experimentally determined (1 0 0) $Fe_{82}Ga_{18}$ dispersive surface energy values of 127 ± 15 mJ/m^2 and 924 ± 20 mJ/m^2 for passivated and plasma-cleaned surfaces, respectively.

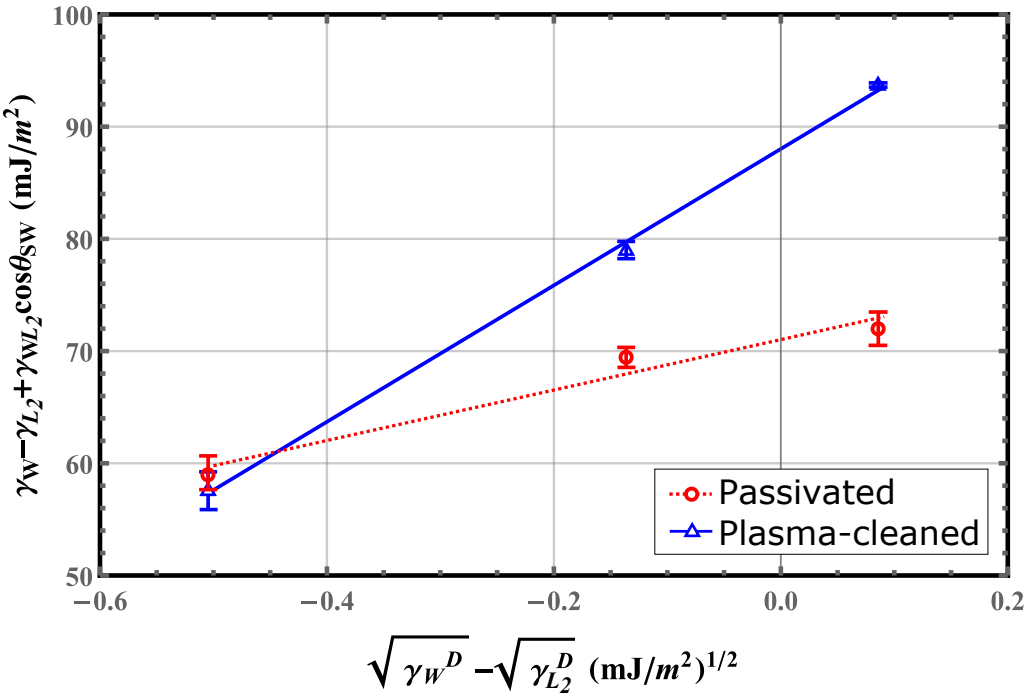

Figure 3.16: The plot shows data from the two-liquid-phase contact angle experiment. Data is presented as $[\gamma_W - \gamma_{L_2} + \gamma_{WL_2}\cos\theta_{SW}]$ *vs.* $[(\gamma_W^D)^{1/2} - (\gamma_{L_2}^D)^{1/2}]$ *in order to obtain the dispersive component of the Galfenol surface energy from the slope,* $2(\gamma_S^D)^{1/2}$*. Red circles and blue circles show the passivated and plasma-cleaned* (1 0 0) $Fe_{82}Ga_{18}$ *surfaces, respectively.*

It is also worth noting that this is the highest surface energy value ever measured using the two-liquid-phase contact angle technique, the closest being 461 mJ/m^2 for negatively-charged β-tricalcium phosphate.[110] The difference between these two values results from the passivated oxide layer at the Galfenol surface.

We have chosen the external liquid (under which we perform our experiments) in a fashion such that it does not chemically react with the surface. We also use three different alkanes with increasing molecular weight. Hexadecane is a well-known model system for oil-water emulsion problems[126,127] and a very commonly used alkane for various surface energy measurements. In our case, we find that in this system the contact angles for the passive surface and the high energy metallic surface are

almost similar. It shows a distinct difference for the other two lower molecular weight alkanes. We can consider two cases for this scenario. The measurements in this two liquid system exhibit contact angles for water on both the passive and high energy surface to be much lower than 90°. We can say that these surfaces are hydrophilic. Typically a hydrophilic surface is also oleophobic.[126,127] Since hexadecane is a model for oil, we can take that it is phobic to the surfaces. We think that this oleophobicity leads to less surface energy interactions with the surface and hence does not influence the water contact angle on the surface. The other case is that hexadecane is a high molecular weight alkane. The high energy metallic surface might attract some large alkanes to its surface making itself attain a much lower energy state. This is not favorable for lower molecular weight alkanes as they cannot cover larger surface areas of the substrate. This makes the high energy surface lose its characteristic which then behaves in a very similar fashion as the passive surface. A deeper investigation into both of these ideas is beyond the scope of this current work.

Surface composition of passivated surface

The surface of the samples were analyzed by XPS and show the presence of an expected oxide layer consisting of both iron oxides and gallium oxides, shown in Figures 3.17a and 3.17c, respectively (red peaks).

It should be noted that the peak fits of Fe 2p and Ga $2p_{3/2}$ regions are used solely for the for the purose of getting an approximate quantification of the amount of elemental Ga and Fe under the oxide layer and are not meant to be rigorous fits identifying specific oxide species. Figures 3.17(b,d) are Fe 2p and Ga $2p_{3/2}$ regions of

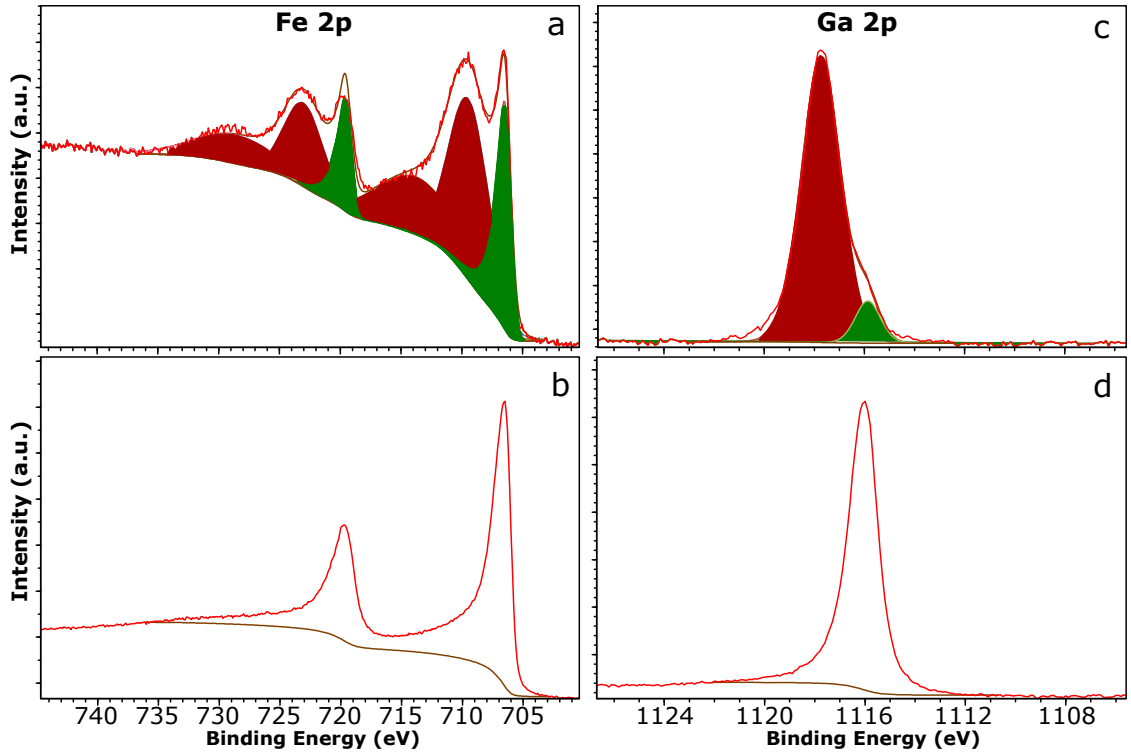

Figure 3.17: Surface characterizations of $Fe_{82}Ga_{18}$. (a,c) XPS scans of the Fe 2p binding energy region and Ga $2p_{3/2}$ region, respectively, for polycrystalline $Fe_{82}Ga_{18}$. The red fitted areas in (a,c) represent iron oxides and gallium oxides, respectively, while the green fitted areas represent metallic Fe and Ga signatures, respectively. (b,d) XPS scans of Fe 2p and Ga $2p_{3/2}$ regions for the same sample after sputtering down for 180s, respectively. Both peaks are only indicative of respective metallic signatures.

the same sample in Figures 3.17(a,c) after Ar ion sputtering for 180s, the oxide peaks have disappeared demonstrating the oxidized layer sits on top of the Galfenol.

To compare experimental results with DFT results, we will quantify the surface terminations of Galfenol using the peak fits from the oxidized samples rather than the sputtered sample due to likely changes in stoichiometry resulting from preferential sputtering. Both Fe 2p and Ga $2p_{3/2}$ regions in Figures 3.17(a,c) show measurable peaks for metallic Fe and Ga, showing that we are probing the entirety of the oxide overlayer and seeing through to the underlying metallic substrate. Using the peak areas of Ga 2p $_{3/2}$ and Fe 2p and adjusting with relative sensitivity factors from the

Kratos Vision Library, and the instrument transmission function based of the peak fit we calculate 90.26% metallic Fe to 9.74% metallic Ga. The inelastic mean free paths of escaping electrons are longer at higher kinetic energy. This means electrons are escaping from much deeper in the Fe 2p spectrum compared to the Ga 2p, hence we are seeing a disproportionately larger amount of metallic Fe compared to Ga. We account for this discrepancy as follows.

We start by estimating the thickness of the oxide layer a using the NIST Electron Effective-Attentuation-Length (EAL) database and confirming with the Thickogram.[128–131] Despite the fact that the oxidized layer is probably a mixture of iron and gallium oxides, for the purpose of calculation we assume the overlayer is largely FeO.[132] We choose FeO due to the much higher total elemental concentration of Fe (34%) relative to Ga (7.7%). The Fe 2p main oxide peak (709.4 eV) and satellite peak (713.7 eV) have a separation of 4.3 eV which is closest to the expected separation of Fe(II) in FeO.[132]

The parameters entered into the NIST EAL database to find the EAL of Fe 2p and Ga 2p electrons through the FeO overlayer are discussed in the Supplementary Section. The practical EAL for Ga 2p electrons attenuated to 7.76% Ga (from Ga 2p peak fit) is $\lambda_{EAL,Ga}$ ~6.65 Å with film thickness of 17 Å, whereas for Fe 2p electrons attenuated to 18.4% Fe (from Fe 2p peak fit) is $\lambda_{EAL,Fe}$ ~12.4 Å with a film thickness of 21 Å. Oxide overlayer thickness approximations were confirmed and found to be consistent with those calculated using the Thickogram, where determined thicknesses are 17.9 Å and 20.5 Å, respectively. We averaged the two FeO thickness values to t_{FeO} ~19 Å for subsequent calculations.

By dividing the overlayer thickness by λ_{EAL}, we find the number of EALs in the overlayer thickness: $t_{FeO} = 2.87\lambda_{EAL,Ga} = 1.43\lambda_{EAL,Fe}$. The probability of an electron escaping from below a depth, d, is given in Equation 3.8.

$$P(d) = \exp(-d/\lambda_{EAL}) \tag{3.8}$$

The percentage of metallic signal originating from below the oxide overlayer is 5.8% for Ga and 21.6% for Fe, a ratio of 0.27:1 for Ga:Fe. Correcting the metallic Fe contribution of 90.26% by this ratio gives a corrected value of 24.91% Fe coming from an equivalent depth as the 9.74% Ga. From these corrections, we determined that the approximate surface termination Ga:Fe ratio is 0.39:1, which is a more Ga-rich substrate surface of $Fe_{72}Ga_{28}$ compared to bulk $Fe_{82}Ga_{18}$.

We realize that given another oxide overlayer the ratio of the substrate composition will differ. After recalculating with a Fe_2O_3 overlayer, we find the same Ga-rich surface composition Ga:Fe ratio of 0.27:1. Therefore, the ratio of Ga:Fe at the substrate surface is insensitive to the oxide overlayer.

The XPS data clearly shows preferential surface segregation of the Ga at the near-surface of the Galfenol. Since we are averaging over many layer into the Galfenol, it is likely that at the very surface termination layer the Ga surface enrichment is even greater.

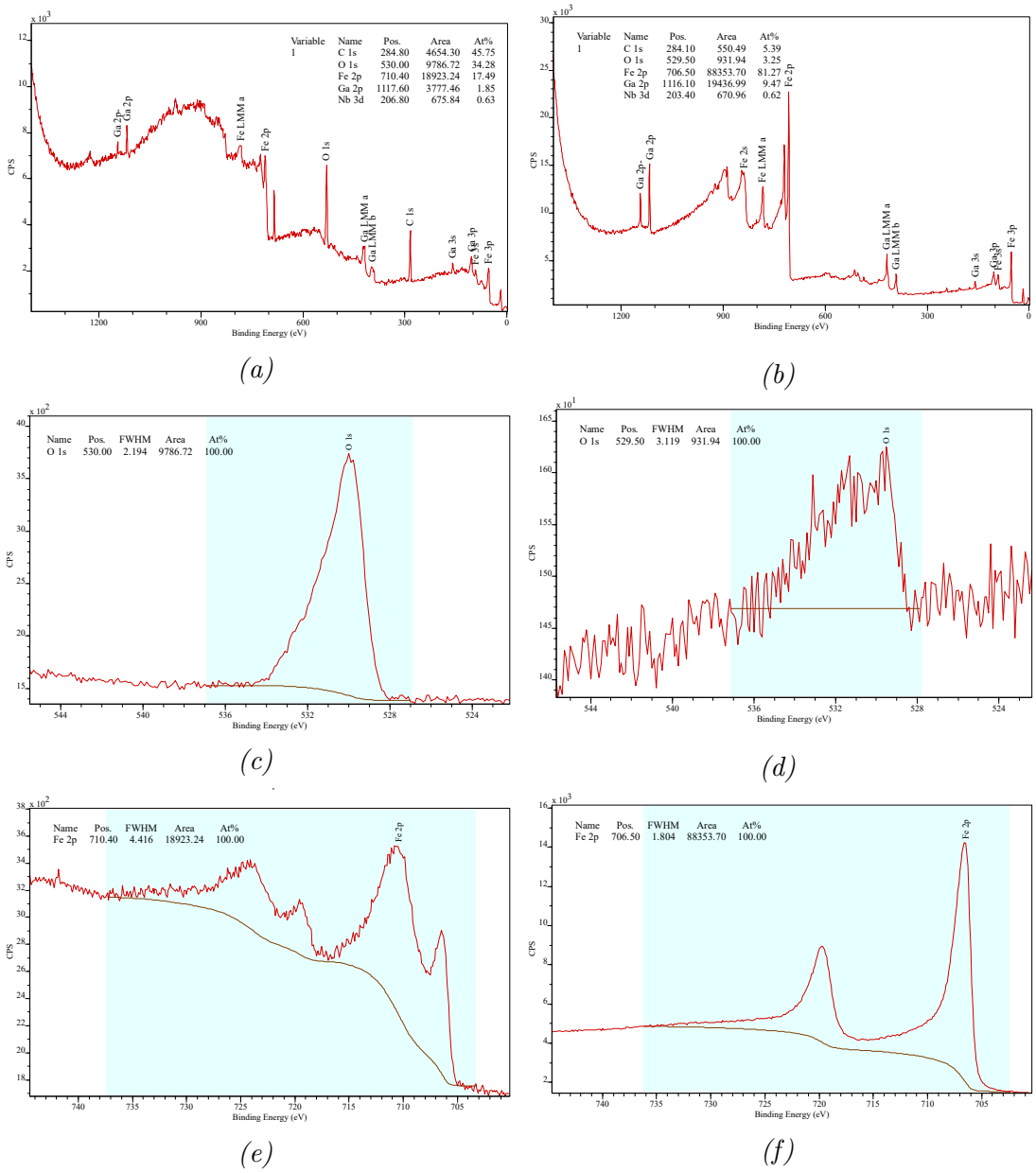

Figure 3.18: (a),(c),(e) These are plots of the full survey, Fe 2p, and O 1s binding energy regions, respectively, at the surface of well-polished and acetone sonicated polycrystalline $Fe_{81}Ga_{19}$. (b),(d),(f) The same sample and region, except this has been sputtered to a depth of 5nm below the surface and then scanned.

Comparison of experimental and DFT results

As discussed previously, XPS results indicate a 28.11% Ga composition at the near-surface of $Fe_{82}Ga_{1}8$. This Ga surface atomic composition is consistent with our DFT

calculations in Figure 3.15(c) where 30% Ga coverage becomes favorable at lower Ga chemical potentials (μ_{Ga} < -3.0 eV).

According to DFT calculations on Galfenol (1 0 0) facets, a Ga-poor surface with 25% Ga coverage has a surface energy of ∼1750 mJ/m^2. For metals, DFT calculations tend to over-predict exact values by a factor of ∼1.3, bringing this surface energy to ∼1450 mJ/m^2.[133] Furthermore, by following the trend in Figure 3.15(c) of decreasing surface energy with increasing %Ga coverage, we can assume that a DFT surface energy value for the experimentally determined 28.11% Ga coverage lies between the 25% Ga value (∼1750 mJ/m^2) and the 50% Ga value (∼1300 mJ/m^2). While of the same order of magnitude as the measured value of 924 ± 20 mJ/m^2 on the plasma-cleaned surface, the DFT value for 50% Ga coverage of ∼1300 mJ/m^2 is larger than the measured value by a factor of ∼1.4. Again, the results from the XPS data suggest an even greater Ga surface enrichment than measured, hence it is reasonable to compare the experimental surface energy result to the DFT result for 50% Ga coverage.

3.3.2 Conclusions on (100) experimental procedure

The results in this study have confirmed the need for precise sample preparation procedures in the pursuit of non-destructive surface energy measurements on bare metal surfaces. A clear increase in surface energy is observed after a controlled plasma cleaning is administered to the (1 0 0) single crystal $Fe_{82}Ga_{18}$ surface, due the removal of an iron oxide and gallium oxide layer. There is ∼ 400 mJ/m^2 difference between

the experimental and DFT results, which may be a result of trace oxide present on the Galfenol surface or due to over-predicted DFT simulation. This can be solved with further optimization of the plasma treatment with a higher plasma power and exposure time.

We have good agreement between experimentally measured results and DFT calculations of (1 0 0) FeGa facets. The following sections will extend this technique to more facets.

3.3.3 (110) and (111) FeGa surface

Experimental results

The two-liquid-phase contact angle experiment was performed on (1 1 0) and (1 1 1) surface of $Fe_{82}Ga_{18}$. The same polishing and plasma-cleaning procedure has been applied to these samples as in Section 3.3.1.

Figure 3.19 plots the dispersive component of the solid surface energy where the slope is, again, used to calculate the dispersive component of the solid surface energy from Equation B.5. The green curve representing the (1 1 0) $Fe_{82}Ga_{18}$ surface has a slope of 43.4. This provided an experimentally determined (1 1 0) $Fe_{82}Ga_{18}$ dispersive surface energy value of 470 ± 35 mJ/m^2 for a plasma-cleaned surface. Figure 3.20 plots the polar component of the solid surface energy. The green curve has a slope of 15.3, and according to Equation B.9 the polar surface energy component of 58.2 ± 9.2 mJ/m^2. As a result, the total experimental surface energy for (1 1 0) $Fe_{82}Ga_{18}$ is 528 ± 36 mJ/m^2.

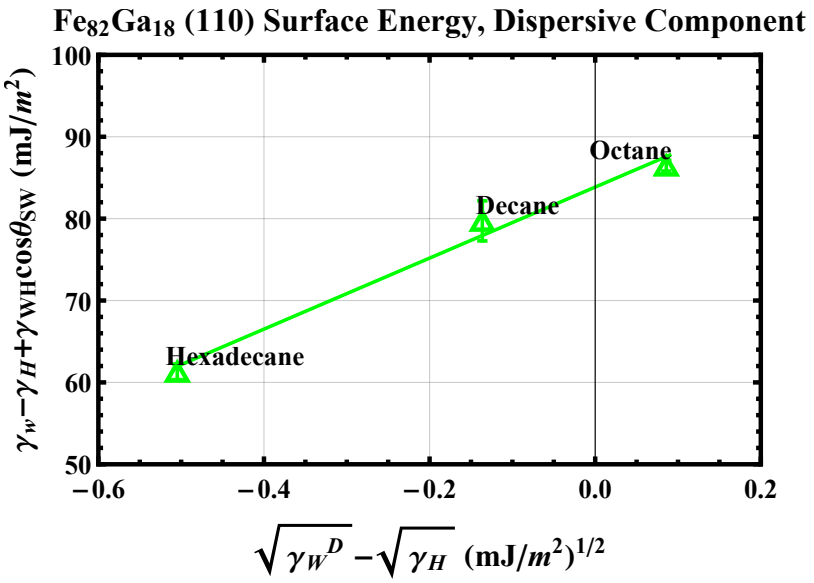

Figure 3.19: The plot shows data from the two-liquid-phase contact angle experiment. Data is presented as $[\gamma_W - \gamma_{L_2} + \gamma_{WL_2}\cos\theta_{SW}]$ *vs.* $[(\gamma_W^D)^{1/2} - (\gamma_{L_2}^D)^{1/2}]$ *in order to obtain the dispersive component of the Galfenol surface energy from the slope,* $2(\gamma_S^D)^{1/2}$*. Blue circles show the plasma-cleaned* $(1\,1\,0)$ *$Fe_{82}Ga_{18}$ surfaces.*

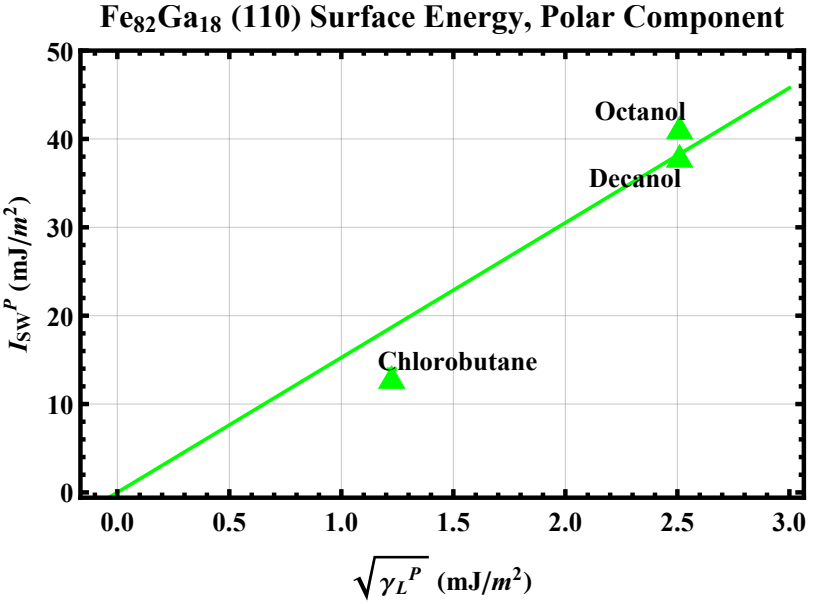

Figure 3.20: The plot shows data from the two-liquid-phase contact angle experiment. Data is presented as I_{SW}^P *vs.* $(\gamma_L^P)^{1/2}$ *in order to obtain the polar component of the* $(1\,1\,0)$ *surface energy from the slope,* $2(\gamma_S^P)^{1/2}$*. Green triangles show the plasma-cleaned* $(1\,1\,0)$ *$Fe_{82}Ga_{18}$ surfaces.*

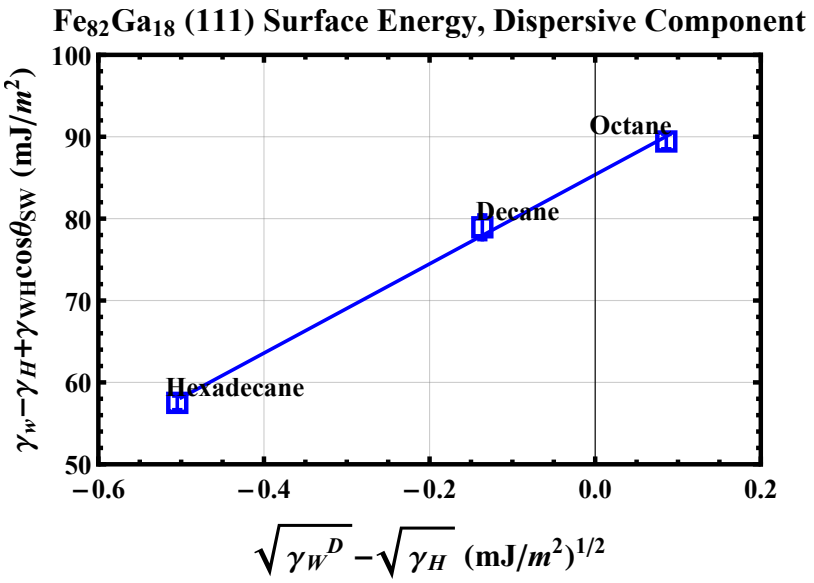

Figure 3.21: The plot shows data from the two-liquid-phase contact angle experiment. Data is presented as $[\gamma_W - \gamma_{L_2} + \gamma_{WL_2}\cos\theta_{SW}]$ *vs.* $[(\gamma_W^D)^{1/2} - (\gamma_{L_2}^D)^{1/2}]$ *in order to obtain the dispersive component of the Galfenol surface energy from the slope,* $2(\gamma_S^D)^{1/2}$*. Blue squares show the plasma-cleaned* $(1\,1\,1)$ $Fe_{82}Ga_{18}$ *surfaces.*

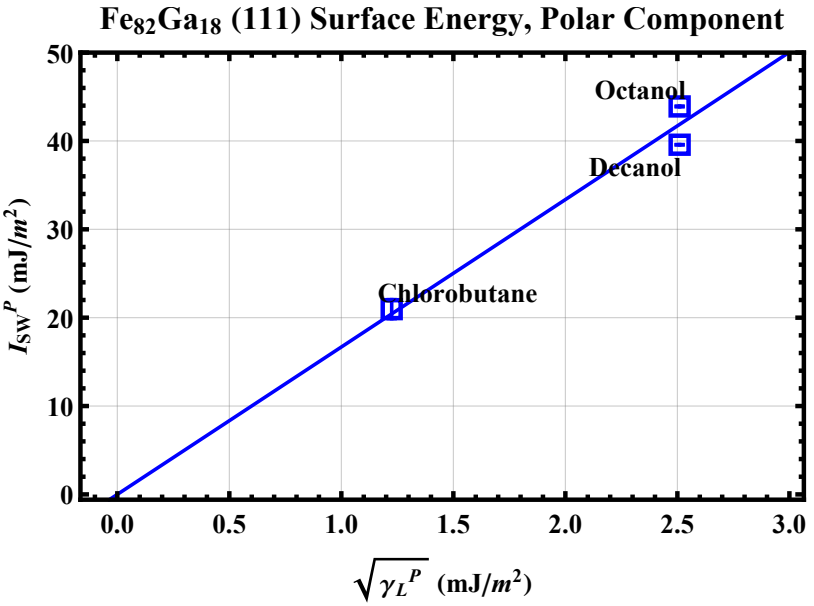

Figure 3.22: The plot shows data from the two-liquid-phase contact angle experiment. Data is presented as I_{SW}^P *vs.* $(\gamma_L^P)^{1/2}$ *in order to obtain the polar component of the* $(1\,1\,1)$ *surface energy from the slope,* $2(\gamma_S^P)^{1/2}$*. Green triangles show the plasma-cleaned* $(1\,1\,1)$ $Fe_{82}Ga_{18}$ *surfaces.*

Figure 3.21 plots the dispersive component of the solid surface energy where the slope is, again, used to calculate the dispersive component of the solid surface energy from Equation B.5. The blue curve representing the (1 1 1) $Fe_{82}Ga_{18}$ surface has a slope of 54.5. This provided an experimentally determined (1 1 1) $Fe_{82}Ga_{18}$ dispersive surface energy value of 742 ± 80 mJ/m^2 for a plasma-cleaned surface. Figure 3.22 plots the polar component of the solid surface energy. The blue curve has a slope of 16.7, and according to Equation B.9 the polar surface energy component of 69.6 ± 4.9 mJ/m^2. As a result, the total experimental surface energy for (1 1 1) $Fe_{82}Ga_{18}$ is 811 ± 80 mJ/m^2.

There is a significant error associated with the (1 1 1) facet. We attribute this to both having only one (1 1 1) sample available for experimentation and the small surface area of the sample, seen below in Figure 3.23. The sample size was approximately 5x4mm, and water sessile drops in these alkane environments can have a base diameter of 4mm therefore only one contact angle measuerment could be made on this lone (1 1 1) sample per plasma cleaning. Even when initially wetting the (1 1 1) surface, a single water droplet almost filled the entire sample surface. If the droplet was not dropped precisely in the center of the sample, the sessile drop would spread outside of the sample and onto the Polyfast mount, which was just as active (hydrophilic) after Ar plasma treatment.

DFT determination of surface energy

From Costa *et al.*,[84] we have a range of decreasing surface energy values with increasing %Ga surface coverage. For ~50%Ga coverage on a (1 1 0) $Fe_{81.25}Ga_{18.75}$ surface,

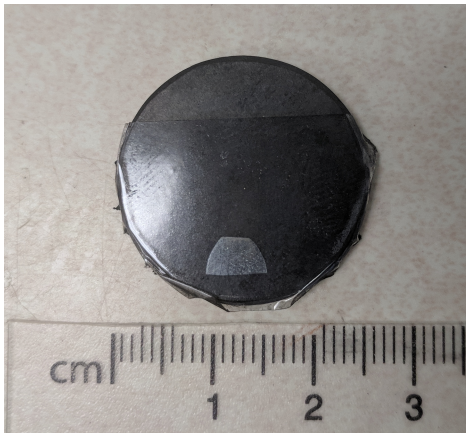

Figure 3.23: The photo shows the sample of (1 1 1) *mounted in Polyfast, a conductive thermoset. The sample is approximately 5mm by 4mm.*

the surface energy is ∼1400 mJ/m^2. A 100%Ga coverage surface has a surface energy of ∼950 mJ/m^2. For ∼75%Ga coverage on a (1 1 1) facet of the same composition, the surface energy is ∼1600 mJ/m^2. A 100%Ga coverage surface has a surface energy of ∼1350 mJ/m^2.

Also considering the (1 0 0) DFT results in Costa *et al.*, a trend of $\gamma_{110} < \gamma_{100} < \gamma_{111}$ for $Fe_{81.25}Ga_{18.75}$ with >50% Ga coverage is observed for DFT calculations. This result conflicts with the trend predicted by broken-bond-model for similarly structured α-Fe, where $\gamma_{110} < \gamma_{111} < \gamma_{100}$. Another XPS measurement must be performed on this surface to estimate the near-surface composition on (1 1 0) and (1 1 1) $Fe_{82}Ga_{18}$ surfaces. This will allow for a more accurate comparison of experimental values with DFT calculations. Preferably, angle-resolved XPS could reveal the true surface composition ratio between Fe and Ga terminations. This is problematic from an experimental perspective because this would require transporting a freshly plasma-cleaned sample between buildings. The plasma-cleaning process discussed in Section 3.2 keeps the FeGa sample oxide-free by transporting it in the hydrocarbon liquid it

will be tested in. Transport in a gaseous environment, even if the gas is inert, is far more unstable because there is a risk of trace oxygen exposure. One practice used to transport air-sensitive samples is to seal the samples in two sealable plastic bags after the cleaning treatment.

3.3.4 Conclusions on new process for measuring high surface energy materials

These results are consistent with the prediction of Fowkes where the surface interaction of a metal with water is almost completely dictated by dispersive interactions. This is due to the high dispersive surface energy component measurement relative to the polar component for (1 0 0), (1 1 0), and (1 1 1) Galfenol surfaces. There is still a polar contribution possibly due to the effective dipoles at the surface, as discussed in Chapter 1. There could have been an increase in the dipole concentration at the surface due to the plasma cleaning process, but the two-liquid-phase model does not show this based on the contact angle measurements made on Galfenol. There is more to investigate on the polar interaction and dispersive interaction at a metal surface that are outside the scope of this study.

In the past, experimental surface energy measurements for high-energy metal surfaces have been avoided for their complexity coupled with a lack of thorough experimental practices including fine polishing to nanometer roughness, removing surface contamination, and isolation from oxygen. We have presented a rigorous experimental process for high surface energy measurements with reasonable agreement to

DFT calculations, thus showing promise for characterizing any metal surface non-destructively. This study hopes to supplement not only our research goals, but the greater Material Genome Initiative community searching for experimental confirmation of complex material properties. We will use these results to create a total energy model for abnormal grain growth.

3.4 Surface energy role in abnormal grain growth

As mentioned in Chapter 1, the overall objective of this project is to evaluate the role of surface energy in the abnormal grain growth mechanisms of Galfenol. Section 3.2 and 3.3, focused on developing protocol for measuring surface energy on pure single crystal Galfenol. There is a clear surface energy difference between the three measured facets of $Fe_{100-x}Ga_x$ (x = 18) as seen in Figure 3.24 and Table 3.5. The (1 0 0) facet has the greatest experimentally measured total surface energy at 1003 ± 20 mJ/m^2. This is an expected result as it is very difficult to produce abnormally grown (1 0 0) grains in FeGa rolled sheet. The surface energy is so high compared to (1 1 0) and (1 1 1) that even sulfur contamination cannot easily produce AGG (1 0 0) grains.[4,5] In contrast, the (1 1 0) facet has the lowest measured surface energy at 528 ± 36 mJ/m^2. It is ~ 284 mJ/m^2 less than the closest measured surface energy from the (1 1 1) facet. This was also expected since AGG of the (1 1 0) facet is the most commonly grown grain for rolled thin sheet polycrystalline Galfenol.

The total surface energy values shown in Table 3.5 will now be used in the total interface energy model to draw conclusions on how AGG is affected by the surface

Table 3.5: Experimentally measured surface energies (1 0 0)*,* (1 1 0)*, and* (1 1 1) *single crystal* $Fe_{82}Ga_{18}$ *using the two-liquid-phase method.*

Facet	γ_S^D **(mJ/m^2)**	γ_S^P **(mJ/m^2)**	γ_S **(mJ/m^2)**
(1 0 0)	924 ± 20	79 ± 6	1003 ± 20
(1 1 0)	470 ± 35	58 ± 9	528 ± 36
(1 1 1)	742 ± 80	70 ± 5	812 ± 80

energy of most common Galfenol grain orientations: {1 0 0}, {1 1 0}, and {1 1 1}. The measured values represent the non-contaminated surface energy values. This section will measure the surface energy of an abnormally grown (1 1 0) $Fe_{100-x}Ga_x$ (x=17) rolled sheet that has been annealed in an environment containing H_2S gas. The presence of H_2S gas during the anneal causes sulfur segregation to occur at the surface and promote AGG.[35,48] The sulfur layer is maintained as the sample cools in the furnace it was annealed in. We take advantage of this situation by applying the two-liquid-phase contact angle procedure to these sulfur-contaminated samples. By measuring the surface energy of a sulfur-contaminated (1 1 0) Galfenol grain, we can calculate a contamination factor, k, to assess the effect of sulfur-contamination in the total interface energy model.

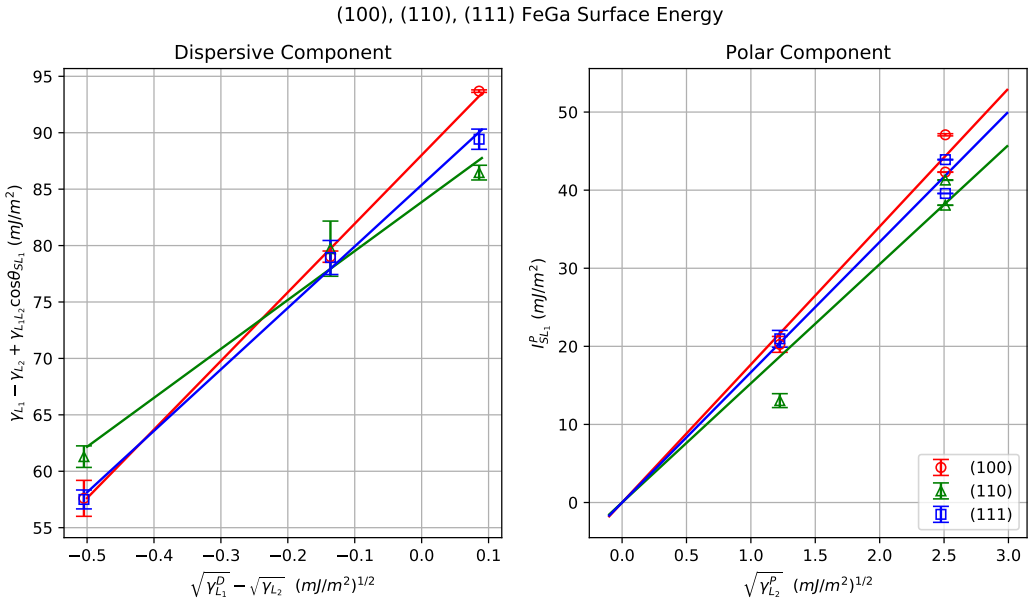

Figure 3.24: These figures show the (1 0 0), (1 1 0), *and* (1 1 1) *dispersive and polar surface energy components represented as red, green, and blue linear fits, respectively. The slope of the dispersive and polar plot is* $2(\gamma_S^D)^{1/2}$ *and* $2(\gamma_S^P)^{1/2}$.

3.4.1 Total Interface Energy Model

A total interface energy model is used to quantify the dominant driving force for AGG in terms of competing surface and grain boundary energies where each are determined by solid/vapor and solid/solid interfaces, respectively, of all grains in the metals. Both the total grain boundary energy and total surface energy equations adapted from work by Na *et al.*.[11] Much of the 3D model has been modified to model grains as tetrakaidecahdron rather than hexagonal rods.

This model assumes a steady state thermal condition with grains arising from primary recrystallization. Consider a sheet with surface area, A, and thickness, t, composed of N grains of size, S_{hkl}, where $S_{hkl} \leq A$. The size of the grain is an area in 2D and a volume in 3D. Assume that the matrix grain radius, r_m, remains constant

during AGG. We make the following simplifying approximations as shown in Figure 3.25: a circular growth for an abnormal grain with radius r_{AGG} engulfs a hexagonal matrix grain array with uniform diaganols $2r_m$.

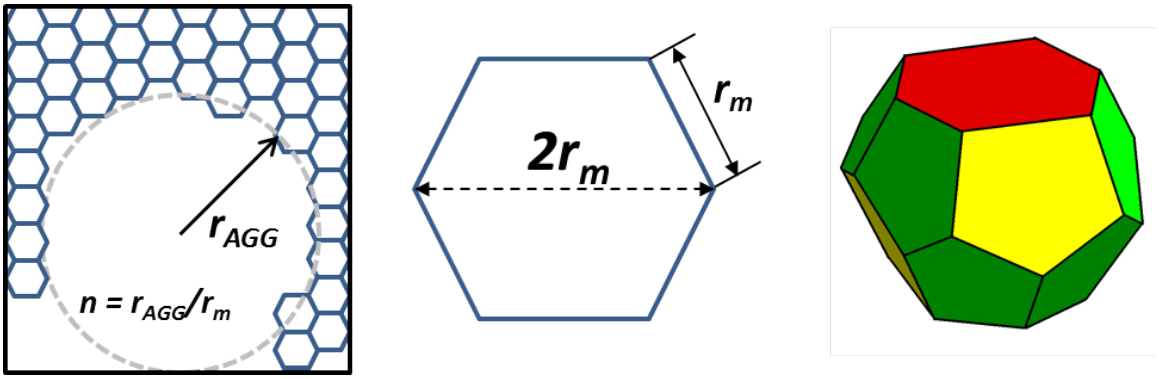

Figure 3.25: This is an illustration of the unit grain geometries that are modelled in the following derivation. The through grain case ($t < 2r_{AGG}$) will consider the 2D interpretation where the AGG grain is a circle and the matrix grains are hexagons. The non-through grain case ($2r_m < 2r_{AGG} < t$), all grains have the geometry of a tetrakaidecahedron.

These assumptions give us the total grain boundary energy for a given AGG ratio of $n = r_{AGG}/r_m$, shown in Equation 3.9 for the 2D case and Equation 3.10 for the 3D case.

$$E_{GB}^{2D}(r_m) = \left[\frac{gA}{r_m} - n^2 r_m\right] \cdot 3t\gamma_{GB} \tag{3.9}$$

$$E_{GB}^{3D}(r_m) = \left[g_1 \cdot At\frac{1}{r_m} - g_2 \cdot r_m^2 n^3\right] \gamma_{GB} \tag{3.10}$$

where g, g_1, and g_2 are geometric constants of values 0.3849, 1.18372, and 13.3923, respectively. The term γ_{GB} is the average grain boundary energy per unit area. For this study, we use the value of $\gamma_{GB} = 1000\text{mJ/m}^2$ from Fe-3%Si,[134] as done in Na *et al.*.[11] The 2D model assumes that the crystal grain goes through the thickness of the

sample, $t < 2r_{AGG}$. The 3D model assumes that the crystal grain does not reach the other side of the sample, $2r_m < 2r_{AGG} < t$.

The total surface energy for the 2D and 3D cases are shown in Equations 3.11 and 3.12, respectively:

$$E^{2D}_{surf.}(r_m) = 3\sqrt{3}\left(1 + \frac{2t}{\sqrt{A}}\right)\left[(\gamma_{110} - \frac{1}{2}\gamma_{100} - \frac{1}{2}\gamma_{111})n^2 r_m^2 + \frac{A}{3\sqrt{3}}(\gamma_{100} + \gamma_{111})\right] \tag{3.11}$$

$$E^{3D}_{surf.}(r_m) = 16\sqrt{2}\left(\frac{1}{t} + \frac{2}{\sqrt{A}}\right)\left[(\gamma_{110} - \frac{1}{2}\gamma_{100} - \frac{1}{2}\gamma_{111})n^3 r_m^3 + \frac{At}{16\sqrt{2}}(\gamma_{100} + \gamma_{111})\right] \tag{3.12}$$

where γ_{100}, γ_{110}, and γ_{111} are the surface energies of non-contaminated $Fe_{100-x}Ga_x$ (x = 18) from Table 3.5.

The abnormally grown (1 1 0) grain size relative to matrix grain sizes, $f_{110} = r_{110}/r_m$, is determined by equating the total grain boundary and surface energies. Equations 3.13 and 3.14 show the 2D and 3D (1 1 0) area fraction, respectively, as a function of r_m for a given thickness, t.

$$f^{2D}_{110}(r_m) = \frac{\left(2\pi t/\sqrt{3}r_m\right)\gamma_{GB} - \left(1 + 2t/\sqrt{A}\right)(\gamma_{100} + \gamma_{111})}{(3t/r_m)\,\gamma_{GB} + 3\sqrt{3}\left(1 + 2t/\sqrt{A}\right)\left(\gamma_{110} - \frac{1}{2}\gamma_{100} - \frac{1}{2}\gamma_{111}\right)} \tag{3.13}$$

$$f_{110}^{3D}(r_m) = 8\sqrt{2}\frac{g_1 r_m^2 - \left(1/t + 2/\sqrt{A}\right)(\gamma_{100} + \gamma_{111})r_m^3}{(g_2 r_m^2)\,\gamma_{GB} + 16\sqrt{2}\left(1/t + 2/\sqrt{A}\right)\left(\gamma_{110} - \frac{1}{2}\gamma_{100} - \frac{1}{2}\gamma_{111}\right)} \tag{3.14}$$

2D case ($t < 2r_{AGG}$)

Figure 3.26 shows a plot of the total grain boundary, E_{GB}, and surface energy, E_{surf}, as a function of r_m for increasing values of n. Normal grain growth (NGG) occurs at $n = 1$ since the AGG grain and matrix grains are defined to be the same size throughout the anneal. AGG occurs when $n > 1$ because the AGG grain size is initially defined greater than matrix grain sizes, hence the AGG grain will grow larger than the matrix grains throughout an anneal. The total grain boundary energy curve drops off very quickly as r_m increases due to the $1/r_m$ term in Equation 3.9. This steep drop is also attributed to the subtracted $n^2 r_m$ term, especially as the AGG ratio n increases. In contrast, $E_{surf}(r_m)$ decreases at a lower rate than $E_{GB}(r_m)$ curve. The intersection of these energies signifies the critical matrix grain radius, r_c, where the dominant driving force for AGG transitions from grain boundary to surface energy. The $E_{GB}(r_m)$ curve decreases at a higher rate with an increasing AGG ratio n. This indicates that the grain boundary energy weakens as driving force for AGG as n increases. If AGG was only driven by $E_{GB}(r_m)$, grain boundaries would ultimately lose mobility at some critical radius.[11] However, since it has been observed that an AGG grain can grow to 99% of the sample area, the surface energy must drive AGG at some point in the the AGG process (see Figure 1.12).

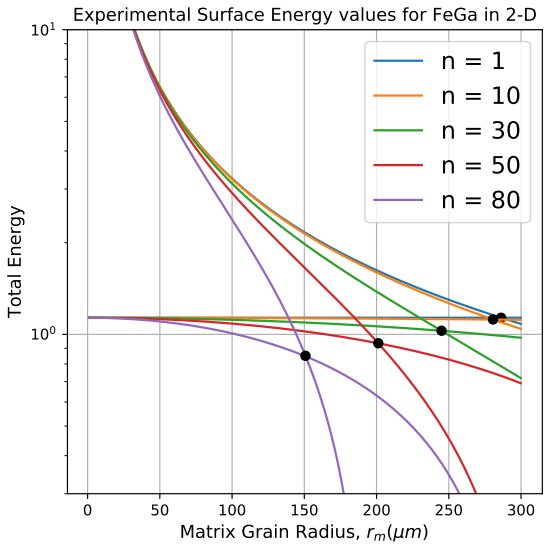

$n = r_{AGG}/r_m$	r_c (μm)
1	286.2
10	280.6
30	245.0
50	201.2
80	150.8

Figure 3.26: This plot shows the total grain boundary and surface energies as a function of matrix grain radius, r_m, for the 2D case using experimentally measured surface energies from Section 3.3. The considered sample thickness is $t = 0.45mm$, and the sample area is $A = 25x25mm$. Curves are shown with differing values of n where $n = 1$ is for the NGG condition and $n > 1$ is for the AGG condition. The table to the right shows the intersection points of the grain boundary energy and surface energy curves. These intersections represent the critical matrix grain radius, r_c, where the driving energy of AGG switches from grain boundary energy to surface energy.

Figure 3.27a shows the area fraction curves of an AGG (1 1 0) $Fe_{100-x}Ga_x$ (x = 18) grain as determined by Equation 3.9. For a thickness, t, at $f_{110} = 1$, matrix grains are sufficiently small enough for AGG (1 1 0) grains to fully consume the entire sample. At $f_{110} = 0$, matrix grains are too large for any AGG to occur. As the sample thickness increases, the decreasing rate of f_{110} curve decreases. This means that an AGG through grain can grow to higher area fractions on the sample in the presence of greater matrix grains as the sample thickness increases. More importantly, the maximum matrix grain radius for $f_{110} = 1$ increases with thickness. It has been experimentally observed that there is an upper thickness limit for (1 1 0) Galfenol AGG, but this model does not currently account for this trend.[11] What this model

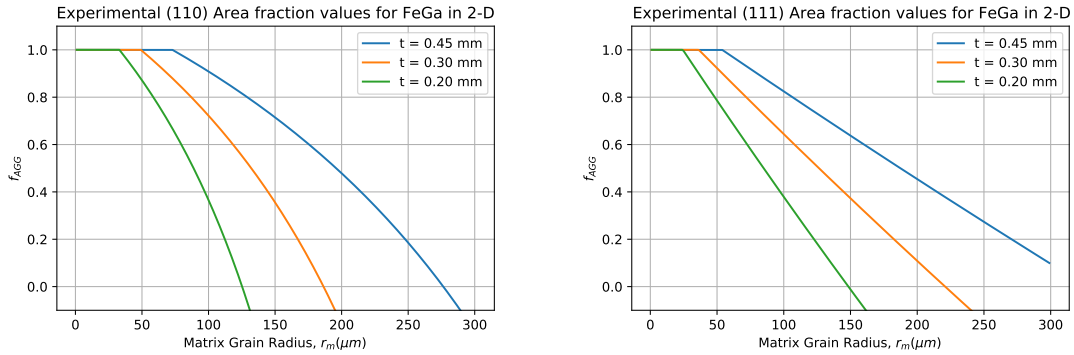

(a) *(b)*

Figure 3.27: (a,b) These plots respectively show the area fraction of abnormally grown (1 1 0) *and* (1 1 1)*, f_{AGG}, for thicknesses of $t = 0.20, 0.30, 0.45$ mm.*

could consider is the thickness dependence for other abnormally grown grains. In Na *et al.*, many small (1 1 1) grains are the dominant AGG grain at a sample thickness of $t = 0.2$mm (Figure 3.28). I have experimentally determined that for $Fe_{100-x}Ga_x$ (x = 18), orientation dependent surface energies follow the trend, $\gamma_{110} < \gamma_{111}, \gamma_{100}$. In this way, the (1 1 1) facet is the next most likely to abnormally grow after (1 1 0), if only surface energy is considered. Figure 3.27b shows the area fraction of an abnormally grown (1 1 1) $Fe_{100-x}Ga_x$ (x = 18) grain. The equation for this curve simply switches the γ_{110} and γ_{111} term in Equation 3.13. For $t = 0.2$mm, the (1 1 1) area fraction, f_{AGG}^{111}, is greater than f_{AGG}^{110} for $r_m \gtrapprox 100\mu$m. This means that an abnormally growing (1 1 1) grain will consume larger matrix grains than (1 1 0). However, it does not explain why many small (1 1 1) grains will preferentially grow instead of (1 1 0) when $t = 0.2$mm, as seen in Figure 3.28.

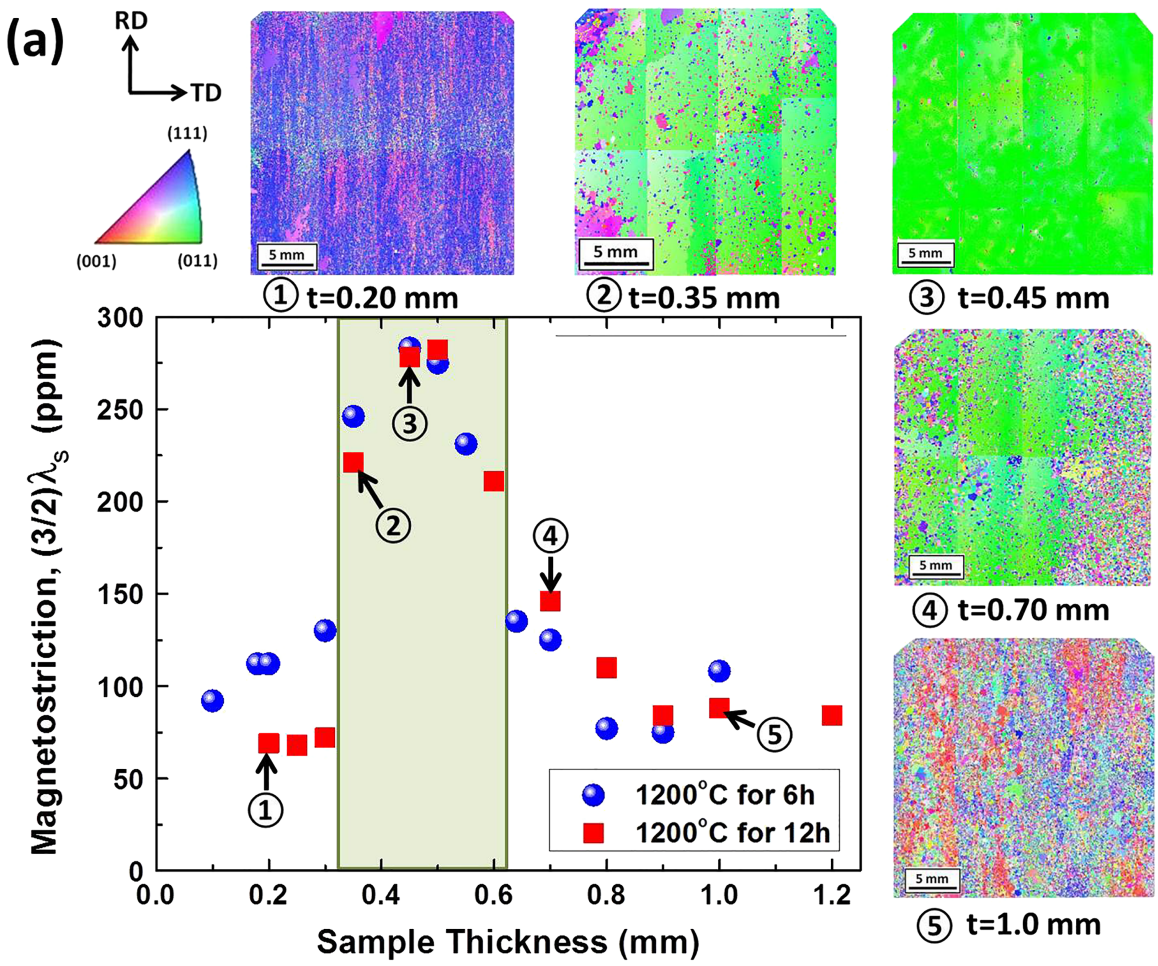

Figure 3.28: Observed magnetostriction as a function of sample thickness in 1.0 %NbC-added $Fe_{81}Ga_{19}$ rolled sheet annealed at 1200°C under a sulfur atmosphere and EBSD-scanned images inserted for samples corresponding to each thickness. Extracted from Na et al.[11]

3D case ($2r_m < 2r_{AGG} < t$)

We briefly consider the case that the AGG grain is not as thick as the sample thickness by modeling grains as tetrakaidecahedrons. Figure 3.29 shows $E_{GB}(r_m)$ and $E_{surf}(r_m)$ for the 3D case. It is immediately apparent that no intersection of the two curves at any value of n, hence there is no critical radius at any n. As n increases, both curves drop significantly at steeper rates as r_m increases. At the same time, both curves are

divergent at every n. As discussed previously, if AGG was only driven by $E_{GB}(r_m)$, grain boundaries would ultimately lose mobility at some critical radius. Therefore, we should not see (1 1 0) AGG to 99% of the sample surface as we do in experiments.

We see more model to experiment contradiction in Figure 3.30 where $f_{AGG} = 1$ only occurs at $r_m = 0$ for all thicknesses. This also tell us that (1 1 0) AGG to >99% of a Galfenol surface should not be possible. For this reason, the 3D case is not physical and we will only consider the 2D (through-thickness grain) total interface model for rolled/annealed thin sheet Galfenol AGG.

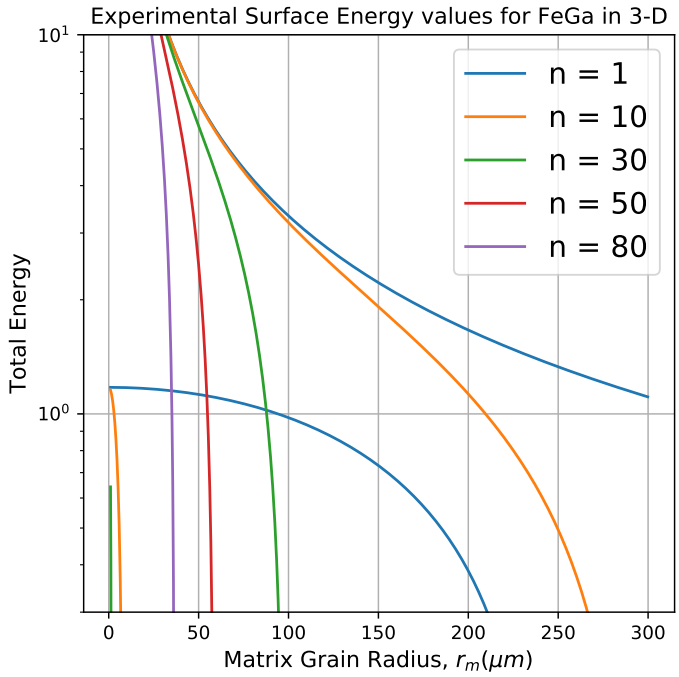

Figure 3.29: This plot shows the total grain boundary and surface energies as a function of matrix grain radius, r_m, for the 3D case. The considered sample thickness is $t = 0.45mm$, and the sample area is $A = 25x25mm$. Curves are shown with differing values of n where $n = 1$ is for the NGG condition and $n > 1$ is for the AGG condition. The curves are divergent of each other, hence there is no critical matrix radius where energy dominance switches.

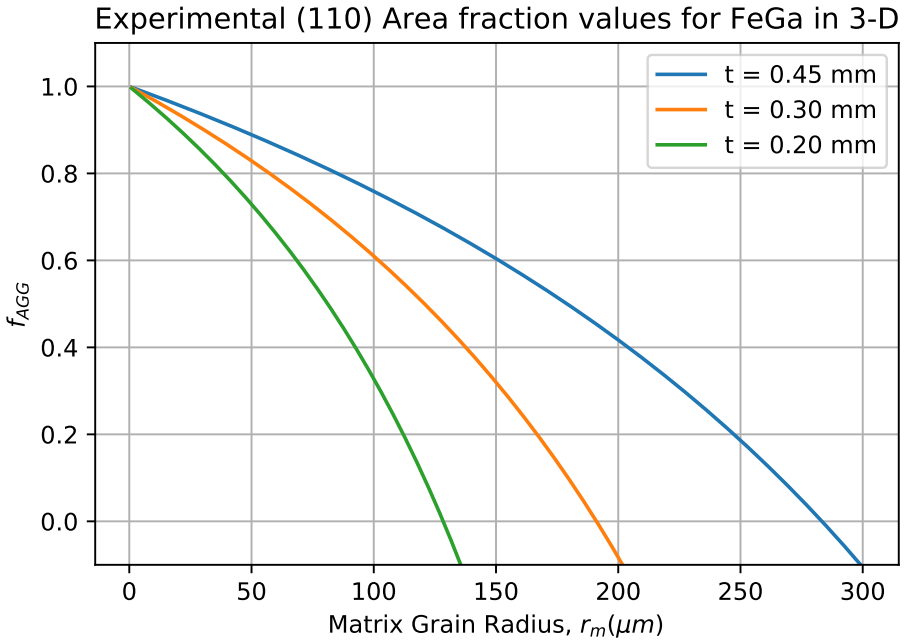

Figure 3.30: This plot shows the area fraction of abnormally grown (1 1 0)*,* f_{AGG}*, for thicknesses of* $t = 0.20, 0.30, 0.45$ *mm. This is for the 3D case.*

Sulfur contamination factor

A contamination factor, k, can be incorporated into the surface energy of each crystal plane. This will further determine the effect of sulfur on the surface energy of Galfenol crystal planes. Resultantly, the enhancement of AGG under a sulfur contaminated anneal can be understood.

Each surface energy, γ_{hkl}, in Equation 3.13 is replaced with $k\gamma^0_{hkl}$, where k is an experimentally determined proportionality constant, as defined by Equation 3.15, and γ^0_{hkl} is the surface energy of a crystal facet $(h\,k\,l)$ with no contamination. There is no contamination for $k = 1$, *e.g.* argon annealed Galfenol, and surface contamination for $k < 1$, *e.g.* Ar + H_2S annealed. The contamination factor will be applied to all surface energies. A plot of (1 1 0) area fraction for a range of contamination factors,

$0.1 \leq k \leq 1.0$. The maximum matrix radius grain for full AGG coverage ($f_{AGG} = 1$) increases as k decreases. This consistent with experimental observations of 99% AGG coverage with increased sulfur contamination. Again, this model does not predict an upper limit to sulfur contamination.

$$k = \frac{\text{sulfur contaminated SE}}{\text{uncontaminated SE}} = \frac{\gamma_{hkl}}{\gamma^0_{hkl}} \tag{3.15}$$

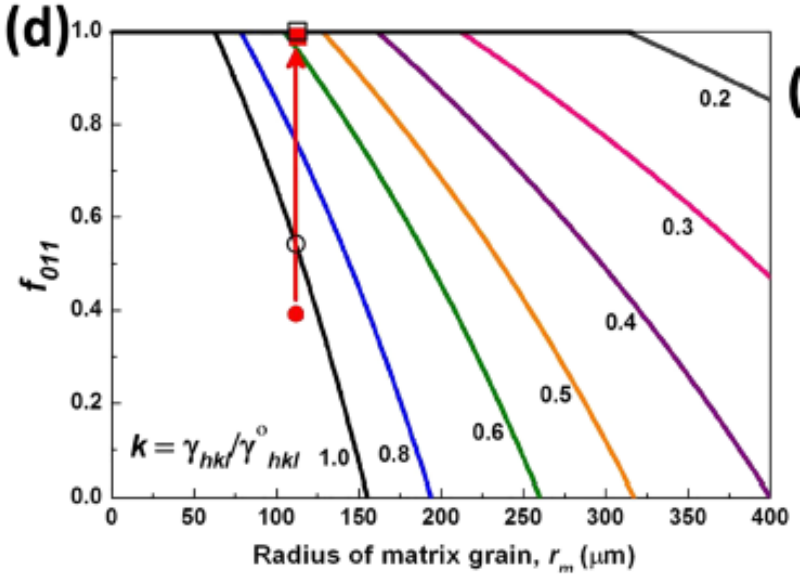

Figure 3.31: Area fraction of an abnormal (011) grain, f_{011}, as a function of matrix grain radius, r_m, calculated from the both energy equations. Plots for varying specific surface energies (k) correspond to the intersecting points of both energies at a given ratio (n) and matrix grain radius. Extracted from Na et al..[11]

The uncontaminated surface energies for the (1 0 0), (1 1 0), and (1 1 1) planes have been measured in Section 3.3. To determine the contamination factor, the surface energy of a sulfur-contaminated surface must be measured. There are a number of challenges with this measurement if the two-liquid-phase contact angle method is to

be used successfully.

Samples must be well polished with a vibratory polisher ($R_a < 1$nm) before being annealed in a sulfur environment. The roughness will likely increase during the high temperature anneal, so roughness must be as low as possible before annealing. The sulfur contaminated surface must then be maintained after removal from the annealing furnace. Samples must be transferred to six different hydrocarbon environments under an inert atmosphere, similar to Section 3.3 where samples were quickly placed in vials filled with hydrocarbon liquids *under a nitrogen gas back-fill* after plasma-cleaning. This must happen very quickly to minimize surface oxidation.

It is also necessary to start from an as-rolled polycrystalline Galfenol sheet. In this way, we perform an annealing procedure that is known to produce abnormally grown Goss (1 1 0) textures. If a highly-textured or single-crystal sample was annealed a second time to obtain a sulfur contaminated surface, it is not certain that the texture will be maintained. A sulfur-anneal was attempted with a directionally solidified single-crystal (1 0 0) $Fe_{83}Ga_{17}$ sample to contaminate the surface with sulfur. Unfortunately, a number of factors caused this experiment to fail. The initial surface had no visible grain boundaries present, as expected of a single-crystal sample. Upon visual inspection after a 1 hr anneal in Ar + H_2S at 1200°C, the sample surface had a network of grain boundaries present. The largest grains were measured with two-liquid-phase method, but the contact angle spreading was very slow. This indicative of an oxidized surface which was confirmed through the surface energy calculation. The dispersive surface energy of this surface was $\gamma^D = 113 \pm 8\text{mJ/m}^2$, and this value agrees with the passivated FeGa surface energy measured in Section 3.3.

For this reason, an as-rolled $Fe_{100-x}Ga_x$ (x = 18) rolled sheet will be annealed in Ar + 0.5% H_2S to produce a Goss-textured, sulfur-contaminated surface.

3.4.2 Sulfur contaminated surface energy measurement

A 0.8mm thick piece of polycrystalline $Fe_{100-x}Ga_x$ (x = 18) was cold rolled until a thickness of 0.45mm was reached. The rolling produced a slightly curved thin sheet which may result in tilted Goss textures after annealing in sulfur. Six 3/4x3/4in were cut from this sheet and placed in a tube furnace. The tube was filled with stagnant Ar + H_2S gas and annealed at 1200°C for 6 hours. This annealing recipe has been shown to produce (1 1 0) abnormally grown Goss textures.[35,44,51,55] A glove bag was placed over the tube furnace entrance, sealed, and filled with high purity argon after the furnace cooled. The samples were removed from the tube furnace and placed in six different liquid mediums for the two-liquid-phase contact angle experiment. The liquid environments were *n*-octane, *n*-decane, *n*-hexadecane, 1-chlorobutane, 1-octanol, and 1-decanol.

The contact angle measurement follows the same procedure described in Section 3.2 to minimize risk of oxidation and increase accuracy of the most stable contact angle measurement. The largest observable grains were probed with DI water sessile drops due to the expectation of abnormally grown Goss textures to consume large areas of the annealed surface. Probed areas were characterized with EBSD for crystal orientation and AFM for roughness.

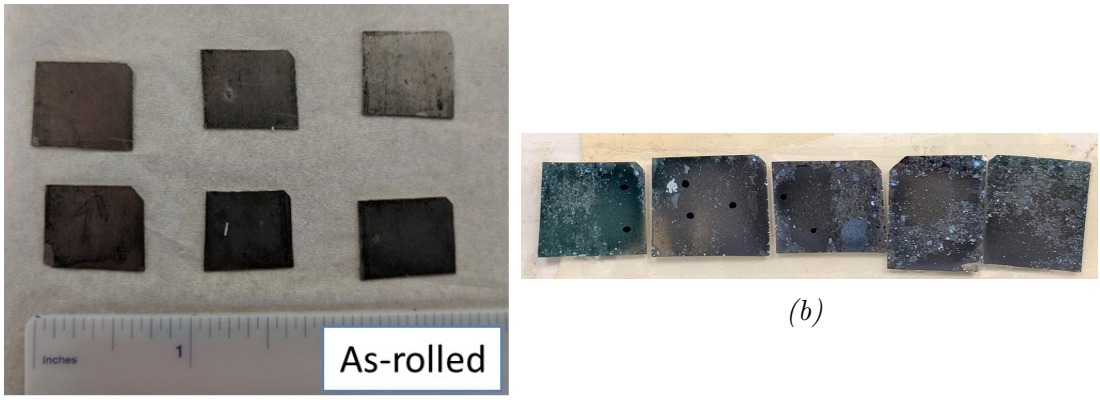

(a) (b)

Figure 3.32: (a) All as-rolled $Fe_{82}Ga_{18}$ samples of 0.45mm thickness cut into 3/4x3/4in squares. (b) Five of the six samples after sulfur annealing and two-liquid-phase contact angle measurements. The blue tint on the surfaces are indicative of sulfur contamination.

Results

A blue tint was observed on the Galfenol surfaces upon removing the six samples from the tube furnace, as seen in Figure 3.32b. According to Dr. Suok-Min Na, this is an indication of a sulfur-contaminated metal surface.

Shown in Table 3.6 are the most-stable contact angles determined from advancing and receding contact angles measurements by Equation 3.5. Sessile droplets were video recorded and analyzed on the Kruss DSA10 software. Probe water droplets

Table 3.6: Most stable contact angles for (1 1 0) *Goss textured polycrystalline $Fe_{82}Ga_{18}$ in bulk n-alkane environment for a sulfur-contaminated surface.*

Bulk Liquids	θ_{ms} (°)
n-octane	75.7 ± 3.5
n-decane	83.4 ± 2.0
n-hexadecane	89.2 ± 3.4
1-chlorobutane	99.2 ± 1.7
1-octanol	109.6 ± 3.9
1-decanol	127.8 ± 1.6

very quickly wet to the six samples. Sessile droplets stabilized to an equilibrium

shape between frames, $\Delta t < 0.06$s. Similar to plasma-cleaned samples in Section 3.3, fast wetting on a metal sample is indicative of trace to no oxidation at the surface. Hence, the surface is most likely sulfur-contaminated or completely bare. During contact angle measurements, only one environment, 1-decanol, showed signs of dissolving the probe droplet of DI water. This was apparent when the volume of the DI water sessile drop visibly decreased as video of the droplet was recorded.

EBSD was performed on each sample to confirm a Goss texture in the probed areas. Figure 3.33 shows SEM images of the probed AGG grains along with their respective inverse pole figures and lattice orientations. The green color of the IPF figures indicate that these abnormally grown grains are (1 1 0) Goss grains. Figure 3.33b shows that the sample tested in n-decane has a slightly tilted Goss texture. Figure 3.34b shows the sample tested in n-octane where there were two abnormally grown grains that the sessile droplet triple line probed. Upon visual inspection, the lattice orientations in Figure 3.34b are slightly more tilted Goss textures compared to those in Figure 3.33b. The dominant grains on the n-octane sample both have 23° misorientation angle with respect to the ideal Goss texture (1 1 0)[1 0 0]. The left grain in Figure 3.33b has a 11° misorientation angle with respect to the Goss texture. This could potentially give contact angles and surface energies slightly skewed from the values for the targeted (1 1 0) crystal orientation.

A height contour map and a respective 3D height map measured using AFM is shown in Figure 3.35. The average roughness is $R_a \approx 6.60$nm measured from AFM measurements. This is a clear increase from the routinely produced subnanometer roughness from vibratory polishing. Regardless, any correction to the contact angle

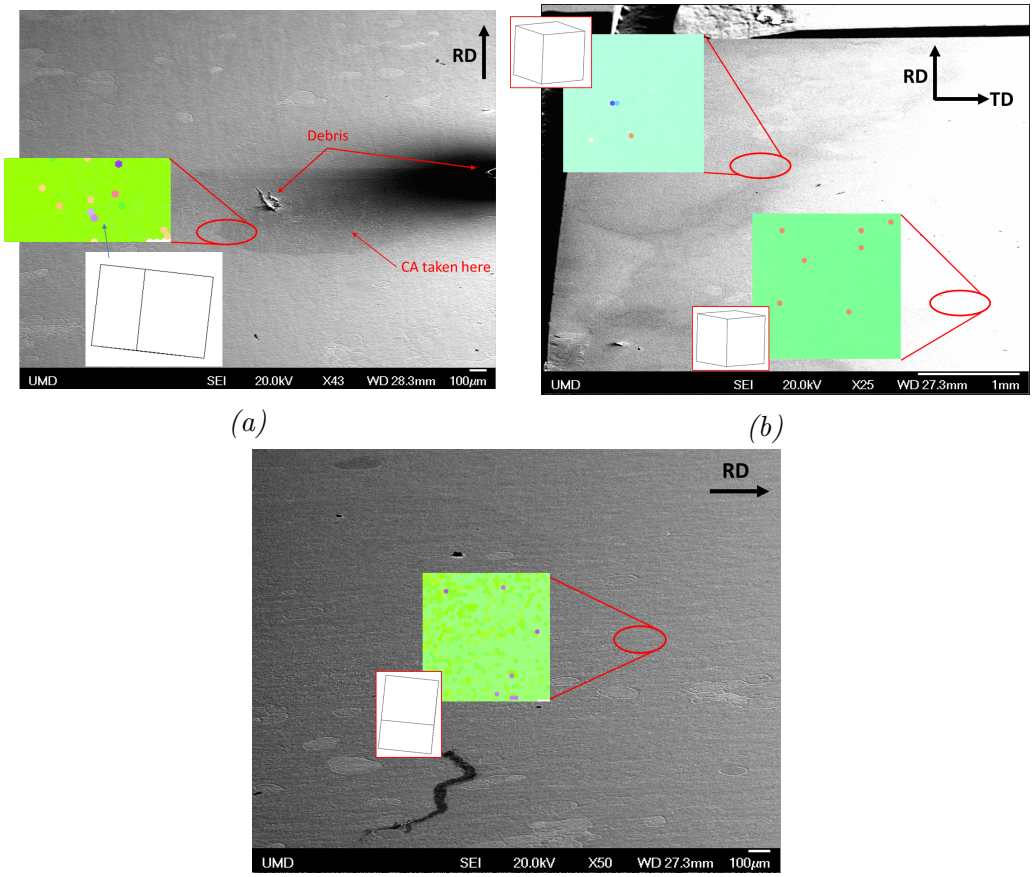

Figure 3.33: (a,b,c) SEM images of regions probed with sessile droplets in n-hexadecane, n-decane, and 1-chlorobutane, respectively. Images are overlayed with inverse pole figures (IPFs) and dominant lattice orientations measured using EBSD. Transverse and rolling directions are displayed in the top right of each image.

on the sulfur-contaminated Galfenol made using Equation 3.3 is negligible. The roughness factor, r, in Equation 3.3 for the sulfur-contaminated surfaces would be 1.0124. With this roughness factor, the real measured contact angle for the n-octane medium would change from 75.7° to 75.5°. This minimal change will not be factored into further calculations.

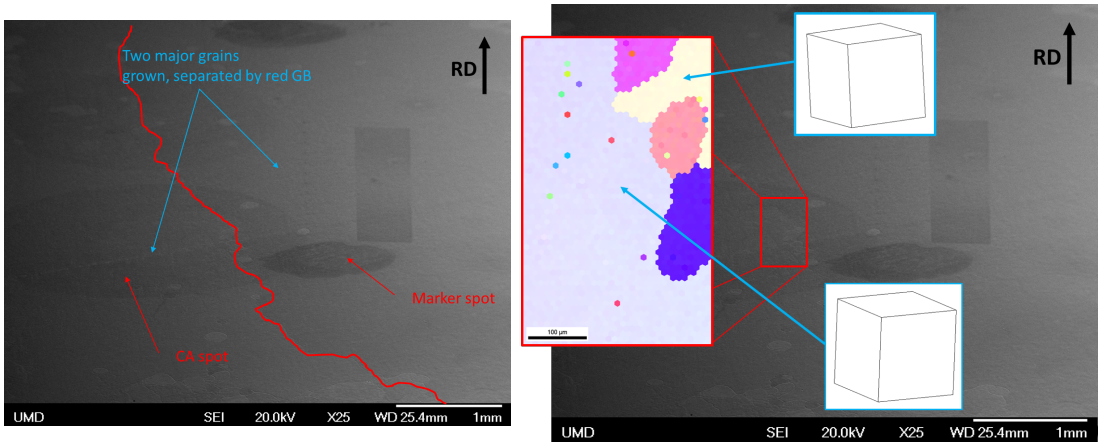

(a) *(b)*

Figure 3.34: (a,b) SEM images of region probed with sessile droplets in n-octane. (a) Shows the two major grains that abnormally grew during the anneal in H_2S. (b) Image is overlayed with an inverse pole figure (IPFs) and dominant lattice orientations of the grain boundary between the two abnormally grown grains measured using EBSD. Rolling direction is displayed in the top right of each image.

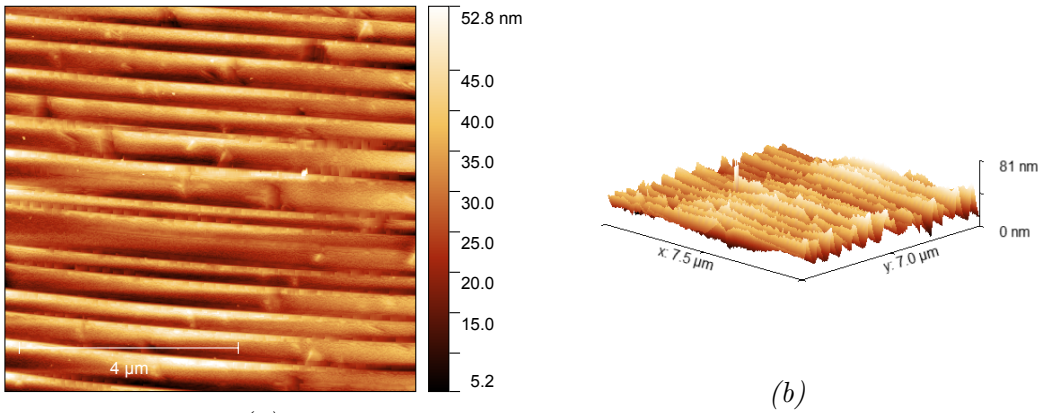

(a) *(b)*

Figure 3.35: AFM measurements of the sulfur-contaminated $Fe_{82}Ga_{18}$ Goss-textured sample tested in 1-octanol. (a) A height contour map of a 7.4x7.4 µm area. (b) A 3D mapping of the same scanned area.

Discussion of sulfur-contaminated surface energy

Surface energy of the sulfur-contaminated (1 1 0) $Fe_{82}Ga_{18}$ surface is calculated plotting Equation B.5 and Equation B.6 using the contact angle values in Table 3.6. Figure 3.36 shows the fitted curves where the slopes tells us the dispersive and polar components of surface energy. The dispersive and polar components calculated from this plot are 207 ± 45 mJ/m^2 and 15 ± 6 mJ/m^2, respectively . Summing these two values, the total surface energy for a sulfur-contaminated (1 1 0) $Fe_{82}Ga_{18}$ surface is 222 ± 45 mJ/m^2. Each point on the dispersive component plot is within two standard

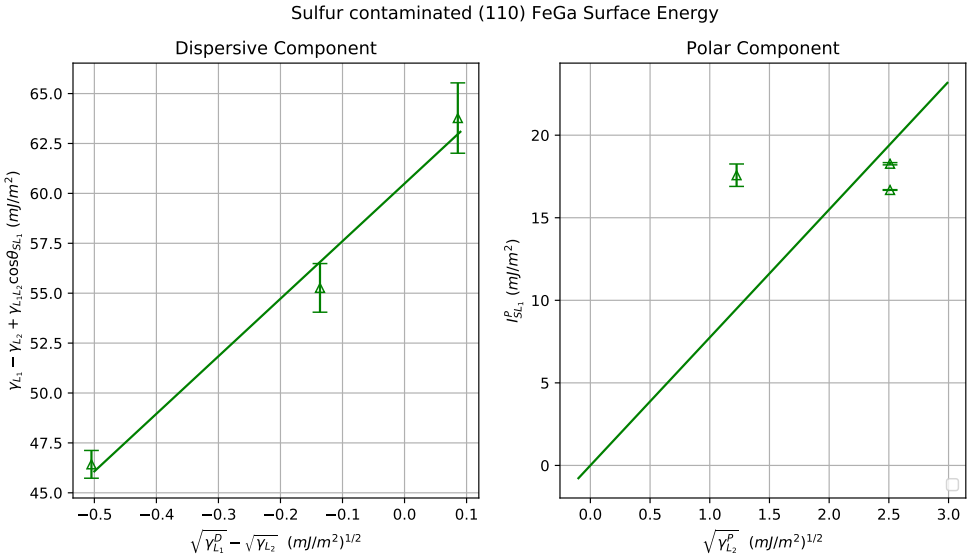

Figure 3.36: These figures show the sulfur-contaminated (1 1 0) $Fe_{82}Ga_{18}$ *dispersive and polar surface energy components represented as linear fits. The slope of the dispersive and polar plot is* $2(\gamma_S^D)^{1/2}$ *and* $2(\gamma_S^P)^{1/2}$.

deviations of the fitted line. The *n*-decane (x = -0.14) data point has the furthest deviation from the fit line, but it is likely skewed due to the *n*-octane (x = 0.09) data point. Figure 3.34b shows that the probed sessile drop area was a heavily tilted Goss grain. This means that there could be a slight decrease in the contact angle

attributed to a higher surface energy crystal orientation. A lower contact angle will increase the y-value in the dispersive component plot. This skews the slope of the fit curve upward. This fact, along with the roughness increase, is a large factor in the high error in the total surface energy for the sulfur-contaminated surface.

On the polar component plot, the 1-chlorobutane data point (x = 1.2) is an outlier from the fit. Most of this error can be solved by increasing the number of bulk liquid environments where the two-liquid-phase method is performed. Many of the possible bulk liquids were not cleared to use by the UMD Department of Environmental Safety at the time of performing these experiments. Other liquids, specifically multiple from for the polar component plot, have a higher density than water. For this reason, the two-liquid-phase method would have to be inverted and the experiment apparatus was not set up for this test.

There is a clear decrease in the surface energy of Goss textured $Fe_{82}Ga_{18}$ after sulfur-contamination. The contamination factor, defined in Equation 3.15, for this sample is $k = 0.42$. This value is used in Equation 3.13 to plot the area fraction of AGG (1 1 0) Goss grains, shown in Figure 3.37a. The curves of $k = 0.60$ and 0.80 are displayed to show the trend of sulfur contamination on f_{AGG}. According to Figure 3.37a, the maximum matrix grain radius at which saturated AGG ($f_{AGG} = 1$) occurs, r_{max}, increases as k decreases. At $k = 1$ (no contamination) $r_{max} \approx 75\mu$m. At the measured value of $k = 0.42$, $r_{max} \approx 173\mu$m. This implicates that the sulfur-contamination effect on orientation-dependent FeGa surface energies has an even greater impact on AGG than previously reported.[11]

Figure 3.37b shows experimental EBSD IPF images of argon-annealed and sulfur-

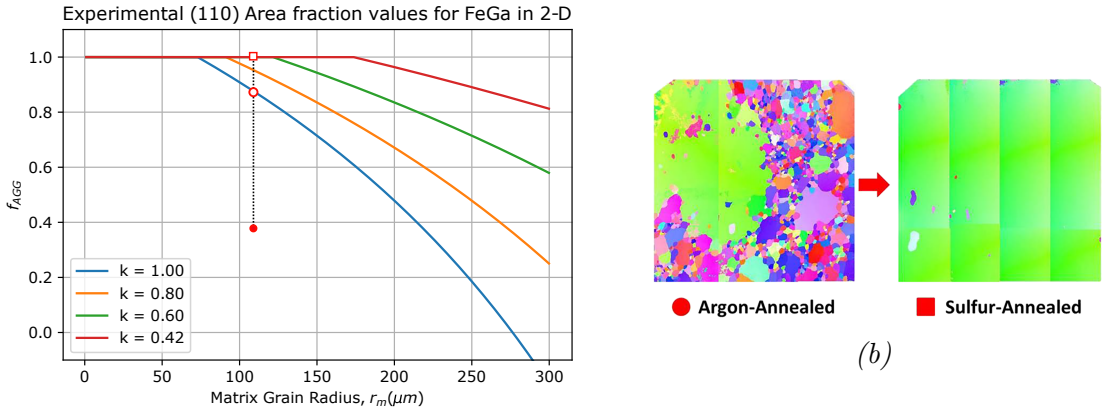

(a) *(b)*

Figure 3.37: (a) Area fraction of an abnormal (1 1 0) *grain,* f_{011}*, as a function of matrix grain radius,* r_m*, calculated from the both energy equations. The thickness of the sample is* $t = 0.45mm$*. Plots for varying specific surface energies (k) correspond to the intersecting points of both energies. The value of* $k = 0.42$ *is experimentally determined. At* $r_m = 110$ μm*, the solid red dot is the experimental* f_{AGG} *argon-annealed sample in (b), the open red dot is the theoretical* f_{AGG} *curve for argon-annealed FeGa, and the hollow square is the theoretical and experimental* f_{AGG} *sulfur-annealed FeGa sample in (b). (b) EBSD-scanned images along normal direction (ND) of the sheet surface for (Fe-19%Ga)+1.0%NbC sheets that were argon- and sulfur-annealed at 1200° C, respectively. Extracted from Na et al..*[11]

annealed $Fe_{82}Ga_{18}$ from Na *et al.*. Represented by a solid red dot on Figure 3.37a, the argon-annealed sample has an abnormally grown Goss grain with an area fraction of $f_{AGG} = 0.39$ with an initial matrix grain size of 110 μm.[11] The predicted area fraction at $k = 1.0$ at $r_m = 110\mu$m is shown by the open red dot to be $f_{AGG} = 0.87$. which is greater than the previously reported theoretical area fraction of the same sample in Na *et al.*, $f_{011} = 0.57$. This may show that particle pinning and/or thermal grooving has an even greater influence on AGG than previously thought. Incorporation of such phenomena would be beneficial for a deeper understanding of AGG. This endeavor is currently beyond the scope of this project.

The open square in Figure 3.37a represents the theoretical value of $f_{AGG} = 1$ for $r_m = 110\mu$m with a contamination factor of $k = 0.42$. This matches the near 100%

coverage of the (1 1 0) Goss grain in the sulfur-annealed sample in Figure 3.37b.

Conclusions

There is a clear decrease in surface energy due to sulfur-contamination on the (1 1 0) facet of $Fe_{82}Ga_{18}$ from 528 mJ/m^2 to 222 mJ/m^2. According to the total interface energy model with a contamination factor $k = 0.42$, this decrease in surface energy increases the critical matrix radius at which surface energy becomes the dominant driving force. We also see an increase in the maximum matrix radius at which full AGG coverage can be achieved by an abnormally growing (1 1 0) Goss grain. We expect that other factors including strain energy, thermal grooving, and particle pinning must be incorporated with the model to improve agreement with experimental observations.

Chapter 4

Patterned surface two-liquid-phase method

4.1 Beyond flat surface two-liquid-phase method

Since Schultz published his seminal paper, his method has been used to measure very high surface energy materials ranging from 50 mJ/m^2 to 487 mJ/m^2 and now over 1000mJ/m^2.[110] However, many of these studies fail to consider the wetting modes of water on their solid surfaces in a bulk *n*-alkane environment. Giljean *et al.* examines the dependence of contact angles on the roughness of high surface energy titanium surfaces using the two-liquid-phase method. They show that, depending on the cleaning technique used to remove surface contaminations, the contact angle will change more with a decrease in roughness. Sound arguments are made for the type of wetting regime (Wenzel, Cassie-Baxter, or somewhere in-between) encountered at each step of wetting. An issue occurs when the authors attempt to use the Cassie-

Baxter equation to calculate the Young contact angle. The Cassie-Baxter equation (Equation 3.4), as defined in the original publication,[135] is designed for a general surface. Many papers, as pointed out by Milne *et al.*,[12] falsely use Equation 4.1 for randomly rough surfaces when this equation is for the special case of a coplanar liquid-vapor and solid-liquid interface, as illustrated in Figure 4.1.

$$\cos\theta_{CB} = f\cos\theta_Y - (1-f) \tag{4.1}$$

To use this simple equation, a surface would have to be patterned with a known geometry of features much larger than the intrinsic surface roughness by at least a factor of 10^3. This allows the effects of a Cassie-Baxter state from the designed roughness to dominate the contact angle interaction, hence the roughness of our well-polished FeGa samples will have negligible effects. This issue is addressed through the theoretical and experimental studies of Bushan *et al.* on superhydrophobic leaves and heterogeneously patterned silicon wafers.[136,137] This patterned roughness must also be small enough spacing to prevent capillary forces from causing the liquid to penetrate the roughness.

Considering all these factors, I postulate that by combining the two-liquid-phase method with a patterned surface of single-crystal Galfenol, the probe water droplet will not spread and a Young's contact angle can be calculated for use in measuring the orientation-dependent surface energy of Galfenol. Single-crystal Galfenol samples were prepared at the DOE Ames Laboratory by the modified Bridgman technique at compositions of $Fe_{100-x}Ga_x$ where $x = 19, 25$. These samples can be cut to obtain

target orientations (1 0 0), (1 1 0), and (1 1 1) using electro-discharge machining. The isotropic surface created by single-crystal samples ensure that the triple-phase-line will maintain exactly the same $L_1 - S$ interaction about the entire droplet perimeter. The patterned surfaces will be etched to have large enough pillars which retain as much surface orientation dependence on the contact angle as possible, as well as small enough gaps to allow for a Cassie-Baxter state in the $L_1 - L_2 - S$ system. A Cassie-Baxter wetting mode would offer the greatest contact angle of the three main wetting modes illustrated in Figure 4.2, and if a well patterned surface can be achieved similar to Figure 4.1, the Young contact angle can be easily calculated from Equation 4.1.

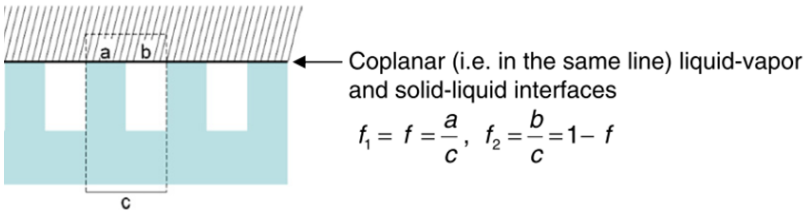

Figure 4.1: Schematic close up of three rough 2-D surfaces. Solid is blue/gray, air is white, liquid is the cross-hatched area above the surface. Liquid–vapor and solid–liquid interfaces of drop are denoted by the black line. A smooth-topped rough surface, which (for zero penetration of liquid) has coplanar solid–liquid and liquid–vapor interface (i.e. interfaces are in line with each other). This yields $f_1 = f$ and $f_2 = (1 - f)$. Image source:[12]

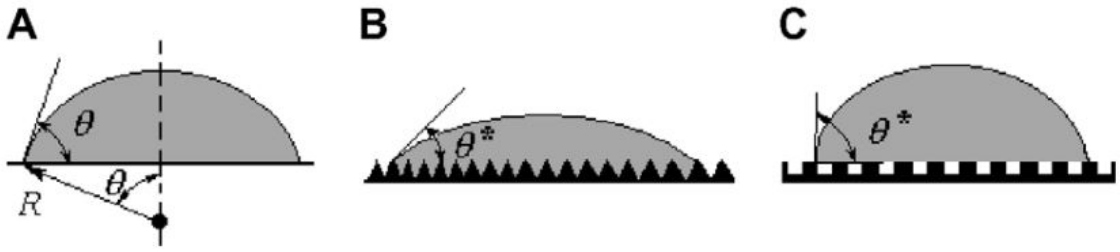

Figure 4.2: Schemes of different wetting regimes. A – flat substrate; B – rough substrate, the Wenzel regime; C – rough substrate with air trapped under the drop, the Cassie–Baxter regime.[13]

4.1.1 Predicted errors in experiment

Possible errors with this method will arise from non-atomically flat surfaces and pillars, imperfect Cassie-Baxter states caused by gravity or capillary forces drawing the probe liquid into the gaps between pillars, and oxide formation at the sample surface. However, such errors should be negligible given extensive polishing protocol, the immiscibility of water with n-alkanes, a controlled surface patterning, and a known cleaning procedure for rough metal surfaces. Therefore, I propose the assumption that our $L_1 - L_2 - S$ system can be treated as the coplanar state depicted in Figure 4.1 is reasonable. Concerning the displacement of n-alkanes by water during the droplet depositing step, the wetting criteria has been proven by Schultz *et al.*[14,106]

Considering a probe water droplet on a well-polished, oxide-free, and *patterned* surface of Galfenol, it is worth investigating the droplet spreading dynamics in this two-liquid-phase experiment. If the spreading speed of a probe droplet is not sufficiently high in this two-liquid-phase system, water has a higher chance of infiltrating the gaps of the patterned surface. If infiltration were to occur, surface energy criteria dictates the complete displacement of the bulk liquid by the probe water droplet. The result is a complete Wenzel state where the observed contact angle will be lower than the flat-surface contact angle. This is a concern because of the potential for complete water wetting ($\theta_{CA} = 0°$) of the surface. Giljean *et al.* studied the roughness effect on water contact angles in an n-Octane environment for three different surface cleaning methods.[14] Surfaces were randomly electro-eroded using Electrical Discharge Machining on a spark erosion machine with adjustable parameters (power,

electrode diameter) which allow realizing samples covering a wide range of roughness parameters from 1.1μm to 20μm.

The first and second cleaning methods were water rinsing with nitrogen drying and successive ultrasonic baths in cyclohexane then acetone, respectively. Both cleaning methods resulted in relatively similar contact angle values for all roughness levels. The third cleaning method involved 100W Ar plasma-cleaning followed by immediate immersion in the *n*-Octane medium. This study gave me the idea of removing the native oxide from Galfenol with Ar plasma, discussed at length in Chapter 3. This plasma cleaning method showed a dramatic decrease in the water contact angle as the roughness decreased.

Giljean *et al.* showed that at higher roughness parameters, a higher percentage of *n*-Octane would be entrapped beneath the water sessile drop. This can be interpreted as experimentally proving the displacement of *n*-octane by water at low roughness values, a Wenzel state. It can also be interpreted as stable Cassie-Baxter states (high percentage of trapped *n*-octane) at higher roughness values.

Equation 3.4 can be rewritten to approximate the amount of *n*-octane trapped under the sessile drop:

$$\cos\theta_{CB} = \Phi_{octane}\cos\theta_{octane} + (1 - \Phi_{octane})\cos\theta_Y \tag{4.2}$$

where Φ_{octane} is the surface fraction of octane entrapped beneath the drop, θ_{CB} the Cassie-Baxter contact angle on the rough surface, θ_{octane} the contact angle of water on octane, $(1 - \Phi_{octane})$ the surface fraction of substrate and θ_Y the Young contact angle

on a smooth surface. Figure 4.3 shows the plot of Φ_{octane} vs. roughness parameter R_a. Values of Φ_{octane} do not reach above 80% since sample surfaces are randomly

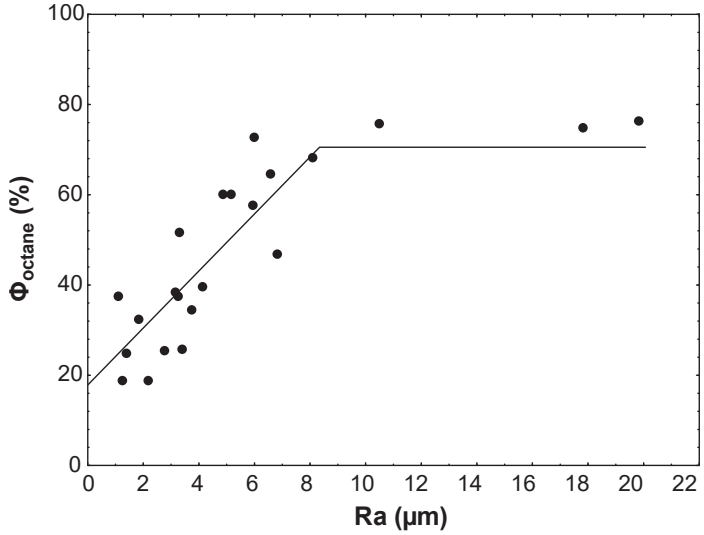

Figure 4.3: Surface fraction of octane entrapped beneath the water sessile drop (Φ_{octane}) after Ar plasma cleaning. The material is a 5 mm thick plate of pure Titanium grade 1. Extracted from Giljean et al..[14]

rough and it is energetically unfavorable for a water droplet to rest at the top of a jagged peak of metal without wetting around the peak. This is especially the case for such a high energy metal surface.

Giljean *et al.* showed that by activating the maximum surface energy of the substrate with Ar plasma cleaning, the resultant high spreading can lead to a kinetic entrapment of the surrounding fluid in the cavities. The surface energy criteria should have dictated the complete displacement of the surrounding fluid.

Consider a plasma cleaned metal sample placed in *n*-octane. Air enclosed in the sample roughness is all removed and the surface is completely wet by *n*-octane as described by the Wenzel model. The second wetting scenario of water on the sample surface must consider the spreading of water on the solid, S_{SW}, and the spreading

of water on n-octane, S_{WO}. Equation 3.6 describes the calculation of the spreading parameter as:

$$S_{12} = \gamma_1 - \gamma_{12} - \gamma_2 \tag{4.3}$$

where S_{12} is the spreading parameter between surface 1 and 2, γ_1 and γ_2 are the surface energies of surfaces 1 and 2, respectively, and γ_{12} is the interfacial energy between 1 and 2. For S_{SW}, we can estimate that the high surface energy of the cleaned substrate leads to a very low (surface/water) interface tension, γ_{SW}. The surface energy of a (1 0 0) FeGa surface was measured to be $\gamma_S \sim 1000$ mJ/m^2, $\gamma_W \approx 72.8$ mJ/m^2, $\gamma_H \approx 21.3$ mJ/m^2, and $\gamma_{WH} \approx 49.8$ mJ/m^2. From these values, it is clear that $S_{SW} \gg S_{WO}$. From a thermodynamic point of view, octane should be completely removed by water.

Giljean *et al.* describes how the kinetics of the triple line overcomes the thermodynamics: "Nevertheless the propagation speed of the triple line has to be considered here. The time required to remove octane is higher than the characteristic timescale taken by the triple line for crossing the width of a cavity (valley), essentially due to the high capillary force driving the spreading of the water drop on this high surface energy substrate. Actually, octane can be considered as trapped in the valley by the propagation speed of the triple line. The profile and the displacement of the triple line in this second wetting stage can be described as a succession of transient pinning and spreading areas. The protruding titanium surface areas locally pull the triple line ahead, whereas valleys filled by octane act as non-wetted areas, retaining transiently (pinning) the triple line. The final wetting situation consists in a water drop sitting on

a mixed surface of titanium and entrapped octane, as described by [the] CB model."

I hypothesize that given a plasma cleaned Galfenol surface, the surface could be patterned with a small enough roughness that a probe water droplet in a two-liquid-phase experiment would be in a Cassie-Baxter state. The sub-nanometer pillar top roughness and high Galfenol surface energy will cause high-speed probe droplet spreading in a two-liquid-phase contact angle experiment. In this way, the bulk liquid will be entrapped in the gaps and a Cassie-Baxter state will be stable. The point of this is two-fold. First, with an engineered patterned surface, the roughness geometry will be known and a Young contact angle can be easily back-calculated. Second, the engineered roughness would be at least four orders of magnitude greater ($\sim 1\mu$m is the limit of commercial photolithographic patterning) than the polished roughness ($R_a \approx 0.5$nm). This justifies the calculation of the Young contact angle because the roughness effect on the water contact angle will be dominated by the engineered roughness.

The spreading speed argument made by Giljean *et al.* was incomplete as it lacked contact angle spreading data. We carried out our own spreading speed experiments on plasma cleaned Galfenol of varying roughness parameters to further describe this kinetic trapping.

4.2 Roughness effect on spreading speed in two-liquid-phase experiment

Sample preparation

A polycrystalline $Fe_{81}Ga_{19}$ sample with a thickness of 0.4 mm was prepared in the Aerosmart lab by using a progressive hot, warm, then cold rolling technique from a randomly oriented polycrystalline Galfenol ingot. The rolled sample is then atmospherically annealed in a tube furnace at 1200° C under an Ar+0.5% H_2S environment for 6h in order to initiate abnormal grain growth of highly magnetostrictive grain orientations. To optimize specific grain growth, pinning particles are incorporate during the rolling process, experimented with different annealing temperatures and times, and modified the annealing environment.[29,35,50,51]

For this study, a 21x27mm $Fe_{81}Ga_{19}$ sample was cut from a rolled sheet and polished to 1200 fine grit size. Over a twenty-five AFM scans, the 1200 grit average roughness was $R_a = 10.03 \pm 2.14$ nm. This polycrystalline Galfenol sample was then cut into nine 7x9mm samples to in order to modify their roughness. One of the nine was kept separate as an "ideally-flat" surface relative to the roughness of the modified surfaces.

Roughness fabrication and measurement

The roughness of each sample was modified using simple sandblasting with different media sizes and material. A sandblasting method was chosen for ease of application

and randomness in the roughness distribution. Simply using high grit sandpaper would leave large striations in uniform directions on the sample surface thus limiting the uniform radial spreading of a sessile drop to a single axis. A siphon-feed sandblaster connected to a 90 psi air compressor with the nozzle positioned normal to the sample surface with approximately one inch of separation. Samples were blasted with media in twenty short pulses where the trigger on the sandblaster was pulled and immediately released.

Each of the eight samples was blasted with different media or combinations of media in order to achieve a range of average roughness, R_a values. From largest size to smallest Media included 8-12 grit garnet, 36 grit SiC, 20 grit silica, and 60 grit silica. The 8-12 grit garnet achieved the largest R_a values of on Galfenol, while the 20 grit silica had the smallest R_a values.

A Tencor Instruments alpha-step 200 profilometer was used to measure roughness values for each sandblasted surface. Five 400 μm line profiles were measured orthogonal to the centerline of the surface, and then the same measurements were made after rotating samples 90°. The averaged roughness values are displayed in Table 4.1.

Table 4.1: R_a values of $Fe_{81}Ga_{19}$ after sandblasted with different media

Media	R_a **(μm)**
8-12 grit garnet	4.36 ± 0.32
8-12 grit garnet + 36 grit SiC	4.17 ± 0.39
36 grit SiC	3.56 ± 0.30
20 grit silica	1.67 ± 0.17
60 grit silica	1.54 ± 0.29

An interesting observation is the difference in topography from the 8-12 grit garnet sandblasted sample to garnet+SiC sample. Figure 4.4 shows the difference in

roughness between the two samples as well as topography differences. The 8-12 garnet sandblasted sample in Figure 4.4a has a relatively spiky roughness expected for a randomly rough surface. The 8-12 garnet + 36 grit sandblasted surface in Figure 4.4b has lower slopes on the roughness spikes and some spikes seem to be flattened slightly. This is likely due to the greater hardness of the SiC media compared to the garnet media. Sandblasting media with a high hardness will remove more target material upon impact compared to a low hardness media.

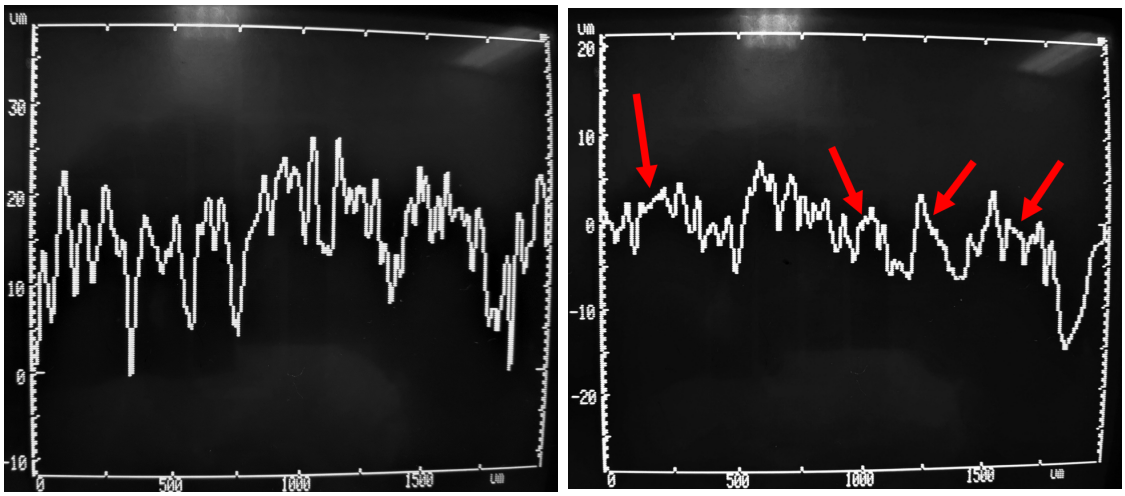

(a) *(b)*

Figure 4.4: These are photos taken of profilometer screens after a measurement on sandblasted polycrystalline FeGa. They show the 2D topography of a given sample. (a) 8-12 grit garnet sandblasting media (b) 8-12 grit garnet + 36 grit SiC sandblasted. The red arrows show "flattened" spikes caused by the harder sandblasting media, SiC.

Each sample was Ar plasma cleaned at 100W for 9 mins to remove the native oxide. After plasma cleaning, the nitrogen purge is kept on as the plasma cleaner door is opened. During this time, samples are quickly dumped into a vial of *n*-hexane to isolate the sample from oxidation for at least 6 hours. The bulk liquid of *n*-hexane was chosen to compare with the *n*-alkane environment used in Giljean *et al.*. Samples are probed with a water sessile drop within 3 hours of plasma cleaning to ensure a

clean metal surface is probed before oxidation. After 6 hours, probe water sessile drops spread slowly on the surface. This is indicative of an oxidized metal surface.

Results and Discussion

We chose to express the spreading speed by extracting the base radius from sessile drop wetting videos. The Kruss DSA10 software can automatically measure chosen parameters in a sessile drop video frame-by-frame. Parameters include contact angle, contact radius, left and right contact angle, and sessile drop volume. The reference distance is taken from the syringe needle outer diameter.

In order to compare the contact radius of each sample, the base radius measurements must be normalized using the volume measurement. By solving the volume equation of a sessile drop for the base radius (solved radius) and dividing the measured radius by the solved radius. This deunitizes the radius measurement. Figure 4.5 shows the normalized base radius vs. time for each sample roughness.

The main feature of the plot is the decreasing maximum radius as roughness increases. This is an expected outcome because n-octane has infiltrated the gaps of the rough samples. The probe droplet kinetically entraps the n-octane in the gaps since the triple-line spreading is propelled from peak-to-peak. However, the gap the water droplet must cross increases with greater surface roughness. This effectively slows the triple-line motion as roughness increases. The speed of the triple-line movement can be interpreted from the changing slope of the base radius curve. The sessile drop stops spreading when the radius remains constant. As the roughness decreases, spreading speed increases since a higher radii are reached in less time. The exception to this

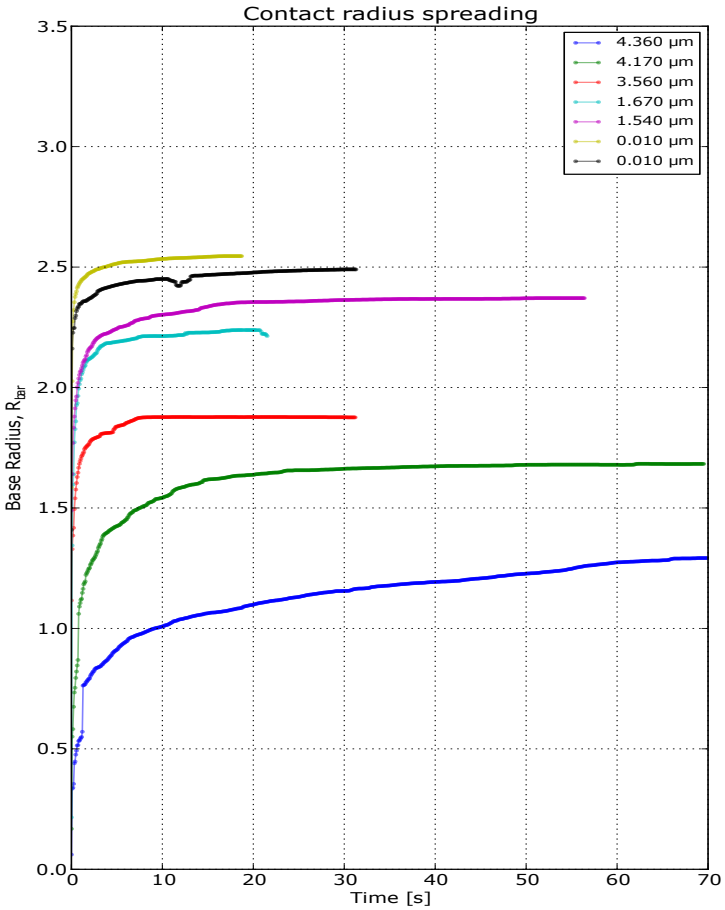

Figure 4.5: This plot shows the deunitized base radius of initially dropped sessile drops vs. time. The samples are polycrystalline $Fe_{81}Ga_{19}$ for a range of roughnesses created by sandblasting different media shown in Table 4.1.

is the R_a =3.560 μm sample where the spreading speed to a stable radius surpasses that of the $R_a = 1.540\mu$m samples. This may be due to the impact crater left by the 36 grit SiC compared to garnet and silica.

This crater difference can be examined through the hardness of each sandblasting media. The hardness of silica is 6-7, garnet is 6.5-7.5, and SiC is 9-10 on the Mohs hardness scale. The greater hardness of SiC will cause more FeGa material to be removed after sandblasting compared to lower hardness media like silica and garnet. The same concept applies for general grinding/polishing procedures. Polishing pads

with higher hardness media will grind away more material than lower hardness media given the same surface.

The R_a =3.560 μm sample was the only sample that was sandblasted with SiC only, yet it had one of the highest contact angle spreading speeds. I postulate that due to the greater hardness of SiC, the surface topography increased in roughness but spike gaps are very wide. The 36 grit SiC grit removed more FeGa material than the 20 grit silica, even though the 20 grit silica is larger in volume. This is because of the higher hardness of SiC compared to silica. However, in removing more sample material, the surface topography has larger gaps rather than shorter and taller gaps. Figure 4.6 shows a digram of this concept. The right illustration is the postulated surface created by the 36 grit SiC sandblast media. Surface # 1 has more dramatic rises and drops than surface # 2. However, it possible for both surfaces to have the same average roughness, R_a, if the peaks are of the same amplitude. This means R_a does not fully describe the surface topography for each surface. Unfortunately, the profilometer used to measure these roughness parameters only measured R_a and these differences are only revealed in our contact angle spreading analysis. Comparing the two surfaces in a contact angle spreading scenario, sample # 2 will have higher contact angle spreading speed because there is a higher surface area of exposed sample. To clarify with Figure 4.2, since $x_1 < x_2$ the sessile droplet will adhere to surface #2 much quicker than surface #1. The roughness of sample #2 is "flatter" than the roughness of sample #1.

This observation of faster contact angle spreading on samples with greater x-components of roughness spikes (as defined in Figure 4.6) has important implications

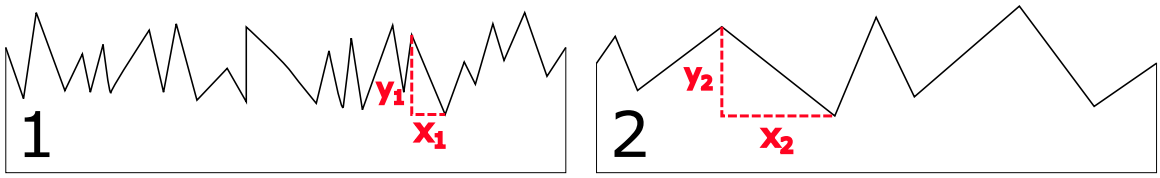

Figure 4.6: These are illustrations of two samples with similar roughness values but different topographies. It is assumed that the values shown have the following relationships: $y_1 \approx y_2$ *and* $x_1 < x_2$.

for the next steps of this investigation. As mentioned previously, the goal of this chapter is to create a surface with a controlled roughness via patterning. Figure 4.1 shows the ideal pattern geometry for this investigation where Galfenol pillars have flat tops and perpendicular pillar walls. If such a geometry can be experimentally achieved, the sessile drop spreading should be sufficiently fast because of the high degree of flatness on the pillar tops. This makes sense because a high area of FeGa is exposed at the pillar tops. If the probe droplet approaches normal to the surface, *i.e.*, the pillar tops, the resulting sessile drop will more likely wet to the pillar tops rather than the pillar walls. The sessile droplet has even less chance to wet the pillar walls (*i.e.*, penetrate the gaps of the pillared surface) when factoring in the presence of a bulk water-immiscible liquid containing the entire system.

Figure 4.7 shows the left and right contact angle evolution over time along with the contact angle rate of change for the roughnesses in Table 4.1. Observing the θ_C vs. time plots, there is a clear increase in the minimum (or equilibrium) contact angle for both left and right contact angles as the roughness increases. The $d\theta_C/dt$ vs. time plots reveal the same trend of an increased contact angle spreading speed for SiC sandblasted samples. The two samples sandblasted with SiC media were the 36 grit SiC sample ($R_a = 3.56\mu$m) and the 8-12 grit garnet + 36 grit SiC ($R_a = 4.17\mu$m).

The contact angle spreading speed ($d\theta_C/dt$) increased from garnet-only sample to the garnet+SiC sample, and even more so with the SiC-only sample. Again, this is likely a matter of a higher hardness sandblast media leaving a larger impact area on the target, thus a greater x-component of the area is exposed. We now see a successive trend in Figure 4.7 where the garnet+SiC sample saw a slight increase in contact angle spreading speed and the SiC-only sample dramatically increased in contact angle spreading speed.

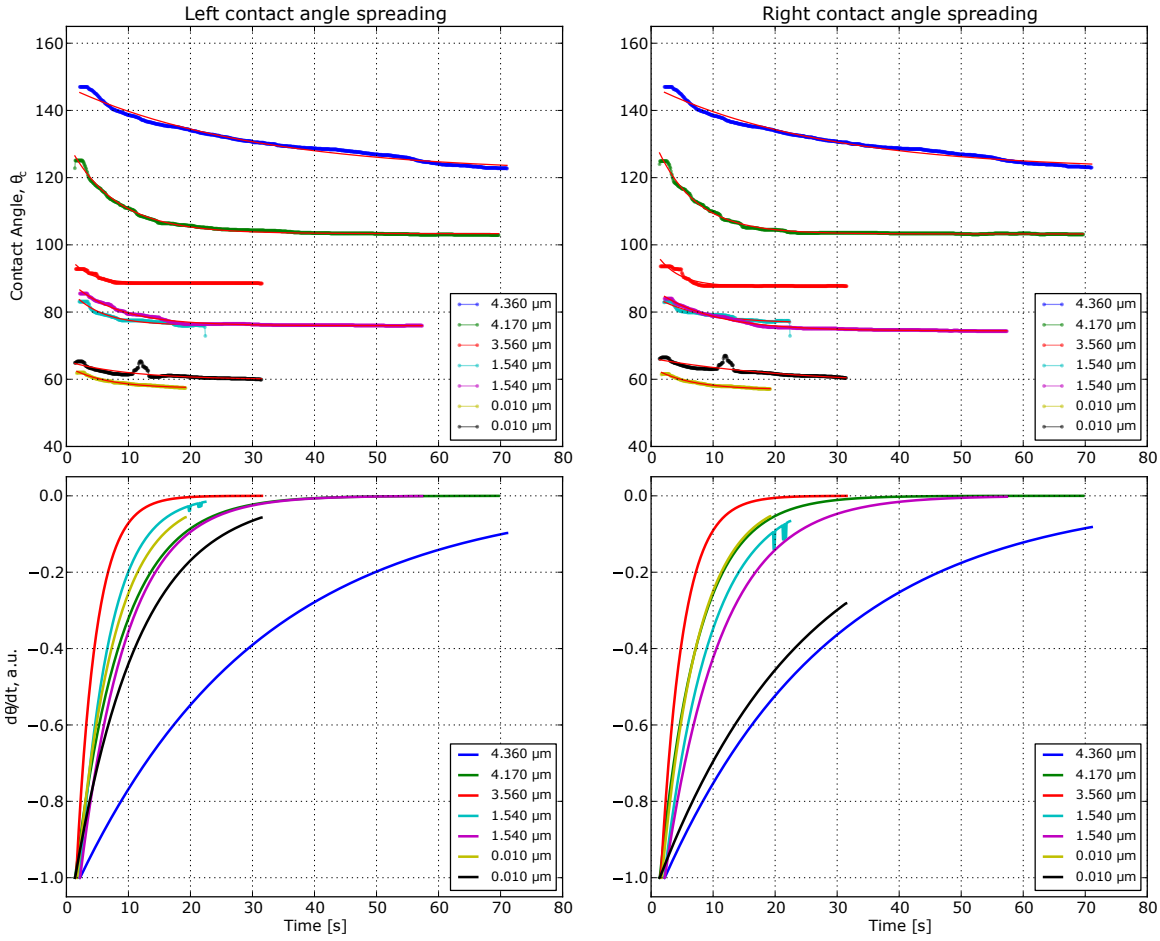

Figure 4.7: These plots show the contact angle change as well as the contact angle rate of change with time for the left and right contact angles. The samples are polycrystalline $Fe_{81}Ga_{19}$ for a range of roughnesses created by sandblasting different media shown in Table 4.1.

A flatter (higher x-component exposed surface area) surface topography will in-

crease spreading speed of a sessile droplet on a plasma-treated Galfenol, or any metal, surface in a two-liquid-phase contact angle experiment. If a patterned Galfenol surface was created with flat-topped pillars, the spreading speed should be high enough to kinetically trap any n-alkane in the gaps and achieve a strict Cassie-Baxter state. This will allow for proper back-calculation of flat-surface contact angle, or Young contact angle, for surface energy measurements on metals. The next section seeks to determine the procedure for creating such a well patterned surface on Galfenol.

4.3 Patterning FeGa by ion milling

Concurrently, I investigated options for patterning Galfenol surfaces using chemical and physical etching processes. The goal of this etching process is to create gap depths of at least 1 μm and maximum gap widths on the order of 10 μm. Polymers can be very easily etched due to their weak chemical bonds and low mechanical strength. Metals are much stronger materials with very strong metallic bonds, making etching very difficult. Considering the definition of surface energy, the amount of energy required to create a new surface on the material, destroying the surface of a metal, a very high surface energy material ($> 1000\text{mJ/m}^2$), is much more energy-costly than a low energy surface like polymer materials ($< 100\text{mJ/m}^2$). Most etching procedures can only hope to effect micron sized roughness levels at metal surfaces. A number of chemical etching processes were carried out, with the help of Thomas Loughran at the UMD Nanocenter FabLab, on samples of Galfenol including Nital, diluted nitric acid, stock hydrochloric acid, piranha solution, etc. Unfortunately, none were able to

etch the surface significantly enough to be implemented as a milling procedure.

The next investigated methods for patterning are all physical etching processes. There are a number of instruments that can controllably etch the surface of a metal, one of which is a focused ion beam (FIB). University of Maryland's AIM lab is fortunate to have two Tescan FIBs that use xenon or gallium as the plasma source. These focused ions have a beam size of approximately 100nm. Using the Xe source there will not only be a higher impact momentum due to a larger atomic weight than Ga, there will be little to no chemical reaction with the FeGa surface because it is an inert gas. However, the time required to etch hundreds of 10μm gaps to a 1μm depth in a 5x5cm area would take over 12 hours to accomplish, costing over $1200 per run. Therefore, the FIB option for physically etching Galfenol patterns is completely inefficient in both time and cost.

Another option available to the Aerosmart group through our collaborations within the University of Maryland community is a high-powered ion mill in the Center for Nanophysics and Advanced Materials (CNAM) operated the Takeuchi Group in the Department of Materials Science and Engineering. This ion mill exclusively uses an argon source to bombard surfaces with a $\sim$500W, 5 in beam.

To test the effectiveness of the ion mill on metals, two samples of (1 0 0) silicon wafers coated with 1813 and 4620 photoresist. The following procedure was used to apply photoresist to the silicon. Silicon wafers were first coated with a common adhesion promoter, HMDS, which chemically bonds its Si atom to the oxygen of oxidized surfaces, accompanied by the release of ammonia (NH_3). The methyl groups of the HMDS fragment thereby form a hydrophobic surface and thus improve resist

wetting and adhesion. This covers the silicon wafer, sits for 5 s, and is then spun for 40 s at 3.05×10^3 rpm. The photoresist is then dropped carefully in the center of the wafer at about a 3 cm diameter, and then spun again for 40 s at 3.05×10^3 rpm. Coated samples are then air-dried overnight to allow the photoresist to dry while retaining an elastic. Conventional photoresist processing would have the user quickly dry the resist on a hot plate, where in a matter of minutes the photoresist will harden and be immediately ready for UV exposure through a photomask with a desired pattern. The hardness of the photoresist after hot plate drying is relatively high compared to air drying, thus in an ion mill designed to physically destroy a surface through impact force, the harder photoresist will wear away quicker than the softer photoresist. Consider a steel ball colliding with a brick wall as opposed to colliding with a sponge at a velocity, v, and coming to a full stop. This system can be described using the concept of impulse, the product of an average force and the time it is exerted. Equation 4.4 expresses this relationship in integral form,

$$\int F dt = m\Delta v \tag{4.4}$$

where F is the impact force, m is the mass of the steel ball, Δv is the change in velocity during the time of collision. Assuming the final velocity is zero and integrate over an average force F_{avg}, Equation 4.4 can be written as:

$$F_{avg}\Delta t = mv_0$$

where Δt is the time of collision, and v_0 is the velocity upon collision. Considering the two situations described above, the impact of the ball on the brick wall will take less time than the impact on the sponge. Since the mass and velocity upon impact of the steel ball do not change, if the time of impact increases the average impact force will decrease. Thus an impact of the Ar ions on a softer photoresist will impart less force and remove less material.

Alternatively, this can be explained considering the greater amount of photoresist material left after an overnight drying as opposed to a quick hard-bake. A hard-bake will quickly remove any solvent from the spun photoresist, leaving a thin and hard resist layer. An overnight dry maintains solvent in the resist layer for a long period of time so that when the resist dries, it maintains solvent molecules that would have been otherwise baked out. By the fact that there is more material for the ion mill's Ar ions to ablate, it will take more time to wear away the photoresist that has been dried overnight. Therefore, the overnight drying process will be used to apply the photoresist.

The 1813 photoresist is more readily available and has a thickness of $\sim 2\mu$m when spin coated using the specified procedure. The 4620 photoresist is slightly more expensive due to greater viscosity, and a spin coated thickness of $\sim 13\mu$m. To obtain a pattern after completely coating FeGa samples with photoresist, the UMD FabLab offers two options. Electron lithography can etch very fine patterns into photoresists. Since it is most desirable to have the entirety of the well-polished sample patterned, or at least the center, the average area of patterning is 5x5cm. For electron lithography, etching this area size would take over 24 hours, thus it is

completely unfeasible. Photomasks simply block out UV light during an exposure based on the desired pattern. It is a highly common and reliable technique, and it is suitable for our experimental needs. The photomask used for this test consisted of an array of circles with decreasing size, as seen in Figure 4.8, where the diameters ranged from 10-520μm. After spin coating and drying, the photoresist is exposed to deep UV light for 60s and then developed in a CD-26 developer to remove the exposed resist. The particular mask used in this experiment helps identify the limits of both the UV exposure instrument and the photoresists themselves. Observations show that the larger circles, 200-500μm, retain some photoresist for the 4620 case, Figure 4.8b, which is not of much concern since the planned feature sizes for the patterned Galfenol surface will only reach 100μm.

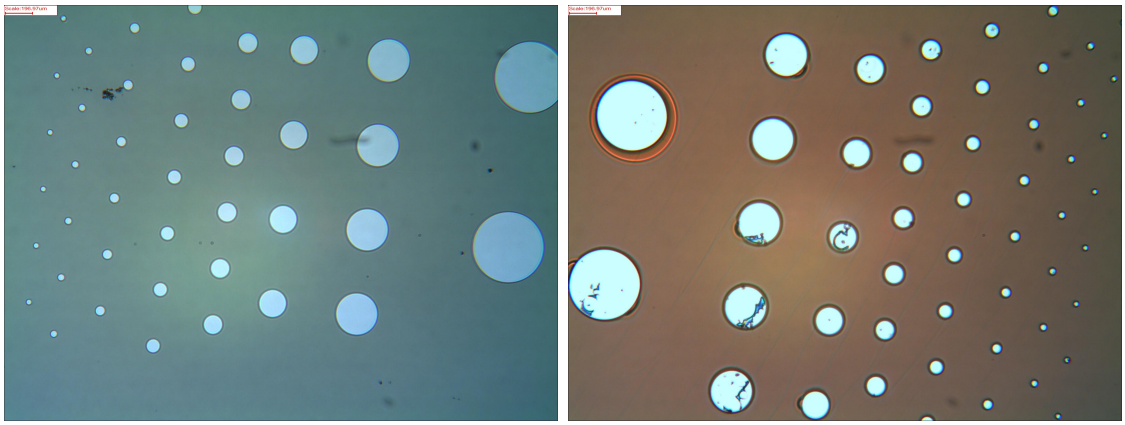

(a) *(b)*

Figure 4.8: (a) This is an image from an optical microscope observing 1813 photoresist after UV exposure using a photomask of smaller and smaller circles. (b) The same mask and exposure on 4620 photoresist.

Both 1813 and 4620 coated silicon wafers were processed in the CNAM Ion Mill for a single 40 minute run. Figures 4.9a and 4.9b show the starting thickness of the 1813 and 4620 coatings to be 2.000μm and 12.10μm, respectively, according to profilometer

measurements. After ion mill exposure, the etch rates of Si, overnight-dried 1813, and overnight-dried 4620 were calculated using thickness measurements obtained using a tilted-stage SEM. The silicon etch rate for the CNAM Ion Mill with an Ar source is 8.4 nm/min. This is consistent with the SOP manual, thus we can confirm that the machine is well calibrated. The thickness of the air-dried 1813 after milling is 1.6μm, giving an etch rate of 10 nm/min. The thickness of air-dried 4620 after milling is 11.8μm, giving an etch rate of 7.5 nm/min. Since the 4620 resist has a lower etch rate than 1813 it will last longer in the ion mill. The 4620 also has a much greater thickness than the 1813. This is beneficial for ion mill etching because there will be a higher edge slope on the photoresist. This means that there will be a high slope in the etched metal edge that approaches an ideal 90° edge, as seen in Figure 4.9d. Approaching an ideal 90° edge will allow for less error in theoretical approximations of a flat contact angle from the engineered patterned roughness depicted in 4.1. For these reasons, the air-dried 4620 photoresist procedure was chosen as the best coating for Galfenol in the ion mill.

The next step in analyzing the proper photoresist procedure was applying the 4620 to well-polished Galfenol and etching it in the ion mill to find the etch rate. Figure 4.10a shows a sample of polycrystalline Galfenol with half of the surface coated with 4620 photoresist. Photoresist was applied using a cotton swab. Figure 4.10b shows the same sample after 40 mins in the ion mill. The non-uniform photoresist coverage caused by cotton swab application resulted in air pockets forming in the high temperatures of the ion mill. This will not be a problem when the photoresist is applied using spin-coating and then post-baked to remove any such air pockets.

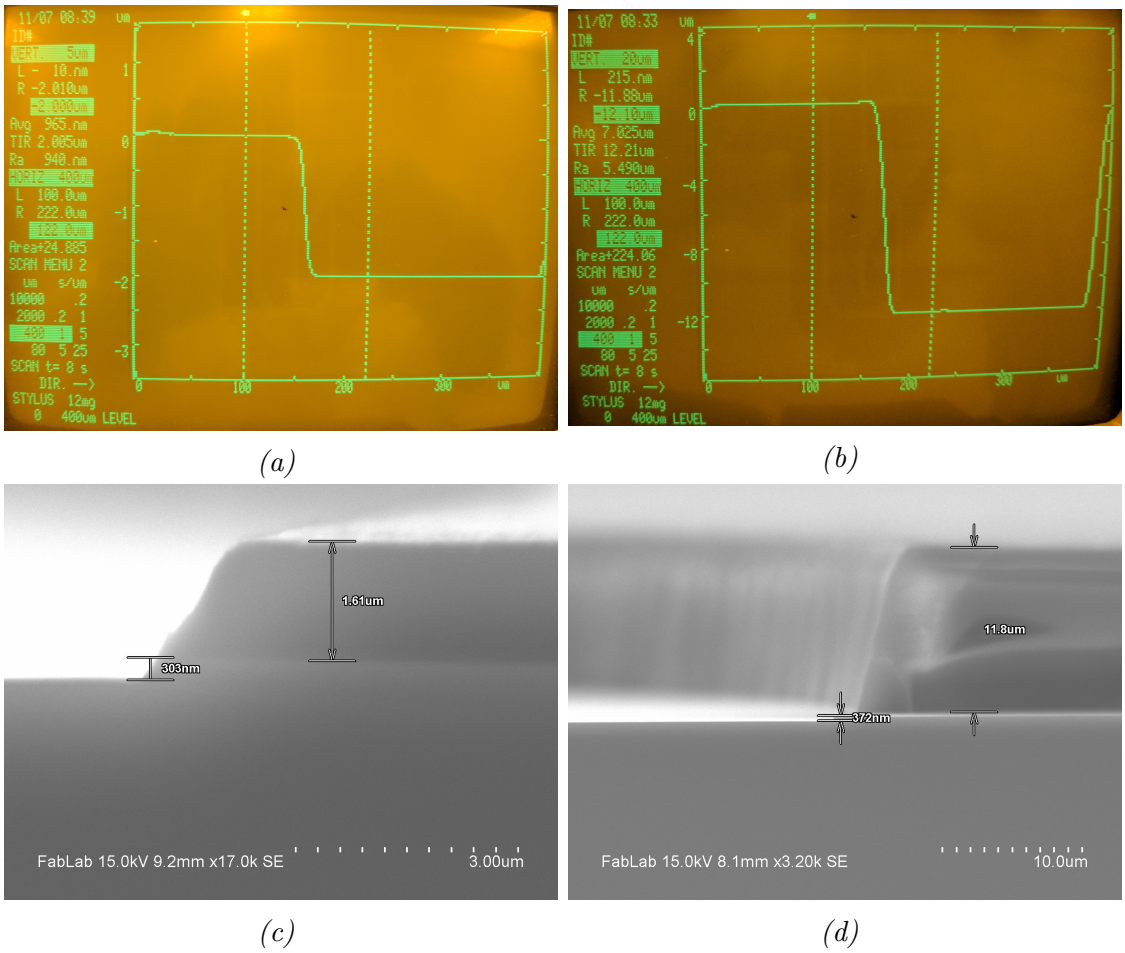

Figure 4.9: (a,b) These are images from a profilometer observing 1813 and 4620 photoresist patterns from Figures 4.8a and 4.8b, respectively, before milling. The step height is 2 µm and 12 µm. (c,d) Same patterns of 1813 and 4620 from (a,b), respectively, seen on profiles in an SEM. 1813 photoresist thickness is 1.61µm after milling and milled Si depth is 303nm. 4620 photoresist thickness after milling is 11.8µm and milled Si depth is 372nm.

Figure 4.10c shows the photoresist removed from the sample revealing a clear color distinction between the milled, left side of sample, and protected, right side of sample, surface resulting from the roughness difference in the two sections.

Using AFM, the step height of the milled Galfenol was measured to be 320 nm after a 30 min ion mill exposure. This means that the etch rate of polycrystalline Galfenol is 10.5 nm/min. Polycrystalline Galfenol will likely have a lower etch rate than single crystal Galfenol due to a greater hardness in polycrstalline Gafenol. This

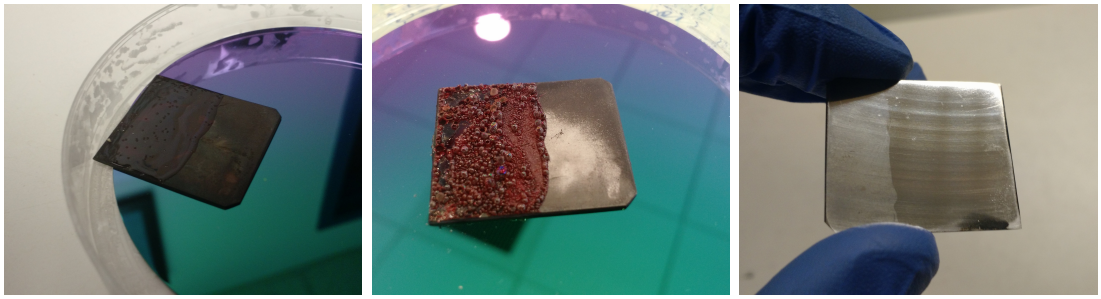

(a) (b) (c)

Figure 4.10: These are photographs of a polycrystalline Galfenol sample coated with 4620 photoresist on approximately half of the surface. The three images show the sample: (a) after overnight air-drying of photoresist, (b) after 30 min Ar ion mill exposure, and (c) after stripping the photoresist from the samples surface.

is a common notion given the grain boundary hardening undergone by any polycrystalline material compared to single crystal counterparts (no grain boundaries). It is also worth noting that the roughness dramatically increases after ion mill exposure. Figure 4.11c shows that the milled section from 0 to 3μm has a greater roughness than the protected section from 3.5 to 8.5μm. The retention of flatness on the protected section is an excellent result for the future contact angle experiments on patterned surfaces as surface finish is just as important as it was for the flat-surface experiments in Chapter 3. For nearly-flat, plasma cleaned Galfenol surfaces in Chapter 3 (R_a < 1nm), the time required for a sessile drop to reach a stable contact angle, t_{spread}^{FeGa} < 0.03s, was much faster than that of a native oxide surface on FeGa, $t_{spread}^{oxide} \approx$ 23s. This decrease in equilibrium spreading time is greatly attributed to removing the native oxide layer combined with the sub-nanometer roughness. Figure 4.5 shows a that as roughness decreases on Galfenol, the spreading speed increases.

The increased roughness of milled sections, which will be the gaps of patterned surfaces, could aid in preventing wetting of the probe droplet between gaps. It is

known that an increase in surface roughness on a desired surface will increase the contact angle of a specific probe liquid. This phenomena was investigated in Section 4.2. This further increases the chances of stabilizing a Cassie-Baxter state for the probe water droplet. Again, a Cassie-Baxter state is useful for increasing the contact angle on the very high energy surface of a metal. A water droplet will likely completely wet a very high energy surface, thus giving no quantifiable information of the surface.

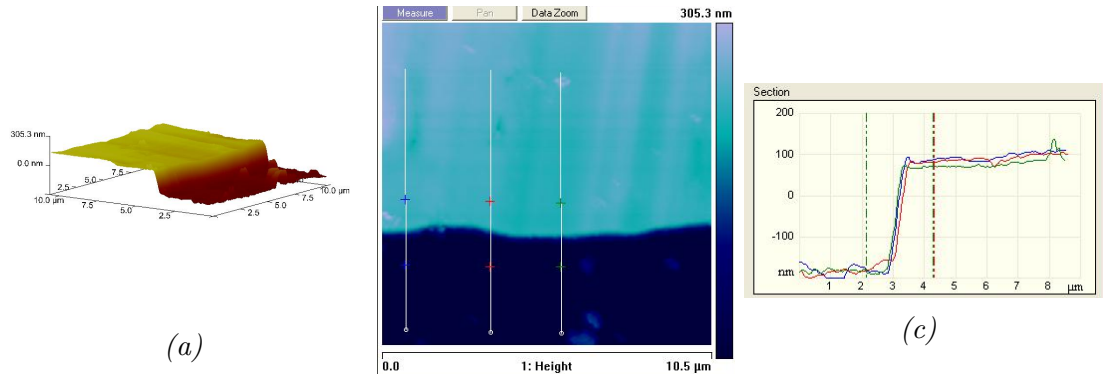

(a) *(b)* *(c)*

Figure 4.11: This is an AFM study of a 10.5x10.5µm area on the ion milled polycrystalline Galfenol depicted in Figure 4.10c. (a) A 3D map of the area. (b) A height contour map of the scanned area with section lines that are shown in (c).

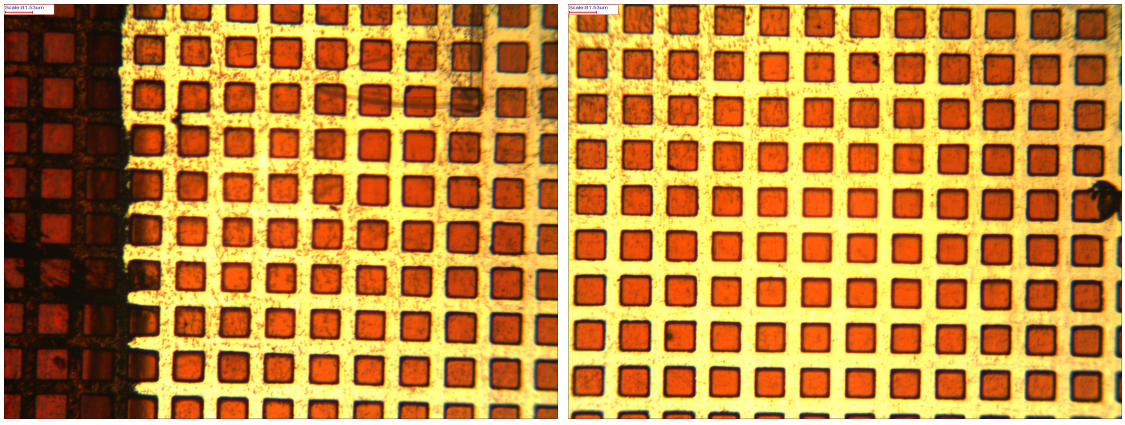

(a) *(b)*

Figure 4.12: (a) This is an image from an optical microscope observing 1813 photoresist after UV exposure using a photomask of smaller and smaller circles. (b) The same mask and exposure on 4620 photoresist.

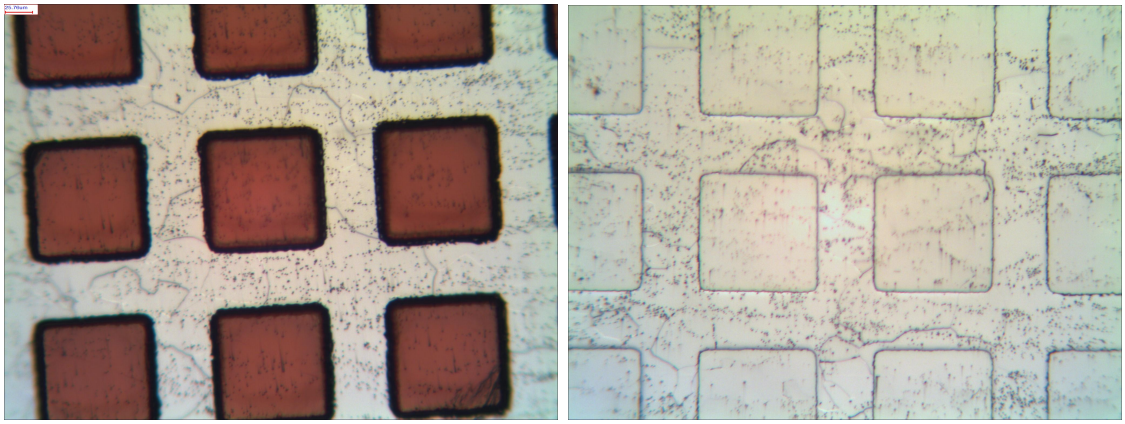

(a) (b)

Figure 4.13: (a) This is an optical image of 4620 photoresist square array ($a = 110\mu m$ and $b = 50\mu m$) on polycrystalline FeGa after ion milling for 2 hours. (b) Photoresist removed, square patterns retain sharp edges with rounded corners arrays have gap depths of 1.5 μm.

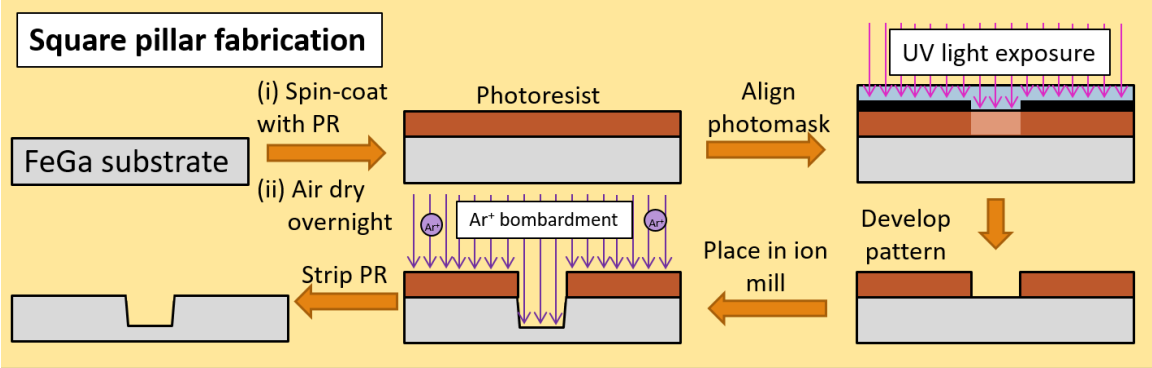

Figure 4.14: This is a diagram of the photolithography process used to pattern a Galfenol surface.

Figure 4.14 shows a schematic of the final patterning process on any Galfenol surface in this study.

4.3.1 Contact angle measurement on patterned surfaces

Figure 4.15 shows an increase of $\sim 10^{\circ}$ in static contact angle from the polished flat FeGa surface. This contact angle increase is clearly indicative of a Cassie-Baxter state in some form based on the fact that any amount of bulk liquid trapped in the

gaps under the sessile drop will cause a contact angle increase. Equation 3.4 can be

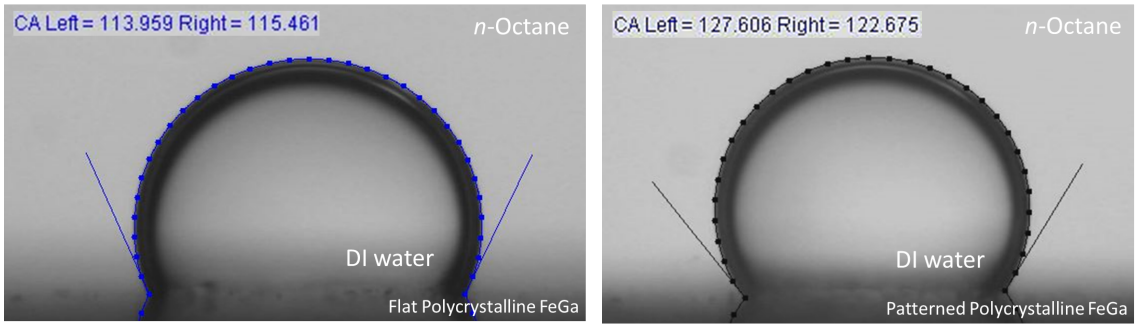

(a) *(b)*

Figure 4.15: (a) This is a snapshot and contact angle measurement of a static water sessile drop on flat polished polycrystalline FeGa in an n-octane environment. Average static contact angle $\approx 114°$*. (b) The same experiment, but now the surface is patterned with square pillars where* $a = 110\mu m$ *and* $b = 50\mu m$*. Average static contact angle* $\approx 125°$*.*

rewritten to approximate the amount of n-octane trapped under the sessile drop:

$$\cos\theta_{CB} = \Phi_{octane}\cos\theta_{octane} + (1 - \Phi_{octane})\cos\theta_Y \tag{4.5}$$

where Φ_{octane} is the surface fraction of octane entrapped beneath the drop, θ_{CB} the Cassie-Baxter contact angle on the rough surface, θ_{octane} the contact angle of water on octane, $(1 - \Phi_{octane})$ the surface fraction of Galfenol substrate and θ_Y the Young contact angle on th smooth Galfenol surface. Octane and water are immiscible liquids, therefore the contact angle between octane and water is taken to be 180° and $\cos\theta_{octane} = -1$. Since colloidal silica polishing can obtain an average roughness of 1.5 nm, see Figure 2.3, we approximate the polished Galfenol surface in Figure 4.15a as an ideally flat surface. Now we consider the obtained contact angles from Figure 4.15 in Equation 4.2, where $\theta_{CB} = 125°$ and $\theta_Y = 114°$, the surface fraction of octane entrapped beneath the drop, Φ_{octane} is 28%.

There is excessive water penetration into the gaps of the patterned polycrytalline FeGa ($a = 110\mu m$ and $b = 50\mu m$). For this reason, the Cassie-Baxter equation cannot be used to extract the flat surface (Young) contact angle. The next section will use patterned roughness models in conjunction with Cassie-Baxter favoribility equations to determine the proper pattern geometry to achieve a Cassie-Baxter mode. This is mainly a geometric model and does not consider the bulk-liquid environment or kinetic trapping caused by high surface energy materials.

4.4 Model of patterned surface

4.4.1 Modeling surface geometry for Cassie-Baxter favoribility

Work backwards from theoretic surface energy values to approximate flat surface contact angles in *n*-alkane environments

Cassie-Baxter favoribility

The Cassie-Baxter favorability equation is from Milne *et al.*[12] for a contact angle $> 90°$. It is derived following a differential energy balance similar to Bico *et al.* to form a general stability criterion as a function of f_1, f_2, and r, defined in Equations 3.3 or 3.4. It is re-derived here for the two-liquid-phase contact angle method, starting with the general Cassie-Baxter equation. Consider Figure 4.16 sessile drop on a well-patterned surface that forms a contact angle. There is a small displacement along

the contact line, dx. The change dF in surface energy per unit length associated with

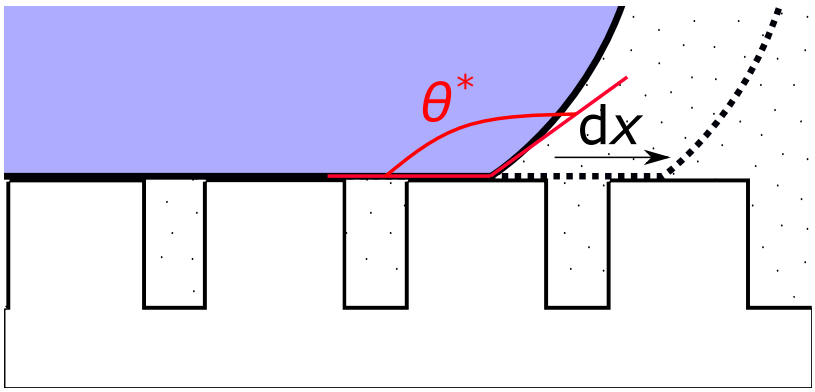

Figure 4.16: This diagram shows a sessile drop spreading on a patterned surface in a Cassie-Baxter state. The contact angle in this Cassie-Baxter state is θ^*. The triple-point advances by a distance dx. The solid white area is the solid, the striped blue area is the probe liquid L_1, and the dotted area is the bulk liquid L_2.

the displacement dx is written as:

$$dF = f_1(\gamma_{SL_1} - \gamma_{SL_2})dx + f_2\gamma_{L_1L_2}dx + \gamma_{L_1L_2}dx\cos\theta^* \tag{4.6}$$

where f_1 is the fraction of solid underneath L_1 and f_2 is the fraction of L_2 underneath L_1. Now using Youngs equation ($\gamma_{SL_2} - \gamma_{SL_1} = \gamma_{L_1L_2}\cos\theta_Y$) and minimizing dF ($\frac{dF}{dx} = 0$), we reveal the general Cassie-Baxter equation:

$$0 = -f_1[\gamma_{L_1L_2}\cos\theta] + f_2\gamma_{L_1L_2} + \gamma_{L_1L_2}\cos\theta^*$$

$$\cos\theta^* = f_1\cos\theta - f_2 \tag{4.7}$$

It is worth noting that the surface energy terms drop out from this equation. This means that the Cassie-Baxter is a purely geometric effect of the surface topography.

However, Chapter 3 found a clear difference in spreading speed and contact angle when a Galfenol surface is plasma-cleaned vs. passivated. Experimentation will show the validity of this statement.

The same process is used to derive the Wenzel equation, where the roughness factor r is the ratio of the actual sample surface area to the projected surface area:

$$dF = r(\gamma_{SL_1} - \gamma_{SL_2})dx + \gamma_{L_1L_2}dx\cos\theta^*$$

$$\rightarrow 0 = -r[\gamma_{L_1L_2}\cos\theta] + \gamma_{L_1L_2}\cos\theta^*$$

$$\cos\theta^* = r\cos\theta \tag{4.8}$$

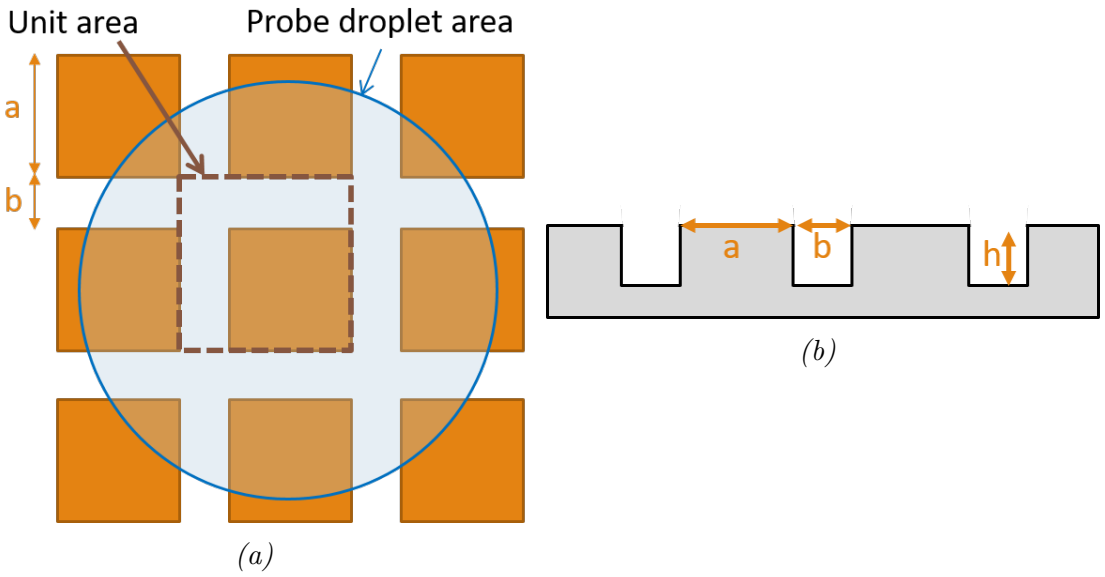

Figure 4.17: Schematics of the pattern geometry that will be modeled for Cassie-Baxter state stability. (a) Top view of the pattern with an overlay of the sessile droplet that will probe the surface. The pillar width is a and the gap width is b (b) Side view of the pattern. The pillar height is h.

A stability criterion can be extracted by equating Equations 4.7 and 4.8 and solving for $\cos\theta$. This model does not account for a state where there is partial gap

penetration, or a CB and Wenzel mixed state. The resulting condition for a stable Cassie-Baxter state is shown in Equation 4.9.

$$\cos\theta < \frac{-f_2}{r - f_1} \tag{4.9}$$

According to the stability criterion, the surface must be hydrophobic enough for the pockets of L_2 to be stable. The geometric quantities f_1, f_2, and r can be calculated if a sample is patterned with a well-defined geometry. The following section will attempt to create such a well-patterned surface experimentally. Before fabrication, this stability criterion will be modeled to find the most capable geometry for stabilizing a Cassie-Baxter state. Again, a Cassie-Baxter state will cause an increase in the contact angle on plasma-cleaned Galfenol. The Cassie-Baxter angle will then be used to calculate the flat surface contact angle to be compared with the most-stable contact angles measured in Chapter 3.

The square pillar design will continue to be the main geometry studied. Figure 4.17 shows the ideal geometry of the patterned Galfenol surface. The parameters f_1, f_2, and r for this geometry are shown below:

$$f_1 = \frac{a^2}{(a+b)^2} \tag{4.10}$$

$$f_2 = \frac{(a+b)^2 - a^2}{(a+b)^2} \tag{4.11}$$

$$r = \frac{(a+b)^2 + 4ah}{(a+b)^2} \tag{4.12}$$

The Cassie-Baxter equation (Equation 4.7)is shown in a flat contact angle θ vs. observed contact angle θ_{obs} plot. The flat surface contact angle values in three n-alkane environments (n-octane, n-decane, n-hexadecane) measured on (1 0 0) single-crystal $Fe_{82}Ga_{18}$ are plotted as horizontal lines on the CB equation plots as a target observed contact angle. A vertical line is placed at $\theta_{CB} = 90°$ since θ_{obs} must be $> 90°$. The CB equation is kept above 100° to allow for a wider margin of experimental error.

The Cassie-Baxter favorability (Equation 4.9) equation is shown in an observed contact angle vs. pillar height plot. This plot contains two dashed lines that create a $\pm 2\sigma$ margin of error area around the blue CB favorability curve. Any gray area on the CB favorability plot signifies a stable CB state for that geometric configuration. The white region will result in a Wenzel state. The critical contact angle θ_{cr} is the contact angle where the Wenzel and CB state are equally likely.

Each plot showcases a specific pattern geometry (*i.e.*, a and b are defined). The first dimensions were chosen to be roughly an order of magnitude lower than the dimensions chosen in Section 4.3 since the . Figure 4.18 shows a theoretical geometry of $a = 19.3\mu$m, $b = 10.0\mu$m. The table inlay for the CB favoribility shows θ_{cr} and $\pm 2\sigma$ margin of error at a pillar height of $h = 1.5\mu$m. This is the maximum gap depth achieved through ion milling on Galfenol in Section 4.3. The blue curve on the CB equation plot shows all θ_{obs} values above the 90° threshold. In fact, this geometry is very far from this threshold as the lowest θ_{obs} value is $\sim 115°$, hence the initial

condition is not at risk of being violated. As the observed contact angle increases, the difference between the calculated flat contact angle and the observed contact angle decreases. The CB-stability plot is less promising as $\theta_{cr} = 152.6°$ at $h = 1.5\mu$m and the predicted θ_{obs} of the three n-alkane environments are $< 130°$. The pillar-gap width ratio (a/b) is 1.163 for this configuration. Adjusting this ratio will modify the limits of both plots. The gap width b is changed first.

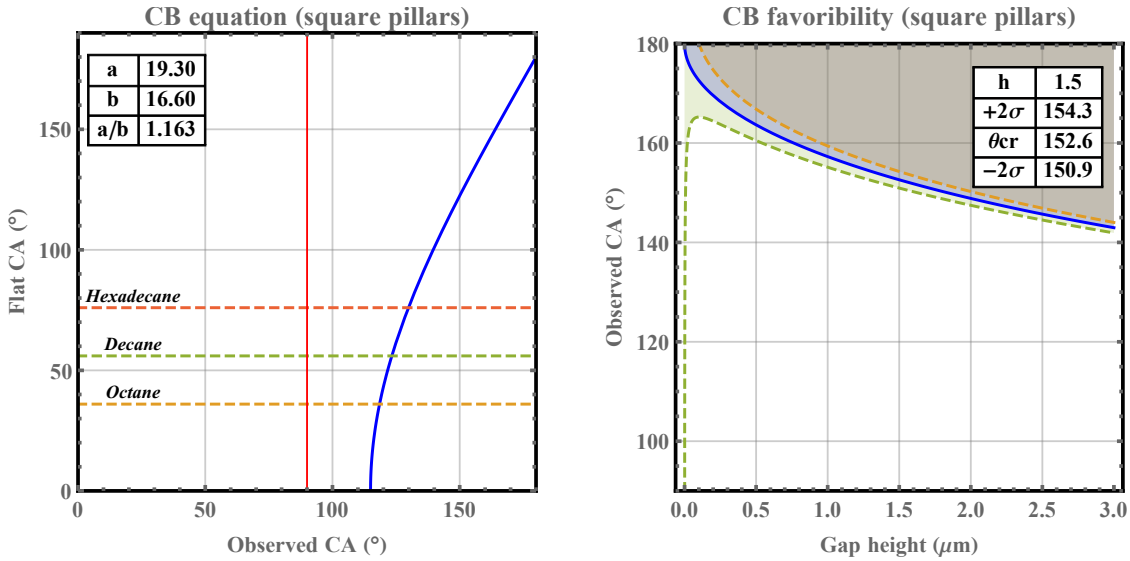

Figure 4.18: Cassie-Baxter favorability and Cassie-Baxter equation for a square pillar geometry of specific dimensions, a (pillar width) and b (gap width). These plots show the geometry of $a = 19.3\mu m$ and $b = 16.6\mu m$.

Figure 4.19 adjusts the parameters to $a = 19.3\mu$m and $b = 6.8\mu$m. While the grey area of CB favorability increases with the a/b ratio (θ_{cr} at $h = 1.5\mu$m decreased to 136.7°), the CB equation curve has dropped below the $\theta_{CB} = 90°$ line specifically for the n-octane case. A Cassie-Baxter state nearly impossible if the water contact angle in n-octane drops below 90°. There is a balance that must be reached where the CB equation stays above 90° and the CB favorability area is sufficient large (*i.e.*, θ_{cr} is

sufficiently low).

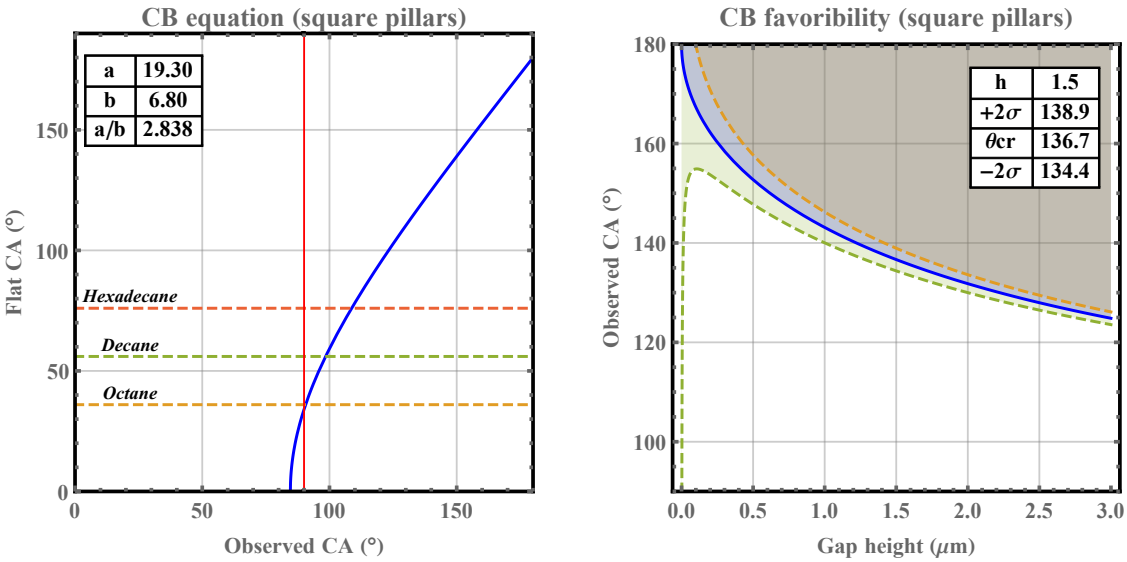

Figure 4.19: Cassie-Baxter favorability and Cassie-Baxter equation for a square pillar geometry of specific dimensions, a (pillar width) and b (gap width). These plots show the geometry of $a = 19.3\mu m$ and $b = 6.8\mu m$.

This balance seems to be achieved ratio of $a/b \approx 1.66$ where $a = 19.3\mu$m and $b = 12.0\mu$m. Figure 4.20 shows the predicted θ_{obs} for n-alkane environments to be $105° < \theta_{obs} < 133°$. This clears the 90° threshold with $\approx 10°$ of error built-in. A ratio of $a/b \approx 1.66$ will be maintained for all geometries going forward. The CB favorability plot shows $\theta_{cr} = 147.0°$ at $h = 1.5\mu$m, which is still too high for a CB state to be achieved in any of the n-alkane environments shown. At this point, both the pillar width and gap width will be lowered (while maintaining $a/b = 1.66$) to increase the likelihood of a CB state.

Figure 4.21 shows a pattern geometry of $a = 1.0\mu$m and $b = 0.6\mu$m. The predicted contact angle range for the n-alkane environments remains at $105° < \theta_{obs} < 133°$, which shows how the CB equation is completely determined by the ratio a/b for this

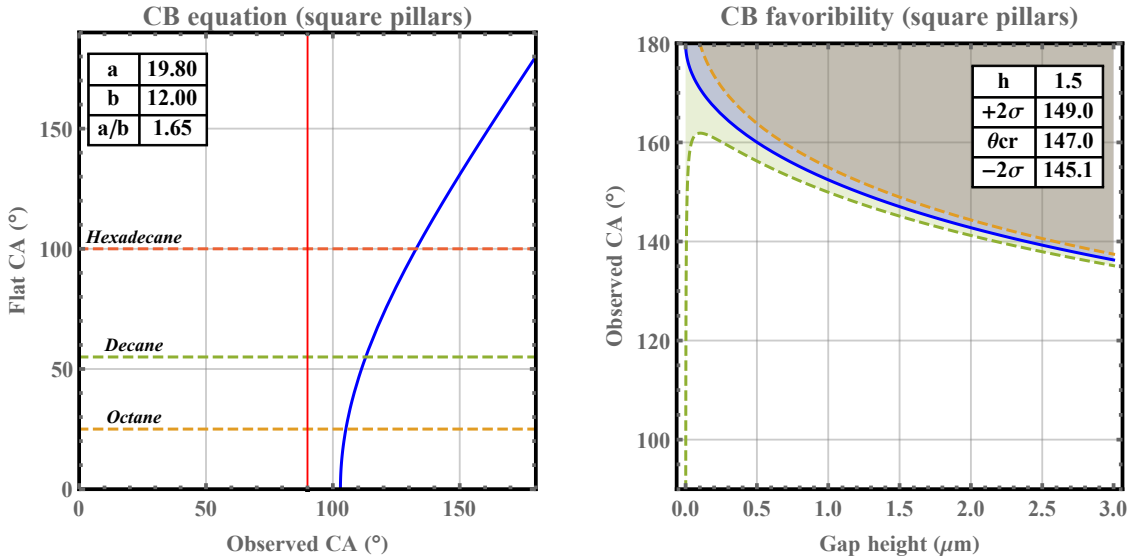

Figure 4.20: Cassie-Baxter favorability and Cassie-Baxter equation for a square pillar geometry of specific dimensions, a (pillar width) and b (gap width). These plots show the geometry of $a = 19.8\mu m$ and $b = 12.0\mu m$.

square pillar geometry. The CB favorability plot shows a dramatic decrease in θ_{cr} where the value at $h = 1.5\mu$m is $\theta_{cr} = 101.9°$. Hence, any $\theta_{obs} > 101.9°$ will likely be in a CB state for this configuration. The next section attempts to fabricate such a patterned Galfenol surface with this geometry in mind.

4.5 Experimental single micron features

In order for such small features ($a = 1\mu$m, $b = 0.6\mu$m)to be fabricated in comparison to the large features in Section 4.3 ($a = 110\mu$m, $b = 50\mu$m), the photolithography process must be slightly altered. This specifically concerns the low photomask resolution and the large area of patterning. Fabricating photomasks with single micron features is difficult because the laser writers used to create photomasks cannot resolve sub-micron features. Electron beam techniques are usually used in sub-micron

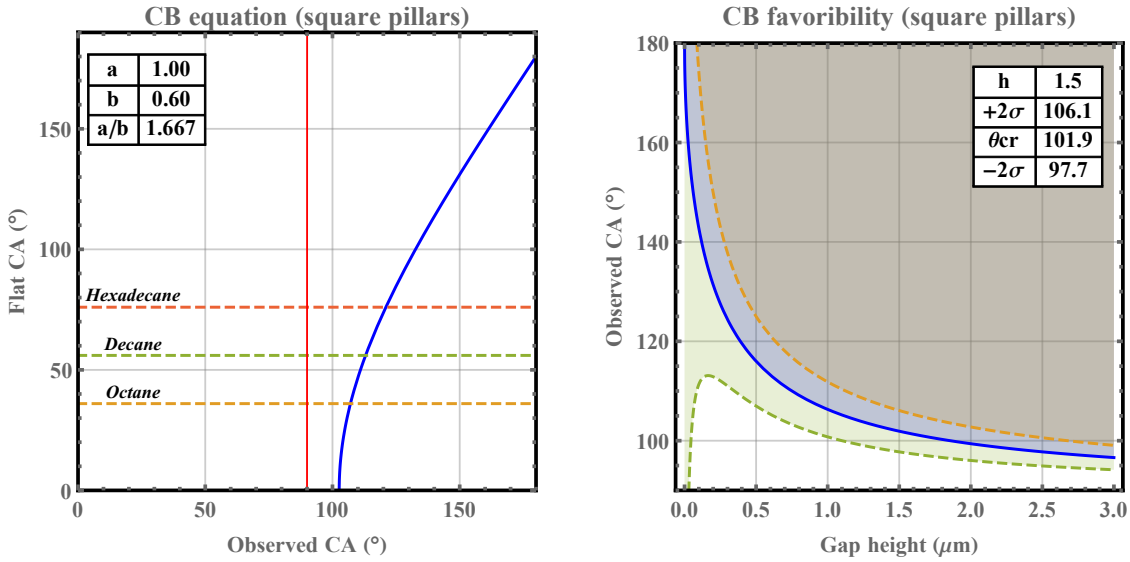

Figure 4.21: Cassie-Baxter favorability and Cassie-Baxter equation for a square pillar geometry of specific dimensions, a (pillar width) and b (gap width). The greatest height attained through ion milling is h = 1.5 μm. These plots show the geometry of a = 1.0μm and b = 0.6μm.

situations. However, our mask size is approximately 1/4x1/4in. The e-beam fabrication time would be over 12 hours (according to multiple sources) and cost thousands of dollars in work time. Mylar photomasks, like the one used in Section 4.3, has a feature size limit of $\sim 10\mu$m.

For these reason, multiple solutions were attempted to decrease the photomask resolution while keeping fabrication time and cost down. The first involved 3D printing techniques on the University of Maryland campus. A 3D pinter can be used to directly print a photoresist on to the sample surface. TerrapinWorks has two micron resolution 3D printers. The Nanoscribe Photonic Professional GT is a laser lithography system allowing 3D printing of true 3D microscale and nanoscale based on two photon polymerization in UV-curable photoresists. The Nanoscribe has the capability to print nanometer scale features, which is more than enough for the di-

mensions discussed above. Unfortunately, the array of squares we wish to fabricate ($\sim 20,000x20,000$ squares) is too great for the Nanoscribe software system to handle. The system would take too long to fabricate this mask before potentially crashing, and the super-users were not willing to take that risk. The nScrypt 3Dn-300HP enables high resolution multilayer deposition of nanoparticle inks and slurries supporting the fabrication of advanced 3D structures, including ceramics. Using the nScrypt, I attempted to print a general purpose photoresist, SU-8, on vibratory polished Galfenol coated with a water-soluble Dextran solution for mask lift-off. The printed lines were supposed to be $< 10\mu$m, but the low roughness caused high wetting of the SU-8 on the Galfenol surface. This resulted in $> 20\mu$m thick lines, which is far higher than our desired dimensions.

The main problem I found with this size limit issue was the gap in photolithographic techniques at the single to sub-micron level. Generally speaking, sub-micron features over large areas ($> 1x1$mm) are either too small to resolve for large-area laser writers or too large-area for e-beams or nanoprinters to complete in a timely and cost-efficient way. This is the case with many scalability issues in science. It is unfortunate that I have neither the time nor resources to address this problem, at the moment. I am forced to increase the feature size of my pattern in order to meet the resolution requirements of a laser writing device to produce a high quality Chromium photomask.

The photomask dimensions were increased to $a = 3.8\mu$m and $b = 1.9\mu$m to meet fabrication specifications and maximize CB state favoribility. Figure 4.22 shows the CB equation and CB favorability for this geometry. The critical contact angle has

increased by $\sim 15^\circ$ to $\theta_{cr} = 116.2^\circ$. This decreases the chance of a CB state, but it is still experimentally possible. This surface is fabricated and measured with the two-liquid-phase method after plasma cleaning.

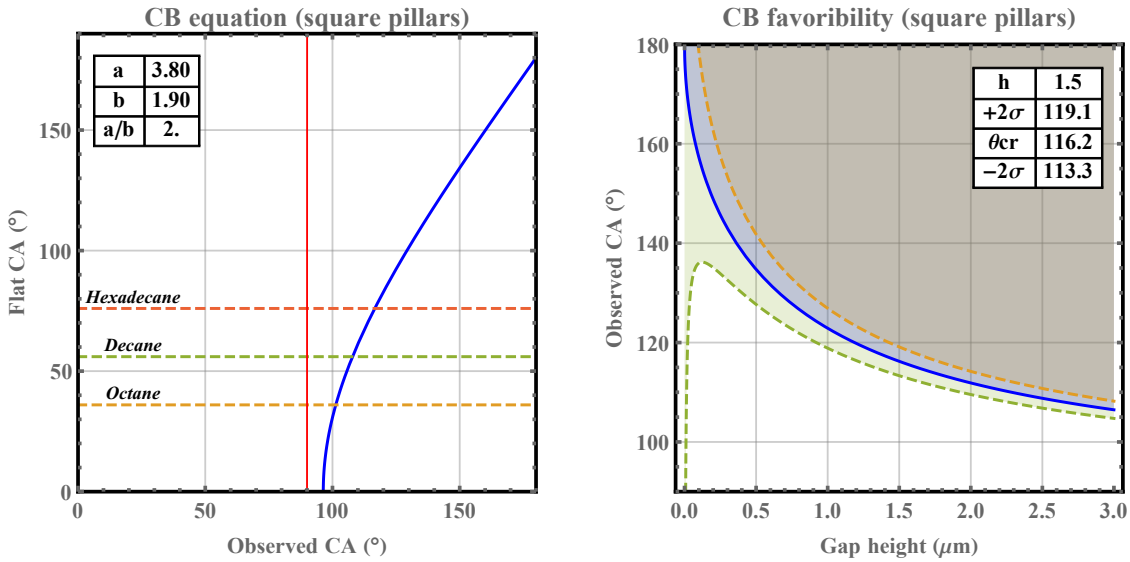

Figure 4.22: Cassie-Baxter favorability and Cassie-Baxter equation for a square pillar geometry of specific dimensions, a (pillar width) and b (gap width). The greatest height attained through ion milling is $h = 1.5\ \mu m$. These plots show the geometry of $a = 3.8\mu m$ and $b = 1.9\mu m$.

Single crystal (1 0 0) $Fe_{82}Ga_{18}$ was first polished according to Table 3.2. The sample area is $\sim$ 0.7cm in diameter, so it must be kept in a mount for polishing as well as for photolithography. This is because a small sample could break the glass photomask by creating a concentrated force during the photomask contact. By increasing the sample area with a mount, the pressure is distributed more evenly. The photoresist application had to be modified to accommodate the smaller photomask geometry. The 4620 and 1813 photoresist used in Section 4.3, even when development times were modified, could not be optimized to produce a crisp pattern, as seen in Figures 4.23a and 4.23b.

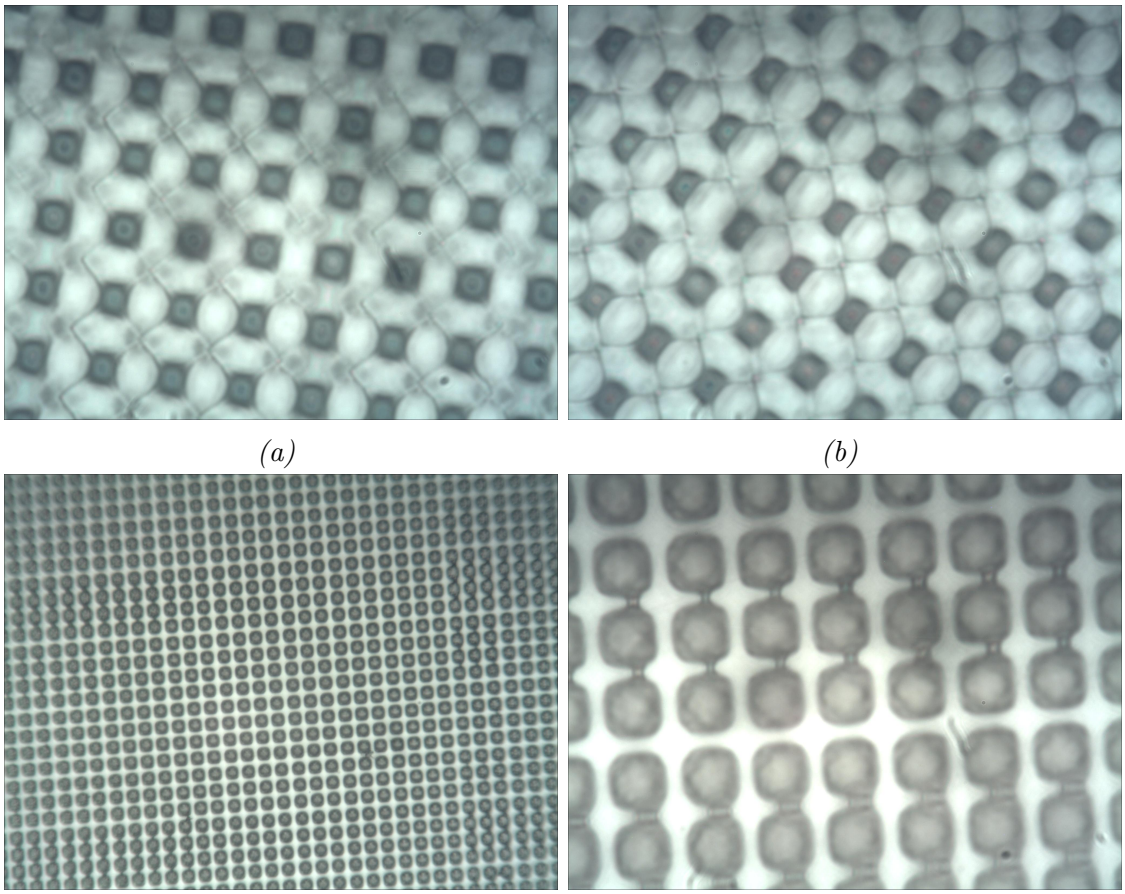

Figure 4.23: (a,b) Both images are from an optical microscope observing 1813 photoresist on single crystal $Fe_{82}Ga_{18}$ after 9s UV exposure using a photomask of a square array where $a = 3.8\mu m$ and $b = 2\mu m$. (a) Development time is 30s. (b) Development time is 20s. (c,d) Images from an optical microscope observing 1818 photoresist on single crystal $Fe_{82}Ga_{18}$ after 19s UV exposure using the same photomask. Development time is 35s. (a) Magnification 50x. (b) Magnification 150x.

New photoresists were applied and the best results came from 1818. The recipe went as follows:

1. Spin coat sample starting at 500 rpm, ramp to 4000 rpm, spin for 40s.
2. Softbake in oven (due to sample being enclosed in a low thermal conduction thermoset, Polyfast) at 90°C for 45 mins.
3. Expose on UV mask aligner with full contact for 19s.

4. Develop for 35s.

The main result is shown on an optical microscope at 50x and 150x in Figures 4.23c and 4.23d. The 50x image shows high uniformity in the pattern. The 150x image shows slight abnormalities in the PR pattern where some gaps are visibly larger than others and some PR squares are not fully developed. Since the sample area is oblong and not completely level, the photomask contact was not fully uniform or fully in contact with the mask. This is problematic for UV exposure on a photomask because diffraction can occur on the edges of the mask pattern. Diffraction will cause uneven exposure on the PR. This can lead to sloped edges, irregular PR thicknesses, and/or joined features after development. The photomask itself may even have some small irregularities present due to being at the limit of the laser writing system. It is clear that some gaps between square features are larger than others, and it is not likely caused solely by UV diffraction. Since this sample was the best developed after a few weeks of trial and error, I moved forward with ion mill patterning, as outlined in Figure 4.17.

In Section 4.3, it took three 45 min runs on the Ar ion mill to a produce 1.5μm depth on polycrystalline FeGa. For this single crystal (1 0 0) $Fe_{82}Ga_{18}$ sample, a single 40 min run produced a $\sim 2\mu$m depth. This increased etching depth is likely due to the decreased hardness from polycrystalline FeGa to single-crystal FeGa. This both decreases the critical contact angle required for a CB state and decreases processing time of patterned metal samples in future tests.

Figures 4.24(a,b) and (c,d) show SEM images of the patterned surface located at

the center area and outside area of the sample, respectively, after ion milling. We observe some joining of the pillars between gaps, which is expected from the imperfect photolithography process.

An interesting observation is the difference in PR coverage in the center of the sample vs. the outside of the sample. Figures 4.24(a,b) show pillars from the center of the sample with fully covered and uniform pillar tops. Figures 4.24(c,d) show pillars from the outside area of the sample with a cross pattern on the pillar tops. The non-uniform pattern can mostly be attributed to the non-uniform contact with the photomask at the UV exposure stage. The pillar top dimensions at the sample center and outer sample are 3.277x4.133μm and 3.226x3.761μm, respectively. The equivalent square pillar width is $a = 3.68\mu$m for the sample center pillars and $a = 3.48\mu$m for the outer sample. Contact angle measurements will be performed at the center of the sample since the pillar tops are the most flat and uniform.

The AFM scan of this patterned surface at the center of the sample is shown in Figure 4.25. The height contour map shows two sectioning profile lines that are shown in Figure 4.25b. There is a definitive difference between these two gaps when they should be equal in width. Profile 1 has a width of 2.1μm and Profile 2 has a width of 2.58μm. The maximum pillar height is $\approx 2.2\mu$m.

From the SEM and AFM measurements, we can enter an approximate pillar width (a), gap width (b), and pillar height (h) into our CB favorability model to estimate the critical contact angle for a CB state at the center of this sample. The CB equation and CB favoribilty are plotted in Figure 4.26 using the equivalent square pillar dimension of $a = 3.68\mu$m, the average gap width of $b = 2.34\mu$m, and the average pillar height

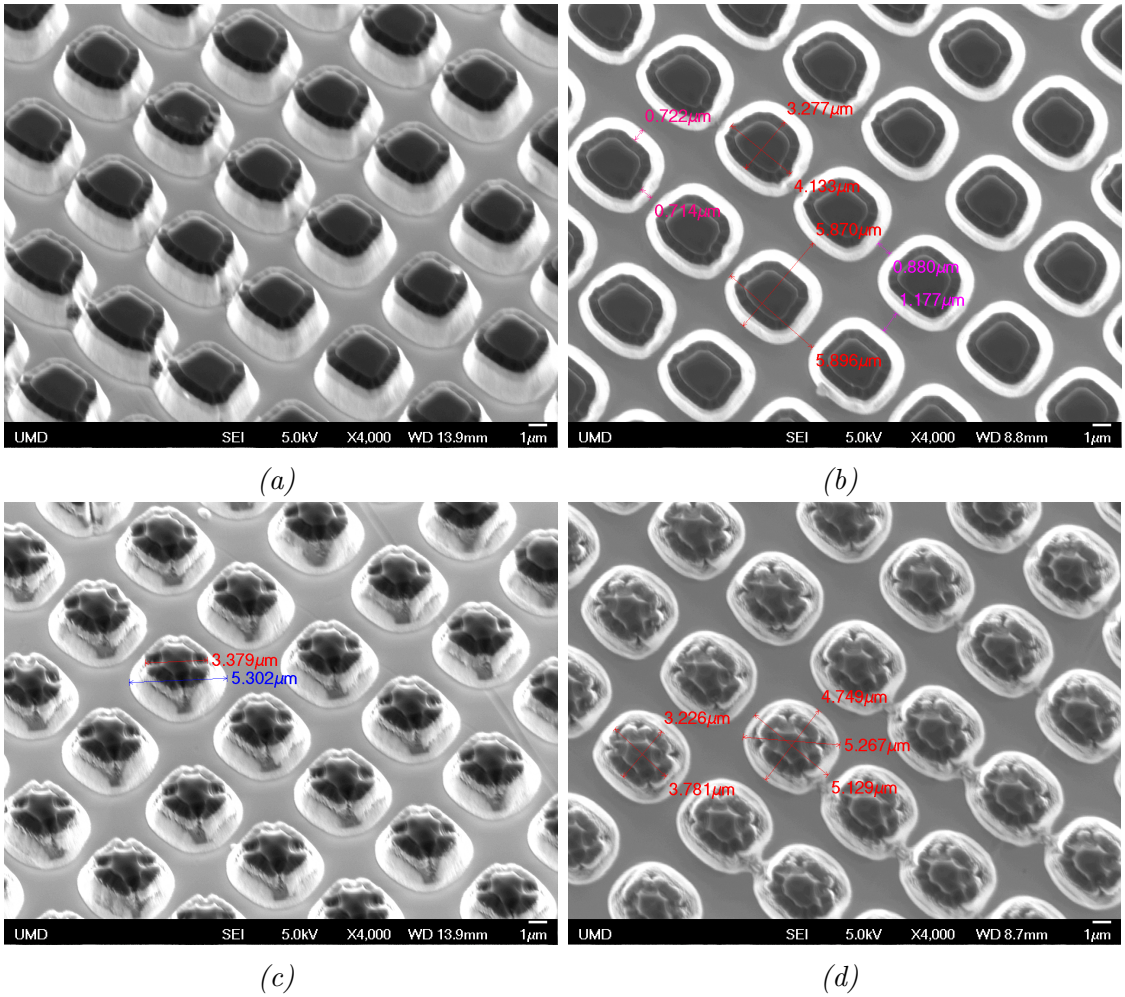

Figure 4.24: (a,b,c,d) SEM images of patterned single crystal (1 0 0) $Fe_{82}Ga_{18}$ *at different angles. (a,b) Located at the center of the sample. (c,d) Located on the outside of the sample.*

$h = 2.2\mu$m. According to our model, while the gap width has increased $\theta_{cr}(h = 1.5)$ to $\sim$120.5°, the greater gap height of $h = 2.2\mu$m decreases θ_{cr} to 114.3°. This is 1.9° lower than the originally predicted θ_{cr} in Figure 4.22 at $h = 1.5\mu$m.

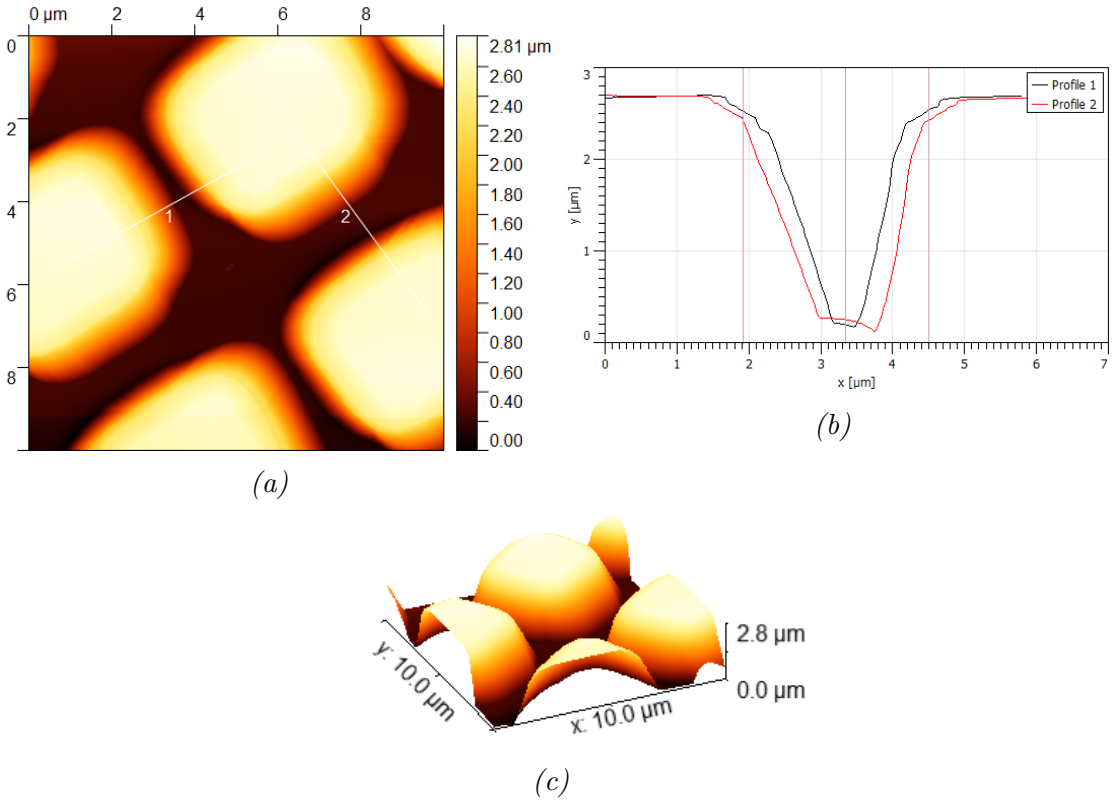

(a)

(b)

(c)

Figure 4.25: These are AFM scans of single crystal (1 0 0) $Fe_{82}Ga_{18}$ *after ion milling. The 1818 photoresist is still present on the square features. The scan area is 10 µm x 10 µm. (a) Height map with sectioned lines. (b) Profile of sectioned lines in (a). (c) A 3D plot of surface topography.*

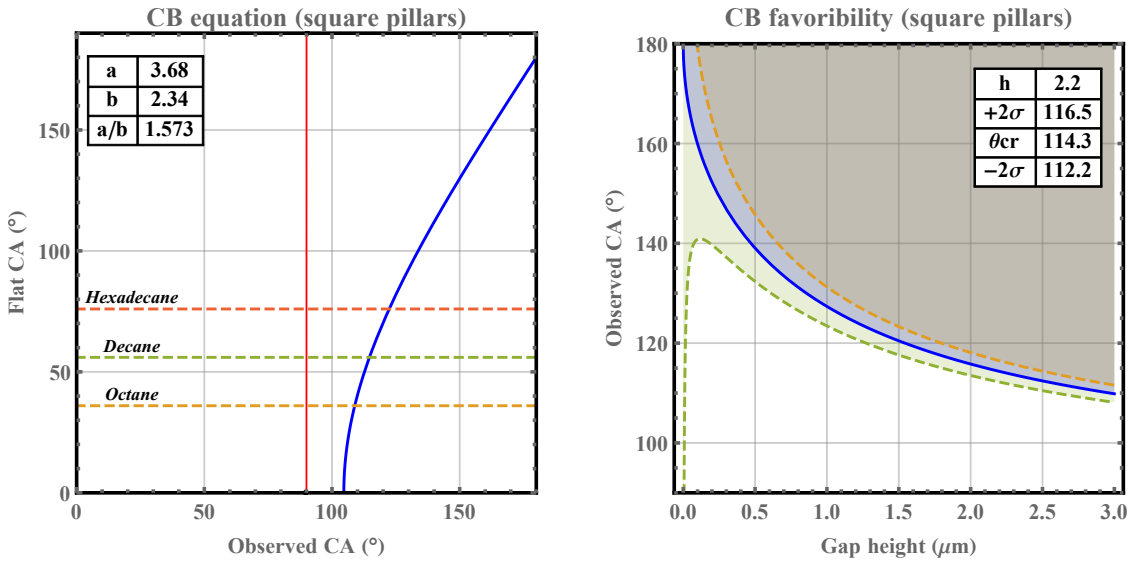

Figure 4.26: Cassie-Baxter favorability and Cassie-Baxter equation for a square pillar geometry of specific dimensions, a (pillar width) and b (gap width). The maximum pillar height by ion milling is h = 2.2 μm. These plots show the geometry of a = 3.68μm and b = 2.34μm.

Contact angle measurement

The sample was cleaned with a 100W Ar exposure for 5 mins on, 5 mins off, and 5 mins on again. This is different from the normal operation as the Branson Barrel Resist Stripper had been malfunctioning at the time due to overheating. After plasma-cleaning, the sample was quickly placed in a vial of n-decane under a nitrogen purge. The sample had to sit in the vial for 5 hours to ensure full penetration of n-decane into the gaps.

The probe water droplet was placed on the patterned sample and the resultant sessile drop reached equilibrium within 3 s. This is a good sign of oxide removal on a rough surface, as we observed in Section 4.2. However, the resultant contact angle averaged over 10 measurements is $\theta_{obs} \approx 89.0 \pm 1.5°$. Figure 4.27 shows one contact angle measurement of a water sessile drop on the patterned Galfenol surface immersed in n-decane. This contact angle is just below the required 90° threshold needed to assume a Cassie-Baxter state. It is likely that this sessile drop is in a mixed Wenzel/CB state where there is partial penetration of the water into the gaps. According to Equation 4.2, the sessile drop penetrates $\sim 36\%$ into the gaps.

Attempts have been made to further observe the sessile drop penetration experimentally, specifically using a confocal microscope similar to how Butt *et al.* did on superhydrophobic polymers.[138] The main issue with applying this technique to a metal is the opaque nature of any metal. Light for the objective lens of a standard inverted confocal microscope will shine through a transparent or translucent polymer. At this point a profile image at multiple depths can be created. For an opaque

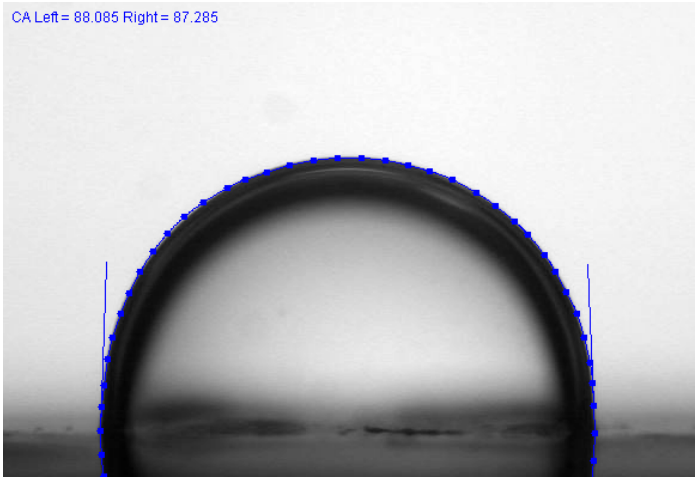

Figure 4.27: This is an image of a water sessile drop on single crystal $Fe_{82}Ga_{18}$ patterned with square pillar array of geometry $a \approx 3.68\mu m$ and $b \approx 2.34\mu m$. The bulk liquid environment is n-decane. The contact angle measured is $\sim 87.7°$.

metal surface, the light path of the objective lens must be diverted to approach the sample from the top. This is achieved with an objective inverter successfully on this patterned surface under the expertise of Amy Beaven, the Director of the Imaging Core in the Department of Cell Biology and Molecular Genetics. However, when this experiment was attempted with a contact angle on the surface while contained in *n*-decane, the microscope lens was too far from the sample surface to resolve a profile image. If the lens were brought closer, it could have contaminated the lens and ultimately not image anything.

Conclusions

The patterned surface was not able to increase the contact angle of the water sessile drop in *n*-octane above the threshold contact angle required for a favorable Cassie-Baxter state. The sessile drop in *n*-octane likely spread into pattern gaps for a number of reasons including the sloped pillar walls and inconsistent patterning across

the sample surface. The sloped pillar walls allowed the spreading contact line to spread into the gaps more easily as opposed to an ideal straight vertical pillar wall (perpendicular to the surface). Spreading contact lines on a high-energy surface have a greater chance to kinetically trap the bulk environment in the gaps if the pillar walls are completely vertical. This is consistent with the spreading dynamics study in Section 4.2 where rough surfaces with lower sloped features had faster spreading speeds. Water more favorably wet such surfaces with lower sloped features, hence their spreading speeds increased. It is difficult to understand the exact wetting dynamics of the water droplet on this patterned surface since we cannot directly observe the sample. Confocal microscopy was the most viable option for this observation, but was unsuccessful due to instrument limitations.

There are a number of adjustments that could be made to experimentally increase the observed contact angle and raise the chance of achieving a CB state. The photolithography process must first be improved. Most UV aligners are not designed for UV exposures on small samples as they tend to break the photomask when full contact is made between mask and sample. The metal sample could potentially be mounted in a large area mount to distribute the pressure evenly, thus allowing for even contact to be created. Even contact can eliminate any diffraction effects on the resulting pattern, as well as create well-defined perpendicular edges on the desired features. The photoresist application process can be constantly tweaked with respect to softbake times, exposure times, development times, etc. to guarantee optimal feature profiles.

The plasma-cleaning process could also be improved regarding the transfer of

samples into vials. A glove bag purged with nitrogen could encapsulate the plasma cleaner door during transfer. The entire plasma cleaning system could be moved into a nitrogen glove box. Unfortunately, the time required to optimize this experiment is beyond the timeline of this dissertation. It is my hope that another researcher in the future will use my investigation as a baseline for the project they are executing.

Chapter 5

Conclusion

This dissertation studied experimental contact angle methods for determining crystal-orientation-specific surface energy values of metals. The contact angle methods consisted of the gallium drop method, flat surface two-liquid-phase method, and patterned surface two-liquid-phase method. Results from the gallium drop method showed contact angle trends that qualitatively agreed with orientation surface energy calculations from the broken-bond model. As with water sessile drops, expected surface energy trends on different crystallographic surfaces from theoretical studies matched the trends of our experimental measurements. However, surface energy values of (1 0 0), (1 1 0), and (1 1 1) $Fe_{82}Ga_{18}$ facets were two orders of magnitude greater than expected theoretical calculations. Error in the gallium drop method came from gallium corrosion of the Galfenol and oxide passivation on the Galfenol surface.

To overcome error introduction due to oxide formation, a two-liquid-phase contact angle approach was implemented in conjunction with Ar plasma surface cleaning methods. This was done by quickly placing the Ar plasma-cleaned in the secondary

liquid under a nitrogen purge. Results using this approach were of the expected order of magnitude and again the expected trend for different crystallographic methods. A third approach using patterned surfaces was attempted, but was not successful. This study did reveal interesting wetting dynamics of water on plasma-cleaned Galfenol in n-octane for varying roughness values and topographies.

Contributions

This dissertation has made a number of contributions to the fields of surface science, abnormal grain growth, and wetting dynamics.

- Created a new contact angle measurement technique in the gallium drop method. In its current state, this method qualitatively measures the surface energy of targeted metal crystal facets.
- Optimized sample preparation processes for a non-destructive metallic surface energy measurement. Processes include sub-nanometer roughness polishing, oxide removal through plasma-cleaning, and sample isolation for maintaining a bare metal surface.
- Measured the highest recorded surface energy using a contact angle method, 1003 mJ/m^2 for (1 0 0) $Fe_{82}Ga_{18}$.
- Successfully measured the surface energy of a sulfur-contaminated Goss-textured Galfenol sample. Experimentally proved that sulfur-contamination decreases the surface energy of (1 1 0) Galfenol facets.
- Expanded on total energy abnormal grain growth model using experimentally

measured surface energy values of (1 0 0), (1 1 0), and (1 1 1) $Fe_{82}Ga_{18}$ facets.

- Measured and analyzed water spreading dynamics on plasma-cleaned Galfenol of varying roughnesses in a two-liquid-phase method. Spreading speed decreased and contact angles increased with an increase in roughness. Surface topography also greatly influenced spreading speed.
- Developed a surface patterning process for Galfenol. This uses standard photolithography methods and physical etching using high-powered Ar ion bombardment. Found limitations of current photolithographic techniques for single micron sized features on Galfenol surfaces.

Suggestions for future work

For the gallium drop method, there may be a way to incorporate the surface energy of the gallium drop plus oxide surface layer and still use the obtained contact angles for solid surface energy measurements. A more concrete measurement of γ_{SL} between liquid gallium and solid would need to be examined, which is a very non-trivial task. These experiments have not been developed yet.

The flat-surface two-liquid-phase method could be fully realized by characterizing the surface composition after plasme-cleaning using XPS. This was attempted multiple times during the course of this research. Every time a measurement was attempted, the sample was shown to be completely oxidized. However, we know that a bare (or trace oxidized) Galfenol surface was measured based on the greatly increased spreading speed of the sessile drop after plasma-cleaning and the agreement of exper-

imental surface energy values with DFT calculations. For this reason, we believe that during transport of plasma-cleaned Galfenol to the XPS chamber (in a doubled-sealed plastic zipped bag filled with nitrogen gas), the sample is contaminated with oxygen. A solution to this would be to connect the plasma cleaner and XPS system through a vacuum line. Another option could involve transporting samples in an n-alkane (as done successfully for two-liquid-phase measurement sample preparation) to a nitrogen glove box, removing the sample, cleaning with methanol and acetone, and then transporting the sample to the XPS in a double-sealed plastic bag. A nitrogen glove box ensures transport in nitrogen, whereas the nitrogen back-fill from the plasma cleaner is not as reliable. The methanol and acetone cleaning will not likely have an effect on the surface composition as it will evaporate on the surface quickly, especially in the high vacuum of an XPS chamber.

For the patterned surface experiments, there are a number of adjustments that could be made to experimentally increase the observed contact angle and raise the chance of achieving a CB state. The photolithography process must first be improved. Most UV aligners are not designed for UV exposures on small samples as they tend to break the photomask when full contact is made between mask and sample. The metal sample could potentially be mounted in a large area mount to distribute the pressure evenly, thus allowing for even contact to be created. Even contact can eliminate any diffraction effects on the resulting pattern, as well as create well-defined perpendicular edges on the desired features. The photoresist application process can be constantly tweaked with respect to softbake times, exposure times, development times, etc. to guarantee optimal feature profiles. The plasma-cleaning process could

also be improved regarding the transfer of samples into vials. A glove bag purged with nitrogen could encapsulate the plasma cleaner door during transfer. The entire plasma cleaning system could be moved into a nitrogen glove box.

This research has the potential for extension to other systems like our whisker sensors with magnetostrictive FeAl alloys, or Alfenol. The importance of Alfenol surface energy lies in the Aerosmart Lab's need for more efficient energy harvesting materials. Goss-textured Alfenol can reach magnetostrictive constants of 184 ppm, and the elusive Cube-textured Alfenol would reach even higher magnetostriction values due to the additional direction of easy magnetic axes. An added benefit of developing a Cube texture is that it will make feasible use of magnetic field annealing to maximize performance[30,31] and thereby eliminate the need for stress annealing or use of pre-stress components in the design of devices that use these materials.[32,139] Clearly, Alfenol AGG is affected differently than Galfenol under sulfur concentrations. This must be due to the differences in orientation-dependent surface energy between Galfenol and Alfenol. Therefore, Alfenol should be measured next in the surface energy measurement process I have created.

As mentioned at the end of Section 3.3, the flat-surface two-liquid-phase process was designed to be transferable to any metal surface. The process I have developed can differentiate surface energies of metal crystal facets with as low as $\sim$20 mJ/m^2 of separation. Many crystal growth mechanisms seen in literature rely on only theoretical calculations of surface energy to drive the models. This dissertation offers a simple, repeatable, and non-destructive method to measure metal surface energies for any crystal facet the user desires. It is my hope that this rigorous process will be

used to confirm theoretical calculations of surface energy for all metals and alloys in future works.

Appendix A

Derivation of Young's Equation

Assuming an ideally flat surface

$$V_{drop} = \frac{\pi R^3}{3}(1 - \cos\theta)^2(2 + \cos\theta) \tag{A.1}$$

$$S_{LV} = 2\pi R^2(1 - \cos\theta) \tag{A.2}$$

Where S_{LV} is the surface area of the droplet liquid-vapor interface. The Gibbs free energy of a droplet is depicted in Equation A.3.

$$G = \gamma_{LV} S_{LV} + \pi(R\sin\theta)^2 \underbrace{(\gamma_{SL} - \gamma_{SV})}_{a} \tag{A.3}$$

where γ_{LV}, γ_{SL}, and γ_{SV} are the liquid-vapor, solid-liquid, and solid-vapor interaction energies, respectively. Let $a = \gamma_{SL} - \gamma_{SV}$.

Assuming the the volume of the droplet remains constant:

$$G = \left[\frac{9\pi V^2}{(1-\cos\theta)(2+\cos\theta)^2}\right]^{2/3} [2\gamma_{LV} - a(1+\cos\theta)]$$

$$\frac{dG}{d\theta} = \left[\frac{9\pi V^2}{(1-\cos\theta)^4(2+\cos\theta)^5}\right]^{1/3} 2\left[a - \gamma_{LV}\cos\theta)\right]\sin\theta$$

$$\left[\frac{dG}{d\theta}\right]_{\theta=\theta_{eq}} = 0 = a - \gamma_{LV}\cos\theta$$

$$\therefore a = \gamma_{LV}\cos\theta$$

Appendix B

Derivation of Schultz's two-liquid-phase method

B.1 Measuring dispersive solid surface energy, γ_S^D

Assuming Young's equation (Equation 1.14) can be applied to a liquid-liquid(bulk phase)-solid ($L_1 - L_2 - S$) system, and the relationship follows:

$$\gamma_{SL_2} = \gamma_{L_1L_2} \cos\theta_{SL_1} + \gamma_{SL_1} \tag{B.1}$$

In this way, γ_{SV}, which is the driving force of spreading the one-liquid-phase method that causes complete wetting on high-surface energy metal surfaces, is replaced by γ_{SL_2}, where $\gamma_{SL_2} < \gamma_{SV}$. Hence, the contact angle in this system is mea-

surable. According to Fowkes,[78] γ_{SL_1} and γ_{SL_2} are given by:

$$\gamma_{SL_1} = \gamma_S + \gamma_{L_1} - 2(\gamma_S^D \gamma_{L_1}^D) - I_{SL_1}^P \tag{B.2}$$

$$\gamma_{SL_2} = \gamma_S + \gamma_{L_2} - 2(\gamma_S^D \gamma_{L_2}^D) - I_{SL_2}^P \tag{B.3}$$

where γ and γ^D are the surface energy and its dispersive component, respectively, and $I_{SL_1}^P$ is a specific (nondispersive) interaction term that encompasses all interactions between the solid and the liquid (dipole-dipole, dipole-induced dipole, hydrogen bonds, π bonds, etc.) except London dispersion interactions.

Substituting Equations B.2 and B.3 into B.1:

$$\gamma_{SL_1} - \gamma_{SL_2} + \gamma_{L_1L_2}\cos\theta_{SL_1} = 2(\gamma_S^D)^{1/2}[(\gamma_{L_1}^D)^{1/2} - (\gamma_{L_2}^D)^{1/2}] + I_{SL_1}^P - I_{SL_2}^P \tag{B.4}$$

L_1 will signify water, L_2 as n-alkanes, and $I_{SL_2}^P$ may be considered equal to zero because the surface free energy of n-alkanes only consists of the London dispersion term. This is because n-alkanes only contain C-C and C-H atoms connected by σ-bonds, with a generic formula of C_nH_{2n+2}. C and H have very similar electronegativities of $\chi_C = 2.55$ and $\chi_H = 2.20$, respectively. This shows that all bonds in n-alkanes are non-polar, hence there are no polar interactions in n-alkanes. Our final equation is

now:

$$\gamma_W - \gamma_H + \gamma_{WH}\cos\theta_W = 2(\gamma_S^D)^{1/2}[(\gamma_W^D)^{1/2} - (\gamma_H^D)^{1/2}] + I_{SW}^P \tag{B.5}$$

In order to calculate the dispersive component of γ_{SV} for a solid surface, the water contact angle must be measured on a solid immersed in n-alkanes. By interpreting Equation B.5 as a classic linear function, $y = mx + b$:

$$\underbrace{\gamma_W - \gamma_H + \gamma_{WH}\cos\theta_W}_{y} = \underbrace{2(\gamma_S^D)^{1/2}}_{m}\underbrace{[(\gamma_W^D)^{1/2} - (\gamma_H^D)^{1/2}]}_{x} + \underbrace{I_{SW}^P}_{b}$$

B.2 Measuring polar solid surface energy, γ_S^P

Beginning with Equation B.4 in the previous section and solving for $I_{SL_2}^P$, with liquid L_1 as water (subscript W):

$$I_{L_2}^P = \gamma_{L_2} - \gamma_{WL_2}\cos\theta_{SW} - 2(\gamma_S^D\gamma_{L_2}^D)^{1/2} + C \tag{B.6}$$

$$C = I_{SW}^P + 2(\gamma_S^D\gamma_W^D)^{1/2} - \gamma_W \tag{B.7}$$

In the above two equations, the values of γ_W, γ_W^D, γ_S^D, and I_{SW}^P are available experimentally from the previous section. Therefore, measurements of γ_{L_2}, γ_{WL_2}, θ_{SW}, and $\gamma_{L_2}^D$ lead to a calculation of the polar interaction $I_{SL_2}^P$.

For calculating the polar interaction between a solid and a liquid from the polar

term of their surface free energy, a geometric-mean relation is used, shown in Equation B.8.

$$I_{SL_2}^P = 2(\gamma_S^P \gamma_{L_2}^P)^{1/2} \tag{B.8}$$

We find γ_S^P by plotting values of $I_{SL_2}^P$ vs. $\sqrt{\gamma_{L_2}^P}$ for a set of chloroalkane and nitroalkane bulk liquids with a polar component of surface tension.

$$\underbrace{I_{SL_2}^P}_{y} = \underbrace{2\sqrt{\gamma_S^P}}_{m}\underbrace{\sqrt{\gamma_{L_2}^P}}_{x} \tag{B.9}$$

Appendix C

Derivation of Total Interface Energy Model for AGG

A total energy model is used to quantify the dominant driving force for AGG in terms of both surface and grain boundary energies. These energies compete with each other. Surface energy and grain boundary energy are determined by the specifics of the solid/vapor and solid/solid interface, respectively, of all grains in the metals. Terms are defined below:

A = surface area of sample

$a = \frac{3\sqrt{3}}{2} r_m^2$ = a matrix grain area

t = sample thickness

$2r_m$ = matrix grain size

γ_{GB} = grain boundary energy

γ_S = surface energy

Total Grain Boundary Energy

I will begin by deriving the total grain boundary energy.

1. **2-D formula**

   Assume a through-thickness grain.

   Grain boundary length = $6r$, Grain area = a, grain size = $2r_m$

   In the case of NGG, $2r_m = 2r_{AGG}$*:*

$$\begin{aligned} E_{GB}(r_m) &= \frac{A}{a}\frac{6r_m}{2}t\gamma_{GB} \\ &= \frac{A}{\frac{3\sqrt{3}}{2}r_m^2}3r_m t\gamma_{GB} \\ &= \frac{2At}{\sqrt{3}}\frac{1}{r_m}\gamma_{GB} \end{aligned}$$

$$E_{surf} = (2A + 4\sqrt{At})\gamma_{surf}$$

   In the case of AGG, if $2r_{AGG} \geq t$*:*

$$r_{AGG} = nr_m$$

$$E_{GB}^{AGG} = \left(\frac{6r_m}{2}\right) t \cdot \gamma_{GB}$$

$$= \left(\frac{A - \left(\frac{3\sqrt{3}}{2} r_m^2\right) n^2 t}{(\frac{3\sqrt{3}}{2} r_m^2) t} \right) t \cdot \gamma_{GB}$$

$$= \left(\frac{2A}{3\sqrt{3}} \cdot \frac{1}{r_m} - n^2 r_m \right) 3t\gamma_{GB}$$

2. **3-D formula** Assume a grain with a shape of tetrakaidecahedron.

   Area of grain boundary (surface area of tetrakaidecahedron):

$$a_T = 6(1 + 2\sqrt{3}) r_m^2$$

   Volume of grain:

$$V_T = 8\sqrt{2} r_m^3$$

   Number of grains:

$$N^* = \frac{V_{total} - V_{AGG}}{V_T} = \frac{At - 8\sqrt{2} r_m^3 n^3}{8\sqrt{2} r_m^3}$$

   Grain Boundary Energy:

$$E_{GB} = N^* \cdot \frac{a}{2} \cdot \gamma_{GB}$$

$$E_{GB}^{AGG} = \left[\left(\frac{At}{8\sqrt{2} r_m^3} - n^3 \right) \frac{6(1 + 2\sqrt{3})}{2} r_m^2 \right] \gamma_{GB}$$

$$= \left[\frac{3(1 + 2\sqrt{3})}{8\sqrt{2}} At \frac{1}{r_m} - \frac{6(1 + 2\sqrt{3})}{2} r_m^2 n^3 \right] \gamma_{GB}$$

$$\boxed{\therefore E_{GB}^{AGG} = \left[1.18372 \cdot At \frac{1}{r_m} - 13.3923 \cdot r_m^2 n^3 \right] \gamma_{GB}}$$

Total Surface Energy

Surface energy depends on surface energy density of the exposed crystal plane, γ_{hkl}, and the area fraction, f_{hkl} of each grain with different orientations (e.g. $f_{110} = S_{110}/A$ in 2-D and $f_{110} = S_{110}/A * t$ in 3-D). Average surface energy:

$$E_{surf} = (2A + 4\sqrt{A}t)\gamma_{surf}$$

Let $C = (2A + 4\sqrt{A}t)$Considering surface energy density of (1 0 0), (1 1 0), and (1 1 1) planes.

$$E_{surf} = \frac{C}{3}(\gamma_{100} + \gamma_{110} + \gamma_{111})$$

$$= C(\gamma_{100}f_{100} + \gamma_{110}f_{110} + \gamma_{111}f_{111})$$

where $f_{100} + f_{110} + f_{111} = 1$.

If AGG of Goss (1 1 0) grain occurs:

$$n = \frac{r_{110}}{r_{100} \text{ or } r_{111}}{}^{(\text{AGG})}_{(\text{matrix grains})}$$

For the 2D case, where $t < 2r_{AGG}$: Assuming $a_{110} \leq A$.

$$f_{110} = \frac{a_{110}}{A} = \frac{\frac{3\sqrt{3}}{2}r_{110}^2}{A} = \frac{3\sqrt{3}}{2A}n^2r_m^2$$

$$f_m = f_{100} = f_{111} = \frac{1}{2}\left(1 - \frac{3\sqrt{3}}{2A}n^2r_m^2\right)$$

$$\rightarrow E_{surf.}(r_m) = C\left[\frac{3\sqrt{3}}{2A}n^2r_m^2\cdot\gamma_{110} + \frac{1}{2}\left(1 - \frac{3\sqrt{3}}{2A}n^2r_m^2\right)(\gamma_{100}+\gamma_{111})\right]$$

$$= C\cdot\frac{3\sqrt{3}}{2A}\left[n^2r_m^2\cdot\gamma_{110} + \left(\frac{A}{3\sqrt{3}} - \frac{1}{2}n^2r_m^2\right)(\gamma_{100}+\gamma_{111})\right]$$

$$= C\cdot\frac{3\sqrt{3}}{2A}\left[(n^2\gamma_{110} - \frac{1}{2}n^2\gamma_{100} - \frac{1}{2}n^2\gamma_{111})r_m^2 + \frac{A}{3\sqrt{3}}(\gamma_{100}+\gamma_{111})\right]$$

$$\boxed{\therefore E_{surf.}(r_m) = 3\sqrt{3}\left(1 + \frac{2t}{\sqrt{A}}\right)\left[(\gamma_{110} - \frac{1}{2}\gamma_{100} - \frac{1}{2}\gamma_{111})n^2r_m^2 + \frac{A}{3\sqrt{3}}(\gamma_{100}+\gamma_{111})\right]}$$

For the 3D case, where $2r_m < 2r_{AGG} < t$:

$$f_{110} = \frac{V_{110}}{V} = \frac{8\sqrt{2}r_{110}^3}{At} = \frac{8\sqrt{2}}{At}n^3r_m^3$$

$$f_m = f_{100} = f_{111} = \frac{1}{2}\left(1 - \frac{8\sqrt{2}}{At}n^3r_m^3\right)$$

$$\rightarrow E_{surf.}(r_m) = C\left[\frac{8\sqrt{2}}{At}n^3r_m^3\cdot\gamma_{110} + \frac{1}{2}\left(1 - \frac{8\sqrt{2}}{At}n^3r_m^3\right)(\gamma_{100}+\gamma_{111})\right]$$

$$= C\cdot\frac{8\sqrt{2}}{At}\left[n^3r_m^3\cdot\gamma_{110} + \left(\frac{At}{16\sqrt{2}} - \frac{1}{2}n^3r_m^3\right)(\gamma_{100}+\gamma_{111})\right]$$

$$= C\cdot\frac{8\sqrt{2}}{At}\left[(\gamma_{110} - \frac{1}{2}\gamma_{100} - \frac{1}{2}\gamma_{111})n^3r_m^3 + \frac{At}{16\sqrt{2}}(\gamma_{100}+\gamma_{111})\right]$$

$$\boxed{\therefore E_{surf.}(r_m) = 16\sqrt{2}\left(\frac{1}{t} + \frac{2}{\sqrt{A}}\right)\left[(\gamma_{110} - \frac{1}{2}\gamma_{100} - \frac{1}{2}\gamma_{111})n^3r_m^3 + \frac{At}{16\sqrt{2}}(\gamma_{100}+\gamma_{111})\right]}$$

Bibliography

[1] Göran Engdahl. *Handbook of Giant Magnetostrictive Materials*. Academic Press, San Diego, CA, 1st edition, 1999.

[2] a. G. Olabi and A. Grunwald. Design and application of magnetostrictive materials. *Materials and Design*, 29(2):469–483, 2008.

[3] By Julie Slaughter, Eric Summers, and Etrema Products. Galfenol Energy Harvesting. *ETREMA Proprietary*, (515):1–7, 2011.

[4] Dale Kohler. Promotion of cubic grain growth in 3% silicon iron by control of annealing atmosphere composition. *Journal of Applied Physics*, 408(5):27–29, aug 1960.

[5] John J. Kramer. Nucleation and growth effects in thin ferromagnetic sheets: A review focusing on surface energy-induced secondary recrystallization. *Metallurgical Transactions A*, 23(7):1987–1998, 1992.

[6] D. A. Porter and K. E. Easterling. *Phase Transformations in Metals and Alloys*. Springer US, Boston, MA, 1992.

[7] J. C. Heyraud and J. J. Métois. Growth shapes of metallic crystals and roughening transition. *Journal of Crystal Growth*, 82(3):269–273, 1987.

[8] S.C. Hardy. The surface tension of liquid gallium. *Journal of Crystal Growth*, 71(3):602–606, may 1985.

[9] V. Hoffmann, R. Schaefer, E. Appel, A. Hubert, and H. Soffel. First domain observations with the magneto-optical Kerr effect on Ti-ferrites in rocks and their synthetic equivalents. *Journal of Magnetism and Magnetic Materials*, 71(1):90–94, 1987.

[10] Abraham Marmur. Solid-Surface Characterization by Wetting. *Annual Review of Materials Research*, 39(1):473–489, 2009.

[11] Suok Min Na and Alison Flatau. Thickness dependence of solid-state single crystal conversion in magnetostrictive Fe-Ga alloy from thin foil to thick sheet. *AIP Advances*, 7(5), 2017.

[12] A. J. B. Milne and A. Amirfazli. The Cassie equation: How it is meant to be used. *Advances in Colloid and Interface Science*, 170(1-2):48–55, 2012.

[13] Gene Whyman, Edward Bormashenko, and Tamir Stein. The rigorous derivation of Young, Cassie–Baxter and Wenzel equations and the analysis of the contact angle hysteresis phenomenon. *Chemical Physics Letters*, 450(4-6):355–359, 2008.

[14] S. Giljean, M. Bigerelle, K. Anselme, and H. Haidara. New insights on contact angle/roughness dependence on high surface energy materials. *Applied Surface Science*, 257(22):9631–9638, 2011.

[15] FX Breu, S Guggenbichler, and JC Wollmann. Handbook of Giant Magnetostrictive Materials. *Vasa*, 2008.

[16] Arthur E. Clark, Marilyn Wun-Fogle, James B. Restorff, and Thomas a. Lograsso. Magnetostrictive Properties of Galfenol Alloys Under Compressive Stress. *Materials Transactions*, 43(5):881–886, 2002.

[17] Tomoyuki Kakeshita, Tetsuya Takeuchi, Takashi Fukuda, Masato Tsujiguchi, Toshio Saburi, Ryuichiro Oshima, and Shunsuke Muto. Giant magnetostriction in an ordered Fe[sub 3]Pt single crystal exhibiting a martensitic transformation. *Applied Physics Letters*, 77(10):1502, sep 2000.

[18] C. Prados, I. Panagiotopoulus, G.C. Hadjipanayis, J.J. Freijo, and A. Hernando. High magnetostriction in low applied magnetic fields in amorphous Tb-Fe (hard)/Fe-B (soft) multilayers. *IEEE Transactions on Magnetics*, 33(5):3712–3714, 1997.

[19] Toshiyuki Ueno and Sotoshi Yamada. Performance of energy harvester using iron-gallium alloy in free vibration. *IEEE Transactions on Magnetics*, 47(10):2407–2409, 2011.

[20] J. D. Verhoeven, E. D. Gibson, O. D. Mcmasters, and J. E. Ostenson. Directional Solidification and Heat Treatment of TerfenoI-D Magnetostrictive Materials. *Metallurgical Transactions A*, 21(August):2249–2255, aug 1990.

[21] J. D. Verhoeven, E. D. Gibson, O. D. McMasters, and H. H. Baker. The growth of single crystal Terfenol-D crystals. *Metallurgical Transactions A*, 18(2):223–231, feb 1987.

[22] O.D. McMasters, J.D. Verhoeven, and E.D. Gibson. Preparation of Terfenol-D by float zone solidification. *Journal of Magnetism and Magnetic Materials*, 54-57:849–850, feb 1986.

[23] MetalPrices.com. Current Terbium Price, 2014.

[24] Anthony King. Analysts shrug off rare earth trade ruling, 2014.

[25] Jayasimha Atulasimha and Alison B Flatau. A review of magnetostrictive iron–gallium alloys. *Smart Materials and Structures*, 20(4):043001, 2011.

[26] Toshiyuki Ueno and Toshiro Higuchi. Magnetic circuit for stress-based magnetic force control using iron-gallium alloy. *IEEE Transactions on Magnetics*, 43(6):2594–2596, 2007.

[27] Yanning Zhang and Ruqian Wu. Mechanism of large magnetostriction of galfenol. *IEEE Transactions on Magnetics*, 47(10):4044–4049, 2011.

[28] Eric M. Summers, Rob Meloy, and Suok-Min Na. Magnetostriction and texture relationships in annealed galfenol alloys. *Journal of Applied Physics*, 105(7):07A922, 2009.

[29] Suok-Min Na and Alison B. Flatau. Surface-energy-induced selective growth of (001) grains in magnetostrictive ternary Fe–Ga-based alloys. *Smart Materials and Structures*, 21(5):055024, may 2012.

[30] J.-H. Yoo, J. B. Restorff, M. Wun-Fogle, and A. B. Flatau. The effect of magnetic field annealing on single crystal iron gallium alloy. *Journal of Applied Physics*, 103(7):07B325, feb 2008.

[31] J.-H. Yoo, S.-M. Na, J.B. Restorff, M. Wun-Fogle, and A.B. Flatau. The Effect of Field Annealing on Highly <newline/>Textured Polycrystalline Galfenol Strips. *IEEE Transactions on Magnetics*, 45(10):4145–4148, oct 2009.

[32] J.B. Restorff, M. Wun-Fogle, A.E. Clark, and K.B. Hathaway. Induced Magnetic Anisotropy in Stress-Annealed Galfenol Alloys. *IEEE Transactions on Magnetics*, 42(10):3087–3089, oct 2006.

[33] Eric Summers, Rob Meloy, and J. B. Restorff. Galfenol alloying additions and the effects on

uniaxial anisotropy generation. *Journal of Applied Physics*, 106(2):024914, 2009.

[34] John L. Walter. Control of Texture in Magnetic Material by Surface Energy. *Journal of Applied Physics*, 36(3):1213, jul 1965.

[35] Suok-Min Na, S.J. Suh, and Alison B. Flatau. Surface segregation and texture development in rolled Fe–Ga alloy. *Journal of Magnetism and Magnetic Materials*, 310(2):2630–2632, mar 2007.

[36] J. L. Gonzalez, A. Rubio, and F. Moll. Human powered piezoelectric batteries to supply power to wearable electronic devices,, 2002.

[37] C. R. Saha, T. O'Donnell, N. Wang, and P. McCloskey. Electromagnetic generator for harvesting energy from human motion. *Sensors and Actuators, A: Physical*, 147(1):248–253, 2008.

[38] Arthur E. Clark, K. B. Hathaway, M. Wun-Fogle, J. B. Restorff, T. A. Lograsso, V. M. Keppens, G. Petculescu, and R. A. Taylor. Extraordinary magnetoelasticity and lattice softening in bcc Fe-Ga alloys. *Journal of Applied Physics*, 93(10):8621, 2003.

[39] Toshiyuki Ueno and Sotoshi Yamada. Technical Information: Vibrational Energy Harvester using Magnetostrictive Material, 2015.

[40] Suok-Min Na, Matthew Rice, Ganesh Raghunath, Vera Klimchenko, and Alison B. Flatau. Magnetostrictive Alfenol Whisker Sensor Performance and Sensitivity to Whisker Thickness. *IEEE Transactions on Magnetics*, 50(11):1–4, nov 2014.

[41] Ganesh Raghunath, Alison B. Flatau, Suok-Min Na, and Brett Barkley. Development of a Bio-Inspired Tactile Magnetostrictive Whisker Sensor Using Alfenol. In *Volume 2: Mechanics and Behavior of Active Materials; Integrated System Design and Implementation; Bioinspired Smart Materials and Systems; Energy Harvesting*, page V002T04A012. ASME, sep 2014.

[42] J.-H. Yoo and Alison B. Flatau. A bending-mode galfenol electric power harvester. *Journal of Intelligent Material Systems and Structures*, 23(6):647–654, feb 2012.

[43] Suok-Min Na and Alison B. Flatau. Temperature dependence of abnormal grain growth and high magnetostriction in Goss-oriented

Fe-Al thin sheets. *Journal of Applied Physics*, 115(17):17A913, may 2014.

[44] Suok-Min Na and Alison B. Flatau. Texture evolution and probability distribution of Goss orientation in magnetostrictive Fe – Ga alloy sheets. *Journal of Materials Science*, 49(22):7697–7706, 2014.

[45] Suok-Min Na and Alison B. Flatau. Global Goss grain growth and grain boundary characteristics in magnetostrictive Galfenol sheets. *Smart Materials and Structures*, 22(12):125026, dec 2013.

[46] Michael Brooks, Eric Summers, J. B. Restorff, and M. Wun-Fogle. Behavior of magnetic field–annealed Galfenol steel. *Journal of Applied Physics*, 111(7):07A907, 2012.

[47] Kong Ling Bing, Tao Li, Huey Hoon Hng, Freddy Boey, Tianshu Zhang, and Sean Li. *Waste Energy Harvesting: Mechanical and Thermal Energies*. Springer Science & Business Media, 2014.

[48] R. G. Aspden, J. A. Berger, and H. E. Trout. New texture in iron and iron base alloys. *Journal of Applied Physics*, 37(3):1195–1196, 1966.

[49] Suok-Min Na and Alison B. Flatau. Secondary recrystallization, crystallographic texture and magnetostriction in rolled Fe–Ga based alloys. *Journal of Applied Physics*, 101(9):09N518, 2007.

[50] Suok-Min Na and Alison B. Flatau. Deformation behavior and magnetostriction of polycrystalline Fe–Ga–X (X=B,C,Mn,Mo,Nb,NbC) alloys. *Journal of Applied Physics*, 103(7):07D304, 2008.

[51] Suok M. Na, Jin Hyeong Yoo, and Alison B. Flatau. Abnormal (110) grain growth and magnetostriction in recrystallized galfenol with dispersed niobium carbide. *IEEE Transactions on Magnetics*, 45(10):4132–4135, 2009.

[52] Suok-Min Na and Alison B. Flatau. Single grain growth and large magnetostriction in secondarily recrystallized Fe-Ga thin sheet with sharp Goss (0 1 1)[1 0 0] orientation. *Scripta Materialia*, 66(5):307–310, 2012.

[53] Suok-Min Na and Alison B. Flatau. Single grain growth and large magnetostriction in secondarily recrystallized Fe–Ga thin sheet with sharp Goss (011)[100] orientation. *Scripta Materialia*, 66(5):307–310, mar 2012.

[54] Suok-Min Na, Andrew Passel, Patrick Downey, and Alison B. Flatau. Magnetostrictive Fe-Ga alloy strips with a preferred orientation for lamination actuators. *Physica Status Solidi (a)*, 210(6):1076–1082, jun 2013.

[55] Suok Min Na, Katherine M. Atwater, and Alison B. Flatau. Particle pinning force thresholds for promoting abnormal grain growth in magnetostrictive Fe-Ga alloy sheets. *Scripta Materialia*, 100(April):1–4, 2015.

[56] John L. Walter. Control of Texture in Magnetic Material by Surface Energy. *Journal of Applied Physics*, 36(3):8–15, 1965.

[57] W. W. Mullins. Theory of Thermal Grooving. *Journal of Applied Physics*, 28(3):333, 1957.

[58] W.W Mullins. The effect of thermal grooving on grain boundary motion. *Acta Metallurgica*, 6(6):414–427, jun 1958.

[59] D. W. Blakely and G. A. Somorjai. The stability and structure of high miller index platinum crystal surfaces in vacuum and in the presence of adsorbed carbon and oxygen. *Surface Science*, 65(2):419–442, 1977.

[60] Hyunsuk Chun, Suok-Min Na, Chaitanya Mudivarthi, and Alison B. Flatau. The role of misorientation and coincident site lattice boundaries in Goss-textured Galfenol rolled sheet. *Journal of Applied Physics*, 107(9):09A960, 2010.

[61] Stephan Schönecker, Xiaoqing Li, Börje Johansson, Se Kyun Kwon, and Levente Vitos. Thermal surface free energy and stress of iron. *Scientific Reports*, 5:14860, jan 2015.

[62] M. Elbaum and J. S. Wettlaufer. Relation of growth and equilibrium crystal shapes. *Physical Review E*, 48(4):3180–3183, oct 1993.

[63] David M. Saylor and Gregory S. Rohrer. Measuring the Influence of Grain-Boundary Misorientation on Thermal Groove Geometry in Ceramic Polycrystals. *Journal of the American Ceramic Society*, 82(6):1529–1536, dec 2004.

[64] C. Bombis, A. Emundts, M. Nowicki, and H. P. Bonzel. Absolute surface free energies of Pb. *Surface Science*, 511(1-3):83–96, 2002.

[65] Richard Tran, Zihan Xu, Balachandran Radhakrishnan, Donald Winston, Wenhao Sun, Kristin A. Persson, and Shyue Ping Ong. Surface energies of elemental crystals. *Scientific Data*, 3(9):160080, sep 2016.

[66] H.P. Bonzel. 3D equilibrium crystal shapes in the new light of STM and AFM. *Physics Reports*, 385(1-2):1–67, 2003.

[67] R C Cammarata. Surface and Interface Stress Effects in Thin-Films. *Progress in Surface Science*, 46(1):1–38, 1994.

[68] Jacob N. Israelachvili. *Intermolecular and Surface Forces*. Elsevier, 2011.

[69] John J. Gilman. Direct Measurements of the Surface Energies of Crystals. *Journal of Applied Physics*, 31(12):2208–2218, dec 1960.

[70] I Egry, E Ricci, R Novakovic, and S Ozawa. Surface tension of liquid metals and alloys–recent developments. *Advances in colloid and interface science*, 159(2):198–212, sep 2010.

[71] By Roger P Woodward and D Ph. Surface Tension Measurements Using the Drop Shape Method. *First Ten Angstroms Inc Technical Information*, pages 1–6, 2008.

[72] Robert J. Good and Carel J. van Oss. The Modern Theory of Contact Angles and the Hydrogen Bond Components of Surface Energies. In *Modern Approaches to Wettability*, pages 1–27. Springer US, Boston, MA, 1992.

[73] Soojin Park and Min-Kang Seo. *Interface Science and Composites*. Academic Press, 2011.

[74] FM Fowkes. Role of surface active agents in wetting. *The Journal of Physical Chemistry*, 57(3):98–103, 1953.

[75] N. D. Lang and W. Kohn. Theory of Metal Surfaces: Charge Density and Surface Energy. *Physical Review B*, 1(12):4555–4568, jun 1970.

[76] Souheng Wu. Polar and Nonpolar Interactions in Adhesion. *The Journal of Adhesion*, 5(1):39–55, jan 1973.

[77] Robert J. Good and L. A. Girifalco. A theory for estimation of surface and interfacial energies. III. Estimation of surface energies of solids from contact angle data. *The Journal of Physical Chemistry*, 64(5):561–565, may 1960.

[78] Frederick M Fowkes. Attractive forces at interfaces. *Industrial & Engineering Chemistry*, 56(12):40–52, 1964.

[79] A Kahouli, A Sylvestre, J-F Laithier, S Pairis, J-L Garden, E André, F Jomni, and B Yangui. Effect of O 2 , Ar/H 2 and CF 4 plasma treatments on the structural and dielectric properties of parylene-C thin films. *Journal of Physics D: Applied Physics*, 45(21):215306, may 2012.

[80] D.H. Shin, C.U. Bang, J.H. Kim, Y.C. Hong, H.S. Uhm, D.K. Park, and K.H. Kim. Treatment of Metal Surface by Atmospheric Microwave Plasma Jet. *IEEE Transactions on Plasma Science*, 34(4):1241–1246, aug 2006.

[81] Samad Ahadian, Siamak Moradian, and Mohammad Amani Tehran. Assessing the equation of state and comparing it with other relationships used for determining the surface tension of solids. *Applied Surface Science*, 256(7):1983–1991, jan 2010.

[82] Dy Kwok and Aw Neumann. Contact angle measurements and interpretation: wetting behavior and solid surface tensions for poly (alkyl methacrylate) polymers. *Journal of Adhesion Science and Technology*, 14(5):719–743, 2000.

[83] H Tavana, F Simon, K Grundke, D Y Kwok, M L Hair, and a W Neumann. Interpretation of contact angle measurements on two different fluoropolymers for the determination of solid surface tension. *Journal of colloid and interface science*, 291(2):497–506, nov 2005.

[84] Marcio Costa, Hui Wang, Jun Hu, Ruqian Wu, Suok-Min Na, Hyunsuk Chun, and Alison B. Flatau. Orientation dependences of surface morphologies and energies of iron–gallium alloys. *Surface Science*, 647:26–32, 2016.

[85] S. G. Wang, E. K. Tian, and C. W. Lung. Surface energy of arbitrary crystal plane of bcc and fcc metals. *Journal of Physics and Chemistry of Solids*, 61(8):1295–1300, 2000.

[86] Gregory S. Rohrer. "Introduction to grains, phases, and interfaces - An interpretation of microstructure," Trans. AIME, 1948, vol. 175, pp. 15-51, by C.S. Smith. *Metallurgical and Materials Transactions B: Process Metallurgy and Materials Processing Science*, 41(3):457, 2010.

[87] Thomas Skidmore, Rudy G. Buchheit, and Mary C. Juhas. Grain boundary energy vs. misorientation in Inconel® 600 alloy as measured by thermal groove and OIM analysis correlation. *Scripta Materialia*, 50(6):873–877, mar 2004.

[88] R. A. Kellogg, A. M. Russell, T. A. Lograsso, A. B. Flatau, A. E. Clark, and M. Wun-Fogle. Tensile properties of magnetostrictive iron-gallium alloys. *Acta Materialia*, 52(17):5043–5050, 2004.

[89] V. Hoffmann, R. Schäfer, E. Appel, A. Hubert, and H. Soffel. First domain observations with the magneto-optical Kerr effect on Ti-ferrites in rocks and their synthetic equivalents. *Journal of Magnetism and Magnetic Materials*, 71(1):90–94, dec 1987.

[90] M.J. Regan, E.H. Kawamoto, S. Lee, and P.S. Pershan. Surface layering in liquid gallium: An x-ray reflectivity study. *Physical Review Letters*, 75(13):2498–2501, 1995.

[91] M.J. Regan, H. Tostmann, P. S. Pershan, O. M. Magnussen, E. DiMasi, B. M. Ocko, and M. Deutsch. X-ray study of the oxidation of liquid-gallium surfaces. *Physical Review B*, 55(16):10786–10790, 1997.

[92] F. Scharmann, G. Cherkashinin, V. Breternitz, Ch. Knedlik, G. Hartung, Th. Weber, and J. a. Schaefer. Viscosity effect on GaInSn studied by XPS. *Surface and Interface Analysis*, 36(8):981–985, 2004.

[93] William M Saltman and Norman H. Nachtrieb. The Electrochemistry of Gallium. *Journal of The Electrochemical Society*, 100(3):126, 1953.

[94] B. B. Alchagirov and a. G. Mozgovoi. The surface tension of Molten Gallium at high temperatures. *High Temperature*, 43(5):791–792, 2005.

[95] Daeyoung Kim, Peter Thissen, Gloria Viner, Dong Weon Lee, Wonjae Choi, Yves J. Chabal, and Jeong Bong Lee. Recovery of nonwetting characteristics by surface modification of gallium-based liquid metal droplets using hydrochloric acid vapor. *ACS Applied Materials and Interfaces*, 5(1):179–185, 2013.

[96] Kyle Doudrick, Shanliangzi Liu, Eva M. Mutunga, Kate L. Klein, Viraj Damle, Kripa K. Varanasi, and Konrad Rykaczewski. Different shades of oxide: From nanoscale wetting mechanisms to contact printing of gallium-based liquid metals. *Langmuir*, 30(23):6867–6877, 2014.

[97] Mohammad Rashed Khan, Collin B. Eaker, Edmond F. Bowden, and Michael D. Dickey. Giant and switchable surface activity of liquid metal via surface oxidation. *Proceedings of the National Academy of Sciences*, 111(39):14047–14051, 2014.

[98] Perrin Walker and William H Tarn. *Handbook of Metal Etchants*. CRC Press, 1991.

[99] S. P. Yatsenko, L. N. Rykova, Yu. A. Anikin, and E. N. Dieva. The corrosion of group VIII

metals in liquid gallium. *Soviet Materials Science*, 8(3):310–313, 1974.

[100] Ka Narh, Vp Dwivedi, Jm Grow, A. Stana, and W.Y. Shih. The effect of liquid gallium on the strengths of stainless steel and thermoplastics. *Journal of materials science*, 33:329–337, 1998.

[101] F. Barbier and J. Blanc. Corrosion of martensitic and austenitic steels in liquid gallium. *Journal of Materials Research*, 14(03):737–744, jan 1999.

[102] Michael Van Order, Suok-Min Na, and Alison B. Flatau. Surface energy measurement of metallic substrates around room temperature using liquid gallium drop method. In *XXIV International Materials Research Congress*, Cancun, Mexico, 2015.

[103] M. Van Order, Suok-Min Na, and Alison B. Flatau. Surface energy measurement of metallic substrates using liquid gallium drop method. In *2015 MRS Fall Meeting*, Boston, MA, 2015.

[104] J Schultz, Kazuo Tsutsumi, and Jean-Baptiste Donnet. Surface properties of High-Energy Solids: I. Determination of the Dispersive Component of the Surface Free Energy of Mica and Its Energy of Adhesion to Water and n-alkanes. *Journal of Colloid and Interface Science*, 59(2):272–276, 1977.

[105] J Schultz, Kazuo Tsutsumi, and Jean-Baptiste Donnet. Surface Properties of High-Energy Solids: II. Determination of the Nondispersive Component of the Surface Freee Energy of Mica and Its Energy of Adhesion to Polar Liquids. *Journal of colloid and interface science*, 59(2):277–282, 1977.

[106] Jacques Schultz and Michel Nardin. Determination of the Surface Energy of Solids by the Two-Liquid-Phase Method. In Malcolm E Schrader and George I Loeb, editors, *Modern Approaches to Wettability: Theory and Applications*, pages 73–100. Springer US, Boston, MA, 1992.

[107] P. Chassin, C Jounay, and H Quiquampoix. Measurement of the surface free energy of calcium-montmorillonite. *CLAY MINER. Clay Miner.*, 21(5):899–907, 1986.

[108] W Smitthipong, M Nardin, J Schultz, T Nipithakul, and K Suchiva. Study of tack properties of uncrosslinked natural rubber. *Journal of Adhesion Science and Technology*, 18(12):1449–1463, 2004.

[109] Yuma Takanashi and Jiro Kumaki. Significant melting point depression of two-dimensional folded-chain crystals of isotactic poly(methyl methacrylate)s observed by high-resolution in situ atomic force microscopy. *Journal of Physical Chemistry B*, 117(18):5594–5605, 2013.

[110] Miho Nakamura, Naoko Hori, Saki Namba, Takeshi Toyama, Nobuyuki Nishimiya, and Kimihiro Yamashita. Wettability and surface free energy of polarised ceramic biomaterials. *Biomedical Materials*, 10(1):011001, 2015.

[111] F Ostendorf, C Schmitz, S Hirth, A Kühnle, J J Kolodziej, and M Reichling. How flat is an air-cleaved mica surface? *Nanotechnology*, 19(30):305705, 2008.

[112] Tammar S. Meiron, Abraham Marmur, and I. Sam Saguy. Contact angle measurement on rough surfaces. *Journal of Colloid and Interface Science*, 274(2):637–644, 2004.

[113] Claire Andrieu and Franqoise Brochard. Average Spreading Parameter on Heterogeneous Surfaces. *Langmuir*, 104(2):2077–2080, 1994.

[114] J. Jiyou Guo and Jennifer A. Lewis. Aggregation Effects on the Compressive Flow Properties and Drying Behavior of Colloidal Silica Suspensions. *Journal of the American Ceramic Society*, 82(9):2345–2358, 1999.

[115] Yusuke Arima and Hiroo Iwata. Effect of wettability and surface functional groups on protein adsorption and cell adhesion using well-defined mixed self-assembled monolayers. *Biomaterials*, 28(20):3074–3082, 2007.

[116] Guillermo Cantero, Aitor Arbelaiz, Rodrigo Llano-Ponte, and Inaki Mondragon. Effects of fibre treatment on wettability and mechanical behaviour of flax/polypropylene composites. *Composites Science and Technology*, 63(9):1247–1254, 2003.

[117] L. T. Zhuravlev. Concentration of Hydroxyl Groups on the Surface of Amorphous Silicas. *Langmuir*, 3(3):316–318, 1987.

[118] G. Kresse and J. Furthmüller. Efficient iterative schemes for ab initio total-energy calculations using a plane-wave basis set. *Physical Review B*, 54(16):11169–11186, oct 1996.

[119] G. Kresse and J. Hafner. Ab initio molecular-dynamics simulation of the liquid-metal–amorphous-semiconductor transition in germanium. *Physical Review B*, 49(20):14251–14269, may 1994.

[120] John P. Perdew, Kieron Burke, and Matthias Ernzerhof. Generalized Gradient Approximation Made Simple. *Physical Review Letters*, 77(18):3865–3868, oct 1996.

[121] G. Kresse and D. Joubert. From ultrasoft pseudopotentials to the projector augmented-wave method. *Physical Review B*, 59(3):1758–1775, jan 1999.

[122] P. E. Blöchl. Projector augmented-wave method. *Physical Review B*, 50(24):17953–17979, dec 1994.

[123] Hui Wang, Y. N. Zhang, R. Q. Wu, L. Z. Sun, D. S. Xu, and Z. D. Zhang. Understanding strong magnetostriction in FeGa alloys. *Scientific Reports*, 3(1):3521, dec 2013.

[124] Hui Wang, Z.D. Zhang, R.Q. Wu, and L.Z. Sun. Large-scale first-principles determination of anisotropic mechanical properties of magnetostrictive Fe–Ga alloys. *Acta Materialia*, 61(8):2919–2925, may 2013.

[125] Hendrik J. Monkhorst and James D. Pack. Special points for Brillouin-zone integrations. *Physical Review B*, 13(12):5188–5192, 1976.

[126] Shayandev Sinha, Khaled A. Mahmoud, and Siddhartha Das. Conditions for spontaneous oil–water separation with oil–water separators. *RSC Advances*, 5(98):80184–80191, 2015.

[127] Philip S. Brown and Bharat Bhushan. Mechanically durable, superoleophobic coatings prepared by layer-by-layer technique for anti-smudge and oil-water separation. *Scientific Reports*, 5(1):8701, aug 2015.

[128] C. J. Powell and A. Jablonski. Evaluation of Calculated and Measured Electron Inelastic Mean Free Paths Near Solid Surfaces. *Journal of Physical and Chemical Reference Data*, 28(1):19–62, jan 1999.

[129] C.J. Powell and A. Jablonski. The NIST Electron Effective-Attenuation-Length Database. *Journal of Surface Analysis*, 9(3):322–325, 2002.

[130] C J Powell and A Jablonski. NIST Electron Inelastic-Mean-Free-Path Database. *U.S. Department of Commerce*, (71), 2010.

[131] Peter J. Cumpson. The Thickogram: a method for easy film thickness measurement in XPS. *Surface and Interface Analysis*, 29(6):403–406, jun 2000.

[132] Toru Yamashita and Peter Hayes. Analysis of XPS spectra of Fe2+ and Fe3+ ions

in oxide materials. *Applied Surface Science*, 254(8):2441–2449, 2008.

[133] K. Lejaeghere, V. Van Speybroeck, G. Van Oost, and S. Cottenier. Error estimates for solid-state density-functional theory predictions: An overview by means of the ground-state elemental crystals. *Critical Reviews in Solid State and Materials Sciences*, 39(1):1–24, 2014.

[134] C G Dunn and J L Walter. Surface energies and other surface effects relating to secondary recrystallization textures in high-purity iron, zone-refined iron, and 0.6 pct Si-Fe. *Transactions of the Metallurgical Society of AIME*, 224(3):518, 1962.

[135] A. B. D. Cassie and S. Baxter. Wettability of porous surfaces. *Transactions of the Faraday Society*, 40(5):546–551, 1944.

[136] Bharat Bhushan and Yong Chae Jung. Wetting, adhesion and friction of superhydrophobic and hydrophilic leaves and fabricated micro/nanopatterned surfaces. *Journal of Physics: Condensed Matter*, 20(22):225010, 2008.

[137] B. Bhushan, Y. C. Jung, and K. Koch. Micro-, nano- and hierarchical structures for superhydrophobicity, self-cleaning and low adhesion. *Philosophical Transactions of the Royal Society A: Mathematical, Physical and Engineering Sciences*, 367(1894):1631–1672, 2009.

[138] Frank Schellenberger, Noemí Encinas, Doris Vollmer, and Hans-Jürgen Butt. How Water Advances on Superhydrophobic Surfaces. *Physical Review Letters*, 096101(March):2–7, 2016.

[139] Eric Summers, Rob Meloy, and J. B. Restorff. Galfenol alloying additions and the effects on uniaxial anisotropy generation. *Journal of Applied Physics*, 106(2):024914, jul 2009.